A STRUCTURAL MODEL FOR THE JAVA MARGIN SUBDUCTION ZONE, INDONESIA, FROM MULTI-CHANNEL AND WIDE-ANGLE SEISMIC DATA

DISSERTATION

zur Erlangung des Doktorgrades

an der Mathematisch-Naturwissenschaftlichen Fakultät
der Christian-Albrechts-Universität zu Kiel

vorgelegt von

YUEYANG XIA

Kiel, 2022

Referent: ....Professor Heidrun Kopp

Koreferent:.. Professor Christian Berndt

Tag der mündlichen Prüfung: 12.July.2022

Zum Druck genehmigt:.. 12.July.2022

………………………………………………………..

Der Dekan

Hiermit erkläre ich, dass ich die vorliegende Doktorarbeit selbständig und ohne Zuhilfenahme unerlaubter Hilfsmittel erstellt habe. Weder diese noch eine ähnliche Arbeit wurde an einer anderen Abteilung oder Hochschule im Rahmen eines Prüfungsverfahrens vorgelegt, veröffentlicht oder zur Veröffentlichung vorgelegt. Ferner versichere ich, dass die Arbeit unter Einhaltung der Regeln guter wissenschaftlicher Praxis der Deutschen Forschungsgemeinschaft entstanden ist. Ich versichere, dass mir noch kein akademischer Titel entzogen wurde.

Yueyang Xia

Kiel, den………………………………………………………………..

Yueyang Xia

ABSTRACT

Convergent plate margins and subduction zones attracted the geophysical community's attention for decades due to their complex geological structure, endmember plate movement signature, and the tremendous geo-hazard (e.g., megathrust earthquakes and earthquake-related tsunamis) re-occurring globally, which result in a loss in both human casualties, and descent of the regional economy. In order to understand the nature of plate margin tectonics, a broad series of geophysical, geological, geochemical, and numerical approaches have been developed in the past decades to collect subsurface information beneath the seafloor and investigate the kinematics of the plate subduction. Active source multi-channel seismic (MCS) streamer hydrophones and ocean bottom seismometers (OBS) are two essential and mature methods to observe the subsurface structure and derive the tectonic plates' physical properties. Both approaches retrieved fundamental and astonishing information about the structural geology and the earthquake triggering mechanisms (Kodaira et al., 2000; Kopp et al., 2006; Mochizuki et al., 2008; Ranero and von Huene, 2000; Sallarès and Ranero, 2019) by the state-of-the-art numerical inversion techniques such as pre-stack depth migration (Yilmaz, 2001), reflection P-wave velocity inversion (Woodward et al., 2008), and P-wave velocity joint inversion from the reflection and refraction travel times (TOMO2D) (Korenaga et al., 2000).

The plate margin offshore Java and the Lesser Sunda islands are located in the eastern portion of the 7000 km long Sunda plate margin, which starts from the Burma and Andaman arc in the north-west to the Banda arc in the south-east, with a maximum oceanic plate age of 140 Ma (Hamilton, 1988). Different geological configurations vary enormously from the west to the east due to the variations in sediment supply and the different nature of the oceanic plates along the convergent plate boundary (McNeill et al., 2017). The Sunda arc hosts earthquakes spanning from moderate magnitude ones (e.g., in 1994 and 2006 Java earthquakes) to some of the largest earthquakes on Earth (e.g., in 2004 and 2006 Sumatra earthquakes). In order to understand the current tectonic structure, the oceanic crust relief, and the temporal evolution of the large volume accretionary mass, we use MCS streamer data and OBS data collected by BGR and GEOMAR in the eastern Java margin and Lesser Sunda margin to image the plate interface reflection, the upper plate tectonic structure, and velocity attributes of the convergent plates.

In this study, we incorporate an innovative seismic processing approach called the Non-Rigid Matching technique applied to the reflection tomography and the pre-stack depth migration and retrieve the structural image of the forearc wedge and the geometry of the plate interface. These geophysical observations reveal the dynamic process of the formation of the accretionary wedge by plates converging and illustrate the existence of subducting seamounts on the plate interface. The depth migrated seismic sections and the high-resolution bathymetry reveal different scales and shapes of the oceanic relief, including large conical seamounts (diameter up to 40 km), linear-shaped ridges, and oceanic plate-bending normal faults with small offsets (< 150 m) ranging from the western side to eastern side of the study area. Except for the relatively small scarps of the oceanic normal faults, seamounts and ridges breach the oceanic sediment cover and come into direct contact with the upper plate. These seafloor topographic structures collide with the convergent plate margin's deformation front, tunnel the upper accretionary plate and result in different structural signatures on different flanks of these subducting reliefs. On the one hand, at the leading edge of the subducting seamount, the upper plate structure features a more active compressional structure (e.g., active fore-thrust, splay fault and imbricate structure). On the other hand, on the trailing edge of the seamount, the gravity-driven extensional deformations (e.g., landslide and slump) overprinted the pre-existing compressional structures. Besides, tunnelling of the oceanic relief results in the upward migration of the décollement, imaged as a strong reversed wavelet polarity compared to the seafloor reflection, and thus contributes to the process of subduction erosion, which removes and transports the upper plate accreted sediment to a greater depth.

Moreover, we compared the observed subducting seamount location with the 1994 tsunami earthquake epicentre, the co-seismic slip model, and the aftershock focal mechanisms. We conclude that the seamount, which is observed offshore eastern Java in seismic profile BGR06_305, can host a seismic locking zone in front of it. Since the décollement at the seamount region is featured by low co-seismic slip during the 1994 co-seismic rupture event, the seamount acts as an earthquake barrier in this rupture's propagation process. Since aftershocks are mainly contributed by normal fault earthquakes, the nucleation could be regarded as a complete stress drop and implies that the seamount is very weakly coupled in the inter-seismic period.

KURZFASSUNG

Konvergente Plattenränder und Subduktionszonen erregten jahrzehntelang die Aufmerksamkeit der geophysikalischen Gemeinschaft aufgrund ihrer komplexen geologischen Struktur, der Signatur der Plattenbewegung und der daraus resultierenden enormen Naturgefahren (z. B. Megathrust-Erdbeben und erdbebenbedingte Tsunamis), die weltweit immer wieder auftreten mit Verlusten sowohl durch menschliche Opfer als auch durch den Niedergang der regionalen Wirtschaft. Um die Plattenrandtektonik zu verstehen, wurde in den letzten Jahrzehnten eine Reihe von geophysikalischen, geologischen, geochemischen und numerischen Ansätzen entwickelt, um Informationen unter dem Meeresboden zu sammeln und die Kinematik der Plattensubduktion zu untersuchen. Mehrkanal-Seismik mit aktiver Quelle und Ozeanboden-Seismometer (OBS) sind zwei wesentliche und ausgereifte Methoden zur Beobachtung der unterirdischen Struktur und der physikalischen Eigenschaften der tektonischen Platten. Beide Ansätze erzielten grundlegende und erstaunliche Erkenntnisse über die Untergrundstruktur und ihre Erdbebenauslösemechanismen (Kodaira et al., 2000; Kopp et al., 2006; Mochizuki et al., 2008; Ranero und Von Huene, 2000; Sallarès und Ranero, 2019) durch modernste numerische Inversionstechniken wie Pre-Stack-Tiefenmigration (Yilmaz, 2001), Reflexions-P-Wellen-Geschwindigkeitsinversion (Woodward et al., 2008) und P-Wellen-Geschwindigkeitsinversion aus den Reflexions- und Refraktionslaufzeiten (TOMO2D) (Korenaga et al., 2000).

Der Plattenrand vor der Insel Java und den Kleinen Sunda-Inseln befindet sich im östlichen Teil des 7000 km langen Sunda-Plattenrandes, der sich vom Burma- und Andaman-Bogen im Nordwesten bis zum Banda-Bogen im Südosten mit einem maximalen Plattenalter von 140 Ma (Hamilton, 1988) erstreckt. Unterschiedliche geologische Konfigurationen variieren enorm von West nach Ost aufgrund des unterschiedlichen Sedimenteintrags und der Beschaffenheit der ozeanischen Platten entlang der konvergenten Plattengrenze (McNeill et al., 2017). Am Sunda-Bogen werden Erdbeben mittlerer Stärke (z. B. die Java-Erdbeben von 1994 und 2006) bis zu einigen der größten Erdbeben der Erde (z. B. die Sumatra-Erdbeben von 2004 und 2006) beobachtet. Um die aktuelle tektonische Struktur, das ozeanische Krustenrelief und die zeitliche Entwicklung des großen Volumens an Akkretionskeilmasse zu verstehen, werden MCS-Streamerdaten und OBS-Daten verwendet, die von der BGR und GEOMAR gemeinsam am östlichen Java-Rand erhoben wurden, um die Plattengrenzflächenreflexion, die tektonische Struktur der oberen Platte sowie das interne Geschwindigkeitsfeld der Untergrundstrukturen abzubilden.

In dieser Studie integrieren wir einen innovativen geophysikalischen Ansatz namens Non-Rigid Matching-Technik, um die Reflexionstomographie und die pre-stack Tiefenmigration zu implementieren und das strukturelle Abbild des Forearc-Keils und der Geometrie der Plattenschnittstelle zu erhalten. Diese geophysikalischen Beobachtungen zeigen den dynamischen Prozess der Bildung des Akkretionskeils durch konvergente Platten und veranschaulichen die Existenz subduzierender Seeberge an der Plattengrenzfläche. Die seismischen Profile in Tiefendarstellung und die hochauflösende Bathymetrie zeigen unterschiedliche Ausmaße und Formen der ozeanischen Reliefs, darunter große konische Seeberge (Durchmesser bis zu 40 km), linear geformte Rücken und die abtauchende ozeanische Plattengrenze mit kleinen Versätzen (< 150 m) von der westlichen bis zur östlichen Seite des Untersuchungsgebiets. Mit Ausnahme der relativ kleinen Verwerfungen in der ozeanischen Platte durchbrechen Seeberge und Rücken die ozeanische Sedimentdecke und kommen in direkten Kontakt mit der oberen Platte. Diese topografischen Strukturen des Meeresbodens kollidieren mit der Verformungsfront des konvergenten Plattenrandes, unterlaufen die obere Akkretionsstruktur und führen zu deutlich unterschiedlichen strukturellen Signaturen an unterschiedlichen Flanken dieses subduzierenden Reliefs. Einerseits weist die obere Plattenstruktur an der Vorderkante des subduzierenden Seebergs aktive Kompressionsstrukturen auf (z. B. aktiver Vorschub, Spreizbruch und Schuppenstruktur). Im Gegensatz zeigt die obere Platte an der Hinterkante des Seebergs Kompressionsstrukturen und schwerkraftbedingte Extensionsstrukturen (z. B. Erdrutsch). Des Weiteren führt die Subduktion der Seeberge auf der ozeanischen Platte zu einer Aufwärtswanderung der Plattengrenzfläche, deren Reflexionen eine inverse Polarität im Vergleich zur Reflexion des Meeresbodens ausweisen und trägt somit zur Subduktionserosion bei, die das angesammelte Sediment der oberen Platte teilweise entfernt und in eine größere Tiefe transportiert.

Darüber hinaus vergleichen wir die beobachtete Position des subduzierenden Seamounts mit dem Epizentrum des Tsunami-Erdbebens von 1994, dem co-seismischen Slipmodell und den Herdmechanismen des Nachbebens. Wir schließen daraus, dass der Seamount, der im seismischen Profil BGR06_305 vor Ost-Java beobachtet wird, in der Lage ist, eine seismische Sperrzone davor zu erzeugen. Da die Seamount-Region während des co-seismischen Bruchereignisses von 1994 einen geringen co-seismischen Versatz aufweist, fungiert der Seamount als Barriere für den Ausbreitungsprozess des Bruches. Da Nachbeben hauptsächlich von Abschiebungsbeben begleitet werden, könnte die Nukleation als vollständiger Spannungsabfall angesehen werden und impliziert, dass das Seeberg in der interseismischen Periode sehr schwach gekoppelt ist.

References:

Hamilton, W. B. (1988). Plate tectonics and island arcs. *Special Paper of the Geological Society of America*, *253*(10), 113–137. https://doi.org/10.1130/SPE253-p113

Kodaira, S., Takahashi, N., Nakanishi, A., Miura, S., & Kaneda, Y. (2000). Subducted seamount imaged in the rupture zone of the 1946 Nankaido earthquake. *Science*, *289*(5476), 104–106. https://doi.org/10.1126/science.289.5476.104

Kopp, H., Flueh, E. R., Petersen, C. J., Weinrebe, W., Wittwer, A., & Scientists, M. (2006). The Java margin revisited: Evidence for subduction erosion off Java. *Earth and Planetary Science Letters*, *242*(1–2), 130–142. https://doi.org/10.1016/j.epsl.2005.11.036

Korenaga, J., Holbrook, W. S., Kent, G. M., Kelemen, P. B., Detrick, R. S., Larsen, H.-C., et al. (2000). Crustal structure of the southeast Greenland margin from joint refraction and reflection seismic tomography. *Journal of Geophysical Research: Solid Earth*, *105*(B9), 21591–21614.

McNeill, L. C., Dugan, B., Backman, J., Pickering, K. T., Pouderoux, H. F. A., Henstock, T. J., et al. (2017). Understanding Himalayan erosion and the significance of the Nicobar Fan. *Earth and Planetary Science Letters*, *475*, 134–142. https://doi.org/10.1016/j.epsl.2017.07.019

Mochizuki, K., Yamada, T., Shinohara, M., Yamanaka, Y., & Kanazawa, T. (2008). Weak interplate coupling by seamounts and repeating M ∼ 7 earthquakes. *Science*, *321*(5893), 1194–1197. https://doi.org/10.1126/science.1160250

Ranero, C. R., & von Huene, R. (2000). Subduction erosion along the Middle America convergent margin. *Nature*, *404*(6779), 748–752. https://doi.org/10.1038/35008046

Sallarès, V., & Ranero, C. R. (2019). Upper-plate rigidity determines depth-varying rupture behaviour of megathrust earthquakes. *Nature*, *576*(7785), 96–101. https://doi.org/10.1038/s41586-019-1784-0

Woodward, M. J., Nichols, D., Zdraveva, O., Whitfield, P., & Johns, T. (2008). A decade of tomography. *GEOPHYSICS*, *73*(5), VE5–VE11. https://doi.org/10.1190/1.2969907

Yilmaz, Ö. (2001). *Seismic Data Analysis*. Society of Exploration Geophysicists. https://doi.org/10.1190/1.9781560801580

Contents

CHAPTER 1

MOTIVATION AND OUTLINE

1.1 Motivation

Subduction zone megathrusts are the tectonic interfaces connecting tectonic plates, which are the most prominent geological units on Earth. When tectonic plates are convergent, the higher density plate sinks and is subducted underneath the relative buoyant one (Dymkova and Gerya, 2013; Shuck et al., 2022; Van Keken et al., 2011). Shear stress continuously builds up along the megathrust, from the trench to the mantle wedge, and is released via aseismic creeping, slow slip events, tremors, and stick-slip behaviour of the interface displacement (Gao and Wang, 2014; Scholz, 2014; Wallace et al., 2016). The latter one is frequently observed and well-known as interplate megathrust earthquakes.

These megathrust earthquakes at convergent plate margins lead to substantial human casualties globally and threaten the coast-living people, which are approximately 10% of the global population (Neumann et al., 2015). In particular, submarine earthquakes potentially have the most devasting impact since they may result in a large displacement of the upper plate seafloor and thus induce high run-up tsunamis, which flush coastal communities and destroy the infrastructure (Bilek and Lay, 2002; Lindsey et al., 2021; Yokota et al., 2016). To understand the nature of earthquake generation, the tectonic configuration of the plate margin subduction zone systems and their physical properties (e.g., geometry, stress, and strength of the megathrust) have to be studied and better understood by the scientific community (Dielforder et al., 2020; Gao and Wang, 2014; Lamb, 2006). In recent decades, geophysical and geochemical expeditions have been conducted to survey these endmember tectonic units globally, especially in the segments where the world's largest earthquakes occur (e.g., in Sumatra margin – 2004 Sumatra Andaman earthquake, and Japan trench - 2011 Tohoku-Oki earthquake) (Brodsky et al., 2020; McCaffrey, 2009; Shearer and Buergmann, 2010).

The plate margin offshore eastern Java attracts the community's attention due to its rough seafloor and ubiquitous seamounts and basement ridges on the oceanic seafloor (Abercrombie et al., 2001; Kopp et al., 2006; Wang and Bilek, 2011). Both active sounding approaches and the satellite remote-sensing reveal that the Indo-Australian plate features a large number of sea-plateaus, seamounts or ridges of different sizes and shapes approaching and colliding with the Java margin (Sandwell et al., 2014). The satellite gravity and bathymetry data also illustrate substantial along-strike heterogeneity on the accretionary wedge of the Java and Lesser Sunda arc, which hints at the impact of the subducting seamount underneath the accretionary wedge (Kopp et al., 2006). Furthermore, two moderate size earthquakes occurred in the eastern Java and Lesser Sunda segment, and both resulted in a significant tsunami with hundreds of local casualties (Ammon et al., 2006; Fan et al., 2017; Polet and Kanamori, 2000; Polet and Thio, 2003). Questions arise from both tectonic and seismogenic perspective of the subducting seamount and the basement ridges, like, do seamounts subduct underneath the Java accretionary wedge, how the upper plate deforms and reacts to the seamount subduction, and does the seamount favour or inhibit the generation of megathrust earthquakes (Scholz and Small, 1997)? Even though both multi-channel seismic (MCS) and ocean-bottom seismometer (OBS) surveys were conducted in the early 21th century by GEOMAR and BGR (Lüschen et al., 2011; Planert et al., 2010), the subducted seamounts, their topographic impact on the upper plate, and their relationship with earthquake hazards are not confirmed from these geophysical observations and studies.

In this thesis, I address and dig into these issues which concerned the scientific community for decades by processing the MCS images and re-interpreting the subduction zone structure with some additional existing geophysical observations (e.g., published OBS velocity models and satellite gravity data). The MCS image processing with pre-stack depth migration (PSDM) and grid-based reflection tomography is assisted by the innovative data processing method of Non-rigid matching (NRM) (Nickel and Sønneland, 1999), which is widely used in medical radiology and photography (Chui and Rangarajan, 2003; Pappu et al., 1995; Thirion, 1996).

The iteratively updated P-wave velocity (vp) model inverted from the ray-based MCS reflection tomography refines the structural image of the accretionary wedge, reveals credible megathrust local dipping angles , and helps to constrain a better geological interpretation regarding the existence of subducting seamounts in the subsurface and the corresponding upper plate deformation.

1.2 Thesis outline

The main content of the thesis consists of 4 chapters, which cover a general introduction of the thesis, two peer-reviewed publications and a submitted manuscript. Finally, I give an outlook on the remaining issues about the study and the possible future projects that could be conducted to enhance our understanding of subducting seamounts and their geological impact on the accretionary complex. I authored the three presented manuscripts. All presented manuscripts have been published in or submitted to peer-reviewed journals.

Chapter 2 provides first an overview of the geological setting of the Indonesian Sunda arc and the eastern Java plate margin from previous studies. Hereafter, I introduce two essential scientific sub-topics regarding convergent plate margins and subduction processes.

The first sub-topic (in ***Sect. 2.2***) is about the two endmember scenarios of the accretionary process and the erosional processes at the convergent plate margins (Clift and Vannucchi, 2004; von Huene and Scholl, 1991). It is inferred that both accretion and erosion processes seem to occur in the eastern Java margin (Bilek, 2010). The accretionary process in the Indonesian Sunda margin describes the continuous growing of the accretionary mass complex by the in-coming sediment flux from the Indo-Australian oceanic crust and the terrigenous material from the Ganges river (McNeill et al., 2017). Meanwhile, as the down-going plate subducts, the upper plate mass volume could also be eroded, reduced, and transported into greater depth by subduction erosion, as is evidenced by the arc-ward deflection of the deformation front in eastern Java. The erosional process is related to the tectonic effects of the subducting relief (seamount, plateau, and ridges) (Martínez-Loriente et al., 2019; Park et al., 2004; von Huene et al., 1997), which are widely observed on the oceanic crust, or the abundant fluid migration from the plate interface into the upper plate (von Huene et al., 2004).

The erosional process further elicits the second sub-topic of the subduction process of the seamount or basement relief that I will briefly introduce in ***Sect. 2.3***. Seamount or basement ridges are observed ubiquitously on the ocean bottom and approaching the plate margins globally, including the Java margin (Bangs et al., 2006; Davidson et al., 2020; Kodaira et al., 2000; Park et al., 2004; von Huene et al., 1997). Depending on the seamount's size and shape, the subducting relief will either impact the upper plate wedge locally by pervasive fracturing (Ranero and von Huene, 2000; Wang and Bilek, 2011) or cause a substantial shortening and thickening of the upper plate (Gerya et al., 2009). Further, I introduce in this chapter the long-term paradox in the geoscience community about how subducting seamounts are affecting the seismicity, especially the large earthquakes (Das & Watts., 2009; Geersen et al., 2015; Kodaira et al., 2002; Singh et al., 2011; Wang and Bilek, 2014, 2011).

Chapter 3 deals with the innovative geophysical method, Non-rigid Matching (NRM) approach, used in the multi-channel seismic data P-wave velocity inversion. This chapter documents the conventional velocity model building issues, difficulties in the grid-based reflection tomography (Jones, 2005), and our data-driven NRM solutions in the residual move-out digitization and imaging optimization. We implemented our method first on two synthetic scenarios which simulate difficult conditions in the real data and then applied it to the *in-situ* MCS lines collected during the RV SONNE 190 SINDBAD cruise in the eastern Java margin (Kopp and Flueh, 2007). The application to the real data (profile BGR06_313) illustrates the capacities of the NRM application in the reflection tomography. On the one hand, the NRM residual move-out auto picking eliminates the human bias in the conventional interactive semblance analysis. On the other hand, it provides sufficient redundancy of residual move-out information and effectively stabilizes the tomographic inversion result. The refined P-wave velocity model inversed by the reflection tomography provides velocity attribute information which contributes to the geological interpretation and further improves the pre-stack depth migration image with more accurate dipping information on the geological units in the subsurface.

Authors' contributions: *YX and DK performed the computations and are responsible for the main processing. HK helped to strengthen the overall scope and added to interpretational aspects and the discussion of the presented results. MS made the data available and was responsible for the navigation and geometry processing. YX wrote the article, and all authors contributed equally to the proofreading and final preparation of the manuscript.*

Chapter 3 is published in Solid Earth as: *https://doi.org/10.5194/se-13-367-2022*

Chapter 4 deals with the detailed geological interpretation of the four PSDM MCS lines offshore eastern Java to the Lesser Sunda islands. Assisted by the NRM and grid-based reflection tomography, we reveal the detailed structure of the accretionary wedge complex and the structure of the megathrust. Accompanied by the multi-beam bathymetry collected during the SO190 cruise, subducting seamounts with different scales are observed and interpreted from the subsurface in three MCS lines offshore eastern Java, Bali, and Lombok, respectively. Compared to another MCS line without subducting seamounts offshore Sumbawa, we investigate the structural impact of subducting seamounts with different sizes and at different depths. Distinctively, we observed direct evidence for subduction erosion, which is the upward migration of the plate interface, in the scenario of the seamount subduction.

Authors' contributions: *YX and DK performed the computations and are responsible for the main processing. HK helped to strengthen the overall scope and added to interpretational aspects and the discussion of the presented results. MS made the data available and was responsible for the navigation and geometry processing. YX wrote the article, and all authors contributed equally to the proofreading and final preparation of the manuscript.*

Chapter 4 is ready for submission to *Journal of Geophysical Research: Solid Earth.*

Chapter 5 deals with the relationship between the subducting seamount and the earthquake phenomena. We compared our geophysical observations (bathymetry and MCS) with the location of the 1994 Java earthquake epicentre, the inverted co-seismic slip model, and the aftershock focal mechanisms. The 1994 earthquake (M=7.8) ruptured right in front of the subducting seamount imaged by the MCS line BGR06_305 offshore eastern Java. Distinctly, the inverted co-seismic slip model from the seismology waveform shows a strong warping signature around the subducting seamount that we observed. This comparison infers that the seamount could hold a seismic locking zone in front of it while subduction advances. However, as a geometrical irregularity, the seamount inhibited the propagation of the co-seismic rupture when the nucleation was approaching the trench. The ubiquitous normal faulting aftershocks and the absence of the thrust fault aftershocks indicate the complete stress drop of the 1994 earthquake, which further reveals that the subducting seamount region is a creeping zone with a very low coupling ratio in the plate interface.

Authors' contributions: *YX and DK performed the computations and are responsible for the main processing. YX, JG, DK, BM, MR, MS, DL and HK helped to strengthen the overall scope and added to interpretational aspects and the discussion of the presented results. MS made the data available and was responsible for the navigation and geometry processing. YX, JG, and HK wrote the article, and all authors contributed equally to the proofreading and final preparation of the manuscript.*

Chapter 5 is published in Solid Earth as: *https://doi.org/10.5194/se-12-2467-2021*

Chapter 6 summarizes the previous chapters' results and discussions and provides an outlook for potential research concerning yet un-fully discovered subducting seamount and megathrust geometries. In the end, I make MCS surveys' acquisitional recommendations and identify areas of interest for future geophysical studies.

References:

Abercrombie, R. E., Antolik, M., Felzer, K., Ekstrom, G., & Ekström, G. (2001). The 1994 Java tsunami earthquake: Slip over a subducting seamount. *Journal of Geophysical Research: Solid Earth*, *106*(B4), 6595–6607. https://doi.org/10.1029/2000jb900403

Ammon, C. J., Kanamori, H., Lay, T., & Velasco, A. A. (2006). The 17 July 2006 Java tsunami earthquake. *Geophysical Research Letters*, *33*(24), 1–5. https://doi.org/10.1029/2006GL028005

Bangs, N. L. B., Gulick, S. P. S., & Shipley, T. H. (2006). Seamount subduction erosion in the Nankai Trough and its potential impact on the seismogenic zone. *Geology*. https://doi.org/10.1130/G22451.1

Bilek, S. L., & Lay, T. (2002). Tsunami earthquakes possibly widespread manifestations of frictional conditional stability. *Geophysical Research Letters*, *29*(14), 18-1-18–4. https://doi.org/10.1029/2002GL015215

Bilek, Susan L. (2010). The role of subduction erosion on seismicity. *Geology*. https://doi.org/10.1130/focus052010.1

Brodsky, E. E., Mori, J. J., Anderson, L., Chester, F. M., Conin, M., Dunham, E. M., et al. (2020). The State of Stress on the Fault Before, During, and after a Major Earthquake. *Annual Review of Earth and Planetary Sciences*, *48*, 49–74. https://doi.org/10.1146/annurev-earth-053018-060507

Chui, H., & Rangarajan, A. (2003). A new point matching algorithm for non-rigid registration. *Computer Vision and Image Understanding*, *89*(2–3), 114–141. https://doi.org/10.1016/S1077-3142(03)00009-2

Clift, P., & Vannucchi, P. (2004). Controls on tectonic accretion versus erosion in subduction zones: Implications for the origin and recycling of the continental crust. *Reviews of Geophysics*, *42*(2). https://doi.org/10.1029/2003rg000127

Das, S., Watts, A. B., Das, S., & Watts, A. B. (2009). Effect of Subducting Seafloor Topography on the Rupture Characteristics of Great Subduction Zone Earthquakes. In *Subduction Zone Geodynamics* (pp. 103–118). https://doi.org/10.1007/978-3-540-87974-9

Davidson, S. R., Barnes, P. M., Pettinga, J. R., Nicol, A., Mountjoy, J. J., & Henrys, S. A. (2020). Conjugate strike-slip faulting across a subduction front driven by incipient seamount subduction. *Geology*, *48*(5), 493–498. https://doi.org/10.1130/G47154.1

Dielforder, A., Hetzel, R., & Oncken, O. (2020). Megathrust shear force controls mountain height at convergent plate margins. *Nature*, *582*(7811), 225–229. https://doi.org/10.1038/s41586-020-2340-7

Dymkova, D., & Gerya, T. (2013). Porous fluid flow enables oceanic subduction initiation on Earth. *Geophysical Research Letters*, *40*(21), 5671–5676. https://doi.org/10.1002/2013GL057798

Fan, W., Bassett, D., Jiang, J., Shearer, P. M., & Ji, C. (2017). Rupture evolution of the 2006 Java tsunami earthquake and the possible role of splay faults. *Tectonophysics*, *721*(September), 143–

150. https://doi.org/10.1016/j.tecto.2017.10.003

Gao, X., & Wang, K. (2014). Strength of stick-slip and creeping subduction megathrusts from heat flow observations. *Science*, *345*(6200), 1038–1041. https://doi.org/10.1126/science.1255487

Geersen, J., Ranero, C. R., Barckhausen, U., & Reichert, C. (2015). Subducting seamounts control interplate coupling and seismic rupture in the 2014 Iquique earthquake area. *Nature Communications*, *6*, 6–11. https://doi.org/10.1038/ncomms9267

Gerya, T. V., Fossati, D., Cantieni, C., & Seward, D. (2009). Dynamic effects of aseismic ridge subduction: numerical modelling. *European Journal of Mineralogy*, *21*(3), 649–661. https://doi.org/10.1127/0935-1221/2009/0021-1931

Von Huene, R., Reston, T., Kukowski, N., Dehghani, G. A., Weinrebe, W., Le Pichon, X., et al. (1997). A subducting seamount beneath the Mediterranean Ridge. *Tectonophysics*, *271*(3–4), 249–261. https://doi.org/10.1016/S0040-1951(96)00241-7

von Huene, Roland, & Scholl, D. W. (1991). Observations at convergent margins concerning sediment subduction, subduction erosion, and the growth of continental crust. *Reviews of Geophysics*, *29*(3), 279. https://doi.org/10.1029/91RG00969

von Huene, Roland, Ranero, C. R., & Vannucchi, P. (2004). Generic model of subduction erosion. *Geology*, *32*(10), 913. https://doi.org/10.1130/G20563.1

Jones, I. F. (2005). 3D PreSDM model building techniques: A review, (3), 921–924. https://doi.org/10.1190/1.1816788

Van Keken, P. E., Hacker, B. R., Syracuse, E. M., & Abers, G. A. (2011). Subduction factory: 4. Depth-dependent flux of H2O from subducting slabs worldwide. *Journal of Geophysical Research: Solid Earth*, *116*(1). https://doi.org/10.1029/2010JB007922

Kodaira, S., Takahashi, N., Nakanishi, A., Miura, S., & Kaneda, Y. (2000). Subducted seamount imaged in the rupture zone of the 1946 Nankaido earthquake. *Science*, *289*(5476), 104–106. https://doi.org/10.1126/science.289.5476.104

Kodaira, S., Kurashimo, E., Park, J. O., Takahashi, N., Nakanishi, A., Miura, S., et al. (2002). Structural factors controlling the rupture process of a megathrust earthquake at the Nankai trough seismogenic zone. *Geophysical Journal International*, *149*(3), 815–835. https://doi.org/10.1046/j.1365-246X.2002.01691.x

Kopp, H., & Flueh, E. R. (2007). *FS Sonne Fahrtbericht / Cruise Report SO 190 - SINDBAD : Seismic and Geoacoustic Investigations Along The Sunda-Banda Arc Transition* (IFM-GEOMAR Report). (H. Kopp & E. R. Flueh, Eds.) (Vol. doi:10.328). Kiel. https://doi.org/doi:10.3289/ifm-geomar_rep_8_2007

Kopp, H., Flueh, E. R., Petersen, C. J., Weinrebe, W., Wittwer, A., & Scientists, M. (2006). The Java margin revisited: Evidence for subduction erosion off Java. *Earth and Planetary Science Letters*, *242*(1–2), 130–142. https://doi.org/10.1016/j.epsl.2005.11.036

Lamb, S. (2006). Shear stresses on megathrusts: Implications for mountain building behind subduction zones. *Journal of Geophysical Research*, *111*(B7). https://doi.org/10.1029/2005jb003916

Lindsey, E. O., Mallick, R., Hubbard, J. A., Bradley, K. E., Almeida, R. V., Moore, J. D. P., et al. (2021). Slip rate deficit and earthquake potential on shallow megathrusts. *Nature Geoscience*, *14*(5), 321–326. https://doi.org/10.1038/s41561-021-00736-x

Lüschen, E., Müller, C., Kopp, H., Engels, M., Lutz, R., Planert, L., et al. (2011). Structure, evolution and tectonic activity of the eastern Sunda forearc, Indonesia, from marine seismic investigations. *Tectonophysics*, *508*(1–4), 6–21. https://doi.org/10.1016/j.tecto.2010.06.008

Martínez-Loriente, S., Sallarès, V., R. Ranero, C., B. Ruh, J., Barckhausen, U., Grevemeyer, I., & Bangs, N. (2019). Influence of Incoming Plate Relief on Overriding Plate Deformation and Earthquake Nucleation: Cocos Ridge Subduction (Costa Rica). *Tectonics*, *38*(12), 4360–4377. https://doi.org/10.1029/2019TC005586

McCaffrey, R. (2009). The Tectonic Framework of the Sumatran Subduction Zone. *Annual Review of Earth and Planetary Sciences*, *37*(1), 345–366. https://doi.org/10.1146/annurev.earth.031208.100212

McNeill, L. C., Dugan, B., Backman, J., Pickering, K. T., Pouderoux, H. F. A., Henstock, T. J., et al. (2017). Understanding Himalayan erosion and the significance of the Nicobar Fan. *Earth and Planetary Science Letters*, *475*, 134–142. https://doi.org/10.1016/j.epsl.2017.07.019

Neumann, B., Vafeidis, A. T., Zimmermann, J., & Nicholls, R. J. (2015). Future coastal population growth and exposure to sea-level rise and coastal flooding - A global assessment. *PLoS ONE*, *10*(3). https://doi.org/10.1371/journal.pone.0118571

Nickel, M., & Sønneland, L. (1999). Non-rigid matching of migrated time-lapse seismic. In *SEG Technical Program Expanded Abstracts 1999* (pp. 872–875). Society of Exploration Geophysicists. https://doi.org/10.1190/1.1821191

Pappu, S., Gold, S., & Rangarajan, A. (1995). A Framework for Non-Rigid Matching and Correspondence. In *Proceedings of the 8th International Conference on Neural Information Processing Systems* (pp. 795–801). Cambridge, MA, USA: MIT Press.

Park, J O, Moore, G. F., Tsuru, T., Kodaira, S., & Kaneda, Y. (2004). A subducted oceanic ridge influencing the Nankai megathrust earthquake rupture. *Earth and Planetary Science Letters*, *217*(1–2), 77–84. https://doi.org/10.1016/s0012-821x(03)00553-3

Park, Jin Oh, Moore, G. F., Tsuru, T., Kodaira, S., & Kaneda, Y. (2004). A subducted oceanic ridge influencing the Nankai megathrust earthquake rupture. *Earth and Planetary Science Letters*, *217*(1–2), 77–84. https://doi.org/10.1016/S0012-821X(03)00553-3

Planert, L., Kopp, H., Lueschen, E., Mueller, C., Flueh, E. R., Shulgin, A., et al. (2010). Lower plate structure and upper plate deformational segmentation at the Sunda-Banda arc transition, Indonesia. *Journal of Geophysical Research*, *115*(B8), B08107. https://doi.org/10.1029/2009JB006713

Polet, J., & Kanamori, H. (2000). Shallow subduction zone earthquakes and their tsunamigenic potential. *Geophysical Journal International*, *142*(3), 684–702. https://doi.org/10.1046/j.1365-246X.2000.00205.x

Polet, Jascha, & Thio, H. K. (2003). The 1994 Java Tsunami earthquake and its “normal” aftershocks. *Geophysical Research Letters*, *30*(9), 3–6. https://doi.org/10.1029/2002GL016806

Ranero, C. R., & von Huene, R. (2000). Subduction erosion along the Middle America convergent margin. *Nature*, *404*(6779), 748–752. https://doi.org/10.1038/35008046

Sandwell, D. T., Müller, R. D., Smith, W. H. F., Garcia, E., & Francis, R. (2014). New global marine gravity model from CryoSat-2 and Jason-1 reveals buried tectonic structure. *Science*, *346*(6205), 65–67. https://doi.org/10.1126/science.1258213

Scholz, C. H. (2014). The rupture mode of the shallow large-slip surge of the Tohoku-Oki Earthquake. *Bulletin of the Seismological Society of America*, *104*(5), 2627–2631. https://doi.org/10.1785/0120140130

Scholz, C. H., & Small, C. (1997). The effect of seamount subduction on seismic coupling. *Geology*, *25*(6), 487. https://doi.org/10.1130/0091-7613(1997)025<0487:TEOSSO>2.3.CO;2

Shearer, P., & Buergmann, R. (2010). Lessons Learned from the 2004 Sumatra-Andaman Megathrust Rupture. In R. Jeanloz & K. H. Freeman (Eds.), *Annual Review of Earth and Planetary Sciences, Vol 38* (Vol. 38, pp. 103–131). https://doi.org/10.1146/annurev-earth-040809-152537

Shuck, B., Gulick, S. P. S., Van Avendonk, H. J. A., Gurnis, M., Sutherland, R., Stock, J., & Hightower, E. (2022). Stress transition from horizontal to vertical forces during subduction initiation. *Nature Geoscience*, *15*(2), 149–155. https://doi.org/10.1038/s41561-021-00880-4

Singh, S. C., Hananto, N., Mukti, M., Robinson, D. P., Das, S., Chauhan, A., et al. (2011). Aseismic zone and earthquake segmentation associated with a deep subducted seamount in Sumatra. *Nature Geoscience*, *4*(5), 308–311. https://doi.org/10.1038/ngeo1119

Thirion, J.-P. (1996). Non-rigid matching using demons. *Proceedings CVPR IEEE Computer Society Conference on Computer Vision and Pattern Recognition*, 245–251. https://doi.org/10.1109/CVPR.1996.517081

Wallace, L. M., Webb, S. C., Ito, Y., Mochizuki, K., Hino, R., Henrys, S., et al. (2016). Slow slip near the trench at the Hikurangi subduction zone, New Zealand. *Science*, *352*(6286), 701–704. https://doi.org/10.1126/science.aaf2349

Wang, K., & Bilek, S. L. (2011). Do subducting seamounts generate or stop large earthquakes? *Geology*, *39*(9), 819–822. https://doi.org/10.1130/G31856.1

Wang, K., & Bilek, S. L. (2014). Invited review paper: Fault creep caused by subduction of rough seafloor relief. *Tectonophysics*. https://doi.org/10.1016/j.tecto.2013.11.024

Yokota, Y., Ishikawa, T., Watanabe, S. I., Tashiro, T., & Asada, A. (2016). Seafloor geodetic constraints on interplate coupling of the Nankai Trough megathrust zone. *Nature*, *534*(7607), 374–377. https://doi.org/10.1038/nature17632

CHAPTER 2

INTRODUCTION

2.1 Geological setting of the Sunda arc and the eastern Java margin

2.1.1 The tectonic setting of the Sunda Arc

The 5000 km Sunda Arc is a classic convergent plate margin with the Indo-Australian plate underthrusting the Eurasian or Sundaland plate. It extends westward from Flores to Java and then trends north-west towards Myanmar, passing through Sumatra and the Andaman Nicobar ridge before terminating at the Indo-Burman ranges (Hamilton, 1988). The tectonic evolution of the arc has been controlled by the active subduction of the Indo-Australian plate since the Eocene-Oligocene (Hall, 2002; Hall and Smyth, 2008; Hamilton, 1988; Moore et al., 1982), following the Eocene collision of India with Eurasia. Given the great lateral extent of the Sunda arc, segmentation and variations in several geological parameters are observed along the margin (Moore et al., 1980). The age of the subducting lithosphere increases from 90 Ma off Sumatra (Hamilton, 1988) to more than 140 Ma offshore Sumba (Heine et al., 2004). The variation in plate age correlates to an increase in trench depth from <2000 m off Burma to >7000 m off Bali and Lombok. Given the arc's curvature, the subduction orientation changes from almost orthogonal off Java to highly oblique off the Andaman Islands and Burma (McCaffrey, 2009; Moore et al., 1980). The current convergence rate along the arc ranges from 67 mm/yr in the direction of N14.9°E off Java (Fig. 1) (Bock et al., 2003; Tregoning et al., 1994) to 46 mm/yr at N18°E near north-west Sumatra (Delescluse and Chamot-Rooke, 2007).

Sedimentation on the oceanic plate and in the Sunda trench is dominated by the transport of quartzose terrigenous detritus from the Himalayas, carried by the Ganges and Brahmaputra rivers into the Bay of Bengal and the Nicobar fan and deposited in the Sunda trench (McNeill et al., 2017; Moore et al., 1982). Sediment derived from Java and Sumatra terranes during the Neogene has been trapped in the forearc basins and has largely not reached the trench (Moore et al., 1982). The north-western portion of the Sunda convergent margin is dominated by subduction accretion, where sediment transfer to the upper plate is documented in a large accretionary prism offshore Sumatra and western Java (Karig et al., 1980). Offshore central Java to Bali (109°E-115°E) in the projection of the Roo Rise, subduction erosion causes a deflection of the Java trench and deformation front towards the arc by 40 km on average from the normal curvature trend of the deep-sea trench (Fig. 1) (Kopp et al., 2006, Krabbenhoeft et al., 2010). This trend is reflected in the thickness of the trench sediment infill, which diminishes with increasing distance from the Ganges-Brahmaputra system from ~5000 m off northern Sumatra to less than 400 m off eastern Java (Moore et al., 1982, 1980). Further to the east, the trench is void of sediment infill except for isolated sediment patches (Masson et al., 1990).

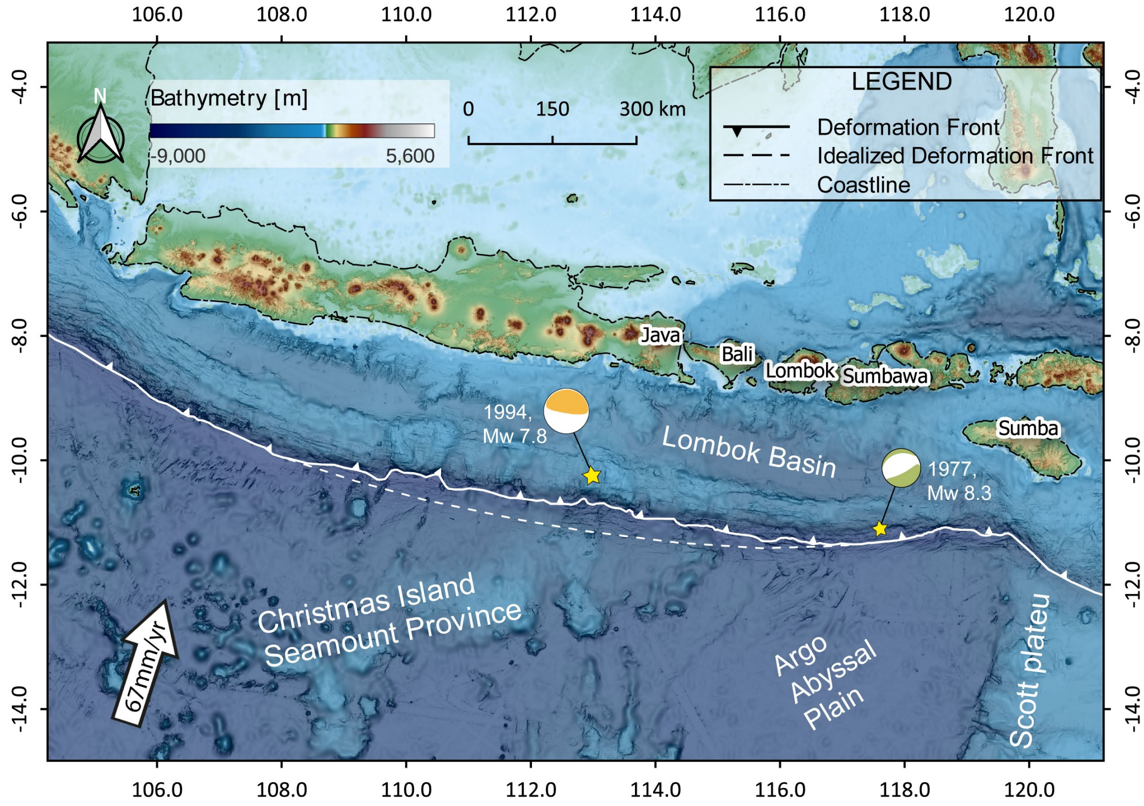

Figure 1. Bathymetry and topography map of the Java - Lesser Sunda islands margin. The Indo-Australian oceanic crust, featuring oceanic relief of different sizes and shapes, is subducting underneath the overriding Sundaland plate. Please note that the subducting oceanic relief impact the overriding accretionary wedge and cause the 600 km long embayment of the deformation front (white dashed line). Two significant earthquakes (Abercrombie et al., 1994; Bilek and Engdahl, 2007) occurred in the past 50 years, and both of the events triggered tsunamis with unexpected run-ups.

Along-arc segmentation is also manifested in the seismogenic behaviour of the plate interface. The Andaman-Sumatra section of the Sunda subduction zone has produced numerous large magnitude thrust earthquakes (Mw>8.0) in the past; some of which generated destructive tsunamis (Bilham, 2005; Lay et al., 2005), including the 2004 Sumatra-Andaman earthquake (Mw = 9.1-9.3) and tsunami, resulting in more than 289,000 casualties in 13 countries around the Indian Ocean (Levy and Gopalakrishnan, 2005). Crossing the trans-tensional regime of the Sunda Strait (Lelgemann et al., 1999), an absence of large interplate thrust earthquakes (Mw>8.0) is observed offshore Java and to the east (Newcomb and McCann, 1987; Okal, 2012) for the entire era of instrumental seismicity. However, for long recurrence intervals, the observation period may be too limited. Significant seismicity, including large magnitude events, is documented for the outer rise area offshore Java to Sumba. The majority of these events are normal faulting earthquakes (Newcomb and McCann, 1987), which originate on deep-penetrating plate-bending related normal faults that are ubiquitous in the bathymetry data of the region (Masson et al., 1990; Kopp, 2011).

2.1.2 The tectonic setting of the Java margin

The Java margin forms the eastern prolongation of the Sunda subduction zone between the Sunda Strait and Bali/Lombok (105°E-115°E). Information on the crustal structure along this segment of the Sunda arc is mainly based on the analysis of wide-angle and multi-channel (MCS) seismic lines (Karig et al., 1980; Kopp, 2002; Kopp et al., 2009, 2006, 2002, 2001; Lüschen et al., 2011; Moore et al., 1980; Müller et al., 2008; Planert et al., 2010; Shulgin et al., 2011). The deeper structure beneath the arc has been investigated using body wave travel-time tomography (Fukao and Obayashi, 2013; Widiyantoro et al., 1996; Widiyantoro and Van Der Hilst, 1997; Zenonos et al., 2019) and also by SS precursor stacks for the 410 and 660 km mantle discontinuities (Dokht et al., 2018).

Two contrasting oceanic tectonic regimes enter the subduction system offshore Java: "normal" oceanic crust is under-thrusting off western Java (105°E to 109°E). In contrast, convergence is characterized by the subduction of the Roo Rise oceanic plateau, which forms the eastern extension of the Christmas islands seamount province off central and eastern Java (109°E to 115°E) (Fig. 1). The Roo Rise is manifested in a ~400 km broad bathymetric plateau dotted with isolated seamounts with an average elevation of >2000 m above the surrounding ocean floor (Shulgin et al., 2011). It covers an area of approximately 100 000 km^2 offshore central-eastern Java (Shulgin et al., 2011). The Christmas island seamount province is formed through the shallow recycling of the delaminated continental lithosphere entrained in the mantle, based on the isotope analyses of volcanic rocks (Hoernle et al., 2011). Refraction tomography studies have shown that the crustal thickness of the Roo Rise close to the trench is between 12 km to 18 km, with a lower P-wave velocity than conventional oceanic crust (Shulgin et al., 2011) (v_p = 6.6 km/s compared to v_p = 7.2 km/s at the oceanic Moho).

Interplate megathrust earthquakes of large magnitude (Mw > 8) are not documented for the Java margin (Newcomb and McCann, 1987; Okal, 2012) for the instrumental period. However, two tsunami megathrust earthquakes occurred at a shallow depth close to the trench (Bilek and Engdahl, 2007; El Hariri and Bilek, 2011). The 1994 earthquake, Mw=7.8, ~50 km landward of the trench, occurred with a hypocentre depth of ~18 km, generated a tsunami with a run-up height of over 10 m, and killed more than 200 people (Polet and Kanamori, 2000; Tsuji et al., 1995). The 2006 earthquake (Mw=7.6) with a hypocentre depth of ~15 km (Ammon et al., 2006), caused a tsunami with an average run-up height of 8 m, reaching maximum values of 20 m (Fritz et al., 2007), and resulted in more than 700 casualties. The event decay time retrieved from GPS analysis is in the order of hundreds of days and thus much longer compared to conventional megathrust earthquakes (Raharja et al., 2016). Both earthquakes resulted in unusual post-seismic normal fault type aftershock activity landwards of the trench (Abercrombie et al., 2001; El Hariri and Bilek, 2011). El Hariri and Bilek (2011) find that static Coulomb stress changes from the mainshock cannot fully explain the occurrence of the normal fault aftershocks in the periphery of the seismic rupture.

In addition, the 1994 event is regarded as an example of nucleation over a subducting seamount (Abercrombie et al., 2001; Wang and Bilek, 2014). In contrast, Bilek and Engdahl (2007) and El Hariri and Bilek (2011), suggested that the rupture of the 2006 earthquake was terminated by subducted seafloor relief. Koulali et al. (2018) note that the 1994 rupture halted adjacent to a segment of the accretionary prism with a critical taper on the verge of failure, which may have acted as a barrier.

Inversion of continuous GPS data from western Java from 2008 to 2010 reveals two patches of interplate locking offshore western Java and downdip of the 2006 earthquake (Hanifa et al., 2014), resulting in a slip-deficit along the plate interface. Assuming continuously accumulating seismogenic stress over a period of 300 years, for which no large megathrust earthquakes are documented, this would imply an accumulated seismic moment of as much as 1.6×10^{21} Nm (~Mw 8.7) in western Java (Hanifa et al., 2014). In central and east Java, GPS information reveals a weakly coupled plate interface, with a maximum coupling rate of 0.4 (Widiyantoro et al., 2020).

2.1.3 The tectonic setting of the Bali, Lombok, Sumbawa margins - Argo Abyssal plain

The eastern portion of the Sunda subduction system is characterized by the under-thrusting of the Argo abyssal plain, located seaward of the deep-sea trench offshore Bali, Lombok, and Sumbawa (115°E to 119°E). To the east, the Argo abyssal plain is bordered by the Scott plateau (Fig. 1), which forms a continental promontory of the Australian lithosphere and marks the transition from oceanic subduction to continent-island arc collision along the Banda arc. With a mean water depth of 5500 m, the Argo abyssal plain is largely devoid of terrigenous sediment (Moore et al., 1982; Planert et al., 2010). The crust of the Argo Abyssal plain has an average thickness of 8.6 km, typical for the oceanic crust, and its age can be traced back to 125 Ma off Bali and 150 Ma off Sumbawa island (Heine et al., 2004). The roughness of the seafloor turns from rugged offshore Bali and Lombok to generally smooth offshore Sumbawa and Sumba (Lüschen et al., 2011) (Fig. 1). Pronounced oceanic basement structures characterize the seafloor and trend at angles between 45° and 60°, roughly parallel to the magnetic anomalies (Lüschen et al., 2011). These are either conical seamounts on the Roo rise or inherited structures mirroring the original spreading fabric (Planert et al., 2010). On the outer rise seaward of the trench, a pervasive pattern of plate-bending induced normal faulting with throws up to 500 m and fault segment length of up to 60 km is observed starting at about 40 km seaward of the trench axis. The bathymetry and MCS data show a strong horst and graben relief in the trench, which is the surface expression of faults that cut deep into the oceanic basement (Lüschen et al., 2011). Localized slope material failure and local slumping are massively developed and pose a potential risk for tsunamigenesis (Brune et al., 2010; Lüschen et al., 2011). The forearc high rises to a water depth of less than 2500 m (Kopp, 2011). To the north, a mature forearc basin, the Lombok basin, has an average water depth of 4400 m and is limited by the subduction of the Roo Rise to the west and the Scott plateau to the east (Planert et al., 2010). The basin and the adjacent forearc high are uniformly developed along the entire segment. They are not disturbed by the subduction of pronounced basement relief as observed, e.g., further to the west in the Roo Rise segment of eastern Java (Krabbenhoeft et al., 2010). In correlation with the diminishing sediment fill in the trench, the size and volume of the accretionary prism decrease towards the Banda arc. The transition from the oceanic domain of the Argo abyssal plain to the continental domain of the Scott plateau occurs over a distance of less than 50 km and is associated with an increase in crustal thickness of about 5 km, which is mainly accommodated by the upper crust (Planert et al., 2010; Kopp, 2011).

Bali, Lombok, Sumbawa, and Sumba islands lack dense onshore GPS monitoring, so the locking (coupling) status is not well constrained (Wang and Bilek, 2014). Earthquake activity along this segment is dominated by outer rise events, including the prominent Mw 8.3 normal-fault-type (intraplate) earthquake off Sumba island in 1977 (Fig. 1) (Lynnes and Lay, 1988). This event generated a tsunami with a run-up height of up to 5.8 m (Gusman et al., 2009). The hypocentre depth was determined at ~29 km (Gusman et al., 2009) from global catalogues. The mechanism of typical outer rise events is a normal fault type and fulfils the lithosphere bending interpretation of Chapple and Forsyth (1979). The seismic moment study shows that the tsunami is generated by tectonic deformation rather than another tsunami generating force like a landslide (Gusman et al., 2009). Outer rise earthquakes are observed globally, e.g., in Central Chile (Marot et al., 2012), Eastern Java (Lynnes and Lay, 1988), Japan (Lay et al., 2011), Tonga Trench (Beavan et al., 2010) and typically occur at shallow depth (< 30 km) (Lefeldt and Grevemeyer, 2008).

2.2 The accretionary and erosional processes at plate margins

Though the Java margin features a large volume of the accretionary wedge scraped from the Indo-Australian plate, local landward trench movement and landslide scarps also indicate the history of subduction erosion (Bilek, 2010; Kopp et al., 2006). Despite geological studies having been conducted in the past years (e.g., Lüschen et al., 2011; Planert et al., 2010b; Shulgin et al., 2011), how exactly the mechanism of subduction erosion works in Java is not fully understood, and the mass balance between accretionary processes and erosional processes is not adequately constrained from geophysical observations. In this section, we will first revisit the historical observations in global subduction zones regarding the accretion and erosion processes and the physical mechanisms behind them.

2.2.1 History of the convergent plate margins' geophysical observations

Convergent margins are plate boundaries where the lower plate (typically oceanic) is subducted beneath the upper plate. The upper plate is typically composed of 20 -50 km thick layers of continental or island arc rocks (Hamilton, 1988; Stern, 2020). Along these margins, the mass of the upper plate material could either undergo significant growth by the process of sediment accretion or undergo a loss of material by tectonic erosion.

The community first recognized the thick sequence of the sediment rocks, which are scarping off the oceanic crust attached to the upper plate during plate convergence (Fig. 2a) (Hamilton, 1988; Karig and Sharman, 1975) by active geophysical surveys. Meanwhile, similar accretionary structures (sedimentary secessions) and oceanic crust (ophiolitic detritus) found in ancient orogenic belts in the eastern Alps (Dietrich, 1976) were interpreted as being derived from an ancient accretionary margin. A common view shared by the community before the 1980s is that sedimentary accretion is the dominant process in almost all convergent plate margins, even in the region with thin sediment cover (Karig, 1982).

Later in the 1990s, assisted by more active seismic surveys and deep-sea drilling (Deep Sea Drilling Project (DSDP) and Ocean Drilling Program (ODP)), the community noticed that sediment accretion might not be as ubiquitous as they thought, and tectonic erosion along modern convergent margins was documented convincingly.

First and astonishingly, no active sediment accretion is found in the trench and forearc of the western Pacific (von Huene et al., 1980). Rather than large piles of sediment, dredging only retrieved volcanic rocks, intrusives, serpentinite and fresh peridotite rocks in the trench of the Marianas (Bloomer, 1983; Fisher and Engel, 1969). The DSDP and ODP core-samples further revealed the substantial subsidence (maximum 1000 m) of the upper plate in Peru and Japan, which is further interpreted as direct evidence of subduction erosion in these two margins (Keller, 1980; von Huene and Lallemand, 1990). Von Huene and Lallemand (1990) further calculated the cross-sectional area of the eroded material (480 km^2 in Peru Margin, and 800 km^2 in Japan Trench,) by using the restored paleo-water depth and subsidence information from the benthic foraminiferal stratigraphy study (Keller, 1980). Thus, this substantial subsidence and the hypothetical erosional process of the forearc explain the observed long-term landward retreat of the trench along the Peru and Japan margins.

In their seminal review, von Huene and Scholl (1991) further summarized that convergent plate margins are divided into those showing continuous long-term accretion of sediment from the oceanic plate (accretionary margins) and those dominated by the long-term landward retreat of the trench since most of the in-coming sediment is subducted beneath the massif of the basement (non-accretionary margins) (Fig. 2) (Clift and Vannucchi, 2004; von Huene and Scholl, 1991).

The variations in sediment supply and the rate of plate convergence govern the balance between accretion and non-accretion. The accretionary process is favoured in regions with a slow convergence rate (<7.6 cm/yr) and with thick trench sediment on the oceanic plate (> 1 km). It occurs at the seaward position of an active buttress of consolidated accretionary material or core buttress of framework rocks (Fig. 2a) (von Huene and Scholl, 1991).

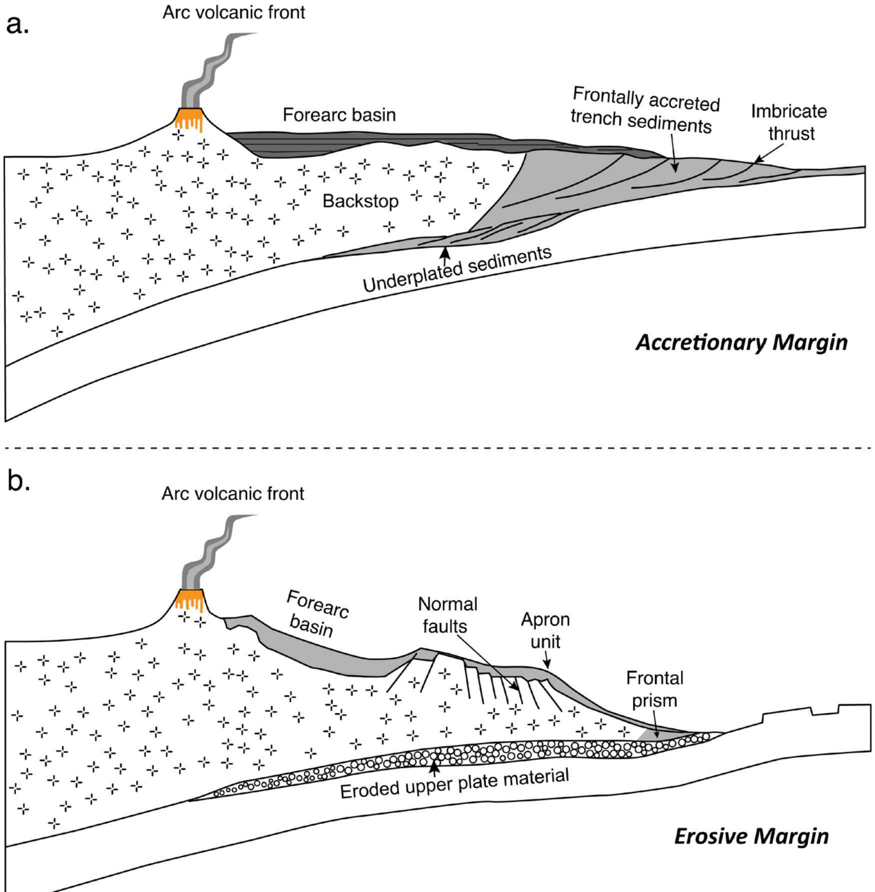

Modified based on Clift & Vannucchi (2004)

Figure 2. Two endmember scenarios of active convergent plate margins: **a.** accretionary and **b.** erosive. Accretionary margins, such as Sumatra and Cascadia, are characterized by large forearc accretionary wedge systems with a large volume of sediment secessions. In contrast, erosive margins, such as Middle America and Tonga, feature a steep upper plate composed of volcanic and mantle rocks.

In contrast, erosive margins (or non-accretionary margins) preferentially exist in fast convergence regions (> 6 cm/yr) and where the oceanic sediment cover is thin (< 1 km). These non-accretionary margins comprise a total length of 19 000 km and occupy 45% of the convergent margins on earth (von Huene et al., 2004). Unlike the sediments scraped off the incoming plate, the frontal prism in the erosive margin is thought to be a contractional structure composed of disaggregated material from the upper plate (Fig. 2b). The majority of the erosive upper plate consists of the fractured continental crust and an overlying thin sediment apron unit (Fig. 2a).

Further, the evidence of tectonic erosion is also observed in the rock outcrops in the Northern Apennines of Italy (Vannucchi et al., 2008). A fossil erosion subduction channel with 500 m thickness shows two décollements were simultaneously active at the top and base of the subduction channel. Massive extensional features related to subduction erosion are observed above the 150° C depth (~ 5 km absolute paleodepth), which is regarded as the updip limit of megathrust earthquakes (Vannucchi et al., 2008). Further, the veins observed at intermediate depth (3-5 km paleodepth) show the alteration from co-seismic (fast) and inter-seismic (slow) slips in the historical seismic cycles in the Northern Apennines.

2.2.2 The hypothetical mechanisms of subduction erosion

The mechanism of subduction erosion has long been discussed. A major branch of the discussion is related to fluid migration along the plate interface. The earliest concepts from the 1980s consider that either a strong physical abrasion procedure or a weak abrasion with fluid assistance promotes subduction erosion (von Huene et al., 2004). Muruachi and Ludwig (1980) proposed a model where basal erosion occurs through the removal of fragments due to the upward migration of the over-pressured fluid from the subducted sediments. Von Huene and Lallemand (1990) further propose that along the plate interface near lithostatic fluid pressure is preserved and favours the formation of a slurry of water and rock fragments. Inspired by the fault valve model (Sibson et al., 1988), Moore (1989) proposed that if the fluid pressure along the décollement is near lithostatic, hydraulic dilation and fracturing could occur along the décollement zone and lead to significant erosion. In this scenario, super-lithostatic pressures are more likely to occur near the top of the décollement, and the fluid pressure gradient is likely to be at maximum just above the décollement. Thus, the *stoping* and fluidization of the upper plate will occur above the interface and lead to basal erosion of the wedge (Le Pichon et al., 1993).

Another branch of models regarding fluid-related tectonic erosion is proposed based on the critical wedge taper theory (Dahlen et al., 1984; Davis et al., 1983; Wang et al., 2010). The condition of subduction erosion could be fulfilled when the effective basal strength and the effective upper plate strength are identical in the scenario of the wedge taper without cohesion. In this scenario, one of the two Coulomb failure slips (planes) on the upper plate will share the same dip as the plate interface and favours the strong wedge shortening and basal erosion. Dahlen (1984) further argued that this condition requires a relatively high basal strength. In the seminal review of the dynamic Coulomb wedge, Wang and Hu (2006) proposed a subduction erosion model driven by the episodic megathrust earthquake cycle using the elastic Coulomb wedge theory. In their model, subduction erosion is favoured during the co-seismic stage on the outer forearc of the plate margin, as the co-seismic strengthening of the frontal wedge will induce a rise of fluid pressure in the forearc and the increase of the effective basal friction and thus fulfil the Dahlen (1984) condition transiently.

Another branch of the hypothesis of basal erosion is related to the subduction of seamounts and basement ridges. The chain-saw model proposed by Hilde (1983) and Balance et al. (1989) demonstrates that the oceanic horst-and-graben structures, which act as strong teeth, could rasp material from the upper plate into a greater depth. Unfortunately, geophysical evidence related to this model is rarely clearly observed and testified in the 1980s - 2000. Le Pichon et al. (1993) further demonstrated that subducting seamounts would induce local fluid drain, increasing fluid pressure, the upward migration of the décollement, and thus tectonic erosion.

Other hypotheses also exist regarding the megathrust mechanical coupling. Uyeda and Kanamori (1979) infer that the transition from accretion to erosion results from decreasing mechanical coupling. Later Ruff and Kanamori (1980) and Kanamori (1986) showed the magnitude of the megathrust earthquakes increases with convergent velocity and decreases with the age of the subducted oceanic crust. Thus, the earthquake's magnitude was considered to be a measure of the mechanical coupling and accretionary VS erosional phenomena. This concept was later disproved by the systematic review by von Huene and Scholl (1991), who stated that no correlation is found between the earthquake magnitude and the signature of accretion or non-accretion.

Since the physical evidence of the saw-chain model or physical abrasion model is hardly observed, the preferred model of subduction erosion in recent decades is related to the hydro-fracturing process at the base of the upper plate and the upward migration of the décollement. Questions may arise regarding some dry trenches that are entirely devoid of oceanic pelagic sediment and the resultant low fluid supply from the sediment rocks, such as in the northern Chile and Peru margins. Von Huene et al. (2004) reveal that materials transported from the forearc middle slope could be deposited at the trench, form the frontal prism, provide the fluid budget for the elevated pore fluid pressure in the subduction channel and thus favour subduction erosion.

The Java forearc was inferred as a plate margin dominated by tectonic erosion (Bilek, 2010), despite the existence of a large volume accretionary wedge and the lacking of evidence from drilling.

Significant arc-ward deflection (40-50 km) of the deformation front in the eastern Java segment implies tectonic erosion, possibly related to subducting relief (e.g., seamounts or ridges) (Kopp et al., 2006). However, the subsurface observation of subducting seamounts, evaluations of the mass balance of the forearc wedge, basal erosion process in the subsurface, and the physical mechanism behind it are lacking to date. In this study, I use state-of-the-art geophysical approaches to reveal the subsurface structure and re-evaluate the accretionary vs erosional phenomena in the Java margin.

2.3 Seamount subduction and its impact on seismic phenomena

Vast global geophysical surveys revealed that the oceanic plates feature many relief structures (seamounts or basement ridges), either scattered or forming chains on the seafloor (Hillier and Watts, 2007). These seamounts have different geometries (e.g., semi-conical mount, linear ridge, flat-top mount, etc.) and different sizes (diameter length: 5 – 100 km) (Das and Watts, 2009). As the mantle dynamics drives the plate motions, these relief structures on the oceanic plate are loaded, collided, dragged to the plates' margins, and further subducted underneath the upper plate. Massive geophysical evidence for subducting seamounts in observed in the global subduction zone subsurface images (e.g., in Hikurangi, Japan trench, Alaska margin, and middle America margin), and their structural and seismogenic impacts are studied (Bangs et al., 2006; Park et al., 2004; Ranero and von Huene, 2000; Wang and Bilek, 2011).

Seamounts initially collide at the toe of the plate margin and further tunnel beneath the continental or accretionary wedge (Dominguez et al., 1998; Ranero and von Huene, 2000). As seamounts feature distinct irregular geometries, the upper plate deformation will respond to brittle or elastic deformations as the seamount subduction advances (Scholz and Small, 1997).

Many forearc topographic features deformed by the subducting seamounts are observed by multi-beam bathymetry. As the seamount is subducted, the upper plate is uplifted as a dome. At the crest of the dome, pervasive fractures are observed (Ranero and von Huene, 2000). At the trailing edge of the subducting seamount, the convergent deformation front is disturbed and forms local grooves and large-scale seafloor embayments (Kopp et al., 2006; Ranero and von Huene, 2000). The grooves and normal faults observed at the trailing edge of the seamount document long-term episodic landslides. At the rear side of the seamount, the conjugate strike slips straddle the buried flanks of the seamount and offset the frontal thrusts (Davidson et al., 2020). As the seamount subducts further downdip, these topographic effects diminish. However, to what extent the overriding plate and seamount are still deforming and how stress evolves at the seamount goes deep is not fully understood (Ruh et al., 2016).

Numerical modelling (Ruh, 2016) and sandbox analogue model (Dominguez et al., 1998) also reveal very similar and pervasive fracturing with different patterns around the subducting seamount like *in-situ* geophysical observations. Thrust faults developed ahead of the seamount, and at the seamount's rear flank, some faults show strike-slip motion (Dominguez et al., 1998). At the trailing side of the seamount, the upper plate is eventually cut by normal faults in various orientations due to the collapse of the upper plate in the seamount's wake (Dominguez et al., 2000; Ruh, 2016). In addition, when the seamount size is very large (diameter > 80 km), numerical modelling (Gerya et al., 2009) reveals that the seamount would significantly increase the upper plate bathymetrical elevation, enhance subduction erosion, and even lead to significant shortening of the upper plate framework. These topographic responses on the outer part (frontal wedge) are transient and tend to relax. However, the topographic shortening and uplifting of the inner wedge (continental framework) would be relaxed more slowly and may be sustained for several millions of years after the seamount subduction (Gerya et al., 2009).

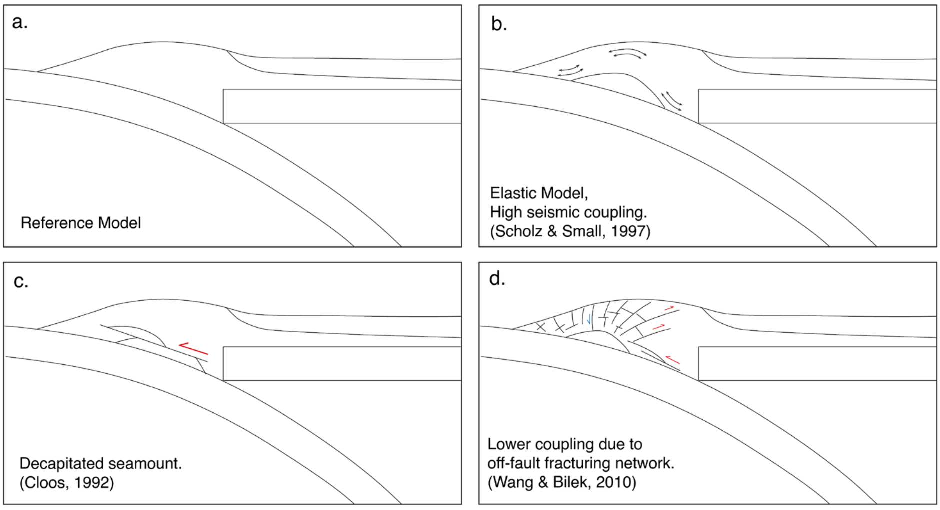

Figure 3. Different scenarios of upper plate deformation and seismogenic implications with subducting seamounts (modified based on Wang and Bilek (2010)). **a.** The schematic cartoon of an accretionary wedge in the island arc type plate margin without the impact of the subducting seamount. **b.** The elastic model cartoon proposed by Scholz & Small (1997) supports the seamount – high seismic coupling concept. **c.** The seamount decapitating model proposed by Cloos (1992) supports the high coupling notion but in a different situation compared to Scholz and Small's (1997) elastic model. **d.** The weakly coupled model proposed by Wang and Bilek (2010) proposes that the seamount will induce a dynamic upper plate off-fault fracturing network and a weakly coupled plate interface in the seamount region.

Regarding the margin wedge's deformation mechanism and the resultant seismogenic potential, the community shares controversial notions. There are three potential mechanical response scenarios based on earlier studies (Fig. 3). (i) Cloos and Shreve (1996) proposed that the seamount could be decapitated or even sheared off along its base, and the sheared surface becomes a seismic asperity (Fig. 3c). (ii) Scholz and Small (1997) proposed that as the seamount is subducted, the upper plate is flexed by an upward push from the seamount underneath (Fig. 3b). This process will increase the normal stress on the plate interface and further increases the interpolate frictional coupling to cause large earthquakes. (iii) As the seamount features an irregular geometry, off-fault networks will be developed at all scales during subduction (Dominguez et al., 1998), and this fault network's complex structure and heterogeneous stresses would provide favourable conditions for aseismic creeping and small earthquakes (Wang and Bilek, 2011) (Fig. 3d).

The historical earthquake observations adjacent to the subducting seamounts region reveal that the subducting seamounts are mostly quiet. In specific regions, earthquake magnitudes will not excess Mw 7.5 (e.g., in 1983, Osa Penisula earthquake Mw = 7.3; in 1999; Quepos earthquake Mw = 6.9). The standard source-time functions of these seamount-related earthquakes illustrate complex source characteristics, implying complex fault networks, and possible summations of smaller earthquakes that occurred simultaneously in the co-seismic stage, as proposed by Wang and Bilek (2010). Mochizuki et al. (2008) report M ~ 7 events repeatedly nucleated in front of a subducting seamount in the southern Japan trench with an interval of 20 years. However, over the past 80 years of recording history, this seamount offshore Japan trench is largely aseismic. Mochizuki et al. (2008) further inferred that the seamount is weakly coupled due to the lack of thrust fault aftershocks and abundant normal fault aftershocks.

Meanwhile, a rare event of seismic nucleation in the Java margin (Abercrombie et al., 2001) somehow supported the Scholz and Small (1997) hypothesis. Based on the bathymetry interpretation from side-scan sonar (Masson et al., 1990), Abercrombie et al. (2001) proposed that the 1994 Java earthquake (Mw 7.8) nucleated on top of a subducting seamount. But the standard source-time function of this earthquake is not complex, which indicates a relatively smoothed fault zone (Wang and Bilek, 2011). So far, the *in-situ* observations on this issue are thus paradoxical.

The Java 1994 earthquake and its seamount genesis seem like a single case. One has to note that in the study of Abercrombie et al. (1994), no seismic image exists to visualize the subsurface structure, which means the exact location of the seamount is unknown. In our study, we use seismic approaches to reveal the plate margin subsurface structure, and provide direct evidence of the seamount subduction, and re-evaluate the long-term seamount-earthquake debate on the Java margin.

References:

Abercrombie, R. E., Antolik, M., Felzer, K., Ekstrom, G., & Ekström, G. (2001). The 1994 Java tsunami earthquake: Slip over a subducting seamount. *Journal of Geophysical Research: Solid Earth*, *106*(B4), 6595–6607. https://doi.org/10.1029/2000jb900403

Ammon, C. J., Kanamori, H., Lay, T., & Velasco, A. A. (2006). The 17 July 2006 Java tsunami earthquake. *Geophysical Research Letters*, *33*(24), 1–5. https://doi.org/10.1029/2006GL028005

Ballance, P. F., Scholl, D. W., Vallier, T. L., Stevenson, A. J., Ryan, H., & Herzer, R. H. (1989). Subduction of a Late Cretaceous Seamount of the Louisville Ridge at the Tonga Trench: A model of normal and accelerated tectonic erosion. *Tectonics*, *8*(5), 953–962. https://doi.org/10.1029/TC008i005p00953

Bangs, N. L. B., Gulick, S. P. S., & Shipley, T. H. (2006). Seamount subduction erosion in the Nankai Trough and its potential impact on the seismogenic zone. *Geology*. https://doi.org/10.1130/G22451.1

Beavan, J., Wang, X., Holden, C., Wilson, K., Power, W., Prasetya, G., et al. (2010). Near-simultaneous great earthquakes at Tongan megathrust and outer rise in September 2009. *Nature*, *466*(7309), 959–963. https://doi.org/10.1038/nature09292

Bilek, S. L. (2010). The role of subduction erosion on seismicity. *Geology*. https://doi.org/10.1130/focus052010.1

Bilek, S. L., & Engdahl, E. R. (2007). Rupture characterization and aftershock relocations for the 1994 and 2006 tsunami earthquakes in the Java subduction zone. *Geophysical Research Letters*, *34*(20), 1–5. https://doi.org/10.1029/2007GL031357

Bilham, R. (2005). A flying start, then a slow slip. *Science*. https://doi.org/10.1126/science.1113363

Bloomer, S. H. (1983). Distribution and origin of igneous rocks from the landward slopes of the Mariana Trench: Implications for its structure and evolution. *Journal of Geophysical Research: Solid Earth*, *88*(B9), 7411–7428. https://doi.org/10.1029/JB088iB09p07411

Bock, Y., Prawirodirdjo, L., Genrich, J. F., Stevens, C. W., McCaffrey, R., Subarya, C., et al. (2003). Crustal motion in Indonesia from Global Positioning System measurements. *Journal of Geophysical Research-Solid Earth*, *108*(B8). https://doi.org/10.1029/2001jb000324

Brune, S., Ladage, S., Babeyko, A. Y., Müller, C., Kopp, H., & Sobolev, S. V. (2010). Submarine landslides at the eastern Sunda margin: Observations and tsunami impact assessment. *Natural Hazards*, *54*(2), 547–562. https://doi.org/10.1007/s11069-009-9487-8

Chapple, W. M., & Forsyth, D. W. (1979). Earthquakes and bending of plates at trenches. *Journal of Geophysical Research*. https://doi.org/10.1029/JB084iB12p06729

Clift, P., & Vannucchi, P. (2004). Controls on tectonic accretion versus erosion in subduction zones: Implications for the origin and recycling of the continental crust. *Reviews of Geophysics*, *42*(2). https://doi.org/10.1029/2003rg000127

Cloos, M., & Shreve, R. L. (1996). Shear-zone thickness and the seismicity of Chilean- and Marianas-type subduction zones. *Geology*, *24*(2), 107–110. https://doi.org/10.1130/0091-7613(1996)024<0107:SZTATS>2.3.CO;2

Dahlen, F. A. (1984). Noncohesive Critical Coulomb Wedges: an Exact Solution. *Journal of Geophysical Research*, *89*(B12), 10125–10133. https://doi.org/10.1029/JB089iB12p10125

Dahlen, F. A., Suppe, J., & Davis, D. (1984). Mechanics of Fold-and-Thrust Belts and Accretionary Wedges: Cohesive Coulomb Theory. *Journal of Geophysical Research*, *89*(B12), 10087–10101. https://doi.org/10.1029/JB089iB12p10087

Das, S., & Watts, A. B. (2009). Effect of Subducting Seafloor Topography on the Rupture Characteristics of Great Subduction Zone Earthquakes. *Subduction Zone Geodynamics*, (November), 103–118. https://doi.org/10.1007/978-3-540-87974-9

Davidson, S. R., Barnes, P. M., Pettinga, J. R., Nicol, A., Mountjoy, J. J., & Henrys, S. A. (2020). Conjugate strike-slip faulting across a subduction front driven by incipient seamount subduction. *Geology*, *48*(5), 493–498. https://doi.org/10.1130/G47154.1

Davis, D., Suppe, J., & Dahlen, F. A. (1983). Mechanics of fold-and- thrust belts and accretionary wedges. *Journal of Geophysical Research*, *88*(B2), 1153–1172. https://doi.org/10.1029/JB088iB02p01153

Delescluse, M., & Chamot-Rooke, N. (2007). Instantaneous deformation and kinematics of the India-Australia Plate. *Geophysical Journal International*, *168*(2), 818–842. https://doi.org/10.1111/j.1365-246X.2006.03181.x

Dietrich, V. J. (1976). Evolution of the Eastern Alps: A plate tectonics working hypothesis. *Geology*, *4*(3), 147–152. https://doi.org/10.1130/0091-7613(1976)4<147:EOTEAA>2.0.CO;2

Dokht, R. M. H., Gu, Y. J., & Sacchi, M. D. (2018). Migration Imaging of the Java Subduction Zones. *Journal of Geophysical Research: Solid Earth*. https://doi.org/10.1002/2017JB014524

Dominguez, S., Lallemand, S. E., Malavieille, J., & Von Huene, R. (1998). Upper plate deformation associated with seamount subduction. *Tectonophysics*, *293*(3–4), 207–224. https://doi.org/10.1016/S0040-1951(98)00086-9

Dominguez, S., Malavieille, J., & Lallemand, S. E. (2000). Deformation of accretionary wedges in response to seamount subduction: Insights from sandbox experiments. *Tectonics*, *19*(1), 182–196. https://doi.org/10.1029/1999TC900055

Fisher, R. L., & Engel, C. (1969). Ultramafic and Basaltic Rocks Dredged from the Nearshore Flank of the Tonga Trench. *GSA Bulletin*, *80*(7), 1373–1378. https://doi.org/10.1130/0016-7606(1969)80[1373:UABRDF]2.0.CO;2

Fritz, H. M., Kongko, W., Moore, A., McAdoo, B., Goff, J., Harbitz, C., et al. (2007). Extreme runup from the 17 July 2006 Java tsunami. *Geophysical Research Letters*, *34*(12), 1–5. https://doi.org/10.1029/2007GL029404

Fukao, Y., & Obayashi, M. (2013). Subducted slabs stagnant above, penetrating through, and trapped below the 660 km discontinuity. *Journal of Geophysical Research: Solid Earth*. https://doi.org/10.1002/2013JB010466

Gerya, T. V., Fossati, D., Cantieni, C., & Seward, D. (2009). Dynamic effects of aseismic ridge subduction: numerical modelling. *European Journal of Mineralogy*, *21*(3), 649–661. https://doi.org/10.1127/0935-1221/2009/0021-1931

Gusman, A. R., Tanioka, Y., Matsumoto, H., & Iwasaki, S. I. (2009). Analysis of the Tsunami generated by the great 1977 Sumba earthquake that occurred in Indonesia. *Bulletin of the Seismological Society of America*, *99*(4), 2169–2179. https://doi.org/10.1785/0120080324

Hall, R. (2002). Cenozoic geological and plate tectonic evolution of SE Asia and the SW Pacific: Computer-based reconstructions, model and animations. *Journal of Asian Earth Sciences*. https://doi.org/10.1016/S1367-9120(01)00069-4

Hall, R., & Smyth, H. R. (2008). Cenozoic arc processes in Indonesia: Identification of the key influences on the stratigraphic record in active volcanic arcs. *Special Paper of the Geological Society of America*, *436*(03), 27–54. https://doi.org/10.1130/2008.2436(03)

Hamilton, W. B. (1988). Plate tectonics and island arcs. *Special Paper of the Geological Society of America*, *253*(10), 113–137. https://doi.org/10.1130/SPE253-p113

Hanifa, N. R., Sagiya, T., Kimata, F., Efendi, J., Abidin, H. Z., & Meilano, I. (2014). Interplate coupling model off the southwestern coast of Java, Indonesia, based on continuous GPS data in 2008-2010. *Earth and Planetary Science Letters*, *401*(December), 159–171. https://doi.org/10.1016/j.epsl.2014.06.010

El Hariri, M., & Bilek, S. L. (2011). Stress changes and aftershock distribution of the 1994 and 2006 Java subduction zone earthquake sequences. *Journal of Geophysical Research: Solid Earth*, *116*(6), 1–14. https://doi.org/10.1029/2010JB008124

Heine, C., Dietmar Müller, R., & Gaina, C. (2004). Reconstructing the lost eastern tethys ocean basin: Convergence history of the se asian margin and marine gateways. *Geophysical Monograph Series*, *149*, 37–54. https://doi.org/10.1029/149GM03

Hilde, T. W. C. (1983). Sediment subduction versus accretion around the pacific. *Tectonophysics*, *99*(2–4), 381–397. https://doi.org/10.1016/0040-1951(83)90114-2

Hillier, J. K., & Watts, A. B. (2007). Global distribution of seamounts from ship-track bathymetry data. *Geophysical Research Letters*, *34*(13). https://doi.org/10.1029/2007gl029874

Hoernle, K., Hauff, F., Werner, R., Van Den Bogaard, P., Gibbons, A. D., Conrad, S., & Müller, R. D. (2011). Origin of Indian Ocean Seamount Province by shallow recycling of continental lithosphere. *Nature Geoscience*, *4*(12), 883–887. https://doi.org/10.1038/ngeo1331

von Huene, R., & Lallemand, S. (1990). Tectonic erosion along the Japan and Peru convergent margins. *Geological Society of America Bulletin*, *102*(6), 704–720. https://doi.org/10.1130/0016-7606(1990)102<0704:TEATJA>2.3.CO;2

von Huene, Roland, & Scholl, D. W. (1991). Observations at convergent margins concerning sediment subduction, subduction erosion, and the growth of continental crust. *Reviews of Geophysics*, *29*(3), 279. https://doi.org/10.1029/91RG00969

von Huene, Roland, Aubouin, J., Azema, J., BLACKINTON, G., CARTER, J. A., COULBOURN, W. T., et al. (1980). Leg 67: The Deep Sea Drilling Project Mid-America Trench transect off Guatemala. *Geological Society of America Bulletin*, *91*(7), 421. https://doi.org/10.1130/0016-7606(1980)91<421:LTDSDP>2.0.CO;2

von Huene, Roland, Ranero, C. R., & Vannucchi, P. (2004). Generic model of subduction erosion. *Geology*, *32*(10), 913. https://doi.org/10.1130/G20563.1

Kanamori, H. (1986). RUPTURE PROCESS OF SUBDUCTION-ZONE EARTHQUAKES. *Annual Review of Earth and Planetary Sciences*, *14*, 293–322. https://doi.org/10.1146/annurev.ea.14.050186.001453

Karig, D. E. (1982). Initiation of subduction zones: implications for arc evolution and ophiolite development. *Geological Society Special Publication*, *10*, 563–576. https://doi.org/10.1144/GSL.SP.1982.010.01.37

Karig, D. E., Moore, G. F., Curray, J. R., & Lawrence, M. B. (1980). Morphology and shallow structure of the lower trench slope off Nias Island, Sunda arc. *The Tectonic and Geologic Evolution of Southeast Asian Seas and Islands. Part 1*, *23*, 179–208. https://doi.org/10.1029/gm023p0179

Karig, Daniel E., & Sharman, G. F. (1975). Subduction and accretion in trenches. *Bulletin of the Geological Society of America*, *86*(3), 377–389. https://doi.org/10.1130/0016-7606(1975)86<377:SAAIT>2.0.CO;2

Keller, G. (1980). Benthic Foraminifers and Paleobathymetry of the Japan Trench Area, Leg 57, Deep Sea Drilling Project. In *Initial Reports of the Deep Sea Drilling Project, 56/57*. U.S. Government Printing Office. https://doi.org/10.2973/dsdp.proc.5657.124.1980

Kopp, H., Hindle, D., Klaeschen, D., Oncken, O., Reichert, C., & Scholl, D. (2009). Anatomy of the western Java plate interface from depth-migrated seismic images. *Earth and Planetary Science Letters*. https://doi.org/10.1016/j.epsl.2009.09.043

Kopp, H, Flueh, E., Petersen, C., Weinrebe, W., & Wittwer, A. (2006). The Java margin revisited: Evidence for subduction erosion off Java. *Earth and Planetary Science Letters*, *242*(1–2), 130–142. https://doi.org/10.1016/j.epsl.2005.11.036

Kopp, Heidrun. (2002). BSR occurrence along the Sunda margin: Evidence from seismic data. *Earth and Planetary Science Letters*, *197*(3–4), 225–235. https://doi.org/10.1016/S0012-821X(02)00484-3

Kopp, Heidrun. (2011). The Java convergent margin: Structure, seismogenesis and subduction processes. *Geological Society Special Publication*, *355*, 111–137. https://doi.org/10.1144/SP355.6

Kopp, Heidrun, Flueh, E. R., Klaeschen, D., Bialas, J., & Reichert, C. (2001). Crustal structure of the Central Sunda margin at the onset of oblique subduction. *Geophysical Journal International*. https://doi.org/10.1046/j.0956-540X.2001.01547.x

Kopp, Heidrun, Klaeschen, D., Flueh, E. R., Bialas, J., & Reichert, C. (2002). Crustal structure of the Java margin from seismic wide-angle and multichannel reflection data. *Journal of Geophysical Research*, *107*(B2). https://doi.org/10.1029/2000jb000095

Lay, T, Ward, S. N., Kanamori, H., Ammon, C. J., Nettles, M., Ekström, G., et al. (2005). The great Sumatra-Andaman earthquake of 26 December 2004. *Science*, *308*(5725), 1127–1132.

Lay, Thorne, Ammon, C. J., Kanamori, H., Kim, M. J., & Xue, L. (2011). Outer trench-slope faulting and the 2011 Mw 9.0 off the Pacific coast of Tohoku Earthquake. *Earth, Planets and Space*, *63*(7), 713–718. https://doi.org/10.5047/eps.2011.05.006

Lefeldt, M., & Grevemeyer, I. (2008). Centroid depth and mechanism of trench-outer rise earthquakes. *Geophysical Journal International*, *172*(1), 240–251. https://doi.org/10.1111/j.1365-246X.2007.03616.x

Levy, J. K., & Gopalakrishnan, C. (2005). Promoting disaster-resilient communities: The great Sumatra - Andaman Earthquake of 26 December 2004 and the resulting Indian Ocean Tsunami. *International Journal of Water Resources Development*, *21*(4), 543–559. https://doi.org/10.1080/07900620500363297

Lüschen, E., Müller, C., Kopp, H., Engels, M., Lutz, R., Planert, L., et al. (2011). Structure, evolution and tectonic activity of the eastern Sunda forearc, Indonesia, from marine seismic investigations. *Tectonophysics*, *508*(1–4), 6–21. https://doi.org/10.1016/j.tecto.2010.06.008

Lynnes, C. S., & Lay, T. (1988). Source process of the great 1977 Sumba earthquake. *Journal of Geophysical Research*. https://doi.org/10.1029/jb093ib11p13407

Marot, M., Monfret, T., Pardo, M., Ranalli, G., & Nolet, G. (2012). An intermediate-depth tensional earthquake (M W 5.7) and its aftershocks within the Nazca slab, central Chile: A reactivated outer rise fault? *Earth and Planetary Science Letters*, *327–328*(January 2003), 9–16. https://doi.org/10.1016/j.epsl.2012.02.003

Masson, D. G., Parson, L. M., Milsom, J., Nichols, G., Sikumbang, N., Dwiyanto, B., & Kallagher, H. (1990). Subduction of seamounts at the Java Trench: a view with long-range sidescan sonar. *Tectonophysics*, *185*(1–2), 51–65. https://doi.org/10.1016/0040-1951(90)90404-V

McCaffrey, R. (2009). The Tectonic Framework of the Sumatran Subduction Zone. *Annual Review of Earth and Planetary Sciences*, *37*(1), 345–366. https://doi.org/10.1146/annurev.earth.031208.100212

McNeill, L. C., Dugan, B., Backman, J., Pickering, K. T., Pouderoux, H. F. A., Henstock, T. J., et al. (2017). Understanding Himalayan erosion and the significance of the Nicobar Fan. *Earth and Planetary Science Letters*, *475*, 134–142. https://doi.org/10.1016/j.epsl.2017.07.019

Moore, G. F., Curray, J. R., Moore, D. G., & Karig, D. E. (1980). Variations in geologic structure along the Sunda Fore Arc, northeastern Indian Ocean. *The Tectonic and Geologic Evolution of Southeast Asian Seas and Islands. Part 1*, *23*(Figure 1), 145–160. https://doi.org/10.1029/gm023p0145

Moore, Gregory F., Curray, J. R., & Emmel, F. J. (1982). Sedimentation in the Sunda trench and forearc region. *Geological Society Special Publication*, *10*, 245–258. https://doi.org/10.1144/GSL.SP.1982.010.01.16

Moore, J. C. (1989). TECTONICS AND HYDROGEOLOGY OF ACCRETIONARY PRISMS - ROLE OF THE DECOLLEMENT ZONE. *Journal of Structural Geology*, *11*(1–2), 95–106. https://doi.org/10.1016/0191-8141(89)90037-0

Müller, C., Kopp, H., Djajadihardja, Y. S., Barckhausen, U., Ehrhardt, A., Engels, M., et al. (2008). From subduction to collision: The Sunda-Banda Arc transition. *Eos*, *89*(6), 49–50. https://doi.org/10.1029/2008EO060001

Muruachi, S., & Ludwig, W. J. (1980). Crustal structures of the Japan Trench: the effect of subduction of oceanic crust. *Initial Rep. Deep Sea Drill. Proj*, *56*, 463–469.

Newcomb, K. R., & McCann, W. R. (1987). SEISMIC HISTORY AND SEISMOTECTONICS OF THE SUNDA ARC. *Journal of Geophysical Research-Solid Earth and Planets*, *92*(B1), 421–439. https://doi.org/10.1029/JB092iB01p00421

Okal, E. A. (2012). The south of Java earthquake of 1921 September 11: A negative search for a large interplate thrust event at the Java Trench. *Geophysical Journal International*. https://doi.org/10.1111/j.1365-246X.2012.05570.x

Park, J. O., Moore, G. F., Tsuru, T., Kodaira, S., & Kaneda, Y. (2004). A subducted oceanic ridge influencing the Nankai megathrust earthquake rupture. *Earth and Planetary Science Letters*, *217*(1–2), 77–84. https://doi.org/10.1016/s0012-821x(03)00553-3

Le Pichon, X., Henry, P., & Lallemant, S. (1993). Accretion and erosion in subduction zones: the role of fluids. *Annual Review of Earth & Planetary Sciences*, *21*(1980), 307–331. https://doi.org/10.1146/annurev.earth.21.1.307

Planert, L., Kopp, H., Lueschen, E., Mueller, C., Flueh, E. R., Shulgin, A., et al. (2010). Lower plate structure and upper plate deformational segmentation at the Sunda-Banda arc transition, Indonesia. *Journal of Geophysical Research*, *115*(B8), B08107. https://doi.org/10.1029/2009JB006713

Polet, J., & Kanamori, H. (2000). Shallow subduction zone earthquakes and their tsunamigenic potential. *Geophysical Journal International*, *142*(3), 684–702. https://doi.org/10.1046/j.1365-246X.2000.00205.x

Raharja, R., Gunawan, E., Meilano, I., Abidin, H. Z., & Efendi, J. (2016). Long aseismic slip duration of the 2006 Java tsunami earthquake based on GPS data. *Earthquake Science*, *29*(5), 291–298. https://doi.org/10.1007/s11589-016-0167-y

Ranero, C. R., & von Huene, R. (2000). Subduction erosion along the Middle America convergent margin. *Nature*, *404*(6779), 748–752. https://doi.org/10.1038/35008046

Ruff, L., & Kanamori, H. (1980). Seismicity and the subduction process. *Physics of the Earth and Planetary Interiors*. https://doi.org/10.1016/0031-9201(80)90117-X

Ruh, J. B. (2016). Submarine landslides caused by seamounts entering accretionary wedge systems. *Terra Nova*, *28*(3), 163–170. https://doi.org/10.1111/ter.12204

Ruh, J. B., Sallarès, V., Ranero, C. R., & Gerya, T. (2016). Crustal deformation dynamics and stress evolution during seamount subduction: High-resolution 3-D numerical modeling. *Journal of Geophysical Research: Solid Earth*, *121*(9), 6880–6902. https://doi.org/10.1002/2016JB013250

Scholz, C. H., & Small, C. (1997). The effect of seamount subduction on seismic coupling. *Geology*, *25*(6), 487. https://doi.org/10.1130/0091-7613(1997)025<0487:TEOSSO>2.3.CO;2

Shulgin, A., Kopp, H., Mueller, C., Planert, L., Lueschen, E., Flueh, E. R., & Djajadihardja, Y. (2011). Structural architecture of oceanic plateau subduction offshore Eastern Java and the potential implications for geohazards. *Geophysical Journal International*, *184*(1), 12–28. https://doi.org/10.1111/j.1365-246X.2010.04834.x

Sibson, R. H., Robert, F., & Poulsen, K. H. (1988). High-angle reverse faults, fluid-pressure cycling, and mesothermal gold-quartz deposits. *Geology*, *16*(6), 551–555. https://doi.org/10.1130/0091-7613(1988)016<0551:HARFFP>2.3.CO;2

Stern, C. R. (2020). The role of subduction erosion in the generation of Andean and other convergent plate boundary arc magmas, the continental crust and mantle. *Gondwana Research*, *88*, 220–249. https://doi.org/10.1016/j.gr.2020.08.006

Uyeda, S., & Kanamori, H. (1979). Back-arc opening and the mode of subduction. *Journal of Geophysical Research*, *84*(B3), 1049. https://doi.org/10.1029/jb084ib03p01049

Vannucchi, P., Remitti, F., & Bettelli, G. (2008). Geological record of fluid flow and seismogenesis along an erosive subducting plate boundary. *Nature*, *451*(7179), 699–703. https://doi.org/10.1038/nature06486

Wang, K., & Bilek, S. L. (2011). Do subducting seamounts generate or stop large earthquakes? *Geology*, *39*(9), 819–822. https://doi.org/10.1130/G31856.1

Wang, K., & Bilek, S. L. (2014). Invited review paper: Fault creep caused by subduction of rough seafloor relief. *Tectonophysics*. https://doi.org/10.1016/j.tecto.2013.11.024

Wang, K., & Hu, Y. (2006). Accretionary prisms in subduction earthquake cycles: The theory of dynamic Coulomb wedge. *Journal of Geophysical Research: Solid Earth*, *111*(6), 1–16. https://doi.org/10.1029/2005JB004094

Wang, K., Hu, Y., von Huene, R., & Kukowski, N. (2010). Interplate earthquakes as a driver of shallow subduction erosion. *Geology*, *38*(5), 431–434. https://doi.org/10.1130/G30597.1

Widiyantoro, S., Gunawan, E., Muhari, A., Rawlinson, N., Mori, J., Hanifa, N. R., et al. (2020). Implications for megathrust earthquakes and tsunamis from seismic gaps south of Java

Indonesia. *Scientific Reports*, *10*(1), 15274. https://doi.org/10.1038/s41598-020-72142-z

Widiyantoro, Sri, & Van Der Hilst, R. (1997). Mantle structure beneath Indonesia inferred from high-resolution tomographic imaging. *Geophysical Journal International*. https://doi.org/10.1111/j.1365-246X.1997.tb00996.x

Widiyantoro, Sri, Van Der Hilst, R., & vanderHilst, R. (1996). Structure and evolution of lithospheric slab beneath the Sunda arc, Indonesia. *Science*, *271*(5255), 1566–1570. https://doi.org/10.1126/science.271.5255.1566

Zenonos, A., De Siena, L., Widiyantoro, S., & Rawlinson, N. (2019). P and S wave travel time tomography of the SE Asia-Australia collision zone. *Physics of the Earth and Planetary Interiors*, *293*(May), 106267. https://doi.org/10.1016/j.pepi.2019.05.010

CHAPTER 3

MANUSCRIPT #1

Reflection tomography by depth warping: a case study across the Java trench

Yueyang Xia(1); Dirk Klaeschen (1); Heidrun Kopp(1,2) and Michael Schnabel(3)

(1) Dynamics of the Ocean Floor, GEOMAR, Helmholtz Centre for Ocean Research Kiel, 24148 Kiel, Germany
(2) Department of Geosciences, Kiel University, 24118 Kiel, Germany
(3) Bundesanstalt für Geowissenschaften und Rohstoffe (BGR), Stilleweg 2, 30655 Hanover, Germany

Published in 2022 in *Solid Earth* 13, 367–392

This chapter contains a manuscript published in *Solid Earth* in its original form. Please note that the publication contains its own reference list and refers to its own figure and page numbers. The manuscript is reproduced with permission of the European Geophysical Union.

Solid Earth, 13, 367–392, 2022
https://doi.org/10.5194/se-13-367-2022

Solid Earth Open Access EGU

Reflection tomography by depth warping: a case study across the Java trench

Yueyang Xia[1], **Dirk Klaeschen**[1], **Heidrun Kopp**[1,2], **and Michael Schnabel**[3]

[1]Dynamics of the Ocean Floor, GEOMAR, Helmholtz Centre for Ocean Research Kiel, 24148 Kiel, Germany
[2]Department of Geosciences, Kiel University, 24118 Kiel, Germany
[3]Bundesanstalt für Geowissenschaften und Rohstoffe (BGR), Stilleweg 2, 30655 Hanover, Germany

Correspondence: Yueyang Xia (yxia@geomar.de)

Received: 6 April 2021 – Discussion started: 14 April 2021
Revised: 23 December 2021 – Accepted: 4 January 2022 – Published: 21 February 2022

Abstract. Accurate subsurface velocity models are crucial for geological interpretations based on seismic depth images. Seismic reflection tomography is an effective iterative method to update and refine a preliminary velocity model for depth imaging. Based on residual move-out analysis of reflectors in common image point gathers, an update of the velocity is estimated by a ray-based tomography. To stabilize the tomography, several preconditioning strategies exist. Most critical is the estimation of the depth error to account for the residual move-out of the reflector in the common image point gathers. Because the depth errors for many closely spaced image gathers must be picked, manual picking is extremely time-consuming, human biased, and not reproducible. Data-driven picking algorithms based on coherence or semblance analysis are widely used for hyperbolic or linear events. However, for complex-shaped depth events, purely data-driven picking is difficult. To overcome this, the warping method named non-rigid matching is used to estimate a depth error displacement field. Warping is used, for example, to merge photographic images or to match two seismic images from time-lapse data. By matching a common image point gather against its duplicate that has been shifted by one offset position, a locally smooth-shaped displacement field is calculated for each data sample by gather matching. Depending on the complexity of the subsurface, sample tracking through the displacement field along predefined horizons or on a simple regular grid yields discrete depth error values for the tomography. The application to a multi-channel seismic line across the Sunda subduction zone offshore Lombok island, Indonesia, illustrates the approach and documents the advantages of the method to estimate a detailed velocity structure in a complex tectonic regime. By incorporating the warping scheme into the reflection tomography, we demonstrate an increase in the velocity resolution and precision by improving the data-driven accuracy of depth error picks with arbitrary shapes. This approach offers the possibility to use the full capacities of tomography and further leads to more accurate interpretations of complex geological structures.

1 Introduction

Reflection tomography and pre-stack depth migration of multi-channel seismic reflection (MCS) data have evolved into standard seismic data processing routines in recent decades, owing to the rapid development of CPU performance and the effective adaption of seismic data processing software. Pre-stack depth migration (PSDM) of near-vertical reflections is the algorithm of choice in reflection seismology to properly image steeply dipping reflectors while accounting for non-hyperbolic move-out caused by lateral velocity variations (Yilmaz, 2001; Jones et al., 2008) and thus is applied in tectonically and structurally complex geological settings in 2-D and 3-D migration strategies (Collot et al., 2011; Han et al., 2017; Li et al., 2018; Shiraishi et al., 2019). However, the quality of subsurface imaging depends on the seismic velocity model that is used for the migration. An exact determination of the velocity field is thus crucial to retrieve an optimal subsurface image.

The velocity field may be determined during PSDM by performing velocity analysis on selected locations using

Published by Copernicus Publications on behalf of the European Geosciences Union.

depth-focusing error analysis (Audebert and Diet, 2008; MacKay and Abma, 1992) or hyperbolic residual move-out (RMO) correction of common image point (CIP) gathers followed by a simple vertical Dix inversion (Dix, 1955) at each location independently. Thus a structural velocity model (Audebert et al., 1997) may be built manually by defining depth horizons. Manual picking or pre-definition of depth horizons, however, are not only time-consuming for seismic processors but, more importantly, may also lead to a subjective interpretation bias (Jones, 2003).

In contrast, the velocity model design based on reflection tomography inverts all CIP locations simultaneously to update the velocity structure and yields a more complete solution than manually designed velocity models (Bishop et al., 1985; Van Trier, 1990; Stork, 1992; Kosloff et al., 1996). While the Dix inversion strips off the layers from top to bottom in a flat-layer approach, the reflection tomography accounts for dipping layers and lateral velocity changes within the streamer length (Jones, 2010). The general procedure for reflection tomography is to go into the pre-stack migrated CIP offset domain and to measure the hyperbolic residual move-out of the depth misalignment (also called depth error) by manual picking or by automatic scanning techniques (Hardy, 2003; Claerbout, 1992). Subsequently, the depth error is inverted to velocity changes to flatten the reflector signals over the entire offset range (Jones et al., 2008; Fruehn et al., 2008; Riedel et al., 2019). For cases where the MCS data do not provide sufficient move-out sensitivity to estimate reliable velocities (i.e. deep target depth), several velocity inversion strategies have been established to combine near-vertical reflections, wide-angle (WA) reflections, and refracted events (Gras et al., 2019; Górszczyk et al., 2019; Melendez et al., 2019).

By relating changes of the CIP depth errors to changes in velocities along source–receiver rays in the direction normal to the local reflector dip, a new velocity can be calculated to minimize the CIP depth errors. To solve the general non-linear inverse tomographic problem, the velocity error is gauged iteratively, inverted, and updated as depicted by the loop in Fig. 1.

To circumnavigate these issues and increase the picking accuracy, we applied a warping technique called "non-rigid matching" (NRM). By calculating the depth error shift of seismic trace samples by comparing neighbouring traces along the complete offset of closely spaced CIP gathers, we improve the depth error estimation without any curvature assumption or predefined depth horizons of the subsurface structure.

Here we present the NRM technique for the depth error estimation as a purely data-driven automatic picking method. We demonstrate the advantages and limitations of the NRM method using a synthetic gather. We then apply a combination of NRM with ray-based reflection tomography to field data of pre-stack depth-migrated seismic sections from the Sunda convergent margin offshore Lombok island, Indonesia. As initial velocity, a wide-angle tomographic inversion of a collocated 2-D ocean-bottom seismometer (OBS) seismic line was used. The reflection profile is characterized by an accretionary prism of strongly folded sediment with limited reflector continuity, which makes manual velocity estimation extremely challenging.

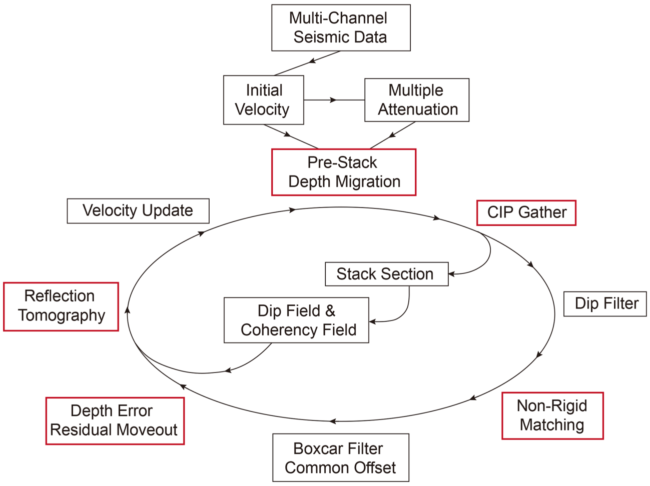

Figure 1. Processing scheme using non-rigid matching in reflection tomography to update the velocity field during pre-stack depth migration of multi-channel seismic reflection data. The main processing steps are marked in red.

2 Method: non-rigid matching and reflection tomography

2.1 Non-rigid and warping matching techniques

The non-rigid matching (NRM) or "warping" methods are computer-based image matching technologies that aim to estimate a flow pattern (vector displacement in three dimensions) of a sequence of images with additional smoothness constraints (Horn and Schunck, 1981; Wolberg, 1990). Compared to a rigid matching like translation, rotation, or even affine transformation, NRM is developed to handle situations when the transformation is non-linear (Pappu et al., 1996). The benefit of NRM regarding the non-linear transformation substantially improves seismic imaging and inversion methods through matching and tracking horizontal and vertical displacements of seismic events with high accuracy in the depth and time domains.

NRM or warping applications were first introduced for 3-D time-lapse seismic data by comparing two seismic cubes acquired at different acquisition times with a special focus on depth formation changes resulting from hydrocarbon production (e.g. Rickett and Lumley, 2001; Aarre, 2008; Tomar et al., 2017). The image displacement warping method of Hall (2006) estimates a full 3-D local vector deviation employing an iterative search of maximum correlation using a deformable mesh for sensitivity and quality analysis, whereas Hale (2009, 2013) based his dynamic image warping (DIW) on 1-D cross-correlation optimization schemes in each dimension to estimate the vector displacements. By solving a set of 1-D equations and separately including spectral whitening and a Gaussian low-pass filter, a stable 3-D solution is achieved iteratively by minimizing the difference of the reference and the current wavefield corrected by the estimated displacements. This method is able to calculate rapid and large shifts, both in time/depth and in space, and overcomes the restrictions of limited shifts due to time/depth windowing used by cross-correlation methods (Zhang et al., 2014). In contrast, the NRM method introduced by Nickel et al. (1999) uses 1-D Taylor expansions for each vector component, which are separately solved for each dimension to converge to a 3-D solution by minimizing the difference of the reference section and the current wavefield corrected by the estimated displacements, as in the warping method of Hale (2009).

In this study, we use the 1-D displacement version (only in the z direction) of the 3-D NRM calculation from Nickel et al. (1999) and Aarre (2008) from a 3-D time-lapse application. Given any actual seismic volume A and a reference seismic volume R, finding the best 1-D depth displacement field Δh between these two is an optimization problem to minimize the difference $d_{[x,y,z]}$ between the displacement-corrected actual seismic volume A and the reference volume R. This process could be expressed as in the following formula:

$$\min[d_{[x,y,z]}] = A_{[x,y,z+\Delta h_{[x,y,z]}]} - R_{[x,y,z]}, \tag{1}$$

where $A_{[x,y,z]}$ represents the actual seismic volume, $R_{[x,y,z]}$ represents the reference volume, $\Delta h_{[x,y,z]}$ represents the 1-D NRM displacement field, and $d_{[x,y,z]}$ represents the difference volume between the reference volume $R_{[x,y,z]}$ and the shifted actual volume $A_{[x,y,z+\Delta h_{[x,y,z]}]}$ in the z direction. Indexes $[x, y, z]$ are customized dimensions (refers to the common depth point (CDP) dimension, common offset dimension, and depth (z) dimension in this study) for the input data. Note that the $\Delta h_{[x,y,z]}$ is only added in the z dimension of $A_{[x,y,z]}$ since this is a 1-D displacement calculation.

The optimization problem of a minimized $d_{[x,y,z]}$ could be achieved by first assuming $d_{[x,y,z]}$ is equal to zero:

$$R_{[x,y,z]} = A_{[x,y,z+\Delta h_{[x,y,z]}]}. \tag{2}$$

After implementing the Taylor expansion for Eq. (2), one could readily get the following formula:

$$R_{[x,y,z]} = A_{[x,y,z]} + \Delta h_{[x,y,z]} \cdot A'_{[x,y,z]} \tag{3}$$

and

$$\Delta h_{[x,y,z]} = (R_{[x,y,z]} - A_{[x,y,z]}) / A'_{[x,y,z]}, \tag{4}$$

by isolating the $\Delta h_{[x,y,z]}$.

Thus, the optimization problem of $d_{[x,y,z]}$ becomes solving the numerical solution of Eq. (4) for a stable and minimized NRM displacement field $\Delta h_{[x,y,z]}$, which would be further used as the input information of the NRM-based RMO auto-tracking, and the seismic gather flattening.

To stabilize the results, and especially not to disturb the waveform by the estimated depth-variant displacements, additional constraints are implemented, e.g. band-limited application of the seismic traces during the iterations of matching starting from the lowest wavenumber, smoothing for spatial continuity, and avoiding vertical shifts that would swap neighbouring depth samples. It should be noted that the estimated displacements to match two sections are not based on peak amplitudes, but to minimize the band-limited amplitude difference between them.

A number of new geophysical applications for pre-stack event tracking using the warping technique have been introduced in the scientific community in recent decades (e.g. Perez and Marfurt, 2008; Reiche and Berkels, 2018; Sripanich et al., 2020). The main objective of all these applications is to efficiently define a reference data ensemble and calculate the displacement shift from any data ensemble to match the reference data ensemble. The unique selection of a reference ensemble depends on the individual purpose of the application. Perez and Marfurt (2008) estimated vertical and spatial displacements with a modified cross-correlation method from Rickett and Lumley (2001). A displacement estimation between 3-D common angle binned migrated sections to a reference stacked volume was used to improve the stack quality and resolution. Reiche and Berkels (2018) sorted the migration data into common offset sections and selected the smallest offset section as a reference section and calculated the displacement from all other offset sections to the smallest offset section in order to calculate the move-out curvature and flatten the common-mid-point (CMP) gather. Sripanich et al. (2020) estimated reflection move-out dip slopes on 3-D CMP gathers directly by a plane-wave destruction filter (Fomel, 2002) to flatten events by nonstationary filters. This processing sequence can be seen as a warping process by an application of time-variant static corrections.

The wide range of possible applications for lateral and vertical displacement estimations even in three dimensions make the NRM and DIW attractive, e.g. quantitative estimations of vertical and horizontal reflector shifts due to repositioning of re-migrated data. As both methods are very similar in that they iteratively minimize the difference of two sections, we use only the NRM for the application of estimating the RMO. The calculation of vertical shifts between a reference section and an actual section is the simplest application and allows us to compare the results to a plane-wave destruction filter (PWD), which is commonly used for estimations of reflector dips.

In this study's NRM application, we calculate the 1-D NRM displacement field in pre-stack depth-migrated CIP volume to quantify the smoothed trace-to-trace displacement in CIP gathers by manipulating the traces in procedures below. As mentioned in the previous paragraphs, the application of NRM for the vertical displacement calculation in a CIP domain also requires a reference CIP gather, similar to the time-lapse application. This can be achieved with a relative reference scheme by duplicating the current CIP gather and shifting the traces laterally to larger offsets by one trace position to form the reference gather. Thus, the calculated relative 1-D displacement shift through Eqs. (1)–(4) between the two gathers correspond then to vertical and spatial smooth event slope dips of a trace to its previous trace. As neighbouring traces of a CIP gather show a strong similarity of the waveform and amplitude without spatial aliasing, the NRM gather matching can then be used to estimate the vertical displacement also known as depth error without any physical assumptions. In this way, the application of NRM for CIP gathers overcomes the limitation of residual move-out estimations inherent in conventional semblance scanning (Neidell and Taner, 1971) of predefined functions like linear, parabolic, or even higher-order curvatures.

2.1.1 NRM synthetic data example

For field MCS data, due to the complex subsurface structure and seismic acquisition geometry, as well as the anisotropic physical world, three main unique classified situations represent the main difficulties for analysing the residual move-out. To test the advantages and shortcomings of the warping method we created a synthetic CIP gather in Fig. 2a. The gather consists of three sets of events including 0.1 % background noise of the maximum amplitude from top to bottom: (1) a symmetrical lateral shifted diffraction-like event with positive amplitude, which is unrealistic but was included because it cannot be approximated by any linear, parabolic, or hyperbolic standard move-out correction; (2) two intersecting parabolic curvature events with opposite polarity. To get the under-corrected positive polarity event to align horizontally, the velocity above it must be reduced whereas aligning the deeper, over-corrected negative-polarity event requires an increase in velocity above it. This situation occurs if the background velocity model is not well adapted to the data, e.g. a vertical velocity increase between the two events; and (3) one parabolic event with a local curvature anomaly, offset-dependent wavelet amplitude, and frequency attenuation. To get the under-corrected general trend of the event horizontally aligned the velocity above must be decreased. To further align the local curvature anomaly the velocity above must locally be increased to fully flatten the signals over the complete offset range.

Because the NRM displacement field in Fig. 2b is calculated in a relative referenced scheme of a trace to its previous trace, the relative dip displacements correspond to a local dip field. The red colour of positive values in each trace shown in Fig. 2b suggests that a corresponding trace sample in Fig. 2a should be shifted downward to match and align to its previous trace sample by the application of the displacement field values. Blue-coloured negative values require shifting in the opposite (i.e. upward) direction. A zero-displacement value appearing at the apex of the symmetrical diffraction events illustrates the fact that the dipping angle at this location of the event is zero. The NRM field of these three sets of synthetic events follows the general local dip trend well.

2.1.2 Depth-variant alignment from relative displacement correction

Since the NRM field contains the full information of the relative depth-variant shifts of the seismic events, the NRM field can be used to flatten the input seismic section, which has several advantages for the depth error calculation and as quality control of the validity of the displacement field. Intuitively the second trace of Fig. 2a must be depth-variant shifted by the amplitudes of the second trace of the NRM field in Fig. 2b to get aligned to the first trace. To further align the third trace of Fig. 2a, the trace must be depth-variant shifted by the amplitude of the third trace of the NRM field in Fig. 2b and additionally shifted by the previous depth corrections which were applied to the second trace. The following equations are documented in the online repository (https://doi.org/10.5281/zenodo.5998288, Xia et al., 2022) as web-based interactive script files. The depth correction alignment can be written as recursive formula Eq. (5):

$$f_{\mathrm{a}[i,:]} = \begin{cases} P_{\mathrm{lin}\left(h_{[i,:]},\, f_{[i,:]}\right)}, & \text{if } i = 1 \\ P_{\mathrm{lin}\left(h_{[i-1,:]},\, P_{\mathrm{lin}\left(h_{[i,:]},\, f_{[i,:]}\right)}\right)}, & \text{if } i = 2 \\ P_{\mathrm{lin}\left(h_{[i-2,:]},\, P_{\mathrm{lin}\left(h_{[i-1,:]},\, P_{\mathrm{lin}\left(h_{[i,:]},\, f_{[i,:]}\right)}\right)}\right)}, & \text{if } i = 3 \\ \ldots\ldots \\ \ldots\ldots \\ \ldots\ldots \end{cases} \tag{5}$$

where $f_{[i,:]}$ is the original synthetic seismic trace array at the ith trace, $h_{[i,:]}$ represents the NRM displacement field at the ith trace, the index i represents the actual trace number index of the dataset ($i \in \{1, 2, 3, 4, \ldots\ldots\}$), and the function P_{lin} represents an irregular linear interpolation function. The function P_{lin} for any corrected sample $f_{\mathrm{a}[i,j]}$ could be expressed as in Eq. (6):

$$\begin{aligned} f_{\mathrm{a}[i,j]} &= P_{\mathrm{lin}\left(h_{[i,:]},\, f_{[i,j]}\right)} \\ &= f_{[i,j]} + \frac{f_{[i,n]} - f_{[i,m]}}{n - m} \cdot (j - m), \end{aligned} \tag{6}$$

where the m and n are the closest irregular (non-integer) index to j in the depth corrected index array $r_{[:]}$ by the NRM field for any given seismic trace $f_{[i,:]}$. Please note that the displacement shifts from seismic amplitudes have much higher precision than the traces' depth sample rate, and the correction of the depth indexes will end up with non-integer num-

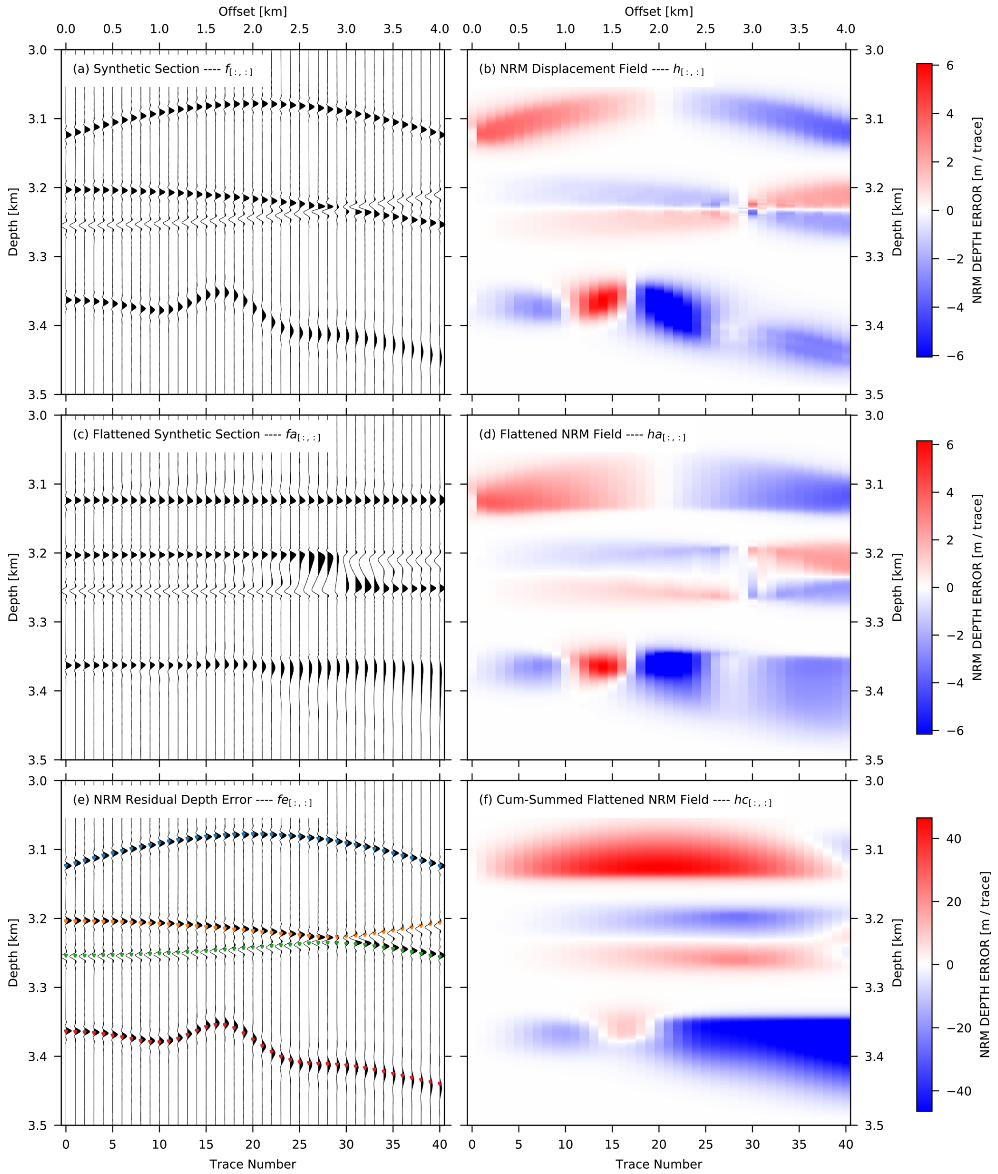

Figure 2. **(a)** Simulated complex geological situations that would be frequently seen in pre-stack depth-migrated (PSDM) common-image-point (CIP) domains. A symmetrical diffraction, two interfering parabolic events with opposite polarity, and parabolic event with a local curvature anomaly, including frequency versus offset signal variations. **(b)** The relative NRM displacement of gather **(a)** calculated from trace n to the previous trace $(n-1)$ for $n>1$. **(c)** Application of the displacement correction from **(b)** to the gather of **(a)**. **(d)** Application of the displacement self-correction of the gather of **(b)**. **(e)** Residual move-out picks calculated from the recursive cumulative sum of the relative depth errors **(f)** at predefined nearest-offset depths. **(f)** Cumulative sum calculated from **(d)**.

bers in the intermediate index array $r_{[:]}$. Therefore, an irregular linear interpolation is needed in the calculation to recover the original regular depth index j. The depth index j will be immediately obtained after the linear interpolation.

Based on the above discussion, any intermediate irregular index $r_{[k]}$ in the array $r_{[:]}$ can be simply expressed by $r_{[k]}=j-h_{[i,j]}$, where j represents the original regular depth index of the array $f_{[i,:]}$, and k represents the index of the NRM-corrected irregular index array $r_{[:]}$, $(j,\,k\in\{1,2,3,4,\ldots\ldots\})$. Since the element $h_{[i,j]}$ is a number with decimal, the intermediate NRM-corrected index array $r_{[:]}$ does not have to be an integer. Thus, the array $r_{[:]}$ could be simply expressed as follows:

$$\begin{aligned}r_{[:]}=&\big[1-h_{[i,1]},\ 2-h_{[i,2]},\ 3-h_{[i,3]},\\&4-h_{[i,4]},\ \ldots\ldots\big],\end{aligned}\tag{7}$$

where the $h_{[i,:]}$ represent the NRM displacement field at the ith trace. By applying Eqs. (5)–(7), one could readily get the flattened synthetic seismic section $f_{\mathrm{a}_{[:,:]}}$ (Fig. 2c). The

Python programming with the flattening of the seismic section in Fig. 2c is documented in the online repository.

The NRM flattened events by the recursive depth-variant correction in Fig. 2c provide quality control of displacement calculation for these three special situations. Generally, the squeeze-and-stretch effect of the non-linear displacement correction is inevitable for a multi-trace gather, but as shown here, the displacement shift correction adequately dealt with most of the simulated examples. The first symmetrical diffraction events get optimally flattened, with no significant change of the wavelet shape. The third non-linear undulation with a wavelet variation effect is effectively flattened at the peak amplitude, but strong wavelet stretch is visible. After the NRM displacement correction, the wavelets at mid-offsets (1.5 to 2.5 km) get squeezed and at far offsets (3.5 to 4.0 km) stretched equivalent to normal move-out stretch effects. The crossing region of the two intersecting events is flattened well but suffers from a significant stretch effect, which introduces substantial artificial low-frequency energy between the two events between offset 2.5 and 3.5 km. Due to the constraint that vertical shifts cannot swap neighbouring depth samples, a false event relation occurred beyond 3 km offset, as clearly seen in Fig. 2c by the opposite signal polarity along the two flattened events (between 3.2 and 3.27 km depth). As a result, in a final stacking procedure of this CIP gather, the NRM displacement correction will lead to wavelet stretching, squeezing artefacts, and destructive summation.

An application of the same procedure of Eqs. (5)–(7) to the NRM field $h_{[:,:]}$ instead of the seismic section $f_{[i,:]}$ results in the depth-corrected (flattened) relative NRM displacement field $h_{\mathrm{a}_{[:,:]}}$, as shown in Fig. 2d. This flattened NRM field will be used for automatic tracking and picking of the continuous events in the CIP gather.

2.1.3 RMO automatic picking by tracking through NRM displacement field

As the flattened NRM relative displacement field contains the information of relative depth shift from trace to trace along depth slices, the estimation of the depth error is achievable by predefining a start tracking depth at the first trace (nearest offset) and analysing the corresponding depth slice of the flattened NRM field in Fig. 2d. Given a pre-defined starting pick z_0 at the nearest offset, the change of the residual reflector depth $\Delta z_{[:,z_0]}$, which is needed for the reflection tomography, can be extracted along the flattened NRM displacement field $h_{\mathrm{a}_{[:,:]}}$ by calculating a cumulative summation $h_{\mathrm{c}_{[:,:]}}$ along the depth slide at depth z_0:

$$\Delta z_{[i,z_0]} = -1 \cdot h_{\mathrm{c}_{[i,z_0]}}, \tag{8}$$

where the array $\Delta z_{[:]}$ represents the depth error relative to reflector depth z_0, array $h_{\mathrm{c}_{[:,:]}}$ represents the depth-corrected cumulative-summed NRM displacement field, and the index i represents the trace number. For any trace $h_{\mathrm{a}_{[i,:]}}$ in Fig. 2d the cumulative summed NRM field $h_{\mathrm{c}_{[:,:]}}$ in Fig. 2f can be calculated by

$$h_{\mathrm{c}_{[i,:]}} = \sum_{k=1}^{i} h_{\mathrm{a}_{[i,:]}}. \tag{9}$$

The array $h_{\mathrm{a}_{[i,:]}}$ represent the ith flattened NRM trace. With the knowledge of the residual reflector depth $\Delta z_{[i,z_0]}$, one could readily get the RMO of any reflector in a seismic gather:

$$f_{\mathrm{e}_{[i]}} = \Delta z_{[i,z_0]} + [z_0, z_0, z_0, \ldots\ldots\ldots, z_0], \tag{10}$$

where array $f_{\mathrm{e}_{[:]}}$ represents the absolute depth of an RMO sequence over the gather for a series of continuous reflectors. By applying Eqs. (8)–(10), and using the simple synthetic seismic (Fig. 2a), the four series of RMO picks illustrated in Fig. 2e represent the auto-tracked RMO depth of the events. The Python programming of Eqs. (8)–(10), the calculation of the RMO of a series of continuous reflectors (Fig. 2e), and the absolute NRM field calculation (Fig. 2f) are documented in the online repository (https://doi.org/10.5281/zenodo.5998288, Xia et al., 2022) as web-based interactive script files.

As a result, all RMO depth error picks follow the amplitude peaks of the seismic events except for the "X"-shaped interfering reflectors. The NRM displacements are misled by the crossing point and switch to an event that should not be followed. This kind of "V"-shaped depth error information will undermine the reliability of the tomographic result because the depth error branch is a combination of two different events. To avoid this mismatch a quality factor is introduced and assigned to each individual pick along the depth error branch. A sliding trace summation window along a depth slice or comparison of a near-offset stack to the individual events can be used. In this example, a sliding trace summation would detect a rapid decrease in quality due to the polarity change resulting in a destructive summation. Picks with lower quality as a predefined threshold can be deleted. In this special case, the two depth error branches of the intersecting events will be split into four individual depth error branches which the reflection tomography will handle correctly as four independent reflection events. If these crossing events happen as a result of interfering noise like surface-related or interbed multiples, the unwanted events should be attenuated prior to NRM by a dip filter in the CIP gather (Fig. 1).

To verify the accuracy of the NRM method we compared the picking results of the NRM method to a plane-wave destruction filter PWD method (Fig. 3). The PWD method is splitting the data into spatially and temporal windows and assumes that the slopes are stationary within each window (Fomel, 2002; Xue et al., 2019). In contrast, the NRM method is iteratively minimizing the amplitude difference (Eqs. 1–4) between an adjusted gather and a reference gather for all events simultaneously. For both methods, the estimated depth error picks in Fig. 3a are near the maximum amplitude peak of the events. On the far offset traces with reduced amplitudes the NRM shows less accuracy (Fig. 3b). Due to the strategy by the NRM method to minimize the band-limited amplitude difference, the strongest near-offset amplitude events will dominate this inversion result. This strategy is useful by comparing two seismic cubes with a special focus on depth or spatial shifts to reduce distortions from low-amplitude events. To avoid small-amplitude events in a CIP gather being underdetermined in their dip estimation an additional gain balancing is recommended before an NRM application.

2.1.4 Effective RMO selection based on semblance analysis

Giving predefined starting depths for the RMO tracking is applicable in a simple synthetic test which contains only few continuous reflectors. However, it is unrealistic to define each reflector's starting depth in real data or complex synthetic examples, which could have several tens of effective reflectors in one migrated CIP gather (Fig. 4a). An efficient approach to determine the reflectors' start-tracking depth is by analysing the flattened CIP gather (Fig. 4c) by a semblance-weighted grid-based scheme.

A semblance $s_{[j]}$ value, which is a quantitative measure of the similarity of a number of traces (Yilmaz, 2001) in the seismic section, is described as follows:

$$s_{[j]} = \frac{\left(\sum\limits_{i=1}^{n} F_{[i,j]}\right)^2}{\sum\limits_{i=1}^{n} F_{[i,j]}^2} \Bigg/ n, \tag{11}$$

where n is the maximum number of traces, $F_{[i,j]}$ represents the seismic section, the index i represents the trace number, and the index j represents the sample depth.

By conducting semblance calculation on the NRM-flattened seismic section (Fig. 4c), the flattened section could not only provide NRM field's quality control but also sheds light on selecting effective reflectors and determining the starting depth for RMOs' auto-tracking. By calculating the semblance value for each depth slice along the flattened seismic section, one can reject unwanted picks, by setting up a threshold of semblance limitation (e.g. 0.5). In the synthetic example with several reflectors (Fig. 4a), RMO picks are digitized in zones of good reflector continuity (semblance > 0.5 and minimum pick depth increment of 12 m; see coloured dots in the left panel of Fig. 4c) and rejected in non-reflection or weak zones (semblance < 0.5) (Fig. 4d). The math applications of this auto-picking and semblance threshold selection schemes are documented in the online repository (https://doi.org/10.5281/zenodo.5998288, Xia et al., 2022).

Because the plane-wave destruction filter (PWD) is widely used to estimate the move-out dip slopes on seismic sections or gathers (Fomel, 2002; Sripanich et al., 2020), we applied the outlined processing sequence of displacement corrections based on a PWD filter in the online repository as an alternative method to the NRM method.

2.2 Methodology of the ray-based grid tomography with CIP depth errors

The basic concept of iterative ray-based grid tomography is to find subsurface velocity perturbations that minimize the residual move-out depth error picks of the initial migrated CIP gathers (Woodward et al., 2008). Conditions that must be fulfilled are preserved arrival times. The calculated arrival time t of ray path for a given depth error pick Δz through the initial velocity model must be preserved in the updated velocity model. That requires that a change of the residual reflector depth Δz must be compensated by small changes in the velocity model $\Delta\alpha_i$ where the index i corresponds to a grid node in a gridded model. For an acoustic reflection it follows the residual migration equation of Stork (1992):

$$\Delta t = 0 = \frac{\Delta z}{\alpha} 2\cos\Theta\cos\Phi + \sum_i \left(\frac{\partial t}{\partial\alpha_i}\Delta\alpha_i\right). \tag{12}$$

Here Δt is the preserved arrival time, Δz is a change in reflector depth, Θ is half the opening angle between source and detector rays at the reflector, Φ is reflector dip, and α the velocity at the reflector depth of the actual model. $\Delta\alpha_i$ is a change in the velocity, and $\partial t/\partial\alpha_i$ is a change in travel time corresponding to a change of velocity α at grid node i. As $\partial t/\partial\alpha_i$ is calculated independently of the ray parameters Θ and Φ, the ray path bending is assumed not to change during a velocity update. From this follows that only small velocity perturbation should be estimated for each iteration step.

The CIP tomography must find the velocity change $\Delta\alpha_i$ that is needed to flatten migrated reflectors and eliminate the picked reflector depth error for each offset h to a new depth z'_h based on Eq. (12):

$$z'_h = z_h + \Delta z = z_h - \sum_i \left(\frac{\partial t}{\partial\alpha_i}\Delta\alpha_i\right) \frac{\alpha}{2\cos\Theta\cos\Phi}. \tag{13}$$

Due to the unknown residual migrated depth z'_h, the CIP tomography minimizes the difference $(z'_h - z'_0)$, where $h = 0$ is the nearest offset of a picked depth error branch, not necessarily zero offset, and h a non-nearest offset. This yields to Eq. (14):

$$\begin{aligned} z_h - z_0 = \sum_i \Bigg[& \left(\frac{\alpha_h}{2\cos\theta_h\cos\Phi}\right)\frac{\partial t_h}{\partial\alpha_i} \\ & - \left(\frac{\alpha_0}{2\cos\theta_0\cos\Phi}\right)\frac{\partial t_0}{\partial\alpha_i}\Bigg]\Delta\alpha_i. \end{aligned} \tag{14}$$

We have a set of linear equations for each pick z_h at offset h along a depth error branch relative to the nearest pick z_0 for offset *0* along the depth error branch and that for many

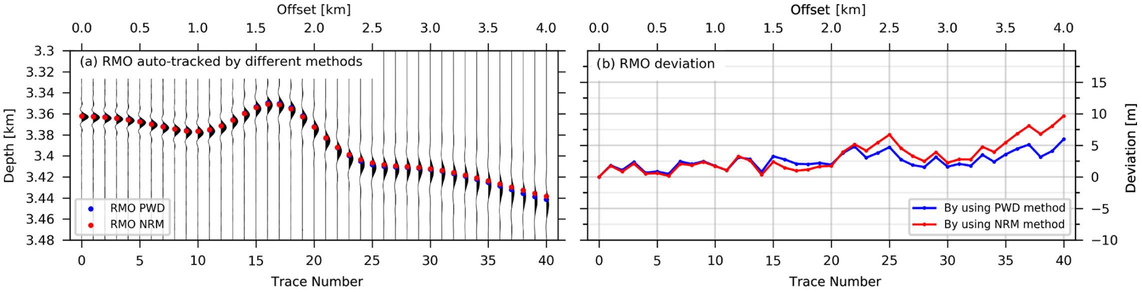

Figure 3. **(a)** Comparison of residual depth error picks between the NRM and PWD method. **(b)** Depth difference between the depth errors of the NRM and PWD method.

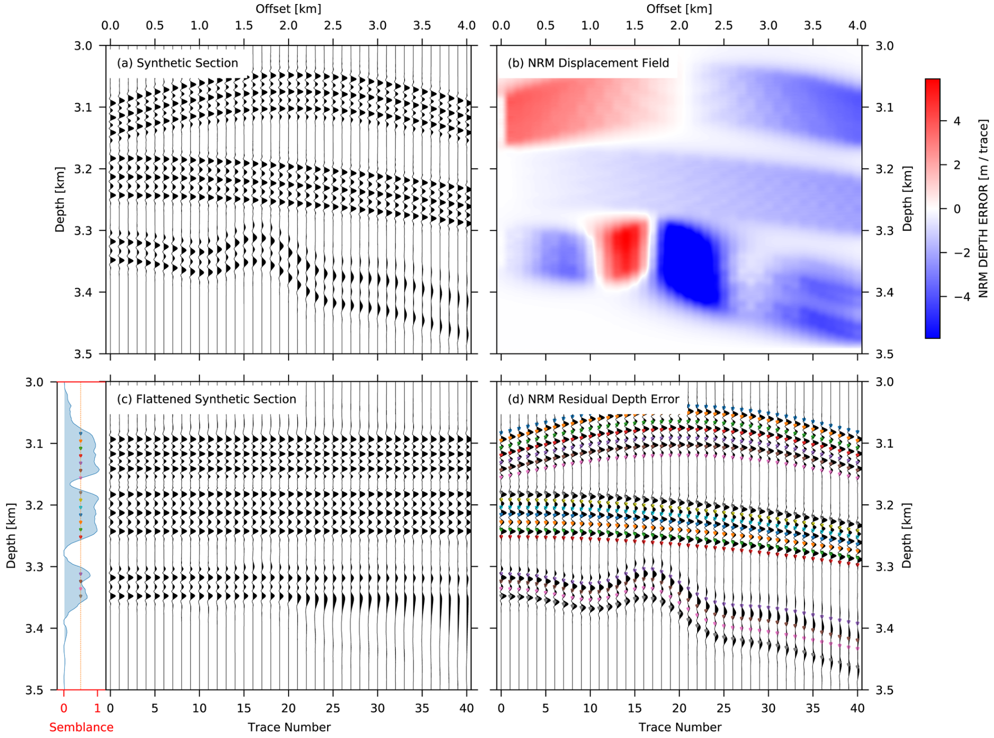

Figure 4. **(a)** Simulated geological situations with multiple sets of reflectors. **(b)** The NRM displacement of gather **(a)** calculated from trace n to the previous trace $(n-1)$ for $n > 1$. **(c)** Application of the "relative-displacement correction" scheme from **(b)** to the gather of **(a)**. **(d)** Residual move-out picks automatically calculated by the semblance-weighted grid-based approach of the relative depth errors of **(b)**.

depth error branches along the whole profile. The tomography equation in matrix notation is written in Eq. (15),

$$\mathbf{PLSW}\boldsymbol{\Delta\alpha} - \boldsymbol{\Delta z} = 0, \qquad (15)$$

where $\mathbf{P}$ weights individual depth error areas, $\mathbf{L}$ is the matrix of the ray path term calculated by the residual migration term in brackets of Eq. (14); $\mathbf{S}$ is a scale length smoother with the predefined wavelength in lateral and vertical direction; $\mathbf{S}\boldsymbol{\Delta\alpha}$ together is the velocity update vector, $\mathbf{W}$ is a damping factor allowing the update magnitude of the model to be adjusted, and $\boldsymbol{\Delta z}$ is our accumulating picked depth errors between non-near and near-offset picks. The aim of the reflection tomography is now to solve the equation to find a $\boldsymbol{\Delta\alpha}$ that will explain the residual depth errors $\boldsymbol{\Delta z}$. The residual depth errors are usually picked manually or automatically tracked by linear or hyperbolic assumptions. While the latter approach is convenient, it needs additional parameters, especially for non-hyperbolic or weak events. Typically, coherence measurements are used and additional outliners must be detected and removed. Despite this, a vertical and spatial smoothness between depth error branches is not guaranteed. Using the application of the NRM-based picking the smoothness of the depth errors $\boldsymbol{\Delta z}$ in space and depth will be guaranteed and stabilize the linear equations and the inversion result. Additional regularization and weighting schemes also need to be applied to find a velocity change $\boldsymbol{\Delta\alpha}$ that will minimize Eq. (15). Details can be further seen in Woodward et al. (2008).

The choice of the parameters of weight **P**, smoothing scale length **S**, and damping factor **W** are strongly data dependent. Tomographic inversion works by iterative velocity updating to minimize the observed residual velocity error (Eq. 15). In the CIP gathers, the depth errors are distributed over the entire offset range and yield the estimation of the interval velocity changes along their ray paths between the source and receiver (Jones, 2010). Due to the linearized approximation in Eq. (14), by ignoring the ray path bending during the estimation of the velocity update, several iterations with only small velocity updates (e.g. $\sim 10\,\%$) are recommended. Additionally, a large volume with a high spatial density of the residual depth errors needs to be picked in order to stabilize the linear equations by the redundancy of information (Jones, 2003). Once there is a conflict occurring between some of the equations in one grid cell, the minority picks (which could be good or bad) will be rejected by the tomography algorithm in order to get a stable and self-consistent result. Unrealistic picks have an unfavourable effect on the tomographic results when they become the majority. Besides the pick density and depth error accuracy $\boldsymbol{\Delta z}$, the smoothing scale length **S** is the most important parameter for the grid tomography.

If the initial velocity is not well determined, e.g. smoothed depth-converted stacking velocities or depth-converted prestack time migration velocities, a long-wavelength to short-wavelength velocity update is a preferred strategy by reducing the smoothing scale length **S** in Eq. (15). The first iteration is applied with a spatial smoothing length covering at least twice the CIP ray path coverage aperture to update the long-wavelength velocity structure only. In the following iterations, the scale length is successively reduced for each iteration to receive increasing velocity details as shown in Woodward et al. (2008).

If an initial background velocity is well determined, e.g. depth-focusing analysis from pre-stack depth-migrated data, each iteration can be applied immediately with multiple scale lengths, starting from the longest to shortest scale length for each velocity update. Independent of the grid-based reflection tomographic inversion strategy it is common to stop the iterations if an iteration does not contribute any more to the flatness of the CIP residual move-out. Qualitative control will give a comparison of the reflectors' horizontal alignment in the CIP gather with respect to a previous iteration or initial iteration. A more quantitative measure to stop an inversion is to define a lower limit of percentage velocity change which must be achieved (e.g. $3\,\%$).

In contrast to the grid-based tomography, where vertical and horizontal velocity gradients are determined during the inversion, the layer-based tomography updates the lateral velocity variation between two user-defined horizons with a predefined vertical velocity gradient. A comparison of layer-based and grid-based tomography results can be found in Riedel et al. (2019) and Sugrue et al. (2004). Model areas in which a priori velocities are known (e.g. the water column above the seafloor) and hybrid models are used to avoid tomographic velocity updates propagating into selected areas. Furthermore, first-order velocity contrasts, resulting in ray-path bending are problematic as they cannot be inverted by finite grid size. Here hybrid models delivered the best results as shown by Jones et al. (2007) and Fruehn et al. (2008). For most of the studies it is common that the grid-based tomography was applied to moderate layered structures in combination with the hyperbolic curvature scanning technique from Hardy (2003) to estimate the depth error in the CIP domain. An application result of a grid-based tomography combined with the NRM technique in a moderate layered structure is shown in Crutchley et al. (2020).

3 Application of a reflection tomography by CIP residual move-out warping across the Java trench

An application of the NRM common image point depth error estimation in combination with an iterative grid-based tomography approach will be presented here in detail for three different structural settings along a profile crossing the Java trench. The complexity of the data examples increases from moderate horizontal layering, to dipping layered reflections, up to small disrupted dipping reflector elements.

In contrast to the processing by Lüschen et al. (2011), where the velocity model was built iteratively from interpreted depth-focusing analysis in a top-down approach, we used a wide-angle tomography model as initial velocity in combination with a data-driven grid-based reflection tomography. The use of wide-angle and refracted velocities may be influenced by anisotropy but gives the most confident velocity in the deeper subsurface due to the limited streamer length.

3.1 Study area and MCS data pre-processing

The multi-channel 2-D reflection seismic profile BGR06-313 that we use in three field examples was acquired by a 3000 m long, 240-channel digital streamer with a group distance of 12.5 m at a towing depth of 6 m. A two-string G-Gun array of 3080 in.^{3} (50.8 L) volume with a nominal shot point distance of 50 m was used as a source across the southern Java trench in the south-eastern part of the Sunda subduction zone (Lüschen et al., 2011) as part of the SINDBAD project during RV *SONNE* Cruise SO190 (Fig. 5).

The seafloor depth ranges from 1.5 km near the shore on the northern part of the line to 6.5 km in the deep-sea trench. Details of our seismic processing sequence are provided in Table 1. In preparation for the Kirchhoff PSDM, the multiple reflections have been attenuated using a free surface multiple prediction (Verschuur et al., 1992) followed by a frequency-split 2-D adaptive least-square subtraction (Robinson and

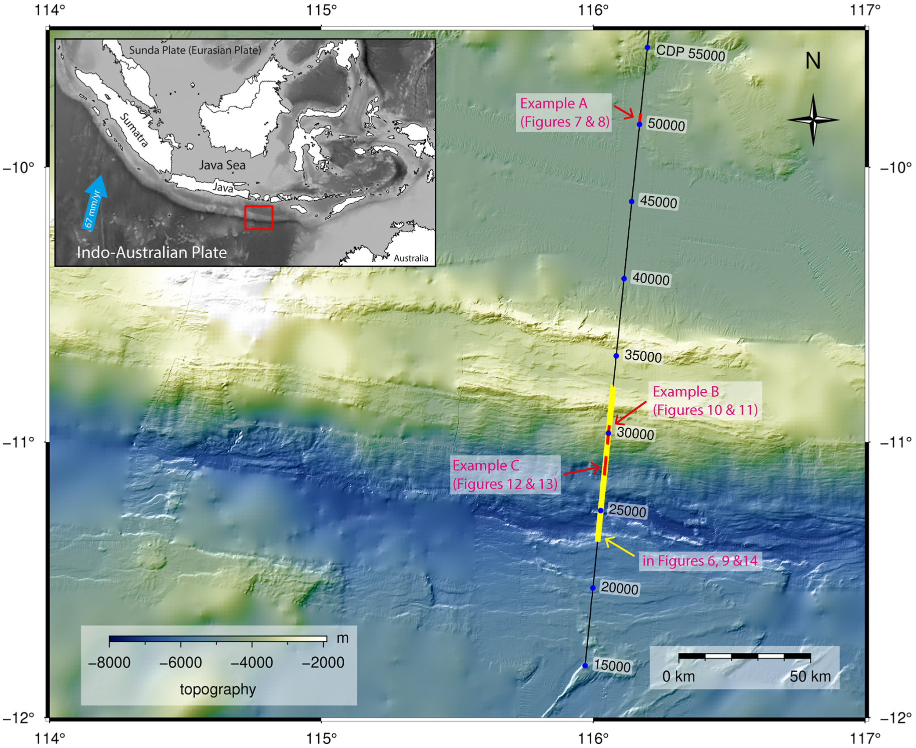

Figure 5. Map of the study area offshore southern Java, created by the authors using the open-source software Generic Mapping Tools (GMT). Local multi-beam bathymetry data were acquired during the SO190 cruise and overlain on the global GEBCO_2020 grid (GEBCO Bathymetric Compilation Group, 2020). The location of the multi-channel and collocated wide-angle seismic profile is shown by a black line. Three examples at locations A, B, and C (marked in red) of the NRM-based velocity update for the depth tomography and pre-stack depth migration result are discussed in detail. Example A is located at shallow depth with simple complexity, whereas examples B and C are crossing the subduction trench and accretionary wedge (yellow line) and show highly complex structures where standard velocity analyses mostly fail because of discontinuous highly dipping structures.

Treitel, 2000; Guitton and Verschuur, 2004), and a Radon transform dip filter (Hampson, 1986).

3.2 Initial velocity building from wide-angle tomography

The initial velocity model for the reflection depth tomography was merged from an OBS velocity tomographic inversion of a collocated 2-D refraction seismic line covered by 46 OBSs with a spacing of 6 km (Planert et al., 2010) and a velocity model estimated from the near-seafloor structure at coarsely sampled CMP locations by interactive semblance velocity analysis. This near-subseafloor velocity adjustment was needed because the MCS reflection and OBS acquisitions were split into two cruise legs and both profiles did not completely coincide as seen by the mismatch of the seafloor depth at the lower slope and the trench axis (Fig. 6a). Due to a gap of three OBS positions in the trench axis the velocity structure was not well determined near the trench axis with lower-slope sediment velocities of more than 3800 $\mathrm{m\,s^{-1}}$ between CDP 25 000–26 500 at a depth of 7000 m (Fig. 6). In the first step, the MCS velocity analysis was based on pre-processed CMP gathers and interactively picked semblance with an increment of 500 CMP locations. Based on this smoothed stacking velocity a pre-stack time migration was subsequently applied and a second interactive semblance velocity analysis on the migrated CIP with the same increment delivered a smoothed and depth converted velocity model for the upper 2 km below the seafloor. To finalize the initial tomography model building, the adjusted velocity at shallow depth was merged with the wide-angle velocity model and used for the following NRM tomography (Fig. 6b).

As an additional constraint for the tomography, a hybrid model with the seafloor as a fixed boundary was chosen to avoid velocity changes propagating into the water column, resulting in depth changes of the seafloor. This was especially needed at the trench axis where side reflections and cross-dipping structures due to the rough seafloor topography were observed (Fig. 5). A regional depth-variant water velocity (Table 2) was extracted from the Climatological Atlas of the World Ocean multibeam (MB) system (Levitus, 1983) and used for the entire profile.

It should be noted that the wide-angle velocity could not be updated at a depth greater than 4 km below the seafloor

Table 1. Seismic processing sequences and image grid sizes.

Sequence step names
Normal and nominal geometry establishment with CMP spacing of 6.25 m
Anomalous and random noise attenuation
Padding interpolated traces to zero offset
Interactive velocity analysis in time domain
Initial time-domain velocity building
Shot interpolation for aliasing elimination (from 50 to 12.5 m shot distance)
Surface-related multiple prediction
Multiple attenuation 1: frequency-split 2d cascaded adaptive filter
Multiple attenuation 2: radon dip filter
Multiple attenuation 3: inside mute and amplitude clipping
Kirchhoff pre-stack time migration
Initial depth domain velocity building (merge with wide-angle model)
* Kirchhoff pre-stack depth migration (PSDM) with common image point gather output
Pre-filtering of CIP (common image point) gather for NRM calculation
NRM displacement field calculation
CIP-gather residual move-out (RMO) pick calculation from NRM field
Dip field, and coherency field estimation from PSDM section
Depth tomography (velocity, residual move-out picks, dip and coherency field)
Update the velocity with tomography result that will minimize the CIP-gather RMO
STOP user defined: if velocity improvement is overall less than 3%
Continue with *

Image grid sizes

Image	Inline x (m)	Depth z (m)
Migration grid	6.25	4
Velocity grid	50	16
CIP gather increment	100 or 200	–
CIP gather offsets	105–3150, incr. 100	–

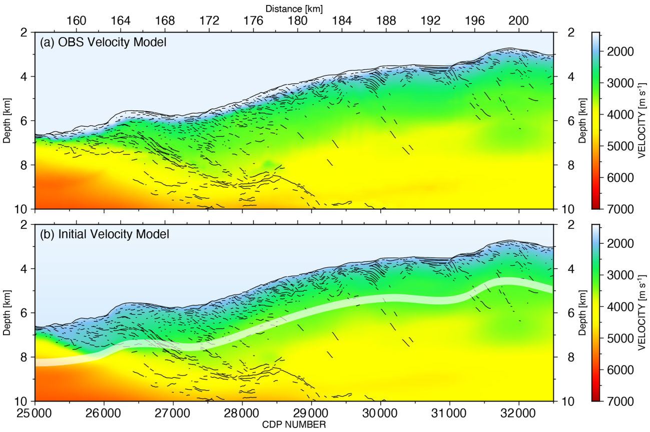

Figure 6. (a) The original OBS velocity model with the line drawing based on the final PSDM image. **(b)** The initial velocity model for the reflection tomography merged from the multi-channel seismic velocity analysis above the white transparent band and the wide-angle velocity model (below the white transparent band). The line drawing is based on the final PSDM image.

Table 2. Regional depth-variant water velocity extracted from the Climatological Atlas of the World Ocean MB system (Levitus, 1983).

Depth z (m)	Water velocity v (m s^{-1})
0	1535
50	1536
100	1531
150	1519
200	1507
500	1491
1000	1484
2000	1491
3000	1506
4000	1523
5000	1541
6000	1559
7000	1577

Table 3. Successive smoothing scale length reduction applied for each iteration of the depth tomography.

Application sequence	Application depth z (m)	Scale length x (m)	Scale length z (m)
1	0	10 000	1008
	13 000	13 000	1008
2	0	5850	720
	13 000	7626	720
3	0	3450	512
	13 000	4485	512
4	0	2000	352
	13 000	2600	352
5	0	1150	240
	13 000	1538	240
6	0	700	160
	13 000	910	160

during the initial velocity building and the subsequent reflection tomographic inversion since the limited streamer length (3 km) does not provide enough residual move-out sensitivity.

3.3 Reflection tomography attribute data

For the automatic residual NRM picking (see Fig. 4c, d from the synthetic example) an initial depth slice increment of 50 m for the residual depth error pick tracking through the NRM displacement field was depth adjusted based on minimum threshold semblance values by scanning along offsets of the CIP gather.

One attribute presented for the tomography is the reflector dip field Φ (Eq. 14) of the migrated section, which determine the ray coverage propagation direction (see Fig. 7e as an example). A second attribute is the spatial variant weight function $\mathbf{W}$ (Eq. 15) calculated from the spatial coherency (Fomel, 2002; Neidell and Taner, 1971) of the depth-migrated structure to weight the picks of the depth error branches (see Fig. 7f as an example).

3.4 Data examples

Each iteration loop in the tomographic processing flow (Fig. 1) included approx. 11 000 depth error branches, each branch with 30 picks, and six sequentially applied scale-length smoothings $\mathbf{S}$ (Eq. 15). Starting from the longest down to the shortest application sequence, each smoothing was applied over the complete depth range (Table 3). In total five iterations of velocity updates were applied, where for the following presentation only the initial and the final results are shown for the purpose of comparison.

In the data examples, we show three different structural settings with results of the velocity model, the corresponding PSDM sections, and the NRM displacement field, as well as the spatial coherence field together with the reflector dip field of the final migrated section. To document the change in the CIP-gather domain in detail, we additionally compare selected subareas of initial and final CIP gathers, the calculated NRM displacement fields, and the residual depth error picks, as well as on overlay display with the CIP gather and the depth error picks.

3.5 Sediment basin NRM tomography

The first field data example, “Example A”, at the northern end of the profile (Fig. 7), is a shallow sediment basin with layered interfaces and continuous reflectivity and represents an optimal site to obtain a reliable velocity model in a 2-D multi-channel seismic survey. A CIP-gather increment of 32 (200 m) was analysed along the profile with the NRM method. In total, five iterations of tomography loops (Fig. 1) were applied to this data example. An enlarged view of the initial velocity model ranging from CDP 46 700 to 50 800 is displayed in Fig. 7a. The resulting initial Kirchhoff pre-stack depth migration (Fig. 7c) retrieves a coherent image of the shallow sedimentary portion, while the energy in the deeper part close to the basement is not very well collapsed, resulting in a series of over-migrated events. The displayed reflector dip field (Fig. 7e) and coherency field (Fig. 7f) are extracted from the final migration section.

The reflector dip is used for the ray propagation direction during the tomography, and the coherency field is used as an additional weighting of RMO depth error picks in spatially coherent subsurface areas. The two attribute fields were recalculated for each iteration of the tomography loops (Fig. 1). After five iterations of the NRM-based depth tomography and Kirchhoff PSDM, the reflection energy is much better collapsed and shows more focussed and continuous signals, especially in the deeper part between 5.2–5.6 km (Fig. 7d). Furthermore, the final velocity model (Fig. 7b) displays lateral velocity variations that mimic the form of the base of the sediment basin. This is well demonstrated by the 3000 m s^{-1} velocity contour that mimics the shape of the boundary between the highly reflective basement (below) and the less reflective but more laterally continuous reflections of the sedimentary sequence (above).

Moving into the pre-stack CIP domain, a series of CIP gathers ranging from CDP 49 000 to 50 600 (same profile range as in Fig. 7) are selected and displayed in Fig. 8a with an increment of 32 (200 m). A dip filter is applied to the gathers to eliminate the extreme dipping events and migration noise. The NRM field in Fig. 8c shows the initial relative displacement values for each data sample. The information below the basement is muted by a digitized basement horizon. The distinct block of blue colour within the red rectangle in Fig. 8c, at a depth of 5.0 to 5.8 km, illustrates a gen-

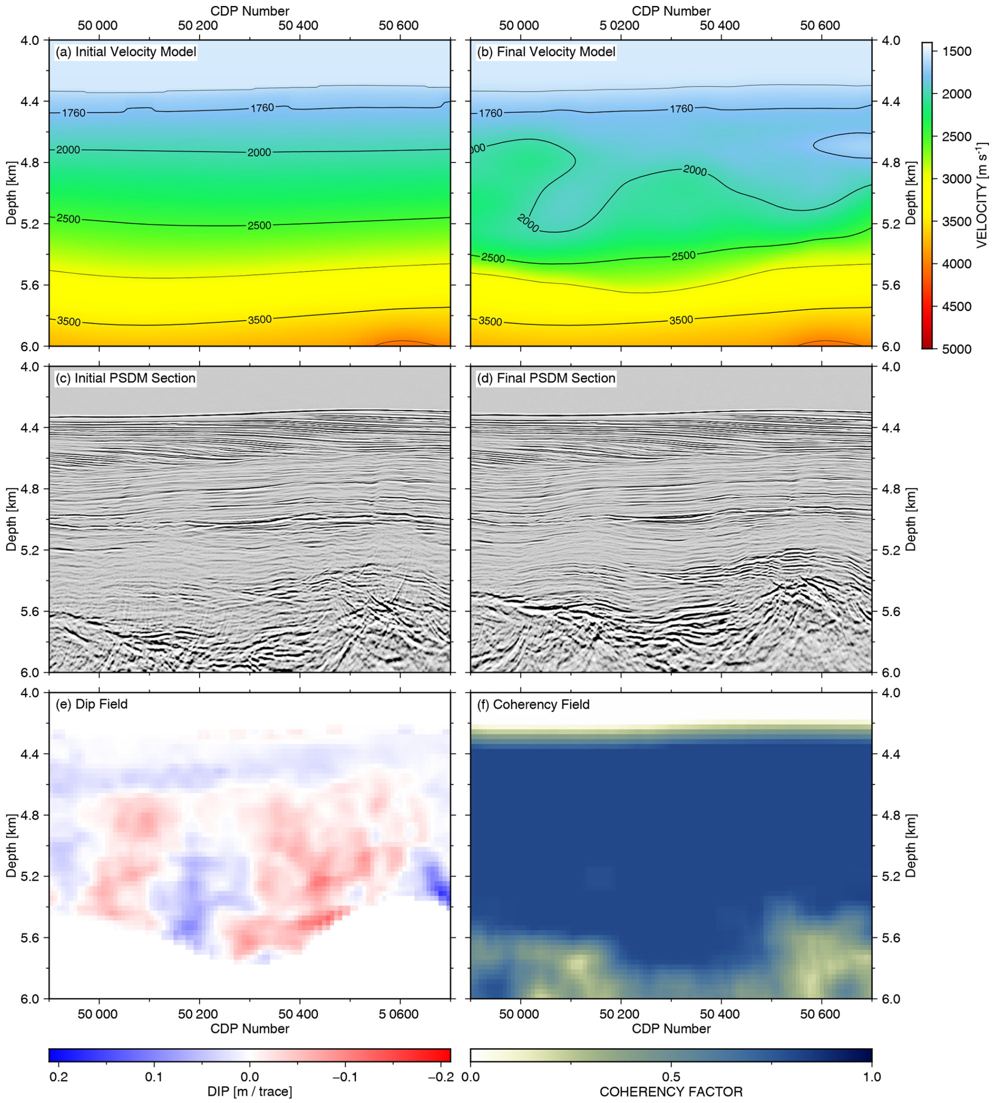

Figure 7. Depth tomography example A from Fig. 5, with CDP ranging from 46 700 to 50 800. **(a)** Initial velocity model merged from velocity analysis and wide-angle refraction tomography. **(b)** Final velocity model after five iterations of NRM-based depth tomography and PSDM. **(c)** PSDM result based on the initial velocity model. **(d)** PSDM result based on the final velocity model. **(e)** Reflector dip field calculated from the final PSDM result. **(f)** Reflector coherency field calculated from the final PSDM result. Note that "migration smile" artefacts at a depth of 5.6 km in **(c)** are significantly reduced in the final PSDM result **(d)**.

eral velocity overestimation in the overlying sediment. The RMO depth error picks calculated from the NRM displacement field, as a data-driven automatic picking method without any assumption of its curvature, are the main input information for the tomography (Fig. 8e). Figure 8b, d, and f show the final flattened CIP gather, NRM displacement field, and RMO depth error picks, respectively.

Compared to the initial data, the updated events in the CIP gather become optimally flattened. The depth of the basement shifts upwards by 0.2 km due to the velocity reduction of the final model. In the final NRM field (Fig. 8d), the velocity overestimation error in the region of the red rectangle is substantially reduced. However, some residual moveout undulations from the initial to the final stage remain, as seen in detail in Fig. 8g and h from the CIP gathers overlain with the RMO depth error curves. Ideally, the final NRM displacement field in Fig. 8d should have no NRM depth shift anymore, and all depth error picks should align horizontally. This cannot always be achieved, as the tomography finds only the solution that minimizes the depth error with respect to the smallest scale lengths (Table 3).

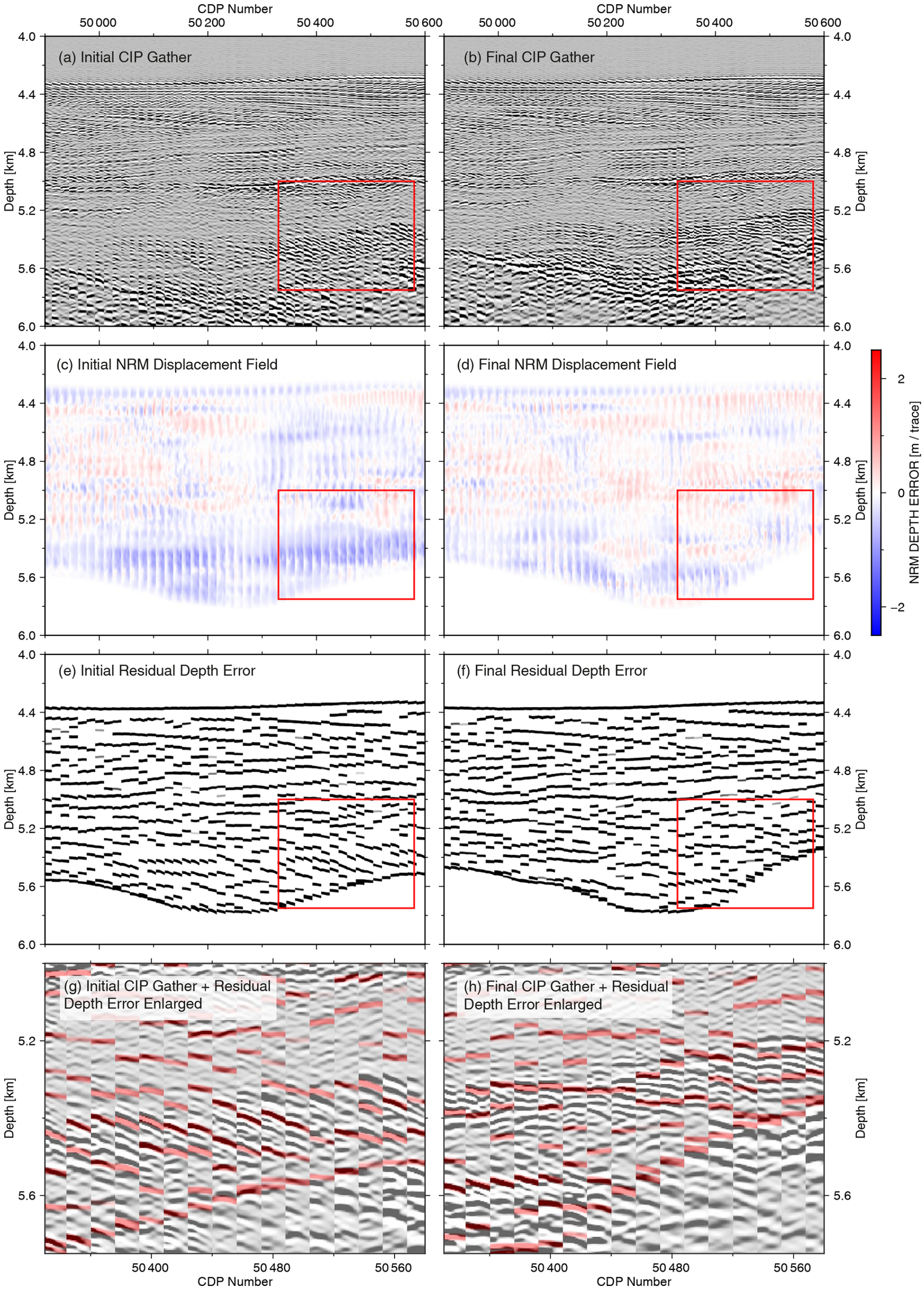

Figure 8. NRM velocity updating of Fig. 7 in CIP domain. **(a)** CIP gathers based on the initial velocity model. **(b)** CIP gathers based on the final velocity model. **(c)** Initial NRM depth shifts in the CIP domain. **(d)** Final NRM depth shift in CIP domain. **(e)** RMO picks calculated from the initial NRM displacement field. **(f)** RMO picks calculated from the final NRM depth displacement field. Note that the overall shift error within the distinct area of velocity overestimation in the red rectangle in **(c)** has been substantially reduced after the tomography **(d)**. CIP gathers **(e)** and **(f)** of the red rectangle from **(c)** and **(d)** respectively overlaid by RMO picks. Strong dipping events in the initial CIP gather **(g)** have been flattened after the final iteration **(h)**.

3.6 Accretionary wedge NRM tomography

In the following, the PSDM profile (location marked by the yellow line in Fig. 5) with the final velocity model overlain in Fig. 9 will be further analysed.

Two data examples (Fig. 5, examples B and C, marked in red) in the blue rectangles within the accretionary wedge in Fig. 9 show distinct levels of complexity. The selected upper-slope area is characterized by strongly folded continuous reflector sequences, whereas the lower-slope area contains only short reflector segments with varying dips. The lack of coherent reflective signals in this highly deformed accretionary prism leads to a severe difficulty in accurately evaluating the residual move-out in the CIP gathers, especially if a constant spatial analysis increment (e.g. 500 CDP = 3125 m) is greater than or equal to the lateral dimensions of velocity structures to be resolved (e.g. the piggy-back basin CDP 30 500–31 000, 3 to 4 km depth in Fig. 9b). As a consequence of the spatially complex reflectivity pattern, the automated CIP analyses were reduced to an increment of 16 (100 m) to achieve more redundancy of depth error estimations during five iterations of the tomography.

3.6.1 Upper-slope NRM tomography

Our second field data example focuses on a sequence of thick sediment tilted by compressive deformation in the region marked by the blue rectangle example B in Fig. 9b. Figure 10 provides a detailed image of the PSDM section and velocity model from the initial and final stages. The final velocity (Fig. 10b) is significantly reduced compared to the initial velocity model (Fig. 10a) in the shallow part and significantly increased compared to the initial model at depths of 5.2–6.2 km. The reflector sequences of the anticline structure between CDP 29 300 and 29 500, from 4.0–4.4 km depth, are more continuous in the final image (Fig. 10d) than in the initial image (Fig. 10c), especially at the top of the anticline. The dip of the folded reflector sequence between CDP 29 800 and 30 100, above 4.8 km, is more continuous in the final image (Fig. 10d), since the residual depth error is better flattened (Fig. 11g and h), and the reflector dip in the PSDM section increases steadily with increasing distance from the apex of the fold (Fig. 10d). By contrast, the initial image in this same region (Fig. 10c) shows an abrupt change in the dip near the apex of the fold.

Comparing the initial and final CIP gathers in Fig. 11a and b inside the red rectangle, strong downward-dipping reflections indicate the requirement to reduce the initial velocity significantly. The NRM displacement field in Fig. 11c provides a more quantitative view of this requirement, seen by the strong blue colour with more than 2 m depth error per trace distance. The RMO picks calculated in Fig. 11e and overlain on the seismic image (Fig. 11g) follow the seismic down-dipping reflection trend quite accurately. After the tomography, the final NRM displacement is significantly reduced (Fig. 11d and f), the residual calculated depth error in the red box (Fig. 11h) is reduced, and the reflectors are in better horizontal alignment.

To the left of the red box between CDP 29 600 and 29 800, above 4.4 km depth, the tomography could only partially remove the depth error (compare Fig. 11c and d). The reflections in this region could only be aligned with velocities far below the water velocity, indicating that side echoes or cross-dipping structures in this region prevent a reliable subsurface velocity determination. To avoid such unrealistic velocity updates during the tomography, a minimum velocity of 1750 m s^{-1} below the seafloor was defined as a precondition.

3.6.2 Lower-slope NRM tomography

In the lower-slope region (Fig. 9a, example C), sediment layers are segmented and folded as a result of the regional compressive deformation exerted by the subduction accretion processes. The initial pre-stack depth migration example is shown in Fig. 12c. After the tomography, the final velocity increased by 500 m s^{-1} on average (Fig. 12b), resulting in a significant increase in the velocity gradient compared to the initial velocity model (Fig. 12a). In the final PSDM section (Fig. 12d), the reflector strength generally increased, and new reflector segments became emphasized compared to the initial migration (Fig. 12c). This is especially evident in the depth range from 6.0 to 6.8 km.

In the initial CIP gathers displayed in Fig. 13a, the reflector distribution appears largely uncorrelated, and no clear trends are visible, particularly within the red box. In the initial NRM displacement field (Fig. 13c), there is a general positive depth error character that dominates the gathers, as indicated by the red colour, especially within the red rectangle and in the initial residual depth error (Fig. 13e).

By increasing the velocities based on the tomography result, this misalignment is reduced both in the final NRM displacement field (Fig. 13d) and in the final residual depth error illustrated by the generally more horizontal alignment of the events (Fig. 13f). In the enlarged view of Fig. 13g and h, the general positive dip trend has been mostly removed. However, local reflector misalignment is still observed, as documented by the local blue colour in the NRM displacement of downward-dipping events (Fig. 13d). Even after the tomography, the two local anomalies of four neighbouring CIP gathers between CDP 28 200 and 28 400, at 5 and 5.6 km depth, were not correctly aligned. These local anomalies have a lateral dimension of ~ 200 m and are therefore 3 times shorter than the smallest horizontal scale length smoothing used for the last iteration of the tomography (Table 3).

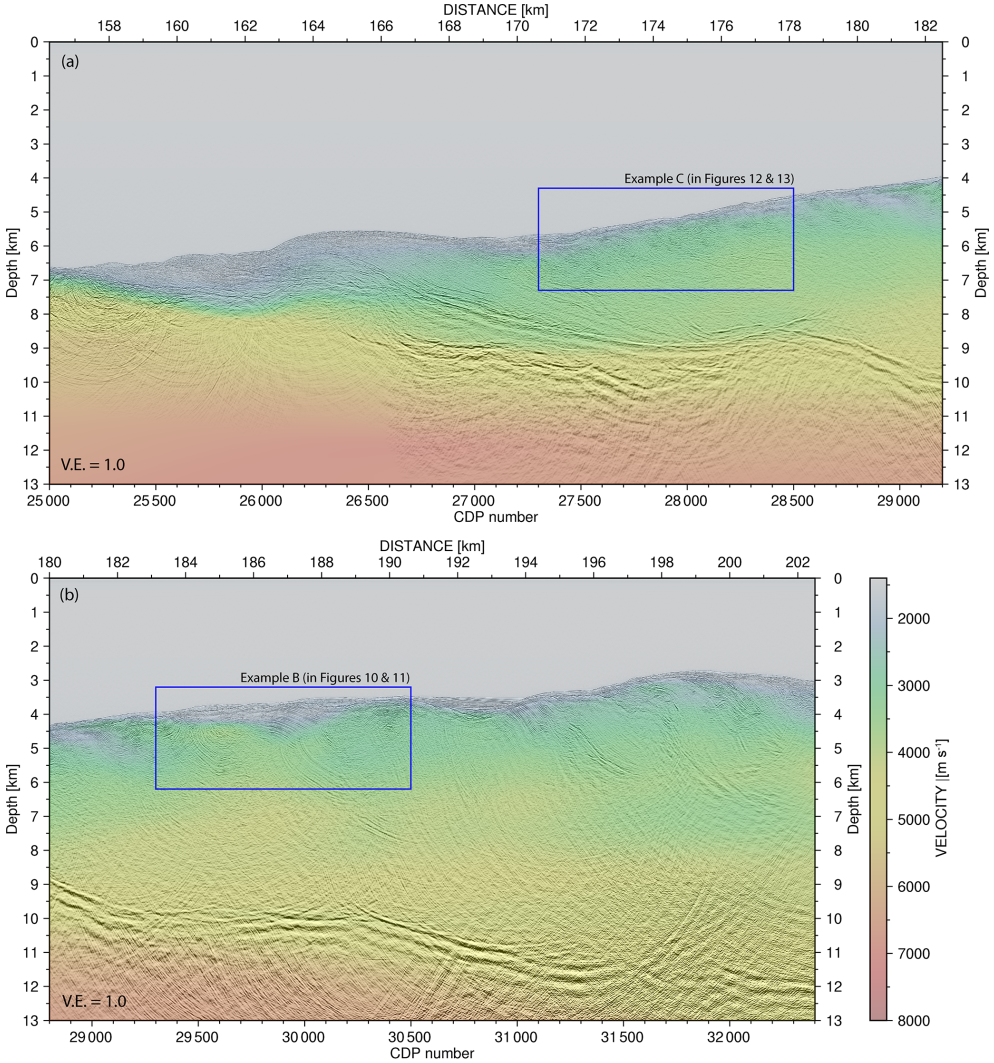

Figure 9. Depth migration stack section of five iterations depth tomography with final velocity model overlain. The location of the profile is illustrated in Fig. 5 as a yellow line. Rectangular boxes are discussed in the section on field data examples from the accretionary wedge. **(a)** Data example C. **(b)** Data example B.

4 Discussion

4.1 Final velocity model and reflectivity structure

The final depth image with the velocity model (Fig. 9) and the final subsurface velocity model (Fig. 14b) compared to the smoothed initial velocity (Fig. 14a) shows local velocity changes in the upper 3 km below the seafloor. To emphasize the differences, the percentage of change is calculated in Fig. 14c.

Close to the trench axis (CDP 25 500–26 000), a velocity reduction of more than 10 % from 2100 to 1800 $\mathrm{m\,s^{-1}}$ is observed relative to the initial velocity (Fig. 14c). The final velocity close to this area increases from 1750 $\mathrm{m\,s^{-1}}$ at the seafloor to 2280 $\mathrm{m\,s^{-1}}$ at the plate boundary at 7400 m depth. In contrast, the uplifted sediment ridge (CDP 26 000–27 000) shows a velocity increase from 1750 to 1850 $\mathrm{m\,s^{-1}}$ in the upper 500 m below the seafloor, whereas the velocity increases up to 2650 $\mathrm{m\,s^{-1}}$ at an observed basement high at 7100 m depth.

On the lower slope (CDP 27 000–29 000) an increase in the velocity of more than 10 % compared to the initial velocity is observed and is comparable to the original OBS velocity. A thin pelagic layer of slope sediment with a maximum thickness of 100 m with velocities of 1750 $\mathrm{m\,s^{-1}}$ covers a highly fractured accretionary prism. The velocity below the slope sediment increases gradually in the upper 1500 m up to 3400 $\mathrm{m\,s^{-1}}$, which is higher than the OBS velocity model. The relatively high velocity of the major part of the accretionary wedge, which is composed of the ancient oceanic pelagic sedimentary rocks, yields long-term compaction and consolidation of the sedimentary structure. Additionally, the

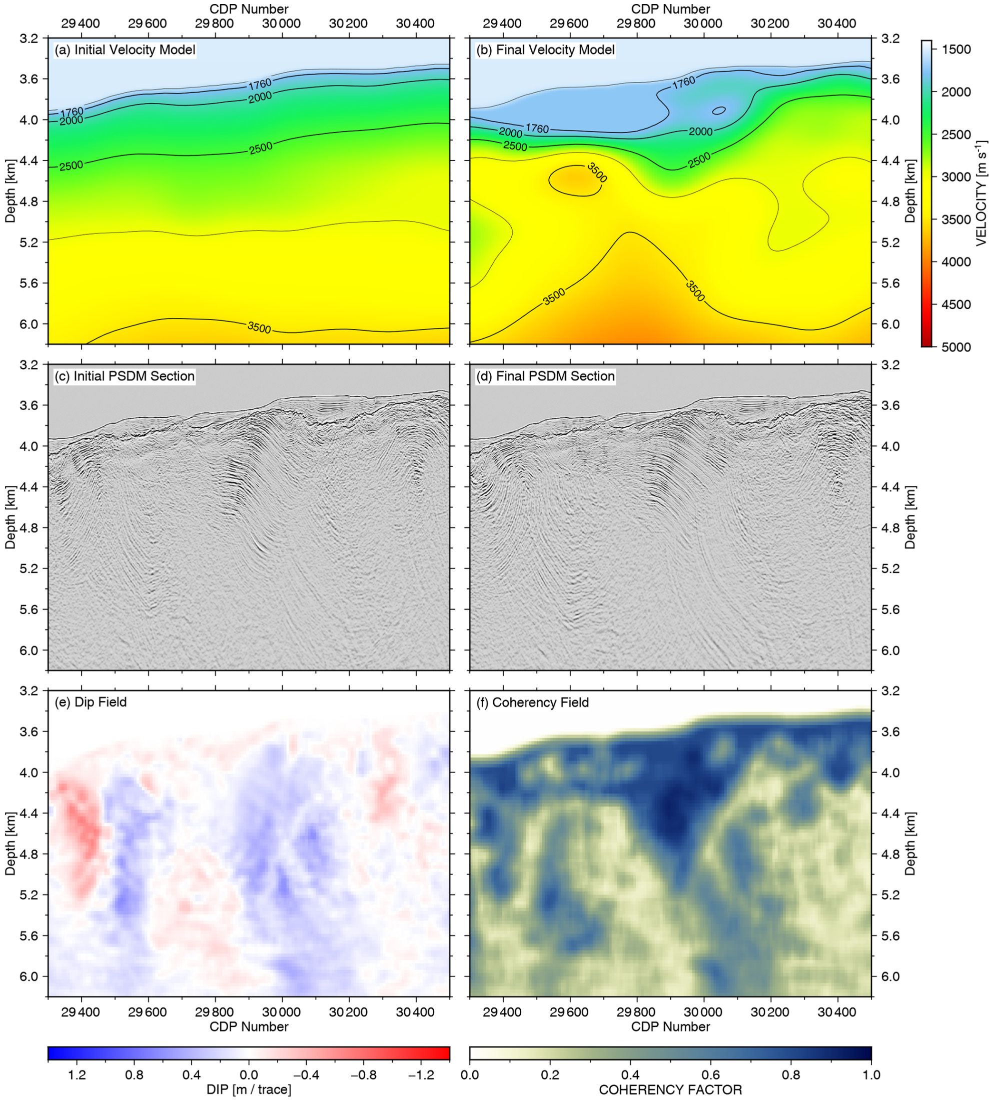

Figure 10. Depth tomography example B in Figs. 5 and 9b, with CDP ranging from 29 300 to 30 500. **(a)** Initial velocity model merged from velocity analysis and wide-angle refraction tomography. **(b)** Final velocity model after five iterations of NRM-based depth tomography and PSDM. **(c)** PSDM result based on the initial velocity model. **(d)** PSDM result based on the final velocity model. **(e)** Reflector dip field calculated from the final PSDM result. **(f)** Reflector coherency field calculated from the final PSDM result. Notice the continuity and reflector dip change of the folded sediment layers at a depth of 4.0–4.8 km in **(c)** and **(d)** based on the change of the initial velocity and final velocity **(a)** and **(b)**, respectively.

complex reflectivity pattern of strongly folded and fractured strata with limited spatial extents (Figs. 9a, 12d) due to compressional tectonic deformation manifests itself in small thrust ridges at the seafloor with a landward-dipping reflectivity pattern below (e.g. CDP 28 300, 28 700).

In between the dipping reflectivity patches, shallow deformed layered sediment structures with reduced velocities of 1900 m s^{-1} are observed with landward increasing thickness from 200 to 500 m and start to form anticline structures with the increasing spatial size and reflector continuity (CDP 28 800–29 000).

On the upper slope (CDP 29 000–32 400) the shallow reflector continuity from the lower slope increases in thickness from 500 up to 2000 m and forms continuous landward-dipping structures (Figs. 9b, 10d). The folded anticline structures (CDP 29 000–29 600) at a depth of 4 to 6 km and a sequence of thrust ridges with intervening piggyback basin (CDP 30 500–31 100, depth 3.5 to 4.5 km), as well as the landward increasing steepening of the thrust sheets, document the long-lasting compressional character of this prism.

In our final PSDM section (Fig. 9), the plate interface of the subduction zone is continuously imaged from profile kilometre 166 to kilometre 202 at a depth between 8 to

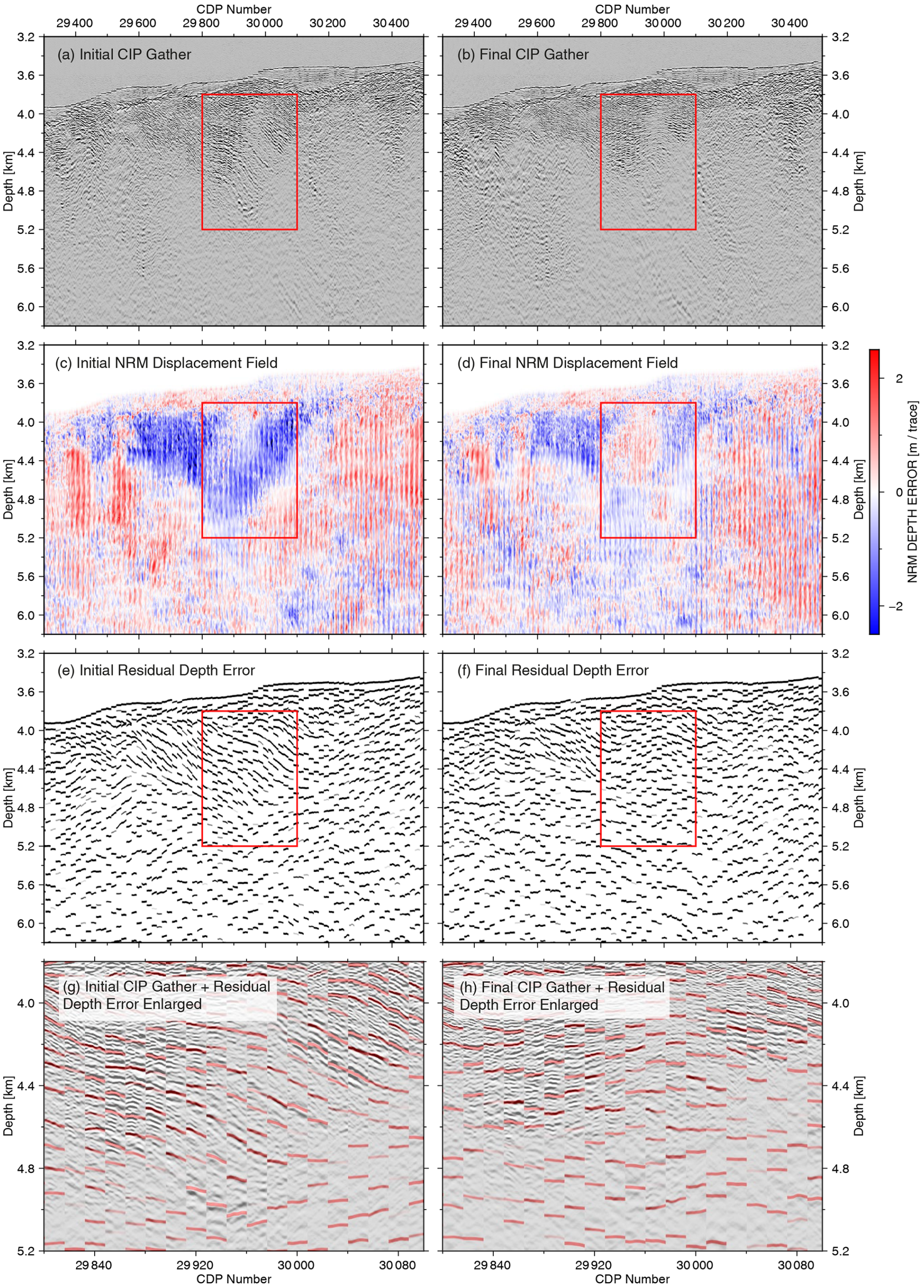

Figure 11. NRM velocity update of Fig. 10 in CIP domain. **(a)** CIP gathers based on the initial velocity model. **(b)** CIP gathers based on the final velocity model. **(c)** Initial NRM depth shifts in the CIP domain. **(d)** Final NRM depth shift in CIP domain. **(e)** RMO picks calculated from the initial NRM displacement field. **(f)** RMO picks calculated from the final NRM displacement field. Note that the distinct area of velocity overestimation in the red rectangle in **(c)** has been substantially reduced after the tomography **(d)**. CIP gathers **(e)** and **(f)** of the red rectangle from **(c)** and **(d)** respectively overlaid by RMO picks. Strong dipping events in the initial CIP gather **(g)** have mostly been flattened after the final iteration **(h)**.

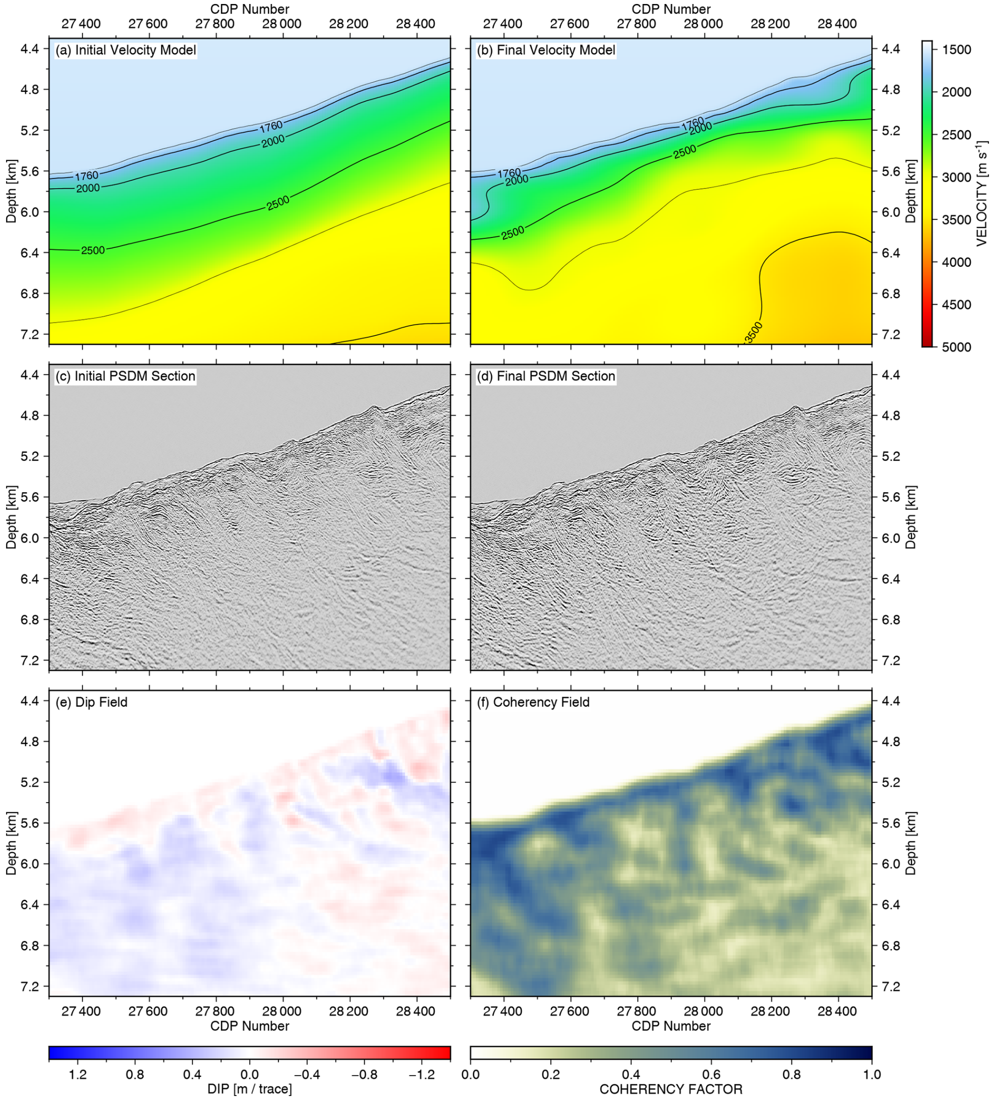

Figure 12. Depth tomography example C in Figs. 5 and 9a, with CDP ranging from 27 200 to 28 600. **(a)** Initial velocity model merged from velocity analysis and wide-angle refraction tomography. **(b)** Final velocity model after six iterations of NRM-based depth tomography and PSDM. **(c)** PSDM result based on the initial velocity model. **(d)** PSDM result based on the final velocity model. **(e)** Reflector dip field calculated from the final PSDM result. **(f)** Reflector coherency field calculated from the final PSDM result. Note that the vertical velocity gradient below the seafloor increased in the final velocity model **(b)** compared to the initial velocity model **(a)** with a result of stronger focusing of reflected energy by the PSDM **(d)** compared to **(c)**.

12 km. Due to the limited streamer length (3000 m) the plate interface in the deeper region is only slightly repositioned, but we did not observe a significant improvement of the reflection amplitude between the initial PSDM and the final PSDM sections. However, a different amplitude versus offset (AVO) distribution in the CIP gather along deeper reflections may be expected due to a change of the ray path bending from velocity updates in the shallow subseafloor. By using longer streamer MCS surveys, implementation of NRM grid-based reflection tomography would benefit the quantification of the plate interface reflection amplitude. This holds true especially for the AVO distribution, angle-dependent reflection coefficients, fluid budget, and its migration paths, which are related to the earthquake phenomena along the megathrust (e.g. Bangs et al., 2015; Sallarès and Ranero, 2019) and may be investigated in future studies.

4.2 Model uncertainties by tomography

In this study, we used a multi-scale length strategy for each iteration (Table 3) because a general background model existed from a wide-angle reflection and refraction tomography (Planert et al., 2010). Due to the limited streamer length, velocity updates deeper than 3 km were not expected, and

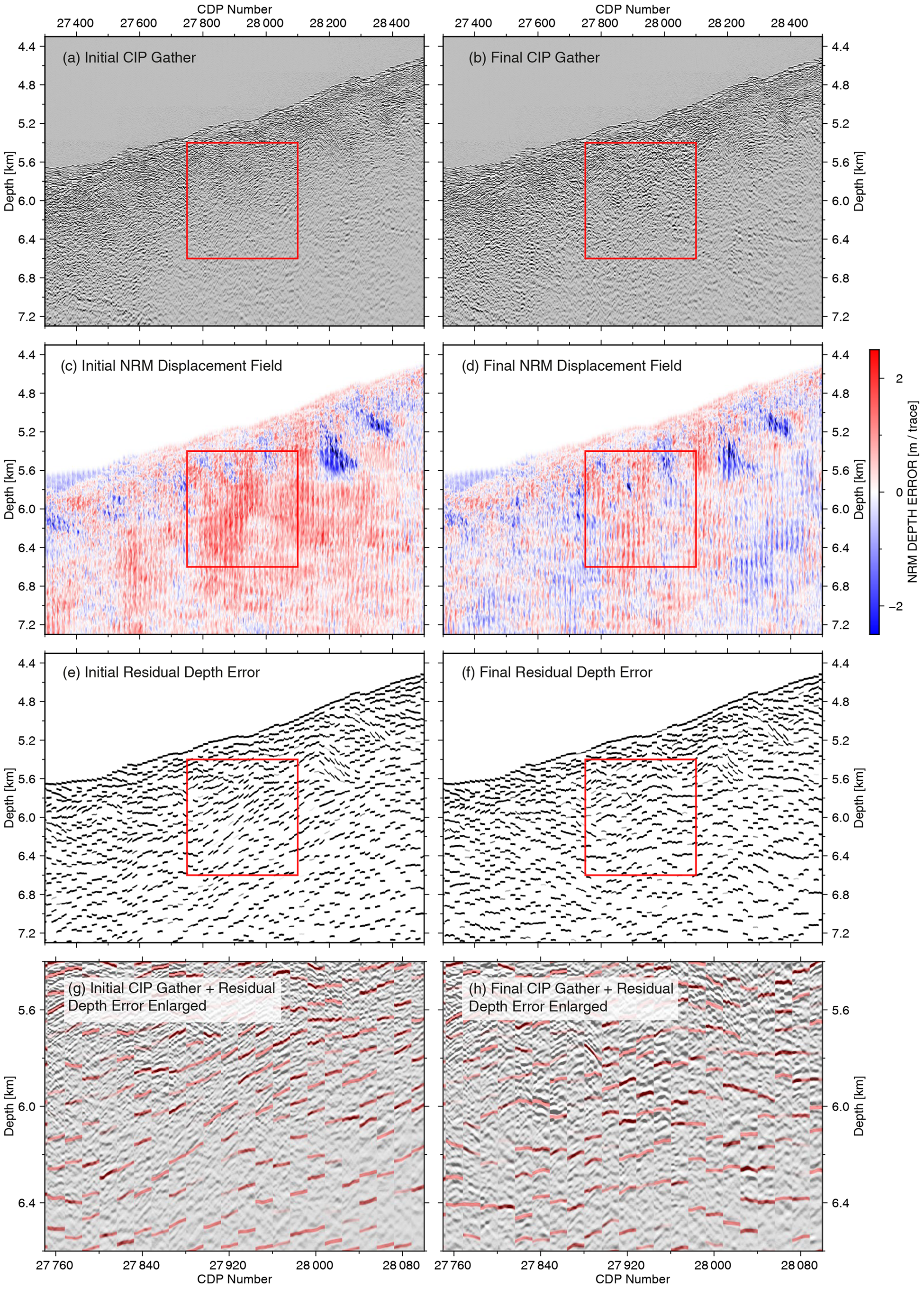

Figure 13. NRM velocity updating of Fig. 12 in CIP domain. **(a)** CIP gathers based on the initial velocity model. **(b)** CIP gathers based on the final velocity model. **(c)** Initial NRM depth shifts in the CIP domain. **(d)** Final NRM depth shift in CIP domain. **(e)** RMO picks calculated from the initial NRM displacement field. **(f)** RMO picks calculated from the final NRM displacement field. Note that the distinct area of velocity underestimation in the red rectangle in **(c)** has been substantially decreased after the tomography **(d)**. CIP gathers **(e)** and **(f)** of the red rectangle from **(c)** and **(d)** respectively overlaid by RMO picks. Strong dipping events in the initial CIP gather **(g)** have only partially flattened after the final iteration **(h)**.

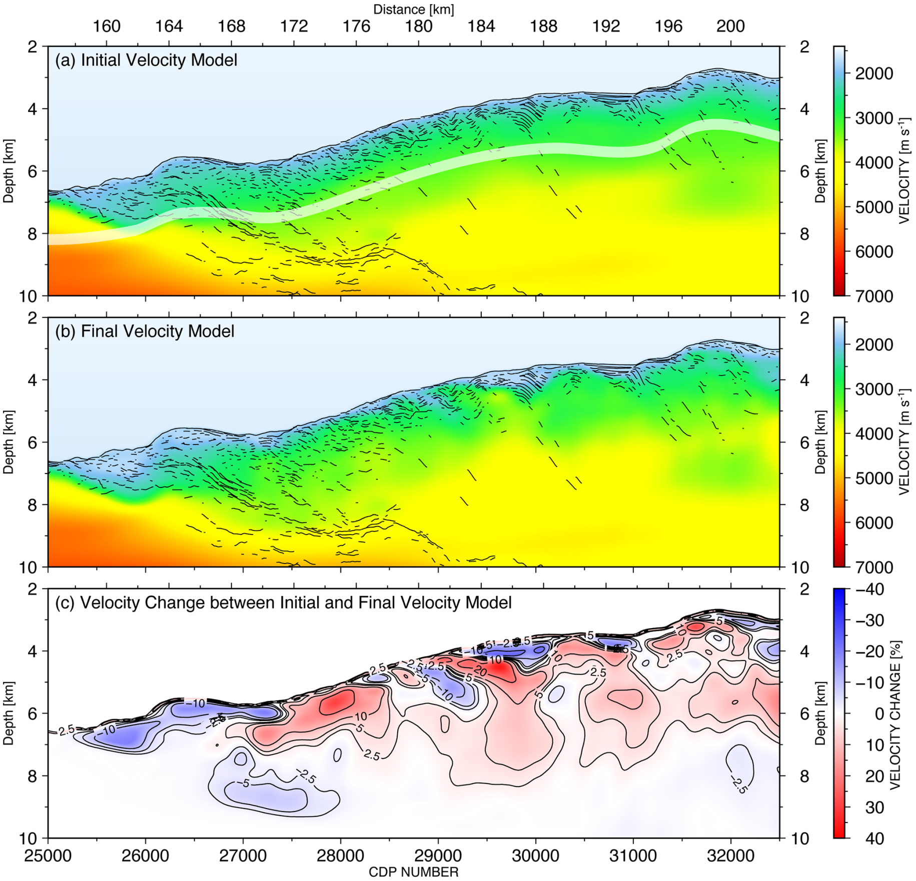

Figure 14. (a) The initial velocity model merged with the wide-angle velocity model (below the white transparent band). The line drawing is based on the final PSDM image. **(b)** The final velocity model calculated from five iterations of the ray-based tomographic velocity inversion. **(c)** The velocity change in percentage from the initial to the final model.

the long scale-length velocity variation by the OBS model was assumed to be well resolved. Our main target in this study was the shallow subseafloor structure up to 3 km depth, which consists of spatially varying reflector size elements and varying dips. As an example, we discuss the data from the upper slope in Figs. 10 and 11 in more detail. The result of the velocity updates and the reflector alignment for each of the five iterations are shown in Fig. 15a–e. The total velocity update is the summation of the individual iteration's velocity update (Fig. 15f). By adding this velocity to the initial velocity will in general be the final velocity model.

After the first iteration (Fig. 15a) a strong velocity decrease of more than 200 $\mathrm{m\,s^{-1}}$ at a depth of 4 km was predicted, even though the CIP gathers after this first iteration show strong misalignments. All six individual scale lengths applied sequentially for a single iteration (Table 3) are illustrated in Fig. 15f as horizontal and vertical lines. The high-velocity increase of 200 $\mathrm{m\,s^{-1}}$ below the velocity reduction was needed to compensate for the velocities above, especially if the CIP gather had before no misalignments. This compensation effect of the interval velocity is common in interactive CIP-gather picking. During additional iterations, the misalignment could successively be reduced (e.g. Fig. 15e), but the final velocity reached unrealistic sediment values of 1300 $\mathrm{m\,s^{-1}}$ due to the reduction of more than 800 $\mathrm{m\,s^{-1}}$ (Fig. 15f) with an initial velocity value of 2100 $\mathrm{m\,s^{-1}}$ at this subsurface depth. We interpreted this as an area of side echo reflections and limited the minimum velocity in this area after each iteration update by a value of 1750 $\mathrm{m\,s^{-1}}$. A careful critical inspection of the velocity model is needed by this purely data-driven method, but also offers the possibility to identify individual side echo reflections, which could otherwise mislead interpretations.

The smallest scale-length smoothing defined for the tomography will determine the highest possible resolution of the velocity update. To have enough redundancy at the smallest scale length, the CIP distance increment (100 m) and depth error increment (50 m) of the depth error branches were chosen so that at least seven neighbour CIP-gather and three depth error picked branches were considered. Any velocity anomalies below this scale length will not be detected. This limitation of detectable velocity anomaly can also be

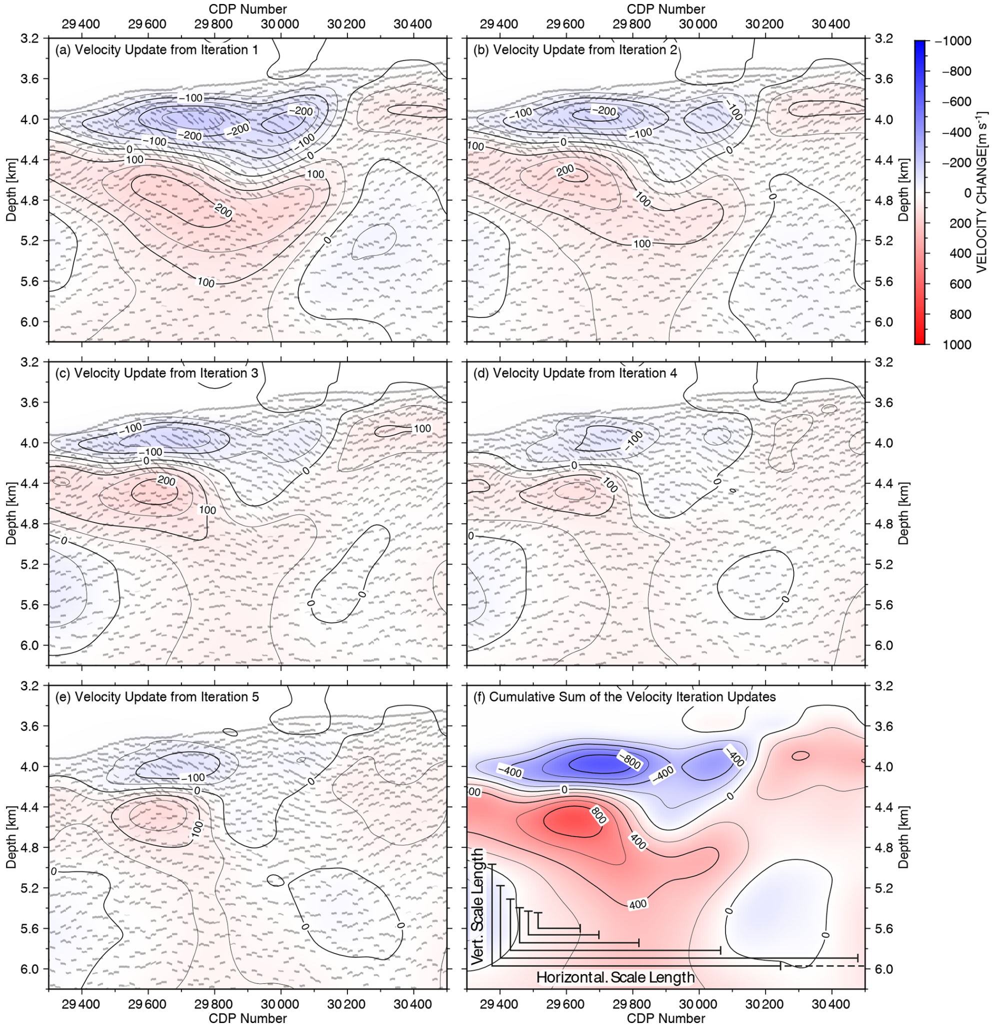

Figure 15. (a–e) Velocity update after each iteration of the gridded tomography together with the CIP depth alignment after each iteration. **(f)** The cumulative sum of the velocity updates from all five iterations together with the horizontal and vertical smoothing length used by the scale length reductions in each iteration.

seen in Fig. 13d at two locations indicated by the blue colour of negative depth errors.

Due to the dense depth error information which is needed for the tomography to stabilize the linear equations (Eq. 13), manual picking is not recommended, especially if several iterations are needed. In this example of the accretionary wedge in Fig. 9 for one single iteration, 11 000 residual move-out branches were automatically picked, where each branch consists of approx. 30 individual depth picks. This number is equivalent to the number of linear equations which must be solved (Eq. 12) during the tomography.

To quantify the model uncertainties and mainly to reduce the migration computation time, new inversion strategies were developed by incorporating a Monte Carlo approach (e.g. Martin and Bell, 2019) and should be incorporated in the future. Instead of getting one final model result, multiple model results were generated based on the sensitivity and resolution of the input data for the migration. To estimate the sensitivity and resolution, which is mainly determined by the acquisition parameters and the subsurface complexity, a checkerboard test with different wavelengths and magnitudes of perturbation added to an initial velocity model will be inverted by a test tomography application. The difference to the initial model, namely the residual errors, can be used to constrain threshold values for model perturbations. The minimum spatial wavelengths and the maximum amplitude perturbation must be fulfilled for any velocity perturbation created randomly for a Monte Carlo simulation, but this analysis will not avoid the detection of side echo velocity anomalies.

To analyse model perturbations independently of the migration velocity, CIP-gather depth errors are de-migrated with their migration velocity. In the model domain, random perturbed populations of velocity input functions are generated, inverted, and updated to the input velocity model to create a possible velocity model. All these populations of velocity models of the inversions can be statistically analysed, averaged, and used for the next iteration of a migration. By analysing the cumulative depth error of the CIP gathers after the migration iterations, convergence to a predefined obtained minimum depth error can be used to stop the inversion process automatically (Martin and Bell, 2019).

4.3 Anisotropic tomography

The wave propagation, namely direction and speed, is strongly influenced by the rock type and is generally depth and azimuth dependent. A fluid-filled orientation of fractures or microcracks can cause anisotropy as well as a preferred orientation of minerals in the deeper crust. There exist several classes of symmetry for anisotropy. But for imaging and inversion often a simple transverse isotropic type with one axis of symmetry is assumed. The symmetry axis can be vertical (VTI), tilted (TTI), or horizontal (HTI). For a weakly anisotropic medium of acoustic waves, the dimensionless Thomsen parameters ε and δ are used to describe the ratio of the velocity variations (Thomsen, 1986).

Complementary datasets like in this study of near-vertical reflections and wide-angle reflection and refractions with more horizontally propagating events offer one possibility to estimate the anisotropic parameters in the illuminated subsurface areas of both datasets. Classical modelling methods are nowadays replaced by inversion strategies due to the constant growth of observation density and increasing computational power. Several developments for weak anisotropy are published, e.g. 3-D joint refraction and reflection tomography (Meléndez et al., 2019) or a ray-based gridded tomography for tilted TI media based on depth alignment of CIP gather (Wang and Tsvankin, 2011).

The ray-based gridded tomography (Eqs. 12–15) together with the non-hyperbolic NRM event tracking and picking can also be used to invert for the anisotropic parameters, e.g. ε or δ. Based on an isotropic velocity and one Thomson parameter, e.g. ε an initial anisotropic migration will be analysed in the CIP domain and a depth error estimated. Instead of calculating a change in travel time, corresponding to a change of velocity $\partial t/\partial \alpha_i$ (Eqs. 12–14), the calculation is modified to a change of the Thompson parameter $\partial t/\partial \varepsilon_i$. By exchanging $\Delta\alpha$ to $\Delta\varepsilon$ and solving Eq. (15), any CIP depth error is corrected due to a change of the parameter ε. An application to real data can be found in Woodward et al. (2008). The initial isotropic velocity should be ideally a velocity depth profile corresponding to a vertical seismic profile (VSP) at each location. To overcome this limitation a significant scale length smoothing $\mathbf{S}$ (Eq. 15) needs to be applied as shown by Wang and Tsvankin (2011).

In the Java trench dataset, where near-vertical and wide-angle and refracted OBS data both exist, a combined analysis is limited to the move-out sensitivity by the streamer length 3–4 km below the seafloor. Additionally, both profiles do not completely coincide especially at the lower slope. The OBS model does not show significant velocity variations along the slope, especially not in the gravitationally driven slump area close to the trench axis. Instead, only a thin low-velocity layer with constant thickness is observed along the accretionary wedge (Fig. 6a). The data gap of OBS positions in the trench axis and the lack of local sediment basin incorporated into the initial wide-angle tomography model (Planert et al., 2010) have reduced the model reliability for further anisotropic analysis in the shallow illuminated area of both datasets.

5 Conclusions

The presented case study shows that CIP depth error estimations by depth warping in combination with a ray-based reflection tomography can improve depth-migrated images from MCS data. The non-rigid warping method provides reliable displacement fields for non-hyperbolic CIP depth errors. A semblance-based event tracking through the displacement field is limited by interfering reflected events. Due to the purely data-driven method of densely sampled depth error information (horizontal distance 100 m, vertical distance 50 m) more detailed spatial information for velocity corrections is available. In combination with a grid-based tomography, where depth errors are compensated for by velocity changes, the inversion from long to short lengths iteratively reduces the depth errors and improves the migration image. We suggest that further developments by integrating statistical analysis of the velocity updates (e.g. the Monte Carlo approach) and extending the tomography for anisotropic parameters will provide new analysis tools for the subsurface image within the limits of ray-based methods.

Code availability. Codes used to implement the depth-variant displacement correction and residual move-out (RMO) auto-tracking on the synthetic seismic section by using the NRM method are available at https://doi.org/10.5281/zenodo.5998288 (Xia et al., 2022).

Data availability. The raw and final results are available upon reasonable request.

Author contributions. YX and DK performed the computations and are responsible for the majority of the processing. HK helped to strengthen the overall scope and added to interpretational aspects and the discussion of the presented results. MS made the data available and was responsible for the navigation and geometry processing. YX wrote the article, and all authors contributed equally to the proofreading and final preparation of the paper.

Competing interests. The contact author has declared that neither they nor their co-authors have any competing interests.

Acknowledgements. R/V *SONNE* cruise SO190 and the SINDBAD project were funded by the German Federal Ministry of Education and Research (BMBF) under grants 03G0190A and 03G0190B. Yueyang Xia acknowledges funding from the China Scholarship Council (grant 201506400067). Bathymetric data from R/V *SONNE* cruise SO190 can be requested through the German Bundesamt für Seeschifffahrt und Hydrographie (BSH; http://www.bsh.de, last access: 25 October 2021). Seismic reflection line SO190 BGR06-313 is stored at the Bundesanstalt für Geowissenschaften und Rohstoffe (BGR) and can be requested through the Geo-Seas data portal (https://geoseas.bgr.de/bgrwebapp/SO190/BGR06-313_mig_oem.xml, last access: 1 November 2021). The seismic data were processed with Schlumberger's Omega2 seismic processing suite OMEGA; ObsPy, a Python framework for seismology; and Seismic Unix, an open-source software package for seismic research and processing from the Center for Wave Phenomena, Colorado School of Mines. Bathymetry and seismic images are plotted by the Generic Mapping Tools (GMT) and Matplotlib. We thank Nathan L. Bangs and César R. Ranero for insightful comments and suggestions that helped to improve the paper.

Financial support. R/V *SONNE* cruise SO190 and the SINDBAD project were funded by the German Federal Ministry of Education and Research (BMBF) under grant nos. 03G0190A and 03G0190B. Yueyang Xia acknowledges funding from the China Scholarship Council (grant no. 201506400067).

The article processing charges for this open-access publication were covered by the GEOMAR Helmholtz Centre for Ocean Research Kiel.

Review statement. This paper was edited by Charlotte Krawczyk and reviewed by Nathan Bangs and César R. Ranero.

References

Aarre, V.: On the presence, and possible causes, of apparent lateral shifts below the Norne reservoir, 78th Soc. Explor. Geophys. Int. Expo. Annu. Meet. SEG 2008 Las Vegas, 3174–3178, https://doi.org/10.1190/1.3064005, 2008.

Audebert, F. and Diet, J.-P.: A focus on focusing, in: Migration I, Prestack Depth Migration and Velocity Model Building, edited by: Jones, I. F., Bloor, R. I., Boindi, B. L., and Etgen, T., Vol. 25, https://doi.org/10.1190/1.9781560801917, 2008.

Audebert, F., Diet, J.-P., Guillaume, P., Jones, I. F., and Zhang, X.: CRP-Scans: 3D PreSDM velocity analysis via zero-offset tomographic inversion, in: SEG Technical Program Expanded Abstracts 1997, Dallas, Texas, USA, 1805–1808, Society of Exploration Geophysicists, https://doi.org/10.1190/1.1885786, 1997.

Bangs, N. L., McIntosh, K. D., Silver, E. A., Kluesner, J. W., and Ranero, C. R.: Fluid accumulation along the Costa Rica subduction thrust and development of the seismogenic zone, J. Geophys. Res.-Sol. Ea., 120, 67–86, https://doi.org/10.1002/2014JB011265, 2015.

Bishop, T. N., Bube, K. P., Cutler, R. T., Langan, R. T., Love, P. L., Resnick, J. R., Shuey, R. T., Spindler, D. A., and Wyld, H. W.: Tomographic determination of velocity and depth in laterally varying media, Geophysics, 50, 903–923, https://doi.org/10.1190/1.1441970, 1985.

Claerbout, J. F.: Earth soundings analysis: Processing versus inversion, edited by: Heydron, J., Blackwell Scientific Publications London, http://sepwww.stanford.edu/sep/prof/pvi.pdf (last access: 15 February 2022), 1992.

Collot, J. Y., Ribodetti, A., Agudelo, W., and Sage, F.: The South Ecuador subduction channel: Evidence for a dynamic megashear zone from 2D fine-scale seismic reflection imaging and implications for material transfer, J. Geophys. Res.-Sol. Ea., 116, 1–20, https://doi.org/10.1029/2011JB008429, 2011.

Crutchley, G. J., Klaeschen, D., Henrys, S. A., Pecher, I. A., Mountjoy, J. J., and Woelz, S.: Subducted sediments, upper-plate deformation and dewatering at New Zealand's southern Hikurangi subduction margin, Earth Planet. Sc. Lett., 530, 115945, https://doi.org/10.1016/j.epsl.2019.115945, 2020.

Dix, C. H.: Seismic velocities from surface measurements, Geophysics, 20, 68–86, 1955.

Fomel, S.: Applications of plane-wave destruction filters, Geophysics, 67, 1946–1960, 2002.

Fruehn, J., Jones, I. F., Valler, V., Sangvai, P., Biswal, A., and Mathur, M.: Resolving near-seabed velocity anomalies: Deep water offshore eastern India, Geophysics, 73, VE235–VE241, https://doi.org/10.1190/1.2957947, 2008.

GEBCO Bathymetric Compilation Group 2020: The GEBCO_2020 Grid – a continuous terrain model of the global oceans and land, British Oceanographic Data Centre, National Oceanography Centre [data set], NERC, UK, https://doi.org/10/dtg3, 2020.

Górszczyk, A., Operto, S., Schenini, L., and Yamada, Y.: Crustal-scale depth imaging via joint full-waveform inversion of ocean-bottom seismometer data and pre-stack depth migration of multichannel seismic data: a case study from the eastern Nankai Trough, Solid Earth, 10, 765–784, https://doi.org/10.5194/se-10-765-2019, 2019.

Gras, C., Dagnino, D., Jiménez-Tejero, C. E., Meléndez, A., Sallarès, V., and Ranero, C. R.: Full-waveform inversion of short-offset, band-limited seismic data in the Alboran Basin (SE Iberia), Solid Earth, 10, 1833–1855, https://doi.org/10.5194/se-10-1833-2019, 2019.

Guitton, A. and Verschuur, D. J.: Adaptive subtraction of multiples using the L1-norm, Geophys. Prospect., 52, 27–38, 2004.

Hale, D.: A method for estimating apparent displacement vectors from time-lapse seismic images, Geophysics, 74, V99–V107, https://doi.org/10.1190/1.3184015, 2009.

Hale, D.: Dynamic warping of seismic images, Geophysics, 78, S105–S115, https://doi.org/10.1190/GEO2012-0327.1, 2013.

Hall, S. A.: A methodology for 7D warping and deformation monitoring using time-lapse seismic data, Geophysics, 71, O21, https://doi.org/10.1190/1.2212227, 2006.

Hampson, D.: Inverse velocity stacking for multiple elimination, J. Can. Soc. Explor. Geophys., 22, 44–55, 1986.

Han, S., Bangs, N. L., Carbotte, S. M., Saffer, D. M., and Gibson, J. C.: Links between sediment consolidation and Cascadia megathrust slip behaviour, Nat. Geosci., 10, 954–959, https://doi.org/10.1038/s41561-017-0007-2, 2017.

Hardy, P.: High resolution tomographic MVA with automation, in: 66th EAGE Conference & Exhibition, Paris, 2004, p. cp-133, https://doi.org/10.3997/2214-4609.201405668, 2003.

Horn, B. K. P. and Schunck, B. G.: Determining optical flow, Artif. Intell., 17, 185–203, https://doi.org/10.1016/0004-3702(81)90024-2, 1981.

Jones, I. F.: A review of 3D PreSDM model building techniques, First Break, 21, https://doi.org/10.3997/1365-2397.21.3.25408, 2003.

Jones, I. F.: Tutorial: Velocity estimation via ray-based tomography, First Break, 28, 45–52, 2010.

Jones, I. F., Sugrue, M. J., and Hardy, P. B.: Hybrid Gridded Tomography, First Break, 25, https://doi.org/10.3997/1365-2397.2007013, 2007.

Jones, I. F., Ibbotson, K., Grimshaw, M., and Plasterie, P.: Prestack Depth Migration and Velocity Model Building, edited by: Jones, I. F., Bloor, R. I., Biondi, B. L., and Etgen, J. T., Society of Exploration Geophysicists, https://doi.org/10.1190/1.9781560801917, 2008.

Kosloff, D., Sherwood, J., Koren, Z., Machet, E., and Falkovitz, Y.: Velocity and interface depth determination by tomography of depth migrated gathers, Geophysics, 61, 1511–1523, 1996.

Levitus, S.: Climatological Atlas of the World Ocean, EOS T. Am. Geophys. Un., 64, 962–963, https://doi.org/10.1029/EO064i049p00962-02, 1983.

Li, J., Shillington, D. J., Saffer, D. M., Bécel, A., Nedimović, M. R., Kuehn, H., Webb, S. C., Keranen, K. M., and Abers, G. A.: Connections between subducted sediment, pore-fluid pressure, and earthquake behavior along the Alaska megathrust, Geology, 46, 299–302, https://doi.org/10.1130/G39557.1, 2018.

Lüschen, E., Müller, C., Kopp, H., Engels, M., Lutz, R., Planert, L., Shulgin, A., Djajadihardja, Y. S., Lueschen, E., Mueller, C., Kopp, H., Engels, M., Lutz, R., Planert, L., Shulgin, A., and Djajadihardja, Y. S.: Structure, evolution and tectonic activity of the eastern Sunda forearc, Indonesia, from marine seismic investigations, Tectonophysics, 508, 6–21, https://doi.org/10.1016/j.tecto.2010.06.008, 2011.

MacKay, S. and Abma, R.: Imaging and velocity estimation with depth-focusing analysis, Geophysics, 57, 1608–1622, 1992.

Martin, T. and Bell, M.: An innovative approach to automation for velocity model building, First Break, 37, 57–65, https://doi.org/10.3997/1365-2397.n0033, 2019.

Meléndez, A., Jiménez, C. E., Sallarès, V., and Ranero, C. R.: Anisotropic P-wave travel-time tomography implementing Thomsen's weak approximation in TOMO3D, Solid Earth, 10, 1857–1876, https://doi.org/10.5194/se-10-1857-2019, 2019

Neidell, N. S. and Taner, M. T.: Semblance and other coherency measures for multichannel data, Geophysics, 36, 482–497, 1971.

Nickel, M., Sønneland, L., and Geco-prakla, S.: Non-rigid matching of migrated time-lapse seismic SEG 1999 Expanded Abstracts SEG 1999 Expanded Abstracts, Houston, Texas, USA, https://doi.org/10.1190/1.1821191, 1999.

Pappu, S., Gold, S., and Rangarajan, A.: A framework for nonrigid matching and correspondence, edited by: Touretzky, D. S., Mozer, M. C., and Hasselmo, M. E., Advances in Neural Information Processing Systems, 8, MIT Press, Cambridge, MA, 1996.

Perez, G. and Marfurt, K. J.: Warping prestack imaged data to improve stack quality and resolution, Geophysics, 73, 1–7, https://doi.org/10.1190/1.2829986, 2008.

Planert, L., Kopp, H., Lüschen, E., Mueller, C., Flueh, E. R., Shulgin, A., Djajadihardja, Y., and Krabbenhoeft, A.: Lower plate structure and upper plate deformational segmentation at the Sunda-Banda arc transition, Indonesia, J. Geophys. Res.-Sol. Ea., 115, 1–25, https://doi.org/10.1029/2009JB006713, 2010.

Reiche, S. and Berkels, B.: Automated stacking of seismic reflection data based on nonrigid image matching, Geophysics, 83, V171–V183, https://doi.org/10.1190/geo2017-0189.1, 2018.

Rickett, J. E. and Lumley, D. E.: Cross-equalization data processing for time-lapse seismic reservoir monitoring: A case study from the Gulf of Mexico, Geophysics, 66, 1015–1025, 2001.

Riedel, M., Reiche, S., Aßhoff, K., and Buske, S.: Seismic depth imaging of sequence boundaries beneath the New Jersey shelf, Mar. Geophys. Res., 40, 17–32, https://doi.org/10.1007/s11001-018-9360-9, 2019.

Robinson, E. A. and Treitel, S.: Geophysical signal analysis, Society of Exploration Geophysicists, https://doi.org/10.1190/1.9781560802327, 2000.

Sallarès, V. and Ranero, C. R.: Upper-plate rigidity determines depth-varying rupture behaviour of megathrust earthquakes, Nature, 576, 96–101, https://doi.org/10.1038/s41586-019-1784-0, 2019.

Shiraishi, K., Moore, G. F., Yamada, Y., Kinoshita, M., Sanada, Y., and Kimura, G.: Seismogenic zone structures revealed by improved 3-D seismic images in the Nankai Trough off Kumano, Geochem. Geophy. Geosy., 20, 2252–2271, 2019.

Sripanich, Y., Fomel, S., Trampert, J., Burnett, W., and Hess, T.: Probabilistic moveout analysis by time warping, Geophysics, 85, U1–U20, https://doi.org/10.1190/geo2018-0797.1, 2020.

Stork, C.: Reflection tomography in the postmigrated domain, Geophysics, 57, 680–692, https://doi.org/10.1190/1.1443282, 1992.

Sugrue, M., Jones, I. F., Evans, E., Fairhead, S., and Marsden, G.: Enhanced velocity estimation using gridded tomography in complex chalk, Geophys. Prospect., 52, 683–691, 2004.

Thomsen, L.: Weak elastic anisotropy, Geophysics, 51, 1954–1966, https://doi.org/10.1190/1.1442051, 1986.

Tomar, G., Singh, S. C., and Montagner, J.-P.: Sub-sample time shift and horizontal displacement measurements using phase-correlation method in time-lapse seismic, Geophys. Prospect., 65, 407–425, 2017.

Van Trier, J. A.: Tomographic determination of structural velocities from depth-migrated seismic data, thesis, Stanford University, http://sepwww.stanford.edu/data/media/public/oldreports/sep66/66_00.pdf (last access: 15 February 2022), 1990.

Verschuur, D. J., Berkhout, A. J., and Wapenaar, C. P. A.: Adaptive surface-related multiple elimination, Geophysics, 57, 1166–1177, https://doi.org/10.1190/1.1443330, 1992.

Wang, X. and Tsvankin, I.: Ray-based gridded tomography for tilted TI media, in: SEG Technical Program Expanded Abstracts 2011, San Antonio, Texas, USA, 237–242, Society of Exploration Geophysicists, https://doi.org/10.1190/1.3627687, 2011.

Wolberg, G.: Digital image warping, IEEE computer Society Press Los Alamitos, CA, ISBN: 978-08-1868-944-4, 1990.

Woodward, M. J., Nichols, D., Zdraveva, O., Whitfield, P., and Johns, T.: A decade of tomography, Geophysics, 73, VE5, https://doi.org/10.1190/1.2969907, 2008.

Xia, Y., Klaeschen, D., Kopp, H., and Schnabel, M.: Supplementary code for article "Reflection tomography by depth warping: A case study across the Java trench" on Solid Earth (SE-2021-40), Zenodo [code], https://doi.org/10.5281/zenodo.5998288, 2022.

Xue, Z., Zhang, H., Zhao, Y., and Fomel, S.: Pattern-guided dip estimation with plane-wave destruction filters, Geophys. Prospect., 67, 1798–1810, 2019.

Yilmaz, Ö.: Seismic data analysis: Processing, inversion, and interpretation of seismic data, Society of exploration geophysicists, https://doi.org/10.1190/1.9781560801580, 2001.

Zhang, D., Wang, X., Huang, Y., and Schuster, G.: Warping for trim statics, in: SEG Technical Program Expanded Abstracts 2014, Denver, Colorado, USA, 3946–3950, Society of Exploration Geophysicists, https://doi.org/10.1190/segam2014-0281.1, 2014.

CHAPTER 4

MANUSCRIPT #2

Scale-dependent upper plate deformation caused by the subduction of seafloor relief

Yueyang Xia(1); Heidrun Kopp(1,2) Dirk Klaeschen (1); Jacob Geersen(2); Bo Ma(1); and Michael Schnabel(3)

(1) Dynamics of the Ocean Floor, GEOMAR, Helmholtz Centre for Ocean Research Kiel, 24148 Kiel, Germany
(2) Department of Geosciences, Kiel University, 24118 Kiel, Germany
(3) Bundesanstalt für Geowissenschaften und Rohstoffe (BGR), Stilleweg 2, 30655 Hanover, Germany

Pending submission to Journal of Geophysical Research: Solid Earth

---

This chapter contains a manuscript ready for submission to Journal of Geophysical Research: Solid Earth. Please note that the manuscript contains its own reference list and refers to its own figure numbers.

Scale-dependent upper plate deformation caused by the subduction of seafloor relief

Yueyang Xia[1], Heidrun Kopp[1,2], Dirk Klaeschen[1], Jacob Geersen[2], Bo Ma[1], Michael Schnabel[3]

[1]GEOMAR Helmholtz Centre for Ocean Research Kiel, Wischhofstr. 1-3, 24148 Kiel, Germany

[2]Christian-Albrechts-Universität zu Kiel, Christian-Albrechts-Platz 4, 24118 Kiel, Germany

[3]Bundesanstalt für Geowissenschaften und Rohstoffe (BGR), Stilleweg 2, 30655 Hannover, Germany

Corresponding author: Yueyang Xia (yxia@geomar.de), Bo Ma (bma@geomar.de)

Key Points:

- Upper plate deformation scales with variable lower plate subducting relief, identified in seismic depth sections and high-resolution bathymetry across the Java trench.
- Subducting basement highs provoke vertical migration of the décollement and cause permanent brittle deformation of the upper plate.
- Subduction of seafloor topography induces progression from an accretion-dominated domain towards a phase of subduction erosion.

Abstract

The Java - Lesser Sunda margin, which features multi-scale subducting oceanic basement relief and a landward shift of the deformation front, is classified as a neutral (Lombok and Sumbawa) to erosional (Central Java to Bali) margin in comparison to its accretionary counterpart offshore Sumatra. However, a comprehensive analysis of the upper plate structure modulated by the subduction of oceanic basement relief and the associated erosional processes is lacking to date. Here we process and present multichannel reflection seismic profiles offshore eastern Java, Bali, Lombok, and Sumbawa. The new seismic processing routine, which is underpinned by a grid-based tomographic P-wave velocity inversion, provides a more reliable velocity model than previous studies and results in improved resolution of the seismic images with revised reflector dips. The data document the upper plate deformation pattern and the erosional effects of the subducting relief at different scales. The seismic profiles and bathymetric map highlight the diversity and varying scales (diameters from <1 km to ~40 km) of the subducting relief (seamounts, ridges, and normal fault scarps) observed along strike on both the oceanic seafloor and on the submerged subducting interface. Basement relief subduction exerts a first-order control on the forearc seafloor topography, structure of the upper plate, and evolution of the décollement. The impact of different scales of subducting relief on the sedimentary units of the accretionary wedge results in shared characteristics (e.g., a shallower seafloor surface slope and enhanced compressional structure in front of subducting relief). Concurrently, the variation of scales leads to different levels of upper plate deformation. Large and medium scale subducting relief cause a noticeable landward (arc-ward) shift of the deformation front, shortening, and uplift of the accretionary wedge material, steepening of the frontal slope, and strike-slip faulting at the rear of the subducting topography. Small-scale subducting ridges primarily impact the frontal prism resulting in a more localized undulation of the surface slope and over-steepening of the slope at the trench, causing local mass transport (e.g., landslides or slumping). Décollement migration is observed in the vicinity of subducting relief when the height of the oceanic relief is larger than the thickness of oceanic sediment, implying a weak upper plate material compared to Byerlee's law.

1 Introduction

Subduction of rough seafloor relief is widely observed at subduction zones around the globe. Different scales of subducting oceanic basement structures (e.g., seamounts, basement ridges, fault scarps, horst-and-grabens) have been shown to modulate the structure and morphology of the plate interface (Bangs et al., 2006; Barker et al., 2018; Bell et al., 2010; Bonnet et al., 2019; Davidson et al., 2020; Geersen et al., 2015; Kodaira et al., 2000; Martínez-Loriente et al., 2019; Morton et al., 2018; Ranero and von Huene, 2000; Todd et al., 2018), modify regional mass transport (Dominguez et al., 1998; Ruh et al., 2016; Sun et al., 2020b), and result in pervasive and potentially permanent deformation of the upper plate (Wang and Bilek, 2011). Subducting basement relief can further modify the stress distribution (Lallemand and Le Pichon, 1987; Ruh, 2016; Ruh et al., 2016) or enhance fluid expulsion into the wedge material (Chesley et al., 2021; Sun et al., 2020a; von Huene et al., 2004).

Oceanic basement features vary in height and volume and exhibit a wide variety of forms, comprising conical shapes (peaked or flat-top), multiple branches, or parallel ridges (Fig. 1b, c). Seamounts, which represent one of the most common and most widespread topographic features on oceanic plates, have been documented within numerous subduction zone systems, including the Tonga-Kermadec trench (Timm, 2013), Nankai trench (Bangs et al., 2006), Japan and Kuril trenches (Lallemand, 1989), Cascadia (Tréhu et al., 2012), Hikurangi (Bell et al., 2014), and the Central America trench system (Ranero and von Huene, 2000). Upper plate deformation associated with the subduction of oceanic basement relief is manifested by re-entrants or scarps at the lower slope (Ranero and von Huene, 2000), gravitational submarine landslides (Brune et al., 2010), strike-slip faulting (Davidson et al., 2020), regional uplift (Laursen et al., 2002) or the landward shift of the deformation front (Kopp et al., 2006). Underthrusting of oceanic plate topography is a driving factor of subduction erosion, removing material from the toe of the overriding plate as well as from its base. Structural erosive packages removed from the upper plate related to seamount or oceanic relief subduction are documented in seismic studies (Kirkpatrick et al., 2020; Marcaillou et al., 2016).

Subduction of seafloor topography has been associated with marine geohazards including submarine landslides, earthquake seismicity, and tsunamis. A long-standing, controversial discussion has focused on the relationship between seamount subduction and the generation of large earthquakes. This is based on the intuitive hypothesis that the positive relief would increase normal stress, resulting in enhanced coupling patches along the plate interface, which would favor large earthquakes (Cloos, 1992; Cloos and Shreve, 1996; Scholz and Small, 1997).

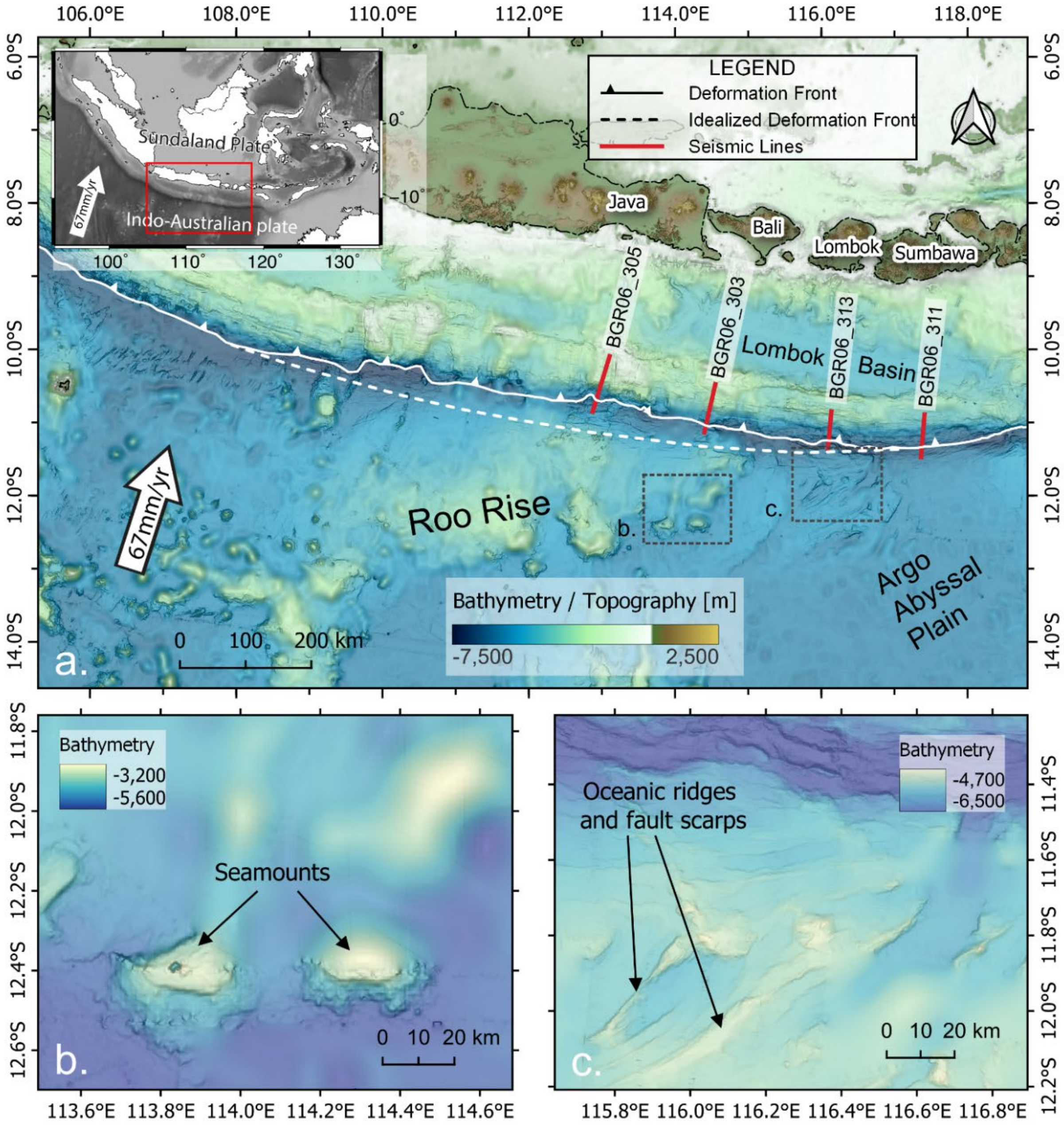

Figure 1 a. Regional tectonic setting and bathymetry of the study area. Red lines indicate the location of the four MCS profiles. The deformation front is shown in a solid white line, and the undisturbed hypothetical trend of the deformation front is shown by the white dashed line. b. A close-up view of the conical seamounts observed on the oceanic crust of the Roo Rise. c. A close-up view of the linear-shaped ridges on the oceanic crust offshore Lombok.

The Java 1994 tsunami earthquake (M_w = 7.8) has been discussed as slip over a subducted seamount (Abercrombie et al., 2001; Bilek and Engdahl, 2007), though the seamount's exact location remains ambiguous due to sparse data coverage (Xia et al., 2021). Recent discussions (Wang and Bilek, 2014) and modeling results (Dominguez et al., 1998; Ruh et al., 2016; van Rijsingen et al., 2019; Yang et al., 2013), however, imply that seamounts or bathymetric basement highs favor aseismic creeping, promote smaller magnitude earthquakes ($M_w < 7$), and potentially act as seismic barriers during the co-seismic phase, due to the complex fault network and heterogeneous stress distribution in the vicinity of the seamount. Underthrusting of basement topography can induce localized uplift of the forearc slope resulting in rapid or long-term gravitational collapse and submarine landslides (e.g., Hühnerbach et al., 2005; Kopp et al., 2006; Ruh, 2016).

Here we discuss the impact of oceanic basement features identified on four re-processed and depth-migrated multi-channel seismic (MCS) profiles from the Java-Lesser Sunda forearc. The grid-based tomography and pre-stack depth migration provide seismic images with corrected reflector dipping angles. The seismic images reveal the response of the upper plate and the plate interface to the subduction of basement relief at various scales, ranging from seamounts to ridges to smaller-scale relief such as subducting fault scarps.

We analyze the scale-dependent effect of the subducting topography on the geometry and deformation of the marine forearc and the accretionary wedge as well as on the evolution of the décollement. Our study documents the progression from an accretion-dominated domain towards a phase of subduction erosion.

2 Tectonic setting of the Java-Lesser Sunda margin

The ~5000 km long Sunda arc extends westward from Flores to Java and then trends northwest towards Sumatra and Myanmar (Hamilton, 1988) (Fig. 1). The tectonic evolution of the Sunda arc is controlled by the active subduction of the Indo-Australian plate underneath Eurasia since the Eocene-Oligocene (Moore et al., 1982; Hamilton, 1988; Hall, 2002; Hall and Smyth, 2008), following the Eocene collision of India with Eurasia. Given the great lateral extent of the Sunda arc, segmentation and variations in several geological parameters are observed along the margin (Moore et al., 1980). The age of the subducting lithosphere decreases towards the west from 150 Ma offshore Sumba to 125 Ma off Bali, reaching 90 Ma off Sumatra (Heine et al., 2004). The plate age variation correlates to an eastward increase in trench depth to >7000 m off Bali and Lombok. Offshore Java and the Lesser Sunda Islands, the subduction orientation is almost orthogonal with a current convergence rate of 67 mm/yr in a direction N 11°E ± 4° (Tregoning et al., 1994; Bock et al., 2003) (Fig. 1).

Information on the crustal structure of the Java-Lesser Sunda marine forearc is mostly based on the analysis of a suite of wide-angle and MCS seismic lines (Karig et al., 1980; Moore et al., 1980; Kopp et al., 2006, 2009; Müller et al., 2008; Planert et al., 2010; Lüschen et al., 2011; Shulgin et al., 2011). An overview of the main geological parameters for each seismic profile presented here is provided in Table 1.

Offshore central Java around 109°E, a change in the tectonic regime from subduction accretion to subduction erosion is related to the underthrusting of the Roo Rise oceanic plateau, which forms the eastern extension of the Christmas Island seamount province, off central and eastern Java (109°E to 115°E) (Kopp et al., 2006) (Fig. 1). In the projection of the Roo Rise from central Java to Bali, subduction erosion causes a deflection of the Java trench and deformation front towards the arc by 40 km on average from the normal curvature trend of the deep-sea trench (Kopp et al., 2006, Krabbenhoeft et al., 2010). The Roo Rise is manifested in a ~500 km broad bathymetric plateau dotted with isolated seamounts with an average elevation of >2000 m above the surrounding ocean floor (Fig. 1b) that covers approximately 100 000 km^2 offshore central-eastern Java (Shulgin et al., 2011). The Christmas Island seamount province is formed through the shallow recycling of the delaminated continental lithosphere entrained in the mantle, based on the isotope analyses of volcanic rocks (Hoernle et al., 2011). Refraction tomography studies have shown that the crustal thickness of the Roo Rise close to the trench is between 12 km to 18 km, with a lower P-wave velocity than for conventional oceanic crust (Shulgin et al., 2011) (vp = 6.6 km/s compared to vp = 7.2 km/s at the oceanic Moho). The marine forearc morphology offshore eastern Java is significantly modulated by the distinct lower plate topography of the Roo Rise entering the trench. Local landslide scarps, frontal embayments (concave-shaped 'cookie bites' or re-entrants), and over-steepened surface slopes, which are interpreted as evidence for mass failure, are observed at the lower slope in the bathymetry (Kopp, 2011) (Fig. 1a, e.g., at 110°E, 112°E, 113°E).

Table 1

MCS Line Number	The surface slope of the mature accretionary wedge/ middle slope [°]	water depth [km] at the trench	water depth [km] of slope break	water depth [km] of forearc high	Distance between the deformation front and the slope break [km]	Distance of the trench retreat [km]	Length of the accretionary wedge [km]
BGR06_311 (Sumbawa)	5.0	6.65	3.62	2.80	43	0	68
BGR06_313 (Lombok)	-	6.62	2.69	2.38	42	16	77
BGR06_303 (Bali)	7.6	5.92	2.27	1.52	37	30	82
BGR06_305 (Eastern Java)	8.3	6.30	2.34	0.75	32	50	99

The easternmost portion of the Sunda subduction system is characterized by the underthrusting of the Argo abyssal plain, located seaward of the deep-sea trench offshore Lombok and Sumbawa islands (115°E to 119°E) (Fig. 1). With a mean water depth of 5500 m, the Argo abyssal plain is largely devoid of terrigenous sediment (Moore et al., 1982; Planert et al., 2010). The crust of the Argo abyssal plain has an average thickness of 8.6 km, indicating a very mature oceanic crust of ~128 Ma to 150 Ma (Seton et al., 2020). The roughness of the seafloor turns from rugged offshore Bali to generally smooth offshore Sumbawa (Lüschen et al., 2011) (Figs. 1 and 2). Offshore Lombok (at ~ 116°E), linear-shaped oceanic basement structures characterize the seafloor and trend at angles between 45° and 60° (Fig. 2), roughly parallel to the magnetic anomalies (Fig. S1) (Lüschen et al., 2011).

These are inherited structures mirroring the original spreading fabric (Planert et al., 2010). On the outer rise seaward of the trench, a pervasive pattern of plate-bending induced normal faults with throws up to 150 m and individual fault segment lengths of up to 60 km is observed starting at about 30 km seaward of the trench axis (Fig. 2) (Lüschen et al., 2011). The bathymetry and MCS data show a strong horst-and-graben relief in the trench, which is the surface expression of faults that have been imaged to cut deep into the oceanic basement (Lüschen et al., 2011).

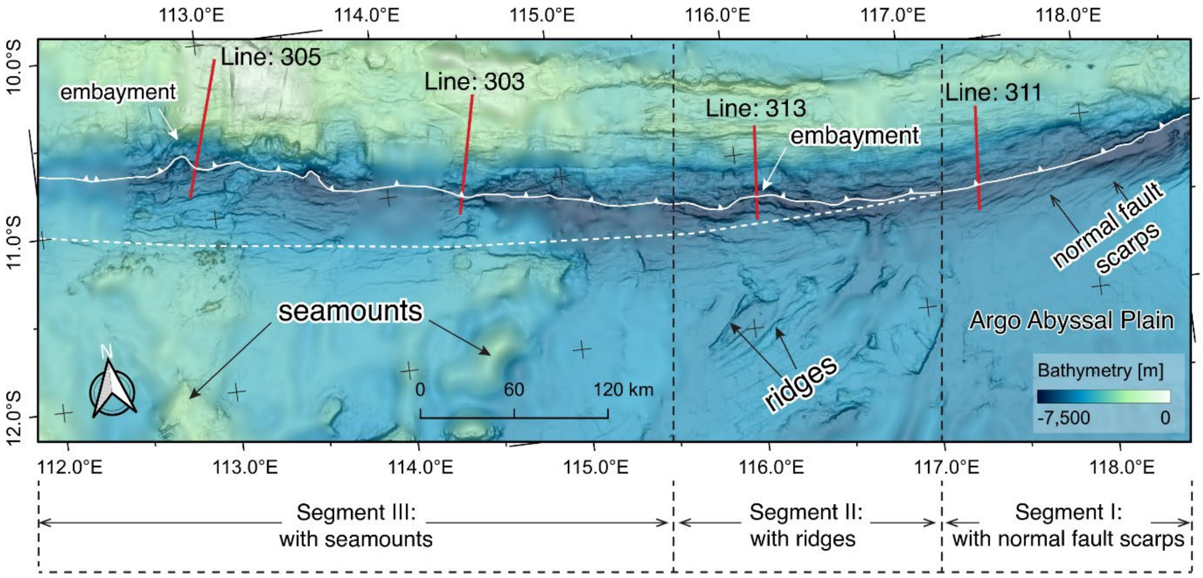

Figure 2. Bathymetry map around profiles BGR06_313 (off Lombok), BGR06_311 (off Sumbawa), BGR06_303 (off Bali), and BGR06_305 (off eastern Java). The solid white line indicates the deformation front, and the white dashed line illustrates the idealized trend of the deformation front. Please note that the study area could be divided into three different geological units (segments) along the strike. In Segment I from ~117° E to ~118.5° E, the oceanic plate is devoid of a large seamount or basement ridge, but is featured by minor bending-related normal faults with a small offset (< 150 m) close to the trench. The oceanic plate in Segment II from ~115.5° E to ~117° E features linear-shaped ridges on the oceanic crust. Segment III from ~112° E to ~115.5° E is featured by numerous conical or semi-conical shape seamounts on the oceanic plate.

To the north, a mature forearc basin, the Lombok basin, has an average water depth of 4400 m and is limited by the Roo Rise subduction to the west and the Scott plateau to the east (Planert et al., 2010) (Fig. 1). The basin and the adjacent forearc high are uniformly developed along the entire Lombok segment and remain largely undisturbed by the subduction of the pronounced basement relief as observed, e.g., further to the west in the Roo Rise segment off eastern Java and Bali, where the forearc high rises to a water depth of less than ~1500 m compared to ~2300-3000 m offshore Lombok-Sumbawa (Krabbenhoeft et al., 2010).

3 Data and Methods

The multi-channel seismic reflection survey used in this study was conducted by the Federal Institute for Geosciences and Natural Resources (BGR) (Müller & Neben, 2006) on RV SONNE SO190 during the SINDBAD Project in 2006. We analyzed four trench dipping MCS profiles (BGR06_311, BGR06_313, BGR06_303, and BGR06_305), which cover the marine forearc offshore Sumbawa, Lombok, Bali, and eastern Java, respectively (Lüschen et al., 2011; Planert et al., 2010; Shulgin et al., 2011) (Figs. 1, 2, Table 1). The seismic source used in the survey is a G-Gun array. The source was towed at a depth of 6 m and has a maximum total volume of 3,100 in^3 (50.8 l). Seismic signals were recorded by a 240-channel digital streamer with a length of 3,000 m.

Previous processing of the seismic data was based on a work flow including common mid-point (CMP) binning, multiple attenuation with Radon filter and wave equation-based prediction, velocity analysis using the focusing technique, and Kirchhoff pre-stack depth migration (Lüschen et a., 2010). In the new processing routine of this study, the major difference is how the PSDM image are iteratively updated in the Kirchhoff pre-stack depth migration. We used the ray-based reflection tomography method with the Non-Rigid Matching (NRM) depth warping technique (Xia et al., 2022) to refine the vp model at shallow depth (< 3 km) and to improve imaging of the shallow sediment structure.

Seismic profiles BGR06_303, BGR06_305, BGR06_311 and BGR06_313 are processed using a routine that includes geometry set-up, common midpoint (CMP) binning (binning size of 6.25 m, CMP fold of 30), zero offset traces padding, bandpass filtering, shot interpolation (2 times), and random noise attenuation (Xia et al., 2021; 2022). The strong multiple reflection caused by the shallow water depth of the forearc high is suppressed by a free surface-related multiple prediction based on the Kirchhoff integral (Verschuur et al., 1992). By using adaptive subtraction (Guitton and Verschuur, 2004), the multiple was eliminated with a cascaded frequency band (Xia et al., 2021). The initial interactive semblance velocity analysis of these four profiles is performed in the time domain with a CMP increment of 250 m and converted to the depth domain. The vp models are subsequently merged with the ocean bottom seismometer (OBS) refraction models of Shulgin et al. (2011) and Planert et al. (2010), except for profile BGR06_303 and BGR06_311, for which no coincident OBS profiles exist. A smooth taper zone at the base of the MCS-derived model was used while merging the refraction vp models to eliminate any abrupt changes in the vp models. The pre-stack depth migration with the velocity model establishment were performed in the depth domain and iteratively refined the vp model and MCS PSDM image by using the ray-based reflection depth tomography with a warping method to minimize the residual depth error (Xia et al., 2022). One example for the improvement of the seismic imaging compared to the study of Lüschen et al. (2011), is the subsurface structure of the MCS profile BGR06_311. The previous interpretation by Lüschen et al. (2011) identified a large thrust fault in the oceanic plate (Fig. 8 in Lüschen et al., 2011). The re-processing improved the seismic image and reveals that the oceanic plate and the décollement below the frontal prism and middle slope are affected by bending-related normal faults in the subsurface (Fig. 3a) rather than thrust faulting, as proposed in the study of Lüschen et al. (2011).

The multibeam bathymetric data in this study were collected during the SO190 cruise, using a 12 kHz SIMRAD EM120 multibeam echo sounder with a 90° beam angle resulting in a swath width of 2 times the water depth. A sound velocity profile was obtained at the beginning of the cruise during a CTD station. Subsequent processing of each sweep was carried out using the MB System software (Caress and Chayes, 1996). Data quality was good to excellent despite several days of high waves producing some bad pings and typical problems with the bottom detect algorithm on steep flanks facing away from the ship. The manually edited data were gridded using the Generic Mapping Tools (GMT) (Wessel and Smith, 1991) using a near neighbor gridding algorithm and were imported into QGIS. In areas not covered by the multibeam soundings, the data were merged with the GEBCO_2020 bathymetry (GEBCO, 2020).

4 Results

We present the four MCS profiles covering the trench and lower slope of the Eastern Java-Lesser Sunda margin starting with the easternmost profile offshore Sumbawa and progressively moving westwards toward Java (Fig. 1, Table 1). The easternmost profile BGR06_311 offshore Sumbawa serves as a reference line for the upper plate accretionary wedge structure, which along this profile is not significantly affected by large-scale (>150 m) subducting relief (Figs. 2, 3a). Profiles BGR06_313 (offshore Lombok), BGR06_303 (offshore Bali), and BGR06_305 (offshore eastern Java), in contrast, are characterized by the subduction of oceanic basement relief of various dimensions, including basement ridges and seamounts. An overview of the different features is provided in Table 2. In the following presentation of the seismic profiles, we distinguish between the oceanic domain and outer rise, the trench, the active frontal prism, the mature accretionary wedge, the forearc high and the forearc basin as the main tectonic units.

Table 2

Subducting Relief ID	Height [km]	Width [km]	Aspect ratio	Distance to trench [km]	Depth (abs) [km]	Depth (below seafloor) [km]	Relief type	Elapsed time of the relief subduction (ka)
Ridge A in BGR06_313	1.3	4.5	0.28	7	7	1.5	Basement Ridge	150
Ridge B in BGR06_313	1.6	6.3	0.25	22	8.5	3.5	Basement Ridge	400
Ridge in BGR06_303	1.3	4.1	0.31	7	5.5	0.5	Basement Ridge	130
Seamount in BGR06_303	2.1	26.2	0.08	36	8	5	Seamount	700
Seamount in BGR06_305	2.7	39.3	0.07	33	7.5	5.5	Seamount	850

4.1 Profile BGR06_311 - offshore Sumbawa

MCS profile BGR06_311 (Fig. 1) is located offshore Sumbawa where the Argo Abyssal plain is subducting below the island arc (Fig. 1). The incoming oceanic crust carries about 420 m of sediment (Fig. 3a, S2, km -10 to 0). In the trench, approximately 500-600 m of sediment has accumulated. This portion of the Java-Lesser Sunda margin (termed Segment I in Figure 2) is not significantly affected by seamount subduction and frontal subduction erosion, which causes a northward deflection of the deformation front further west (Figs. 1a). The incoming seafloor is much smoother than in the Roo Rise domain (Segment III in Fig. 2) to the west and no large-scale (>500 m height) topographic features are observed seaward of the trench (Fig. 2). The high-resolution bathymetry data reveal bending-related normal fault scarps (vertical throw < 150 m) on the outer rise (Figs. 2, 4a), aligned parallel to the magnetic isochrons (Fig. S1) and trending obliquely to the strike of the deformation front. The faults dissect the oceanic basement and the overlying sediment cover (Fig. 3a, km -10 to 0). As the plate subducts, the fault throw is enhanced due to the increased bending of the oceanic crust, resulting in a horst-and-graben structure of the oceanic basement with moderate offsets (100 – 500 m) underneath the frontal prism (Fig. 4c) and the accretionary wedge (Fig. 4b). A previously interpreted thrust fault, dissecting the entire oceanic crust down to Moho depth (Fig. 8 in Lüschen et al., 2011) is not observed in the new depth migrated seismic section presented here.

Landward of the deformation front (profile km 0), approximately 60% of the incoming sediment sequence is frontally accreted, while the remaining sediment constitutes a band of underthrust material with a thickness of ~170 m (Fig. 4c). The frontal prism on this profile (km 0 to 8) is a textbook example of frontal sediment accretion and documents the formation of imbricate thrusts that progressively steepen and rotate landwards to accommodate the incoming material (Fig. 4c). Approximately 8 km landward of the deformation front, the upper plate reflectivity decreases and marks the transition from the actively accreting frontal prism to the mature accretionary wedge (Fig. 3a, km 8 to 41). Landward dipping fore-thrusts and imbricate sediment layers are observed in the accretionary wedge, connecting from the seafloor to the plate boundary at depth (e.g. at around profile km 13 and 20, Fig. 3a). The thrust faults cause minor seafloor offsets and undulations at the lower and middle slope (e.g., around profile km 21 to 23) (Fig. 3a). The surface slope of the accretionary wedge (Fig. 3a, km 10 - 41) is relatively uniform ~5°. A prominent slope break at profile km 42 coincides with a steeply dipping reflector that offsets the seafloor and cuts through the accretionary wedge to connect to the megathrust at 9.5 km depth (Fig. 3a). The décollement is imaged as a coherent reflector from profile km 14 to 50 (Fig. 3a) and is characterized by a reversed polarity relative to the seafloor reflection (Fig. 4d, e). The plate interface dipping angle is around -4.1° underneath the frontal prism and accretionary wedge (Fig. 3a, km 5 - 40).

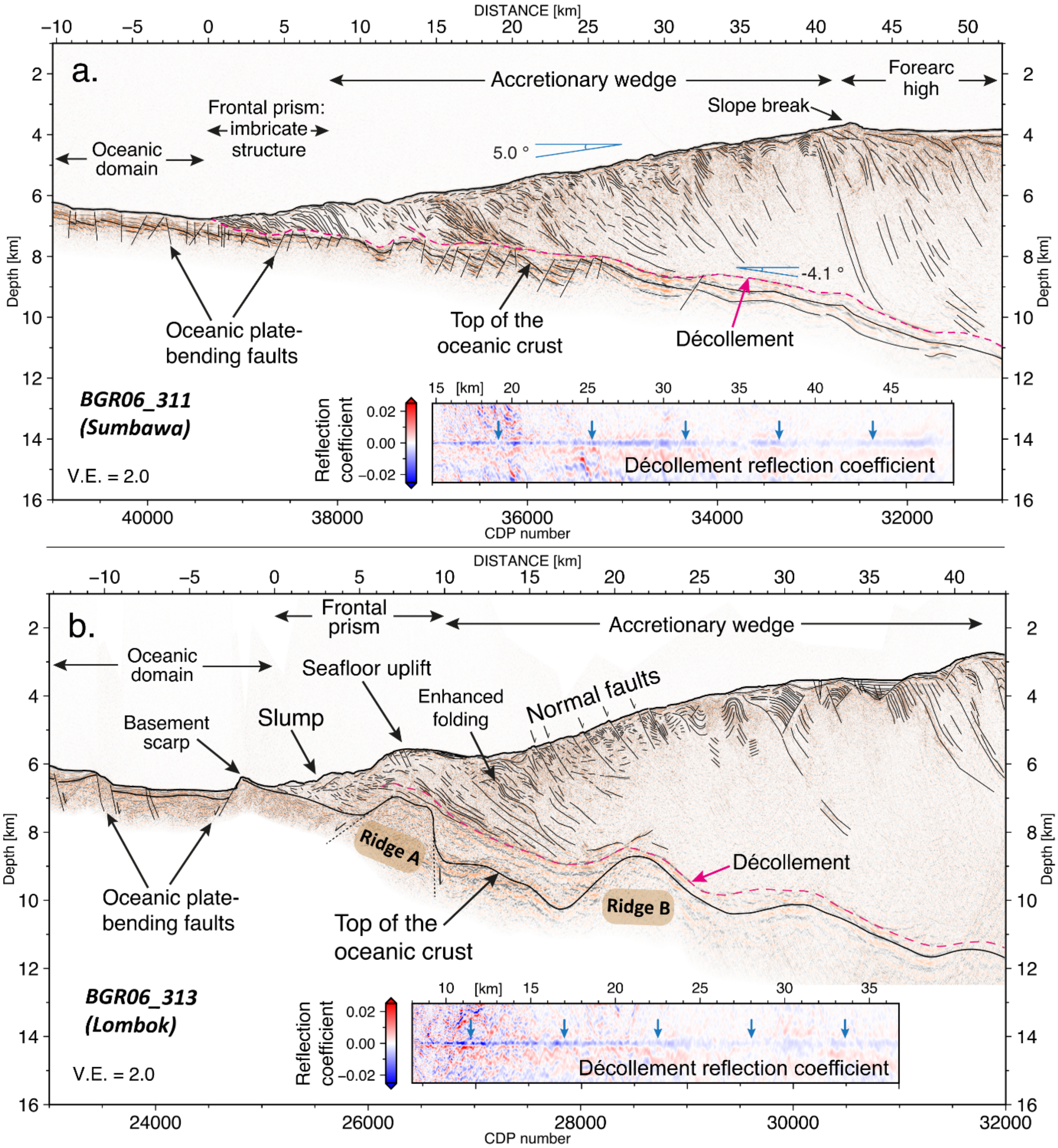

Figure 3 a. MCS depth migration image and the line-drawing of the seismic line BGR06_311 offshore Sumbawa. b. MCS depth migration image and the line-drawing of the seismic line BGR06_313 offshore Lombok. The reflection coefficient subgraph of horizontally aligned décollement is plotted within each subfigure.

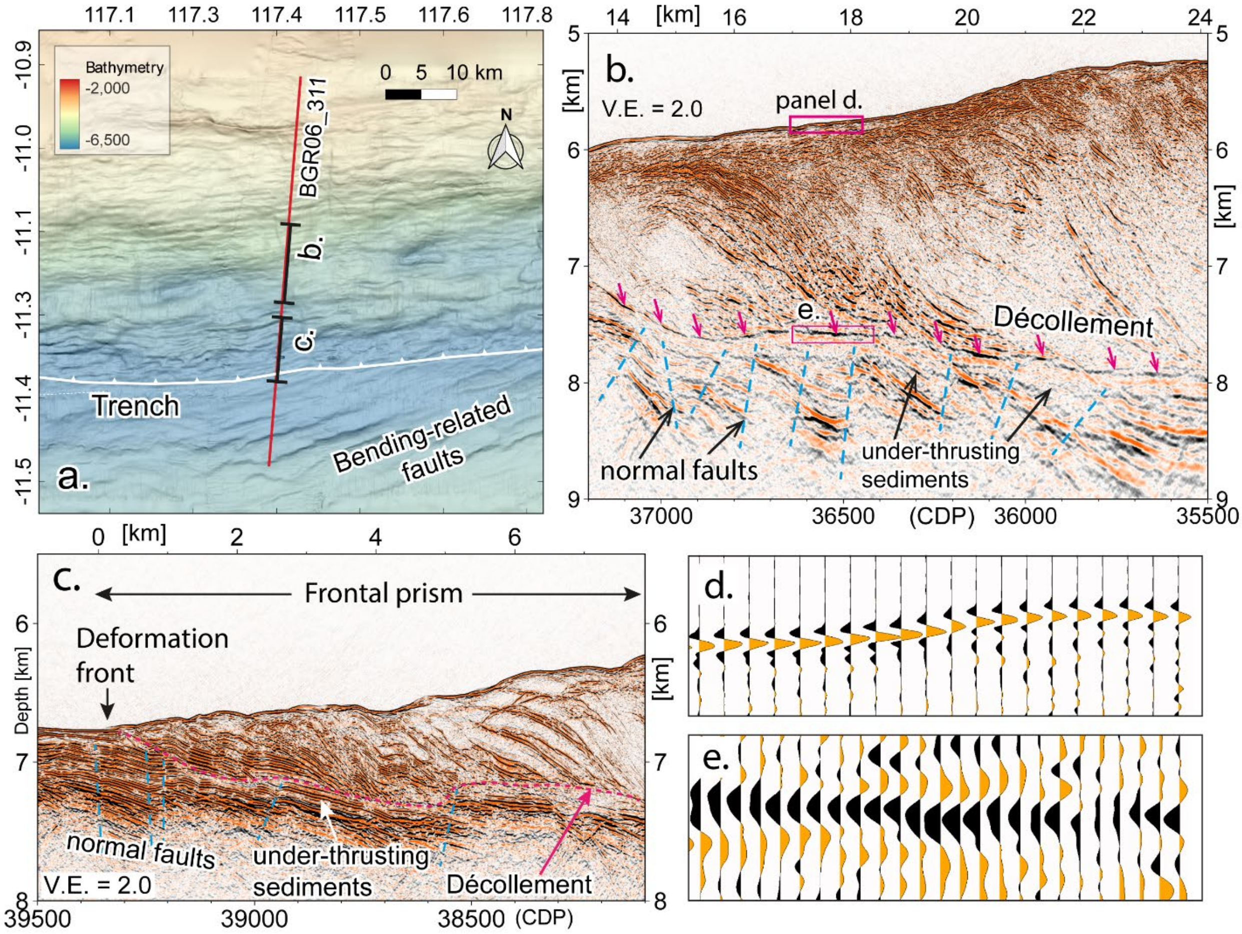

Figure 4 a. Bathymetry map around profile BGR06_311. b. Close-up view of the upper plate lower slope. Plate-bending induced normal faulting affects the oceanic basement. The plate interface reflection features a reversed polarity wavelet compared to the seafloor reflection (compare panels d and e). c. Close-up view of the trench and frontal prism. d. Zoom-in wiggle display of the seafloor reflection. e. Zoom-in wiggle display of the décollement reflection. Orange in-fill indicates positive polarity, and black color in-fill indicates reversed polarity.

4.2 Profile BGR06_313 - offshore Lombok

Profile BGR06_313 trends offshore Lombok, approximately 140 km west of the Sumbawa profile BGR06_311 (Figs. 1 & 2). The outer rise offshore Lombok carries a number of linear-shaped ridges (Fig. 1c, & Segment II in Fig. 2). Here, the trench is partially devoid of any sediment and isolated sediment patches reach a thickness of less than 150 m (Fig. 3b, km -10 to 0), though a sediment cover of 400-500 m is observed on the incoming crust (Lüschen et al., 2011; Planert et al., 2010). The deformation front in this region along the margin (116.1°E) starts to deviate from the normal trend of the trench (Fig. 1, white stippled line), which has previously been attributed to frontal erosion caused by the subduction of pronounced oceanic basement relief (Kopp et al., 2006). At the location where line BGR06_313 crosses the trench, a ~30 km wide embayment at the lower slope is visible in the seafloor bathymetry (Fig. 2). The frontal prism, as observed on the neighboring line BGR06_311 to the east, is disrupted and features little imbricate structure (Figs. 3b and 5a, profile km 0 to 10). The exact location of the deformation front on the profile is obscured by a steep oceanic basement scarp (around profile km -2) with a vertical throw of ~600 m which is currently entering the subduction system (Fig. 3b).

On the subducting crust, a ~1.3 km height oceanic basement high (Ridge A in Figs. 3b, 5a, Table 2) is found at a depth of 7km and ~1.5 km below the seafloor (Figs. 3b, 5a, profile km 5 to 10) underneath the frontal prism. It coincides with a shallowing of the seafloor by about 1000 m (Fig. 5a), where a local seafloor bulge (profile km 6 to 11) extends laterally in a trench-parallel direction for ~30 km (Fig. 5b, Ridge A). Landslide scars on the trench-ward flank of the seafloor bulge (Fig. 5b) are recognized in the bathymetry map and coincide with the chaotic and discontinuous nature of the shallow sedimentary strata in the frontal prism as described above (Fig. 5a km 0 to 6).

Further downdip, a second subducting basement high (Ridge B) with a height of approximately 1.6 km (Table 2) (Figs. 3b and 5c, profile km 17 – 23) coincides with a seafloor surface slope of 9° (Fig. 5c). Shallow landward dipping normal faults offsetting the seafloor (Fig. 5d) are observed here. The internal reflection pattern of the accretionary wedge is characterized by complex and small-scale reflectors (Fig. 5d).

The décollement, which parallels the oceanic basement reflection further downdip (Fig. 3b, profile km 21 and beyond), deviates from the basement between the two basement highs (Ridges A and B) and trends ~1000 m above the top of the oceanic crust (Fig. 3b, profile km 10-21), migrating upward on the leading flank of Ridge A (Fib. 5a, km 6 to 10). It is characterized by a band of reflectors showing a negative reflection coefficient (Figs. 3b, 5e).

4.3 Profile BGR06_303 - offshore Bali

Profile BGR06_303 is located offshore Bali where the easternmost portion of the Roo Rise with its significant basement relief is currently entering the trench (Segment III in Fig. 2). In the trench, the incoming oceanic basement is blanketed by a sediment cover ranging from 300 m to more than 500 m thickness (Figs. 6a and 7c, km -2 to 0). Landward of the deformation front (Fig. 7c, km 0), the horizontally layered trench sediments form imbricate structures (profile km 0-6), and the original stratigraphy is still recognized in the frontal prism (Fig. 7c). At profile km 6 to 10, the seafloor is uplifted by a subducting basement ridge (Figs. 6a and 7c), also traced in the bathymetry as an 18 km long escarpment (Fig. 7a, in the black polygon). This situation is similar to profile BGR06_313 (Fig. 5a,). The ridge disrupts the stratigraphy of the frontal prism as it is underthrust underneath the lowermost slope. Landward of the subducting ridge, underthrusted sediment is observed with an average thickness of 600 m (Fig. 6a).

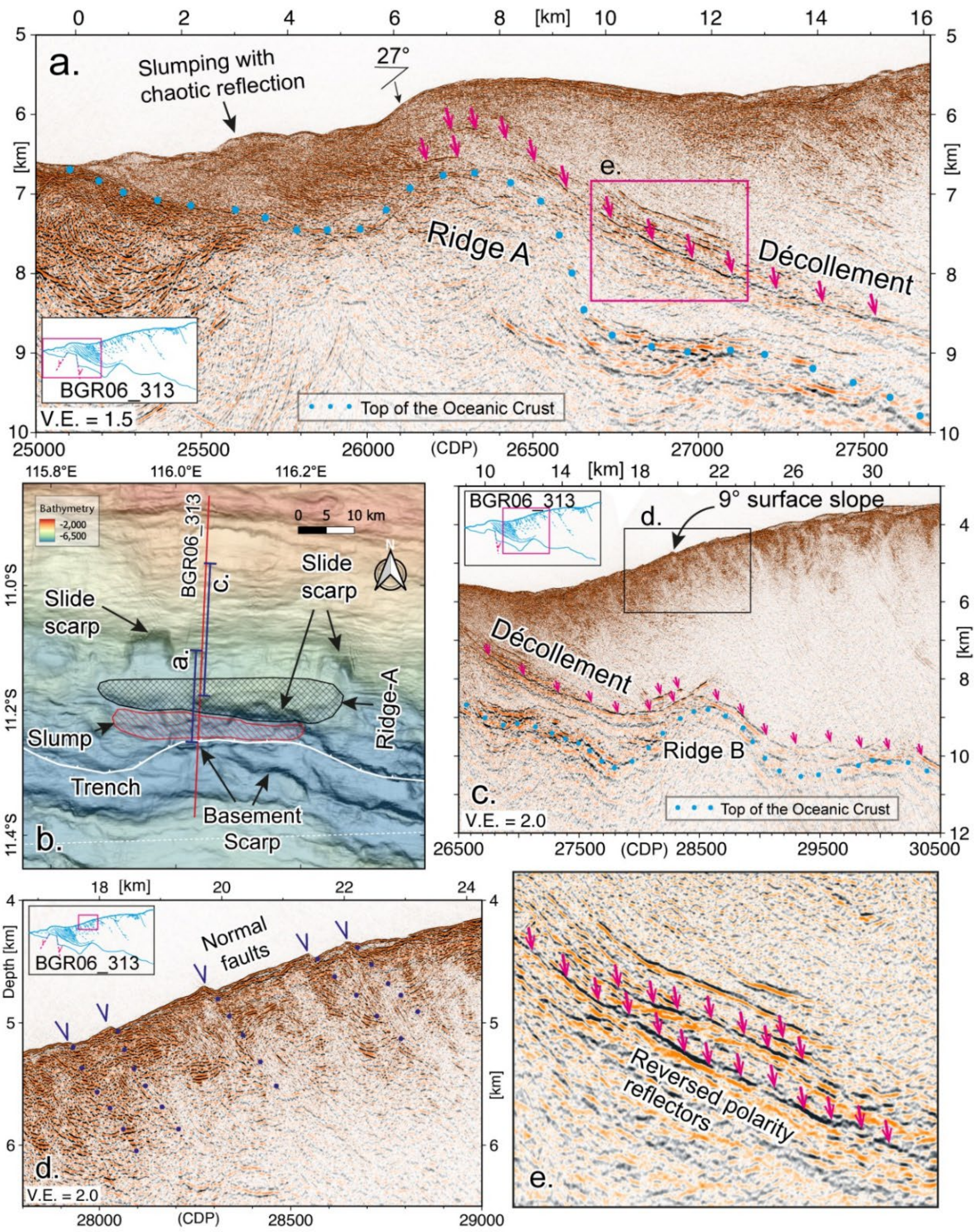

Figure 5 a. Close-up view of subducting Ridge A. Uplift of the upper plate causes a seafloor bulge above the subducting ridge. Mass wasting deposits seaward of Ridge A are characterized by a chaotic internal reflection pattern. b. Upper plate seafloor morphology modulated by subducting ridges offshore Lombok around profile BGR06_313. c. Close-up view of subducting Ridge B. Trend of the décollement indicated by red arrows. Blue dots indicate the oceanic basement. d. Close-up view of the upper plate above Ridge B. Please note that the normal faults (marked by dark blue dots) crop out at the seafloor, indicating recent fault activity. e. Close-up view of the décollement between Ridge A and Ridge B. The reversed polarity reflectors are marked by red arrows.

Above the accretionary wedge, the seafloor features an average slope of 7.6° (Fig. 6a, km 12 to 35) (Table 1). A seafloor slope break at profile km 36-40 corresponds to the surface outcrop of a high-amplitude landward dipping reflector. This reflector reaches the plate interface at ~10 km depth (Fig.

6a). Landward of the slope break, the seafloor slope becomes shallow to horizontal between profile km 38 and 52 (Fig. 6a). The shallow water depth (1500 m) and active thrusting of the accretionary wedge forearc high (most pronounced around profile km 53 and 64), which offsets the seafloor, documents the compressional state of this domain (Fig. 6a, km 50 – 77). The active thrust fault at profile km 51 to 55 is characterized by a reversed polarity (Fig. 7d) compared to the seafloor reflection. The sedimentary strata from km 41 to further landward has been rotated to an angle of ~45° (Fig. 7b).

Underneath the slope break between profile kilometers 30 to 45, a subducting seamount is identified at a depth of 8 km (Fig. 6a). It coincides with a semi-conical bulge in the seafloor bathymetry (Fig. 7a). Landward of the leading flank of the seamount, the décollement lies ~1500 m above the top of the oceanic crust (Figs. 6a, S4, profile km 46 to 62, red dashed line) at a depth of 8 to 12 km. Between the subducted seamount and the ridge (Fig. 6a), the décollement parallels the subducting oceanic basement between km 18 to 30 (Fig. 6a) and is shifted upwards between km 12 and 18 (Fig. 6a). At around profile km 14, the inclination of the décollement is deflected in front of the subducting ridge and steeply trends towards the seafloor, where it crops out at km 8.5. This complex adaptation in the structural level of the décollement is also reflected in the variation of the reflection coefficient (Fig. 6a).

4.4 Profile BGR06_305 - offshore Eastern Java

The westernmost profile of our study locates offshore eastern Java, where the oceanic domain features a large number of seamounts on the Roo Rise plateau (Fig. 1b & Segment III in Fig. 2). The forearc high in this segment reaches a water depth of 750 m and is thus approximately 2000 m shallower than offshore Sumbawa (Table. 1). The northward deflection of the deformation front by about 50 km (Table 1, Fig. 1) has been attributed to frontal subduction erosion due to the impact of oceanic basement relief on the lower slope of the upper plate (Kopp et al., 2006). The incoming plate in the oceanic domain carries ~850 m of well-stratified sediment (Figs. 6b, S5). Oceanic basement and overlying sediments are disrupted by bending induced normal faulting of the oceanic crust as it enters the trench (Fig. 6b, km -10 to 0).

At the deformation front, 40-50% of the sediment is frontally accreted, resulting in imbricate thrusting within the frontal prism (Figs. 6b and 8e, km 0 to 12). Approximately 10-12 km landward of the deformation front, reflectivity decreases, marking the transition from the frontal prism (profile km 0-12) to the mature accretionary wedge (Fig. 6b). The accretionary wedge is dominated by a chaotic reflection pattern of small-scale reflections (Figs. 6b, 8e, profile km 12 – 19) and fine-scale folding (Fig. 8e, profile km 20 – 30). The seafloor surface slope reaches 8.3° (Fig. 6b, km 10 – 30). A distinct slope break at profile km 33 (Figs. 6b, 8d) is associated with a large semi-conical seafloor bulge observed in the bathymetry (smt in Fig. 8c).

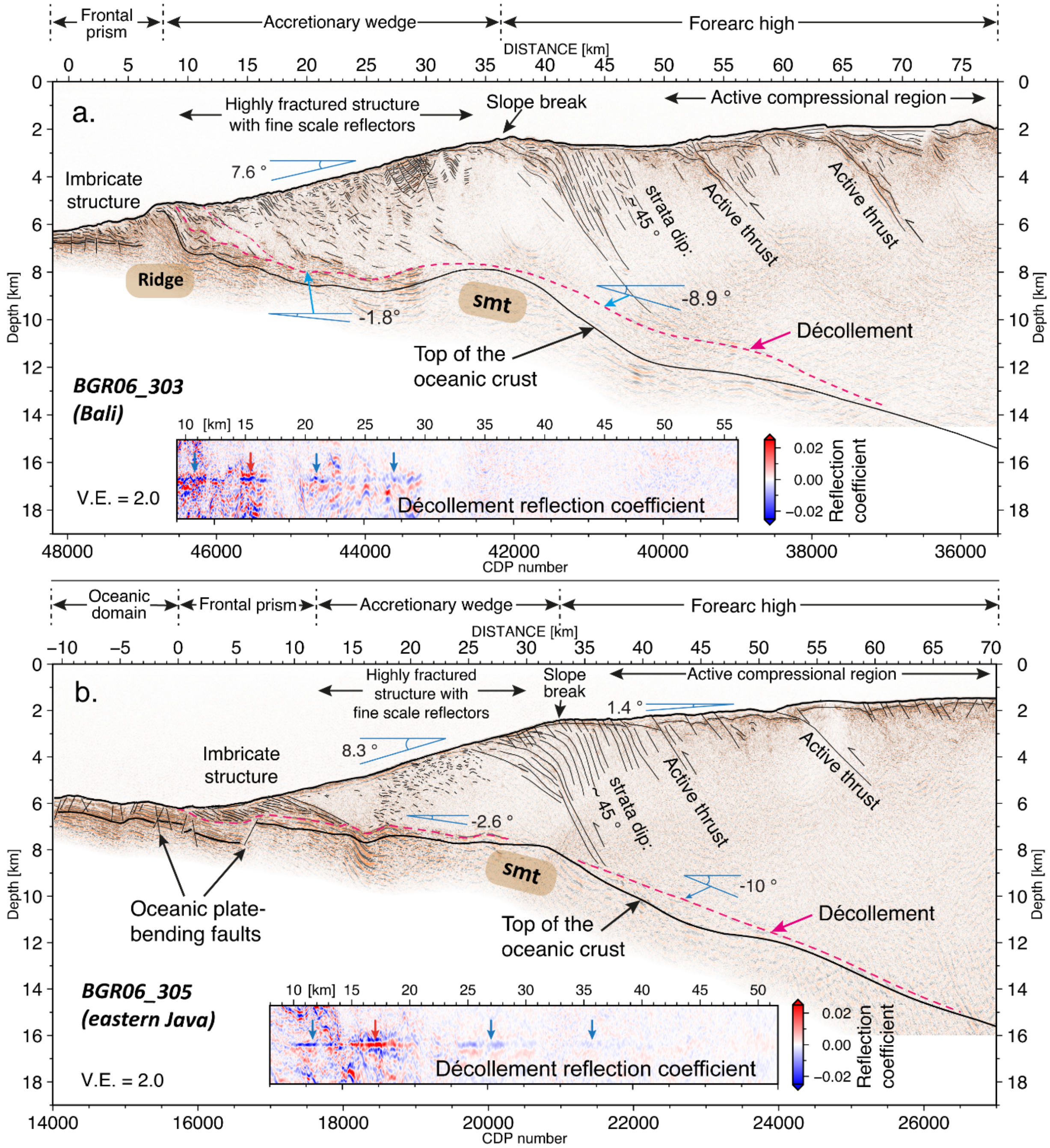

Figure 6 a. MCS depth migration image and the line-drawing of the seismic line BGR06_303 offshore Bali. b. MCS depth migration image and the line-drawing of the seismic line BGR06_305 offshore eastern Java. The reflection coefficient subgraph of horizontally aligned décollement is plotted within each subfigure.

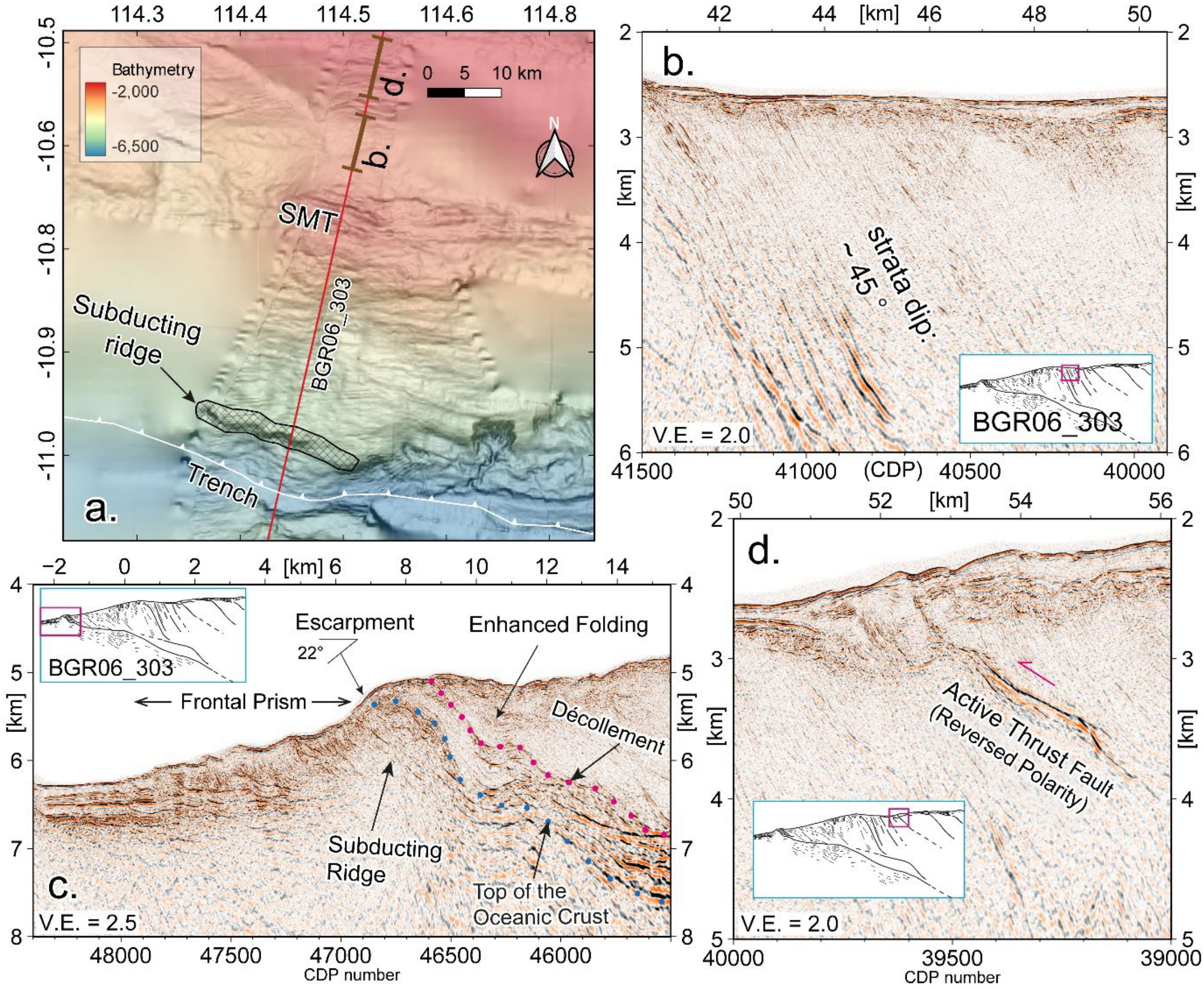

Figure 7 a. Upper plate deformation induced by a subducting oceanic basement topography offshore Bali close to profile BGR06_303. b. Upper plate close-up view of the ~45° dipping reflectors in front of the subducting seamount. c. Close-up view of frontal prism and lower accretionary prism where a subducting basement ridge causes seafloor uplift resulting in a local steep slope angle of 22°. Upper plate deformation in response to the under-thrusting ridge is expressed in enhanced folding in front of the ridge. The décollement is marked by red dots in this panel. d. Close-up view of active thrust fault landward of the seamount. The thrust fault features a reversed polarity wavelet compared to that of the seafloor reflection.

Small-scale, superficial normal faults offset the seafloor (Fig. 8d: black dashed lines) to compensate the extension above the bulge. The bulge coincides with a subducting seamount (Abercrombie et al., 2001; Xia et al., 2021) on the oceanic crust at a depth of about 7.5 km. Profile BGR06_305 cuts the eastern flank of this ~1250 km^2 large seamount (Fig. 8c). The seamount and overlying slope break also mark a change in the dipping angle of the plate interface, which steepens from approximately -2.6° seaward of the slope break to around -10° landward of the seamount (Fig. 6b). The décollement runs parallel to the top of the oceanic crust at depths beyond 12 km (profile km 50 and beyond) but starts to deviate from the oceanic basement at the leading flank of the seamount (Fig. 6b, profile km 35 – 50).

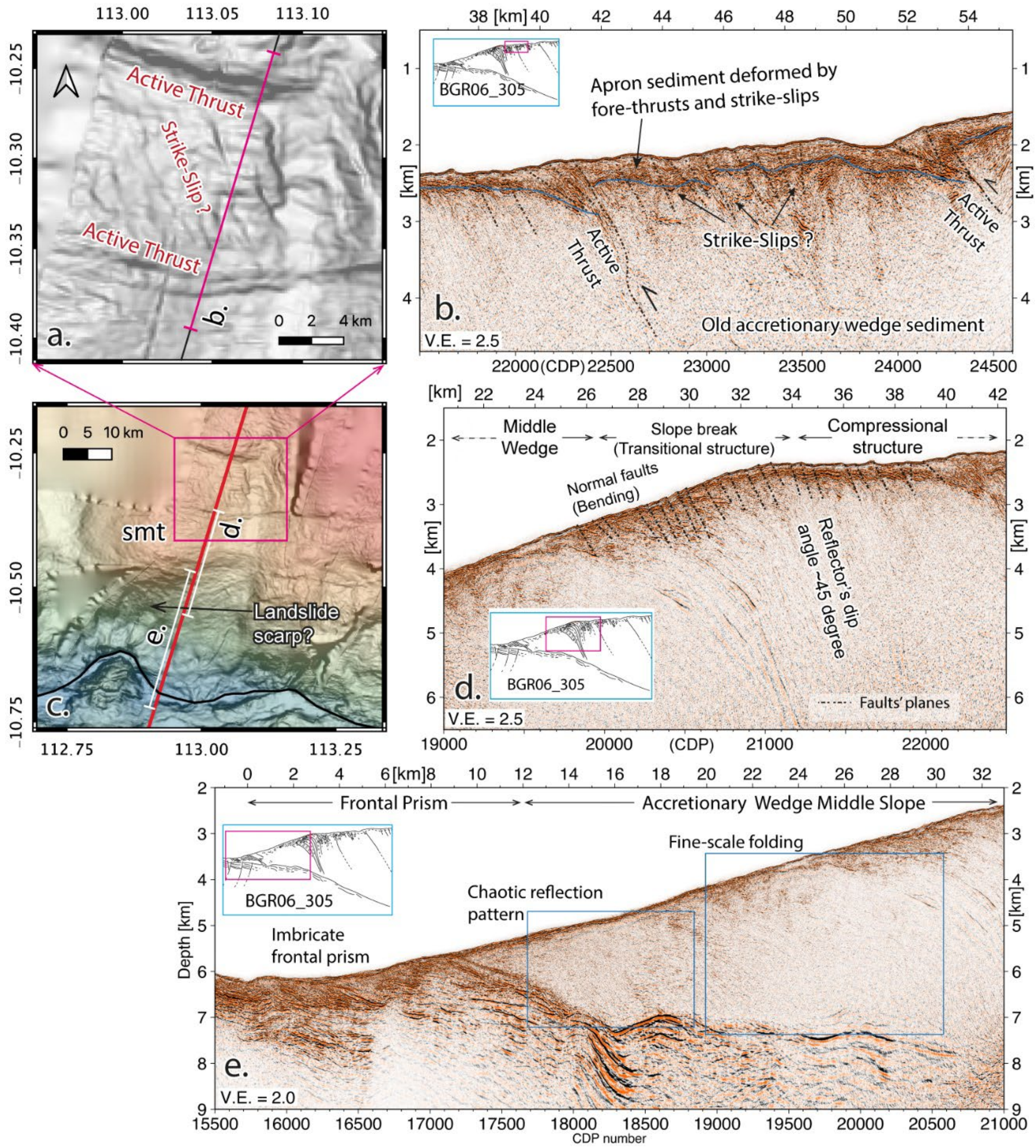

Figure 8 a) Upper plate seafloor morphology landward of subducting seamount offshore eastern Java. Surface traces of thrusts and strike-slip faults are identified in the bathymetry. b) Close-up view of upper plate structures dominated by active thrusting in front of the seamount with a complex pattern of thrust faults and strike-slip faulting. The blue line indicates the basement of the newly deposited apron sediment unit. c) Upper plate seafloor morphology modulated by a subducting seamount adjacent to profile BGR06_305. Seamount subduction induces landslide and mass wasting on its seaward flank. d) Close-up view of the seafloor slope break. Small-scale near-surface normal faults are observed induced by the seafloor curvature, resulting in shallow extension. e. Close-up view of upper plate seismic signatures in the wake of seamount subduction. The chaotic and fine-scale folding reflections dominate the accretionary wedge middle slope. Frontal sediment accretion results in imbricate thrusting of the frontal prism (km 0 - 12).

5 Discussion

Above the seamount and on its landward side (km 33 – 40), the internal reflectors of the accretionary wedge and forearc high feature a coherent structure with steep dipping angles of about 45° (Fig. 6b). A prominent reflector offsets the seafloor at the slope break and cuts through the accretionary wedge down to the plate interface at 9 km depth (Fig. 6b). Further landward, we observe seafloor perturbations in both the seismic data (Fig. 8b) and the bathymetry (Fig. 8a, c). Two thrust faults are actively deforming the uppermost sedimentary unit (Fig. 8a, b), flanked by numerous minor fault planes for which the stress mechanism is not unambiguously discernible from the seismic image (Fig. 8b). On the bathymetry map, these faults feature an oblique orientation of 45° with respect to the strike of the fore-thrusts (Fig. 8a).

Although oceanic relief subduction is observed in many subduction zones (e.g., Bangs et al., 2006; Bell et al., 2010; Tréhu et al., 2012), the comparatively thin oceanic sediment layer (< 1000 m) along the Java margin in combination with the significant accretionary wedge (ranging from 700 - 1000 km^2 per arc length) make this area unique, as oceanic basement relief is observed to breach the oceanic sediment cover to come into direct contact with the upper plate. This setting provides the opportunity to study the impact of basement relief of different scales on the deformation of the upper plate, the forearc mass balance, and the development of the décollement.

The four multi-channel seismic profiles presented in this study illustrate distinctly different subducting oceanic basement features, ranging from large-scale offshore eastern Java (~40 km wide seamounts, > 2.5 km high) to moderate-scale offshore Bali (20-25 km wide seamounts, > 2 km high) to subducting ridges off Lombok (4-7 km wide, > 1 km high) (Table 2). The easternmost profile offshore Sumbawa shows no significant subducting relief but only minor bending fault scarps (< 150 m) and therefore serves as a reference line for the purpose of this discussion. Accordingly, the upper plate structure as well as the trend of the décollement at depth vary between these profiles, documenting the impact of seafloor relief subduction at different scales and different stages of subduction.

5.1 Response of the marine forearc to oceanic basement relief subduction

The subducting oceanic basement relief exerts a first-order control on the seafloor surface slope. Across the accretionary wedge, the seafloor slope increases from 5° offshore Sumbawa to 7.6° offshore Bali and then 8.3° offshore Java (Table. 1). This coincides with the increasing size of the subducted basement features and is particularly evident for the Java and Bali profiles (BGR06_305 and BGR06_303), where large to moderate scale seamounts (scale length along the dip: 20 – 40 km, height > 2 km) of the Roo

Rise push into the wedge (Fig. 1) and the water depth of the forearc high is much shallower (~1000 m) compared to the eastern profiles.

5.1.1 Arc-ward retreat of the trench offshore central Java to Lombok

While the volume and the elevation of the forearc high diminish along the arc from west to east (Table 1) in relation to the decreasing amount of incoming sediment in the trench, the seaward portion of the forearc encompassing the frontal prism and accretionary wedge shows an opposite trend and increases in size (Fig. 1) (Table 1). The seafloor slope break marks the transition from the actively accreting frontal prism and accretionary wedge to the older and fossil forearc (Fig. 2c) On the easternmost profile offshore Sumbawa (BGR06_311), the slope break is located ~43 km from the deformation front (Fig. 3a) and marks a decrease in seafloor slope in the landward direction. Along the Lombok profile (BGR06_313), where relief with smaller scale is currently entering the subduction zone, the slope break is found at a similar distance (42-43 km) (Fig. 3b; see also Fig. 7 in Lüschen et al., 2011). Towards the west, the slope break develops at a distance of ~37 km on the Bali profile (BGR06_303) and at ~32 km on the Java line (BGR06_305) (Fig. 6). This trend coincides with the northward deflection of the deformation front west of 115°E (Fig. 1) and documents the erosive impact of the subducting seamounts on the frontal prism and accretionary wedge of the forearc, decreasing the distance between the deformation front and the slope break (Table 1).

Profile BGR06_305 locates at the central part of the 25,000 km^2 broad region of trench retreat (Fig. 1) and the subsurface structure of this line sheds light on its relation to the along-strike variation of subduction erosion. The northward deflection of the deformation front is mirrored in a similar curved trend of the forearc high's northern boundary, as indicated in the bathymetry data (Fig. S6). Conventionally, a plate margin experiencing significant subduction erosion should not only feature a large trench retreat in the arc-ward direction, as recognized for central Java but also a substantial narrowing and thinning in the middle wedge (Scholl and von Huene, 2007). This is not observed for the Java case, where the marine forearc high is thicker and shallower compared to the surrounding areas (e.g. Shulgin et al., 2011) (Fig. 1). This observation raises the question to what extent is the arc-ward retreat of the trench induced by 1) frontal subduction erosion related to seamount or ridge subduction as discussed above and by 2) trench-normal displacement and translation of the accretionary wedge and forearc high due to the collision and 'pushing' of the numerous large seamounts spanning over the Roo Rise. Distinctively, compared to the profiles BGR06_313 and BGR06_311 off Bali and Lombok, which are located at the eastern portion of the retreating segment, the structural image of line BGR06_305 does not present a larger volume of eroded or underthrusting material in the frontal part of the accretionary wedge (Fig. 6b), indicating that frontal erosion is not the sole contribution to the trench retreat and that the northward pushing of the Roo Rise into the forearc must be considered as an additional effect to explain the arcward deflection of the deformation front as well as of the wedge's northern boundary (Fig. S6).

The structural variations between the four seismic lines further support this concept. A distinct back-thrusting fault, which offsets the northern edge of the forearc high and overlying sediment unit (Xia et al., 2021) at the transition into the forearc basin, is coincidently observed where the maximum arc-ward deflection (50 km) occurs off central Java (profile BGR06_305). Similar back-thrusting is absent in the other profiles off Bali, Lombok, and Sumbawa. This indicates a much stronger regional compressional stress across the forearc high off central Java, likely induced by the pushing of the Roo Rise and its seamounts spanning a distance of over 600 km along the strike of the trench.

5.1.2 Effects of seamount subduction on the surface slope and deformation of accretionary wedge

The two western seismic profiles image the consequences of seamount subduction on the stratigraphy of the accretionary wedge. Above and landward of the seamounts' leading flanks, the sedimentary strata are rotated to steep angles of ~45° (Fig. 6a, b) as they are integrated into the mature portion of the forearc. In front of the largest subducting seamount observed on profiles BGR06_305 and BGR06_303, active fore-thrusts are observed in both the seismic section and the bathymetry map (Figs. 6a and b). They cause offsets between 100 -300 m in the recent sediment apron, increasing to ~500 m in the older accreted sediment (Figs. 6b, 8b). During seamount subduction, its frontal flank pushed the accretionary wedge material landward, and led to the shortening and thickening of the wedge (Fig. 9 d-f). This is documented by the much shallower water depth (< 1600 m) of the forearc high on the eastern Java and Bali profiles compared to the forearc high elevation (> 2300 m) to the east (Table 1) (Fig. 1) as well as by the steeper seafloor slope. The active fore-thrusts, which offset the most recent sedimentary unit and the older accreted material below, result from the thickening and shortening above the seamount's leading flank.

In addition to the active fore-thrusts, the bathymetry map (Fig. 8a) and seismic section (Fig. 8b) document a network of minor fault planes above the subducted seamount offshore eastern Java. These faults trend at an angle of ~45° with respect to the active thrusts (Fig. 8a). We interpret them as strike-slip faults resulting as an expression of the modified stress field in the immediate vicinity of the subducted seamount (Wang and Bilek, 2010). A similar fault pattern has been described for Bennett Knoll on the Hikurangi margin (Davidson et al., 2020). Our seismic line and the seafloor mapping cover only the eastern seamount flank (Fig. 8c), where the structure of the upper plate indicates a complex history of deformation, shortening and thickening of the accretionary wedge in a spatially and temporally evolving stress field around the subducting seamount. A symmetrical pattern including the combination of local strike-slip faults and larger scale thrust faults would also be expected on the seamount's western flank, where bathymetry data are lacking.

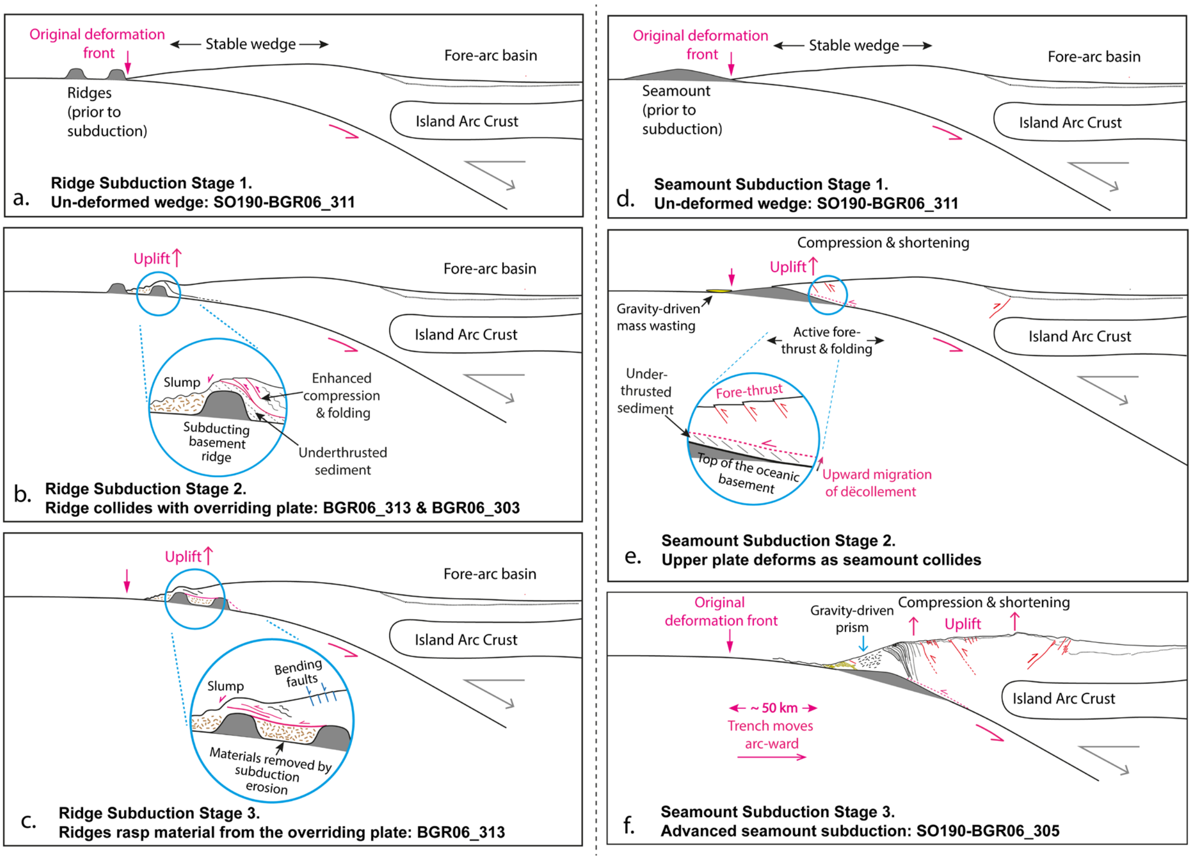

Figure 9. Conceptual sketch of oceanic relief/seamount subduction and associated upper plate deformation showing individual stages of a subducting ridge or seamount. a) Incipient ridge subduction underneath a stable accretionary wedge. b) Under-thrusting of the ridge acts as strong teeth and causes uplift and fracturing of the frontal prism. Fractured materials are deposited in the valley at the trailing side of the ridge. c) The slumping deposit are transported into greater depth as oceanic plate subducts. d) Incipient seamount subduction underneath a stable accretionary wedge. e) Seamount under-thrusting causes uplift of the upper plate in front of the seamount. Please note the adjustment of the structural level of décollement in front of seamount and compression and shortening of the lower slope. f) Compression and uplift are compensated by fore-thrusts and folding on the seaward side of the prism and by back-thrusting at the transition to the forearc basin. Note that the long-term gravity-driven mass wasting in the wake of relief subduction results in a steep surface slope and a chaotic reflection pattern in the accretionary wedge.

At the trailing side of a large-moderate size seamount (e.g., in BGR06_305), an over-steepened surface slope (8.3°, Table 1) and a shallow basal dip (2.6°, Fig. 6b) are observed. This geometry observation follows the prediction of the classic Coulomb wedge model, which implies a tendency for gravitational collapsing of the overriding plate since the taper geometry is over-critical due to the rotation by the seamount subduction at the trailing flank (Dahlen, 1984; Lallemand and Le Pichon, 1987). Theoretically, the over-steepened surface slope and the shallow basal dip will result in a significant gravitation-driven extensional deformation all over the upper plate at the seamount's trailing edge, given the low strength of the megathrust (Gao et al., 2014). The gravity force overcomes the basal shear and leads to pervasive brittle/plastic yielding, and the state of the stress within such a wedge should have the same orientation everywhere (Dahlen, 1984). Evidence of such gravitational collapsing at the seamount's trailing side has been verified in MCS profiles with subducting seamount in North-Ecuadorian margins (Fig. 4b in Marcaillou et al., 2016). However, a discrepancy between our geophysical observation and this concept exists. A dilemma emerges immediately: no widely distributed normal fault nor listric fault is observed at this over-steepened middle wedge. Instead, internal structures of this steep wedge taper revealed in lines BGR06_305 and BGR06_303 show intense compressional signatures, like the chaotic and very fine-scale reflectors over the middle wedge at the seamount trailing side (e.g., in BGR06_305, Fig. 8eb, km 12 - 30). Only minor normal faults are observed at the surface slope break (Fig. 8d, km 24 - 38).

Perhaps these geophysical observations may not be so paradoxical if we consider a continuous and progressive evolution of the upper plate rather than a transient snapshot of its 850 ka long-term deformation history (e.g., the seamount in BGR06_305 has subducted for 850 ka given a convergent rate of 67 mm/yr). On the one hand, compressional debris piles with chaotic reflection signatures are always a characteristic at the toe domain of a single submarine landslide, and the normal fault scarp is only observable at the landslide's headwall domain (Scarselli, 2020). On the other hand, this normal fault scarp at the slide's headwall will immediately be destructed and smeared by the next gravitational slide which will occur (Ruh, 2016) when the seamount subducts deeper. The topographic responses to these episodic slides are the normal faults scarps at the head wall, which are transient, re-constructed, and covered by numerous slide episodes over this seamount's 850 ka subduction history. In contrast, the compressional structural signature at the toe domain of the slide is perpetually preserved over time (Ruh, 2016). Moreover, the upper plate's tectonic response and topographic expression by the subducting seamount are particularly significant when the seamount is in an early stage of collision close to the trench but will diminish progressively and eventually perish when the seamount reaches a greater depth (e.g., Fig. 4 e-h in Ruh et al., 2016). In the end, only minor surface responses (e.g., normal fault scarps) are preserved locally above the seamount's top, before the seamount is fully covered by overriding sediment sequences.

The seamounts and basement highs at the early stage of the subduction (e.g., Ridge A in BGR06_313 in this study, and seamount in the North-Ecuadorian margin, Marcaillou et al., 2016) may result in extensive normal faulting and gravitational collapse at their trailing edges, when the sediment does not completely bury the seamounts (Ruh, 2016). However, given the convergence rate of the plate margin in Java (67 mm/yr) and its crest distance to the trench (average 31 km), the seamount observed in BGR06_305 is not any more at its infant stage of collision. As a consequence of the long-term history of seamount subduction (850 ka) on line BGR06_305 resulting in a series of mass movements over the trailing edge, the stratigraphy above the trailing edge of the seamount is highly disrupted or completely destroyed, resulting in a chaotic reflection pattern dominated by short reflectors (Figs. 6g and 8e, km 12 to 30).

The subducting relief with a large aspect ratio (height/width ~ 0.2 to 0.3) as expressed e.g. in Ridges A and B on the Lombok profile (BGR06_313, Fig. 3b) are characterized by much steeper flanks than the larger subducting seamounts on the Java and Bali profiles (BGR06_305 and BGR06_303). Deformation in response to the subduction of large aspect ratio features is expressed in intense folding ahead and above the ridge (e.g. Fig. 3a, km 9-17), documenting the uplift, deformation and compression of the sedimentary strata that was formerly composing the frontal prism. Ridge A in profile BGR06_313 shows a local slope of 27° at its trailing edge (Fig. 5a, km ~6), hosting slumps with chaotic reflection patterns (Fig 5a, km 0 to 6). Comparable mass wasting is not observed on the Java and Bali lines (Fig. 6a,b). This observation indicates that the higher aspect ratio (height/width ~ 0.28 for Ridge A) of the moderate scale basement relief (width of Ridge A < 10 km compared to tens of km for the subducting seamounts) results in enhanced gravitational collapse at the trailing edge. Furthermore, the relief on BGR06_313 is at an early stage of subduction compared to the seamounts offshore Java and Bali, which are observed at a greater depth so that some ‘healing’ of the lower slope may already have occurred.

In contrast to the three profiles to the west imaging oceanic relief subduction at large to moderate scales, the fourth line offshore Sumbawa (BGR06_311; Fig. 3a) shows no comparable subducting structures. Here, the trend of the top of the oceanic basement is only altered by plate-bending induced normal faults, resulting in a small-scale (1-2 km width) segmentation of the subducting oceanic crust with fault throws less than 150 m close to the trench to less than 600 m below the accretionary wedge (Fig. 3a). The décollement is able to develop as a spatially continuous feature above the subducting topography, and subducted sediment is observed between the décollement and the top of the oceanic crust (see below). Overall, this profile documents a history of sediment accretion and a stable surface slope of the accretionary wedge not disrupted by significant subducting oceanic basement relief.

5.1.3 The evolution of the décollement

The subduction of different seafloor topography along the three western profiles (BGR06_305, BGR06_303, BGR06_313) modifies the structural level of the active décollement. In contrast, along the eastern profile BGR06_311, the décollement is spatially continuous and shows a reversed polarity (Fig. 3a) and negative reflection coefficient, resulting from a negative impedance contrast indicating juxtaposition of densified, accreted material to underthrusted sediment. The décollement marks the top of a 170 m thick unit of subducting sediment, smoothing the smaller scale undulations (< 150 m) of the basement (Fig. 3a). This implies that lower plate topography is not in direct contact with the upper plate.

The décollement follows the long-wavelength trend of the subducting slab, and does not substantially deviate from the top of the oceanic basement (Fig. 3a).

This pattern changes substantially along the neighbouring Lombok line (BGR06_313), where Ridges A and B cause undulations in the basement topography by more than 1.5 km in height over spatial width of less than 7 km (Fig. 3b). The décollement is clearly identified by its negative reflection coefficient (Fig. 3b), caused by the negative impedance contrast to the subducting sediment unit underneath. Landward of Ridge B (Fig. 3b) the décollement starts to diverge from the top of the oceanic crust (profile km 32), migrates upwards and follows a shallower trend. This effect is enhanced between Ridges A and B, where the décollement may be traced ~1.5 km above the top of the oceanic crust.

On line BGR06_303 offshore Bali, the subducted seamount produces undulations in the basement trend where the basement angle changes significantly over short distances from 1.8° to 8.9° (Fig. 6a). This induces a shallowing of the décollement landward of the leading edge of the subducted seamount (around profile km 45 - 65 in Fig. 6a). The décollement reflection amplitude is very weak beyond profile km 35 (Fig. 6a), but we deliberately chose not to apply a stronger gain control in order not to heavily manipulate the amplitudes. The décollement may be traced ~1.5 km above the top of the oceanic crust but deepens again on the trailing flank of the seamount, where it lies less than 500 m above the basement. Further towards the trench, where the basement topography is once more disrupted by a subducted ridge (Fig. 6a, km 5 - 10), the décollement again deviates from the oceanic crust starting at profile km 18 and dissects the seafloor ~8.5 km and ~12 km landward of the deformation front.

The Java profile (BGR06_305) images the largest seamount in our study, but the aspect ratio and hence the changes in subducting basement topography are smaller than on the other lines (Fig. 6b). At the leading edge of the seamount, the décollement trends ~1.2 km above the oceanic basement, and can unambiguously be identified by its negative, however weak, reflection coefficient here (Fig. 6b). Seaward of the seamount, the reflection coefficient of the décollement alternates between positive and negative values, reflecting the impedance contrast between the frontally accreted material in the frontal prism and the underthrust portion of the trench infill (Fig. 8e, km 15 - 20).

5.2 Subduction erosion and implications for wedge strength

5.2.1. Subduction erosion offshore Java-Lombok

The adjustment of the structural level of the décollement has important implications for the mass balance of the forearc. Where the décollement pinches out against subducting topographic features, this enhances localized subduction erosion by removing material from the base of the accretionary wedge (Ballance et al., 1989; Clift and Vannucchi, 2004; Lallemand and Le Pichon, 1987; von Huene and

Scholl, 1991). Ballance et al. (1989) documented the impact of subducting relief on the overriding plate, where the fracturing and thus weakening of arc upper plate rocks resulted in collapse into the grabens of the downthrusting basement. Commonly, geophysical evidence from multi-channel seismic data related to this process is rarely documented (von Huene et al., 2004), due to the limited depth resolution or insufficient horst height. In our study, profile BGR06_313 offshore Lombok images the trapping of material in the wake of ridge subduction resulting from high-stress physical abrasion (Figs. 3b and 5a, also refer to Fig. 4 in Balance et al. 1989, and refer to Fig. 3c, d in Hilde, 1983). The basement ridges (e.g., Ridge A offshore Lombok) feature a high aspect ratio and substantial height (> 1km, Table 2, Fig. 3b), causing fractures, uplift and compressional deformation of the accreted sediment when the ridge's leading flank collides with the tip of the upper plate. As the ridge subducts further, gravitational collapse and slumping at the trailing side disintegrates the accreted sequences (e.g., the under-thrusted sediment between distance km 9 to 21 seaward of Ridge B in Fig. 3b). The disintegrated material is deposited in the protected shadow behind the ridge, in the accommodation space of the graben to the next ridge further updip (Fig. 9 a-c).

Intriguingly, the absolute height/offset of Ridges A and B (1300 – 1600 m) (Fig. 3b, Table 2) is larger than for any of the oceanic ridges (800 – 900 m) observed on the oceanic crust (Fig. 1c). We suggest that this effect is related to the oceanic plate bending as the basement scarps in the trench feature an intermediate offset value of 1000 to 1200 m (Fig. 5b).

The erosional impact of the large conical shape seamounts on lines BGR06_303 and BGR06_305, which feature a significantly lower aspect ratio than the ridges on line BGR06_313 (Table 1) is foremost documented in the re-entrant scars and embayments observed in the bathymetry data (Figs. 1 and 2). In addition to the material removal at the deformation front, Ballance et al. (1989) anticipated an elevated plate boundary in front of subducting seamounts, resulting in enhanced basal erosion. In our data, lines BGR06_303 and BGR06_305 document this deflection of the décollement which may clearly be discriminated from the top of the oceanic crust in front of the seamount (Fig. 6a, b). As a result, sediment subduction and subduction erosion along the Java-Lesser Sunda margin associated with seamount and ridge subduction remove significant volumes of upper plate material to greater depth (Scholl and von Huene, 2007).

5.2.2 Subduction erosion observed at other convergent margins

Similar observations as presented above are also documented in modern MCS surveys at other plate margins, including Costa Rica (Fig. 2 in Edwards et al., 2018) and Japan (Fig. 1c in Chester et al., 2013), where the décollement steps up into the sediment layers in response to changing oceanic basement topography.

These observations are augmented by numerical modeling studies that reveal similar seamount-related basal erosion phenomena under specified boundary conditions. In the study of Morgan and Bangs (2017), stepping up of the décollement close to the subducting seamount *only* happens when weak horizons exist within accreting strata, and thus deeper strata are protected from vertical partitioning. Similar up-stepping of the décollement is also observed above a subducting seamount in the 3D modeling of Ruh (2016), and a weak upper plate, with an effective internal friction coefficient of 0.14 to 0.23, is predefined in all his models.

A weak upper plate is also testified and proved in Integrated Ocean Drilling Program (IODP) sample from Costa Rica and Japan. In Costa Rica, offshore the Osa Penisula, weak clay layers with an internal friction coefficient of 0.2, which is much lower than assumed in Byerlee's law (0.6 to 0.85) (1978), are sampled in the IODP Exp 334 and examined by a shear-friction testing experiment (Namiki et al., 2014). During the Japan Trench Fast Drilling Project (JFAST), similar low shear strength (< 0.2) rocks near and above the décollement zone are substantiated by the friction experiment in all slipping velocity ranges (10 µm s^{-1} to 3.5m s^{-1}) (Remitti et al., 2015; Ujiie et al., 2013).

Though drilling information is lacking for the Java margin, we still anticipate weak upper plate material from previous Coulomb wedge studies (Dahlen, 1984; Davis and von Huene, 1987; Kopp and Kukowski, 2003). Based on the proto-thrust geometry at the deformation front, the surface slope, and the basal dip measured from an MCS profile offshore western Java close to the Sunda Strait, Kopp and Kukowski (2003) derived a weak upper plate internal friction coefficient (0.29), a moderate upper plate fluid pressure ratio (0.46), and a resultant low effective strength of the upper plate of 0.13 in the accretionary wedge. Though the MCS profile in Kopp and Kukowski (2003) locates approximately 600 to 700 km west of this study, we would expect comparable physical properties of the frontal prism and accretionary wedge material as these two regions share a similar history and a sediment supply (McNeill et al., 2017). Such weak sedimentary rocks may thus facilitate the wearing and erosion of the upper plate material by the subduction of rigid oceanic basement scarps, and the up-stepping (migration) of the décollement in scenarios with seamount or ridge subduction.

6 Conclusions

1) From the bathymetry and MCS surveys in the eastern Java margin, distinct oceanic relief is observed: 1) on the oceanic seafloor prior to subduction, and 2) being subducted underneath the overriding plate on the submerged plate interface. Along the margin strike, these oceanic

basement highs feature a large diversity in scales and shapes, including large conical seamounts (diameter up to 40 km), high aspect ratio linear-shape ridges (height/width > 0.25), and oceanic plate bending normal faults with small offsets (vertical throw < 150 m).

2) The larger seamounts and linear ridges, breach the relatively thin sediment cover (< 500 m) on the oceanic crust. Upon collision with the upper plate and subsequent subduction, they deform and fracture the frontal prism and accretionary wedge, modify the seafloor level and surface slope, and permanently erode accreted material by transporting it to greater depth. Subduction erosion caused by underthrusting seamounts is manifested in the up-stepping of the décollement within the accretionary wedge on both the leading and trailing sides of the seamount.

3) In the accretionary wedge of the outer marine forearc, structural impacts from subducting seamounts and ridges share similar patterns in the MCS profiles and might share as well a scale-independent deformation mechanism. Enhanced compression, including active thrust-faulting and folding, is observed at the subducting relief's leading edges to compensate the change of the basal dip and the shortening at the seaward side of the wedge following the theoretical prediction from the Coulomb Wedge. In contrast, at the trailing edge of the relief, the overriding plate features a structureless reflection signature. This pattern likely results from numerous gravitational slumps at the relief's trailing side in its long-term subduction history until they are fully buried by the overriding sediment sequence.

4) Whether the different scales of oceanic relief will lead to a substantial structural response on the upper plate depends on whether or not the height of the relief is larger than the thickness of the pelagic and terrestrial sediment on the oceanic plate prior to subduction. For example, underneath the frontal part of the accretionary wedge offshore Sumbawa (BGR06_311) , small bending fault scarps (<150 m) are smoothed by the 170 m thick under-thrusting sediment. From bathymetryl and subsurface observations, no indication of severe upper plate deformation by the oceanic bending fault scarps is observed off Sumbawa.

Authors contributions. YX and DK performed the computations and are responsible for the main processing. MS made the data available and was responsible for the navigation and geometry processing. YX, HK and JG wrote the article, and all authors contributed equally to proofreading and final preparation of the manuscript.

Competing interest. The authors declare that they have no competing interests.

Acknowledgments. Y. Xia acknowledges funding from the China Scholarship Council (grant 201506400067). R/V SONNE cruise SO190 and the SINDBAD project were funded by the German Federal Ministry of Education and Research (BMBF) under grants 03G0190A and 03G0190B. The seismic data were processed with Schlumberger's Omega2 seismic processing suite OMEGA and Seismic Unix - open-source software package for seismic research and processing, Center for Wave Phenomena, Colorado School of Mines. Bathymetry and seismic images are plotted by the Generic Mapping Tools (GMT) and QGIS.

Data Availability Statement. Bathymetric data from R/V SONNE cruise SO190 can be requested through the German Bundesamt für Seeschifffahrt und Hydrographie (BSH; http://www.bsh.de). Seismic reflection lines BGR06_311, BGR06_313, BGR06_303, and BGR06_305 are available upon reasonable request.

References

Abercrombie, R.E., Antolik, M., Felzer, K., Ekstrom, G., Ekström, G., 2001. The 1994 Java tsunami earthquake: Slip over a subducting seamount. J. Geophys. Res. Solid Earth 106, 6595–6607. https://doi.org/10.1029/2000jb900403

Ballance, P.F., Scholl, D.W., Vallier, T.L., Stevenson, A.J., Ryan, H., Herzer, R.H., 1989. Subduction of a Late Cretaceous Seamount of the Louisville Ridge at the Tonga Trench: A model of normal and accelerated tectonic erosion. Tectonics 8, 953–962. https://doi.org/10.1029/TC008i005p00953

Bangs, N.L.B., Gulick, S.P.S., Shipley, T.H., 2006. Seamount subduction erosion in the Nankai Trough and its potential impact on the seismogenic zone. Geology. https://doi.org/10.1130/G22451.1

Barker, D.H.N., Henrys, S., Caratori Tontini, F., Barnes, P.M., Bassett, D., Todd, E., Wallace, L., 2018. Geophysical Constraints on the Relationship Between Seamount Subduction, Slow Slip, and Tremor at the North Hikurangi Subduction Zone, New Zealand. Geophys. Res. Lett. 45, 12,804-12,813. https://doi.org/10.1029/2018GL080259

Bell, R., Holden, C., Power, W., Wang, X., Downes, G., 2014. Hikurangi margin tsunami earthquake generated by slow seismic rupture over a subducted seamount. Earth Planet. Sci. Lett. 397, 1–9. https://doi.org/10.1016/j.epsl.2014.04.005

Bell, R., Sutherland, R., Barker, D.H.N., Henrys, S., Bannister, S., Wallace, L., Beavan, J., 2010. Seismic reflection character of the Hikurangi subduction interface, New Zealand, in the region of repeated Gisborne slow slip events. Geophys. J. Int. 180, 34–48. https://doi.org/10.1111/j.1365-246X.2009.04401.x

Bilek, S.L., Engdahl, E.R., 2007. Rupture characterization and aftershock relocations for the 1994 and 2006 tsunami earthquakes in the Java subduction zone. Geophys. Res. Lett. 34, L20311. https://doi.org/10.1029/2007GL031357

Bock, Y., Prawirodirdjo, L., Genrich, J.F., Stevens, C.W., McCaffrey, R., Subarya, C., Puntodewo, S.S.O., Calais, E., 2003. Crustal motion in Indonesia from Global Positioning System measurements. J. Geophys. Res. Earth 108. https://doi.org/10.1029/2001jb000324

Bonnet, G., Agard, P., Angiboust, S., Fournier, M., Omrani, J., 2019. No large earthquakes in fully exposed subducted seamount. Geology 47, 407–410. https://doi.org/10.1130/G45564.1

Byerlee, J., 1978. Friction of rocks. Pure Appl. Geophys. PAGEOPH 116, 615–626. https://doi.org/10.1007/BF00876528

Caress, D.W., Chayes, D.N., 1996. Improved processing of Hydrosweep DS multibeam data on the R/V Maurice Ewing. Mar. Geophys. Res. 18, 631–650. https://doi.org/10.1007/BF00313878

Chesley, C., Naif, S., Key, K., Bassett, D., 2021. Fluid-rich subducting topography generates anomalous forearc porosity. Nature 595, 255–260. https://doi.org/10.1038/s41586-021-03619-8

Chester, F.M., Rowe, C., Ujiie, K., Kirkpatrick, J., Regalla, C., Remitti, F., Moore, J.C., Toy, V., Wolfson-Schwehr, M., Bose, S., Kameda, J., Mori, J.J., Brodsky, E.E., Eguchi, N., Toczko, S., 2013. Structure and Composition of the Plate-Boundary Slip Zone for the 2011 Tohoku-Oki Earthquake. Science (80-.). 342, 1208–1211. https://doi.org/10.1126/science.1243719

Clift, P., Vannucchi, P., 2004. Controls on tectonic accretion versus erosion in subduction zones: Implications for the origin and recycling of the continental crust. Rev. Geophys. 42. https://doi.org/10.1029/2003rg000127

Cloos, M., 1992. THRUST-TYPE SUBDUCTION-ZONE EARTHQUAKES AND SEAMOUNT ASPERITIES - A PHYSICAL MODEL FOR SEISMIC RUPTURE. Geology 20, 601–604. https://doi.org/10.1130/0091-7613(1992)020<0601:Ttszea>2.3.Co;2

Cloos, M., Shreve, R.L., 1996. Shear-zone thickness and the seismicity of Chilean- and Marianas-type subduction zones. Geology 24, 107–110. https://doi.org/10.1130/0091-7613(1996)024<0107:SZTATS>2.3.CO;2

Dahlen, F.A., 1984. Noncohesive Critical Coulomb Wedges: an Exact Solution. J. Geophys. Res. 89, 10125–10133. https://doi.org/10.1029/JB089iB12p10125

Davidson, S.R., Barnes, P.M., Pettinga, J.R., Nicol, A., Mountjoy, J.J., Henrys, S.A., 2020. Conjugate strike-slip faulting across a subduction front driven by incipient seamount subduction. Geology 48, 493–498. https://doi.org/10.1130/G47154.1

Davis, D.M., von Huene, R., 1987. Inferences on sediment strength and fault friction from structures at the Aleutian Trench. Geology 15, 517. https://doi.org/10.1130/0091-7613(1987)15<517:IOSSAF>2.0.CO;2

Dominguez, S., Lallemand, S.E., Malavieille, J., Von Huene, R., 1998. Upper plate deformation associated with seamount subduction. Tectonophysics 293, 207–224. https://doi.org/10.1016/S0040-1951(98)00086-9

Edwards, J.H., Kluesner, J.W., Silver, E.A., Brodsky, E.E., Brothers, D.S., Bangs, N.L., Kirkpatrick, J.D., Wood, R., Okamoto, K., 2018. Corrugated megathrust revealed offshore from Costa Rica. Nat. Geosci. 11, 197–202. https://doi.org/10.1038/s41561-018-0061-4

Gao, X., Wang, K., Gao, X., Wang, K., 2014. Strength of stick-slip and creeping subduction megathrusts from heat flow observations. Science (80-.). 345, 1038–1041. https://doi.org/10.1126/science.1255487

Geersen, J., Ranero, C.R., Barckhausen, U., Reichert, C., 2015. Subducting seamounts control interplate coupling and seismic rupture in the 2014 Iquique earthquake area. Nat. Commun. 6, 6–11. https://doi.org/10.1038/ncomms9267

Guitton, A., Verschuur, D.J., 2004. Adaptive subtraction of multiples using the L1-norm. Geophys. Prospect. 52, 27–38.

Hall, R., 2002. Cenozoic geological and plate tectonic evolution of SE Asia and the SW Pacific: Computer-based reconstructions, model and animations. J. Asian Earth Sci.

https://doi.org/10.1016/S1367-9120(01)00069-4

Hall, R., Smyth, H.R., 2008. Cenozoic arc processes in Indonesia: Identification of the key influences on the stratigraphic record in active volcanic arcs. Spec. Pap. Geol. Soc. Am. 436, 27–54. https://doi.org/10.1130/2008.2436(03)

Hamilton, W.B., 1988. Plate tectonics and island arcs. Spec. Pap. Geol. Soc. Am. 253, 113–137. https://doi.org/10.1130/SPE253-p113

Heine, C., Dietmar Müller, R., Gaina, C., 2004. Reconstructing the lost eastern tethys ocean basin: Convergence history of the se asian margin and marine gateways. Geophys. Monogr. Ser. 149, 37–54. https://doi.org/10.1029/149GM03

Hoernle, K., Hauff, F., Werner, R., Van Den Bogaard, P., Gibbons, A.D., Conrad, S., Müller, R.D., 2011. Origin of Indian Ocean Seamount Province by shallow recycling of continental lithosphere. Nat. Geosci. 4, 883–887. https://doi.org/10.1038/ngeo1331

Hühnerbach, V., Masson, D.G., Bohrmann, G., Bull, J.M., Weinrebe, W., 2005. Deformation and submarine landsliding caused by seamount subduction beneath the Costa Rica continental margin - New insights from high-resolution sidescan sonar data. Geol. Soc. Spec. Publ. 244, 195–205. https://doi.org/10.1144/GSL.SP.2005.244.01.12

Karig, D.E., Moore, G.F., Curray, J.R., Lawrence, M.B., 1980. Morphology and shallow structure of the lower trench slope off Nias Island, Sunda arc. Tecton. Geol. Evol. Southeast Asian seas islands. Part 1 23, 179–208. https://doi.org/10.1029/gm023p0179

Kirkpatrick, J.D., Edwards, J.H., Verdecchia, A., Kluesner, J.W., Harrington, R.M., Silver, E.A., 2020. Subduction megathrust heterogeneity characterized from 3D seismic data. Nat. Geosci. https://doi.org/10.1038/s41561-020-0562-9

Kodaira, S., Takahashi, N., Nakanishi, A., Miura, S., Kaneda, Y., 2000. Subducted seamount imaged in the rupture zone of the 1946 Nankaido earthquake. Science (80-.). 289, 104–106. https://doi.org/10.1126/science.289.5476.104

Kopp, H., 2002. BSR occurrence along the Sunda margin: Evidence from seismic data. Earth Planet. Sci. Lett. 197, 225–235. https://doi.org/10.1016/S0012-821X(02)00484-3

Kopp, H., Flueh, E.R., Klaeschen, D., Bialas, J., Reichert, C., 2001. Crustal structure of the Central Sunda margin at the onset of oblique subduction. Geophys. J. Int. https://doi.org/10.1046/j.0956-540X.2001.01547.x

Kopp, H., Flueh, E.R., Petersen, C.J., Weinrebe, W., Wittwer, A., Scientists, M., 2006. The Java margin revisited: Evidence for subduction erosion off Java. Earth Planet. Sci. Lett. 242, 130–142. https://doi.org/10.1016/j.epsl.2005.11.036

Kopp, H., Hindle, D., Klaeschen, D., Oncken, O., Reichert, C., Scholl, D., 2009. Anatomy of the western Java plate interface from depth-migrated seismic images. Earth Planet. Sci. Lett. https://doi.org/10.1016/j.epsl.2009.09.043

Kopp, H., Klaeschen, D., Flueh, E.R., Bialas, J., Reichert, C., 2002. Crustal structure of the Java margin from seismic wide-angle and multichannel reflection data. J. Geophys. Res. 107. https://doi.org/10.1029/2000jb000095

Kopp, H., Kukowski, N., 2003. Backstop geometry and accretionary mechanics of the Sunda margin. Tectonics 22, 1–11. https://doi.org/10.1029/2002TC001420

Lallemand, S., Le Pichon, X., 1987. Coulomb wedge model applied to the subduction of seamounts in the Japan Trench. Geology 15, 1065–1069. https://doi.org/10.1130/0091-7613(1987)15<1065:CWMATT>2.0.CO;2

Laursen, J., Scholl, D.W., von Huene, R., 2002. Neotectonic deformation of the central Chile margin: Deepwater forearc basin formation in response to hot spot ridge and seamount subduction. Tectonics 21. https://doi.org/10.1029/2001tc901023

Lüschen, E., Müller, C., Kopp, H., Engels, M., Lutz, R., Planert, L., Shulgin, A., Djajadihardja, Y.S., Lueschen, E., Mueller, C., Kopp, H., Engels, M., Lutz, R., Planert, L., Shulgin, A., Djajadihardja, Y.S., 2011. Structure, evolution and tectonic activity of the eastern Sunda forearc, Indonesia, from marine seismic investigations. Tectonophysics 508, 6–21. https://doi.org/10.1016/j.tecto.2010.06.008

Marcaillou, B., Collot, J.Y., Ribodetti, A., d'Acremont, E., Mahamat, A.A., Alvarado, A., 2016. Seamount subduction at the North-Ecuadorian convergent margin: Effects on structures, inter-seismic coupling and seismogenesis. Earth Planet. Sci. Lett. 433, 146–158. https://doi.org/10.1016/j.epsl.2015.10.043

Martínez-Loriente, S., Sallarès, V., R. Ranero, C., B. Ruh, J., Barckhausen, U., Grevemeyer, I., Bangs, N., 2019. Influence of Incoming Plate Relief on Overriding Plate Deformation and Earthquake Nucleation: Cocos Ridge Subduction (Costa Rica). Tectonics 38, 4360–4377. https://doi.org/10.1029/2019TC005586

McNeill, L.C., Dugan, B., Backman, J., Pickering, K.T., Pouderoux, H.F.A., Henstock, T.J., Petronotis, K.E., Carter, A., Chemale, F., Milliken, K.L., Kutterolf, S., Mukoyoshi, H., Chen, W., Kachovich, S., Mitchison, F.L., Bourlange, S., Colson, T.A., Frederik, M.C.G., Guèrin, G., Hamahashi, M., House, B.M., Hüpers, A., Jeppson, T.N., Kenigsberg, A.R., Kuranaga, M., Nair, N., Owari, S., Shan, Y., Song, I., Torres, M.E., Vannucchi, P., Vrolijk, P.J., Yang, T., Zhao, X., Thomas, E., 2017. Understanding Himalayan erosion and the significance of the Nicobar Fan. Earth Planet. Sci. Lett. 475, 134–142. https://doi.org/10.1016/j.epsl.2017.07.019

Moore, G.F., Curray, J.R., Emmel, F.J., 1982. Sedimentation in the Sunda trench and forearc region. Geol. Soc. Spec. Publ. 10, 245–258. https://doi.org/10.1144/GSL.SP.1982.010.01.16

Moore, G.F., Curray, J.R., Moore, D.G., Karig, D.E., 1980. Variations in geologic structure along the Sunda Fore Arc, northeastern Indian Ocean. Tecton. Geol. Evol. Southeast Asian seas islands. Part 1 23, 145–160. https://doi.org/10.1029/gm023p0145

Morgan, J.K., Bangs, N.L., 2017. Recognizing seamount-forearc collisions at accretionary margins:

Insights from discrete numerical simulations. Geology 45, 635–638. https://doi.org/10.1130/G38923.1

Morton, E.A., Bilek, S.L., Rowe, C.A., 2018. Newly detected earthquakes in the Cascadia subduction zone linked to seamount subduction and deformed upper plate. Geology 46, 943–946. https://doi.org/10.1130/G45354.1

Müller, C., Kopp, H., Djajadihardja, Y.S., Barckhausen, U., Ehrhardt, A., Engels, M., Flueh, E.R., Gaedicke, C., Keppler, H., Lutz, R., Lüschen, E., Neben, S., Seeber, L., Dzulkarnaen, D.P.S., 2008. From subduction to collision: The Sunda-Banda Arc transition. Eos (Washington. DC). 89, 49–50. https://doi.org/10.1029/2008EO060001

Namiki, Y., Tsutsumi, A., Ujiie, K., Kameda, J., 2014. Frictional properties of sediments entering the Costa Rica subduction zone offshore the Osa Peninsula: implications for fault slip in shallow subduction zones. Earth, Planets Sp. 66, 72. https://doi.org/10.1186/1880-5981-66-72

Planert, L., Kopp, H., Lueschen, E., Mueller, C., Flueh, E.R., Shulgin, A., Djajadihardja, Y., Krabbenhoeft, A., 2010. Lower plate structure and upper plate deformational segmentation at the Sunda-Banda arc transition, Indonesia. J. Geophys. Res. 115, B08107. https://doi.org/10.1029/2009JB006713

Ranero, C.R., von Huene, R., 2000. Subduction erosion along the Middle America convergent margin. Nature 404, 748–752. https://doi.org/10.1038/35008046

Remitti, F., Smith, S.A.F., Mittempergher, S., Gualtieri, A.F., Di Toro, G., 2015. Frictional properties of fault zone gouges from the J-FAST drilling project (M w 9.0 2011 Tohoku-Oki earthquake). Geophys. Res. Lett. 42, 2691–2699. https://doi.org/10.1002/2015GL063507

Ruh, J.B., 2016. Submarine landslides caused by seamounts entering accretionary wedge systems. Terra Nov. 28, 163–170. https://doi.org/10.1111/ter.12204

Ruh, J.B., Sallarès, V., Ranero, C.R., Gerya, T., 2016. Crustal deformation dynamics and stress evolution during seamount subduction: High-resolution 3-D numerical modeling. J. Geophys. Res. Solid Earth 121, 6880–6902. https://doi.org/10.1002/2016JB013250

Scarselli, N., 2020. Submarine landslides - architecture, controlling factors and environments. A summary, Regional Geology and Tectonics: Principles of Geologic Analysis Volume 1: Principles of Geologic Analysis. BV. https://doi.org/10.1016/B978-0-444-64134-2.00015-8

Scholl, D.W., von Huene, R., 2007. Crustal recycling at modern subduction zones applied to the past—Issues of growth and preservation of continental basement crust, mantle geochemistry, and supercontinent reconstruction, in: Memoir of the Geological Society of America. pp. 9–32. https://doi.org/10.1130/2007.1200(02)

Scholz, C.H., Small, C., 1997. The effect of seamount subduction on seismic coupling. Geology 25, 487. https://doi.org/10.1130/0091-7613(1997)025<0487:TEOSSO>2.3.CO;2

Seton, M., Müller, R.D., Zahirovic, S., Williams, S., Wright, N.M., Cannon, J., Whittaker, J.M., Matthews, K.J., McGirr, R., 2020. A Global Data Set of Present-Day Oceanic Crustal Age and

Seafloor Spreading Parameters. Geochemistry, Geophys. Geosystems 21, 0–3. https://doi.org/10.1029/2020GC009214

Shulgin, A., Kopp, H., Mueller, C., Planert, L., Lueschen, E., Flueh, E.R., Djajadihardja, Y., 2011. Structural architecture of oceanic plateau subduction offshore Eastern Java and the potential implications for geohazards. Geophys. J. Int. 184, 12–28. https://doi.org/10.1111/j.1365-246X.2010.04834.x

Sun, T., Ellis, S., Saffer, D., 2020a. Coupled Evolution of Deformation, Pore Fluid Pressure, and Fluid Flow in Shallow Subduction Forearcs. J. Geophys. Res. Solid Earth 125, 1–26. https://doi.org/10.1029/2019JB019101

Sun, T., Saffer, D., Ellis, S., 2020b. Mechanical and hydrological effects of seamount subduction on megathrust stress and slip. Nat. Geosci. 13, 249–255. https://doi.org/10.1038/s41561-020-0542-0

Todd, E.K., Schwartz, S.Y., Mochizuki, K., Wallace, L.M., Sheehan, A.F., Webb, S.C., Williams, C.A., Nakai, J., Yarce, J., Fry, B., Henrys, S., Ito, Y., 2018. Earthquakes and Tremor Linked to Seamount Subduction During Shallow Slow Slip at the Hikurangi Margin, New Zealand. J. Geophys. Res. Solid Earth 123, 6769–6783. https://doi.org/10.1029/2018JB016136

Tréhu, A.M., Blakely, R.J., Williams, M.C., 2012. Subducted seamounts and recent earthquakes beneath the central cascadia forearc. Geology 40, 103–106. https://doi.org/10.1130/G32460.1

Ujiie, K., Tanaka, H., Saito, T., Tsutsumi, A., Mori, J.J., Kameda, J., Brodsky, E.E., Chester, F.M., Eguchi, N., Toczko, S., 2013. Low Coseismic Shear Stress on the Tohoku-Oki Megathrust Determined from Laboratory Experiments. Science (80-.). 342, 1211–1214. https://doi.org/10.1126/science.1243485

van Rijsingen, E., Funiciello, F., Corbi, F., Lallemand, S., 2019. Rough Subducting Seafloor Reduces Interseismic Coupling and Mega-Earthquake Occurrence: Insights From Analogue Models. Geophys. Res. Lett. 46, 3124–3132. https://doi.org/10.1029/2018GL081272

Verschuur, D.J., Berkhout, A.J., Wapenaar, C.P.A., 1992. Adaptive surface-related multiple elimination. Geophysics 57, 1166–1177.

von Huene, R., Ranero, C.R., Vannucchi, P., 2004. Generic model of subduction erosion. Geology 32, 913. https://doi.org/10.1130/G20563.1

von Huene, R., Scholl, D.W., 1991. Observations at convergent margins concerning sediment subduction, subduction erosion, and the growth of continental crust. Rev. Geophys. 29, 279. https://doi.org/10.1029/91RG00969

Wang, K., Bilek, S.L., 2011. Do subducting seamounts generate or stop large earthquakes? Geology 39, 819–822. https://doi.org/10.1130/G31856.1

Wessel, P., Smith, W.H.F., 1991. Free software helps map and display data. Eos, Trans. Am. Geophys. Union 72, 441–441. https://doi.org/10.1029/90EO00319

Xia, Y., Geersen, J., Klaeschen, D., Ma, B., Lange, D., Riedel, M., Schnabel, M., Kopp, H., 2021. Marine forearc structure of eastern Java and its role in the 1994 Java tsunami earthquake. Solid Earth 12, 2467–2477. https://doi.org/10.5194/se-12-2467-2021

Xia, Y., Klaeschen, D., Kopp, H., Schnabel, M., 2022. Reflection tomography by depth warping: a case study across the Java trench. Solid Earth 13, 367–392. https://doi.org/10.5194/se-13-367-2022

Yang, H., Liu, Y., Lin, J., 2013. Geometrical effects of a subducted seamount on stopping megathrust ruptures. Geophys. Res. Lett. 40, 2011–2016. https://doi.org/10.1002/grl.50509

Supplement of

Scale-dependent upper plate deformation caused by the subduction of seafloor relief

Yueyang Xia et al.

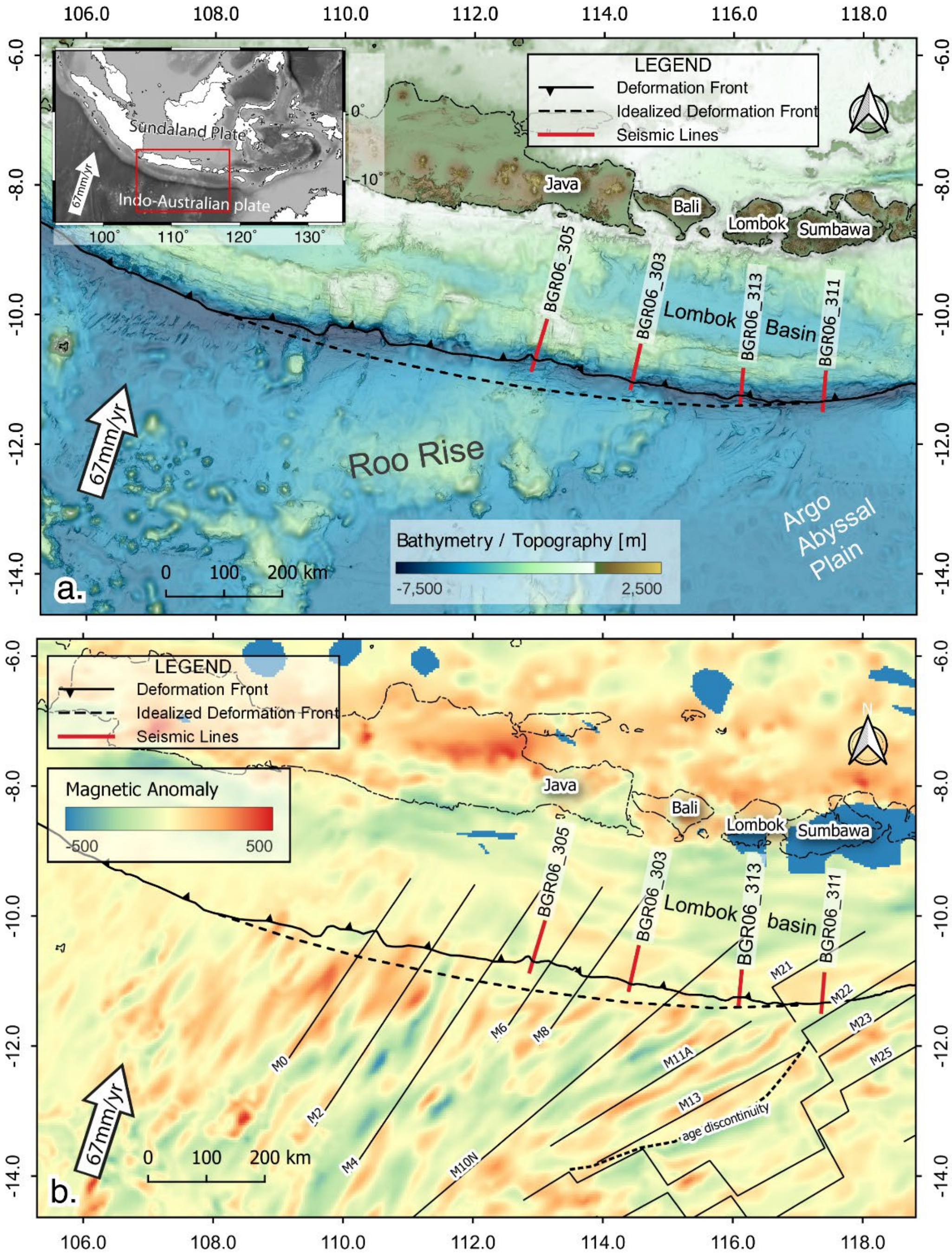

Figure. S1. a. Regional tectonic setting and bathymetry of the study area. Red lines indicate the location of the four MCS profiles. The deformation front is shown in a black line with triangle marks, and the undisturbed idealized trend of the deformation front is shown by the black dashed line. b. Satellite magnetic anomaly in the Java and Lesser Sunda regions. Red lines indicate the location of the four MCS profiles. The deformation front is shown in black line with triangles, and the undisturbed trend of the deformation front is shown by the black dashed line. Magnetic isochrons are indicated by black lines.

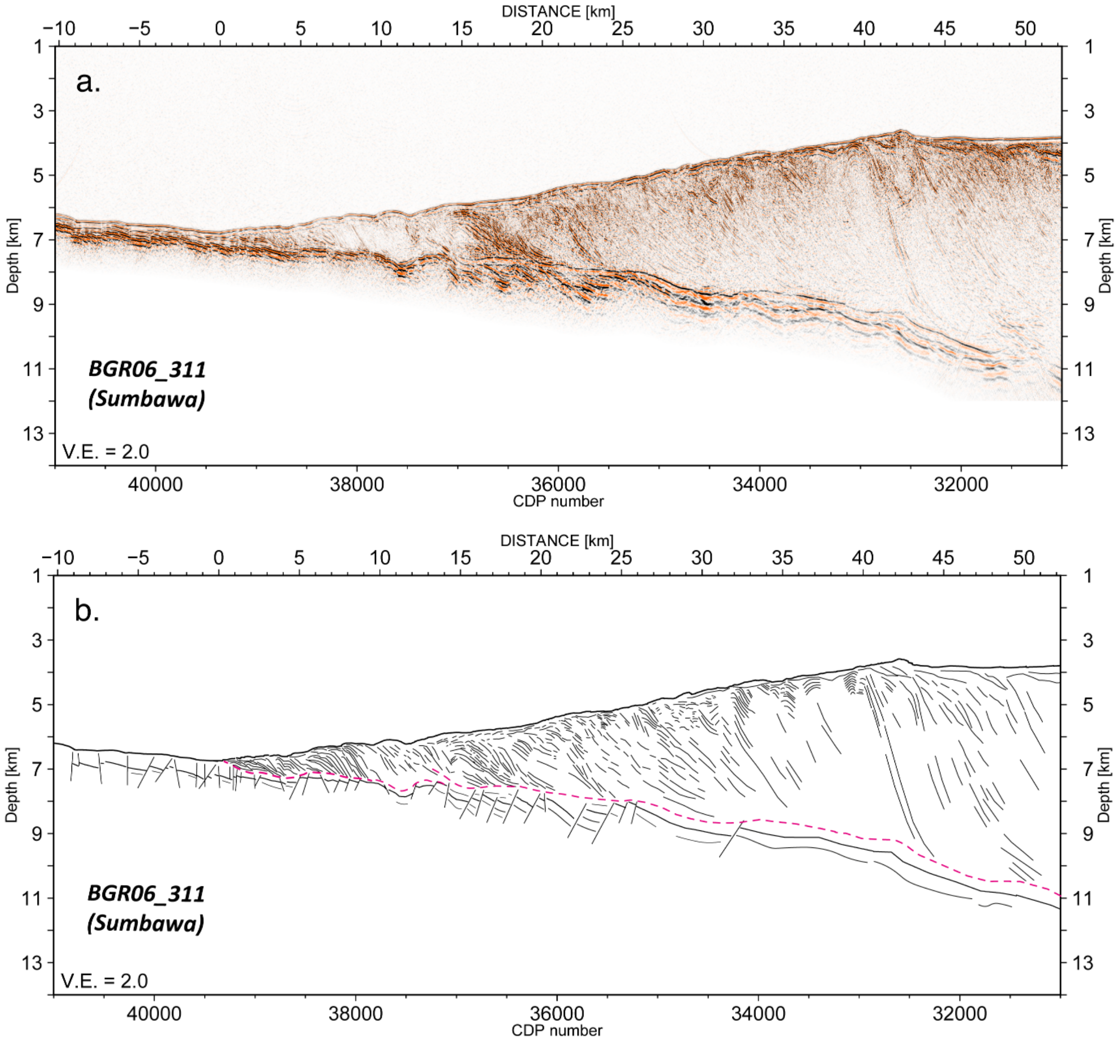

Figure S2 a. Uninterpreted depth section of BGR06_311. b. Line drawing of the seismic section.

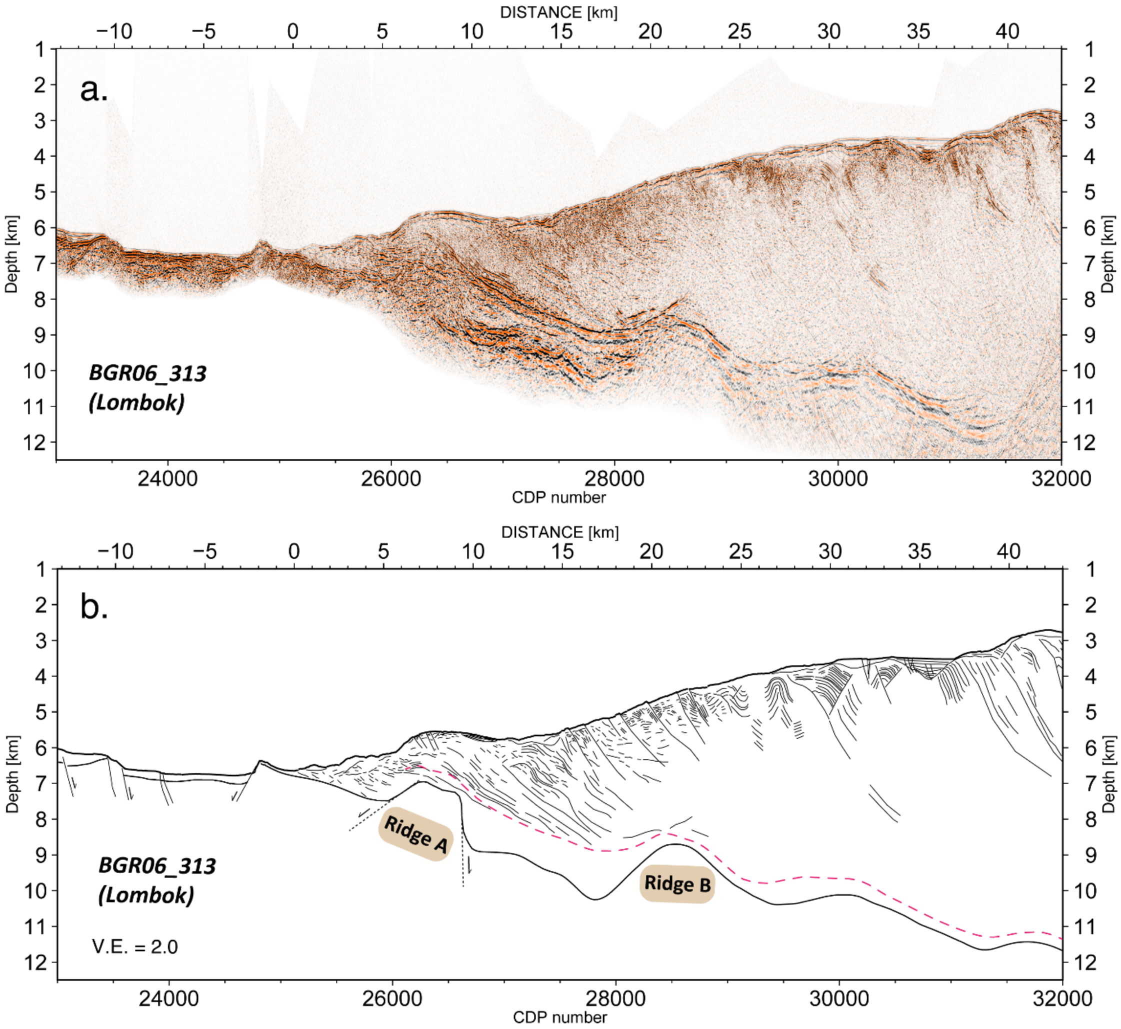

Figure S3 a. Uninterpreted depth section of BGR06_313. b. Line drawing of the seismic section.

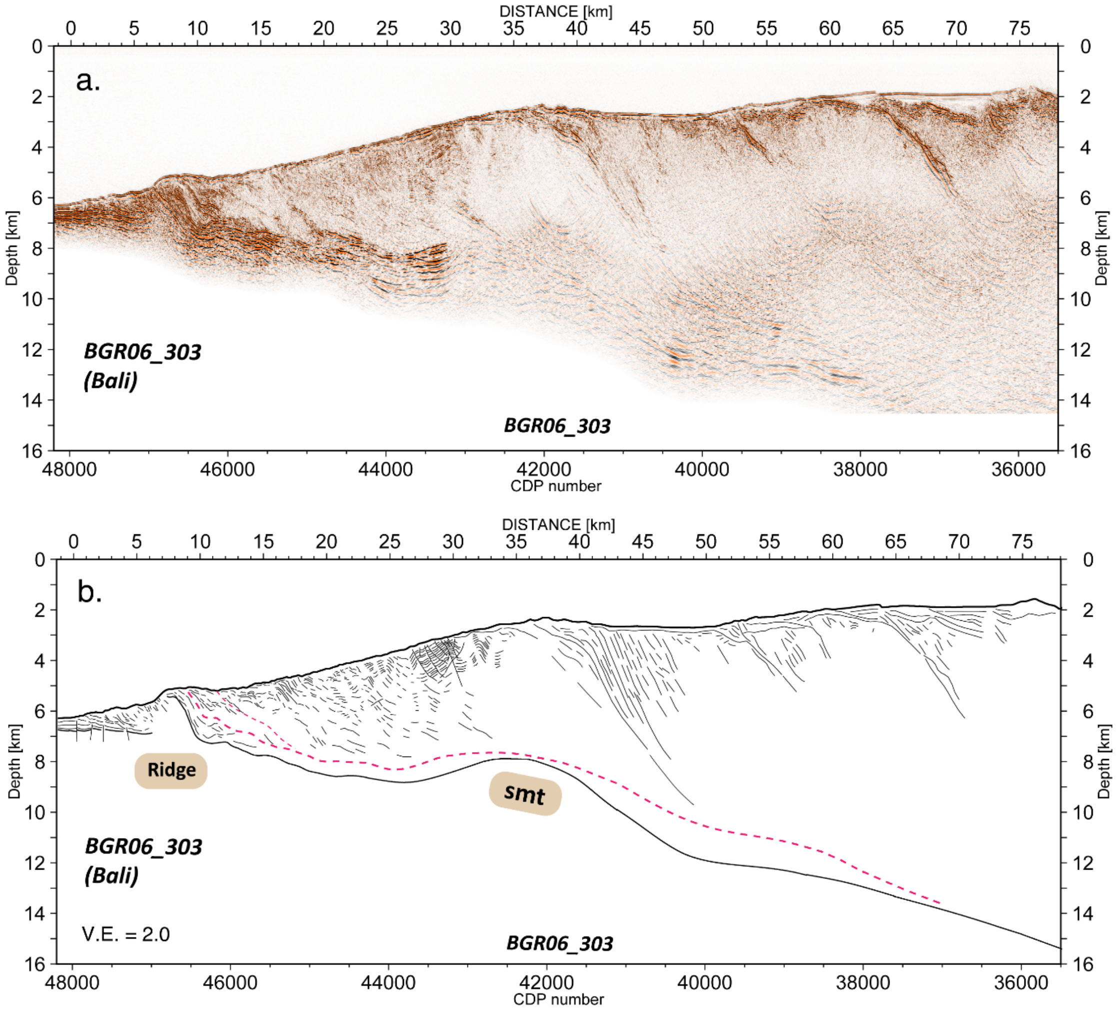

Figure S4 a. Uninterpreted depth section of BGR06_303. b. Line drawing of the seismic section.

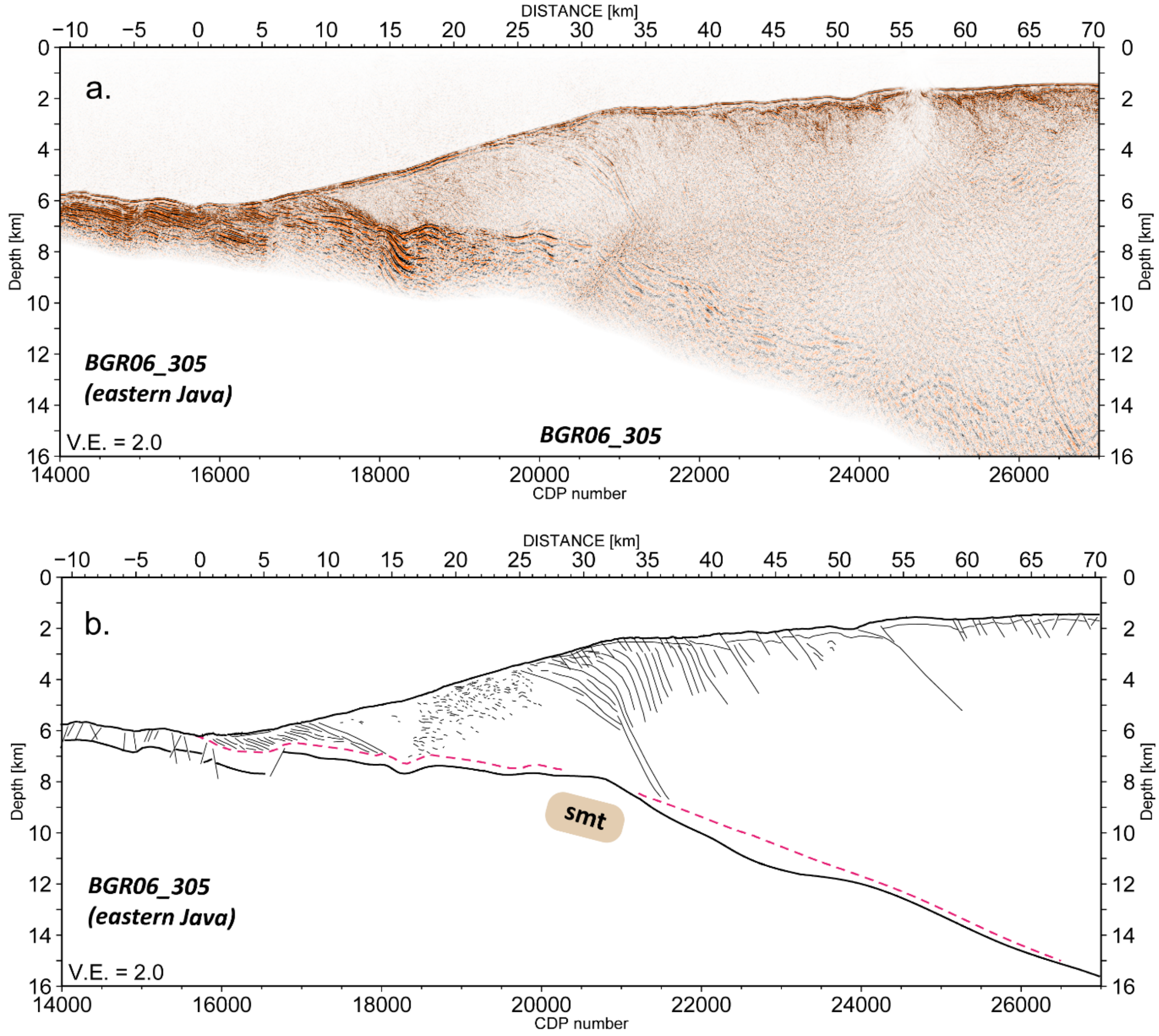

Figure S5 a. Uninterpreted depth section of BGR06_305. b. Line drawing of the seismic section.

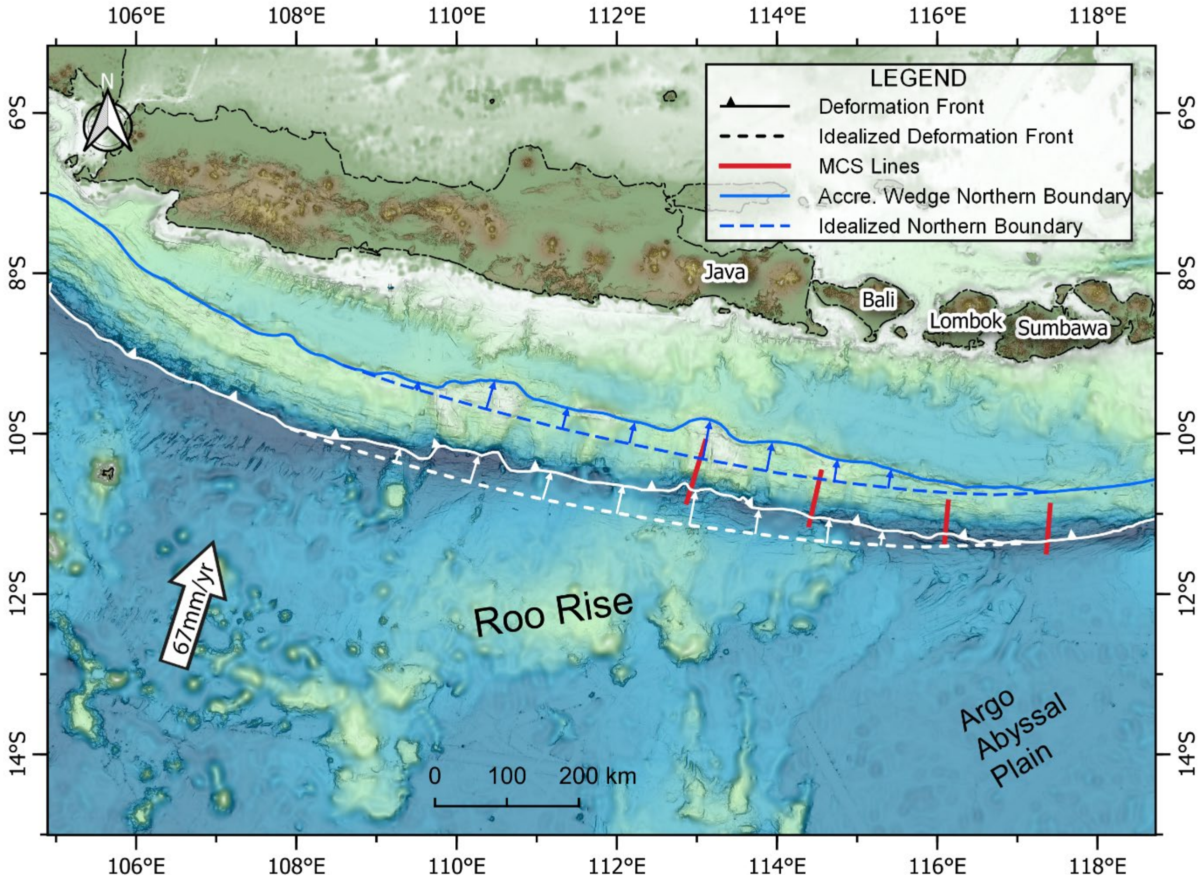

Figure S6. Bathymetry and topography map of the study area offshore Java and Lesser Sunda margin. Both the deformation front (marked in solid white line) and the northern boundary of the accretionary wedge (marked in solid blue line) deflected from their idealized trends (marked as a white dashed line and blue dashed line, respectively) in the arc-ward direction by maximum 50 km approximately over a broad region of 25,000 km^2 from 107.9° E to 117.1° E.

CHAPTER 5

MANUSCRIPT #3

Marine forearc structure of eastern Java and its role in the 1994 Java tsunami earthquake

Yueyang Xia(1); Jacob Geersen (2); Dirk Klaeschen(1); Bo Ma(1); Dietrich Lange(1); Michael Riedel(1); Michael Schnabel(3) and Heidrun Kopp(1,2)

(1) Research Division 4: Dynamic of the Ocean Floor, GEOMAR Helmholtz Centre for Ocean Research, Kiel, Germany
(2) Christian-Albrechts-Universität zu Kiel, Kiel, Germany
(3) Bundesanstalt für Geowissenschaften und Rohstoffe (BGR), Hanover, Germany

Published in 2021 in *Solid Earth* 12, 2467–4277

This chapter contains a manuscript published in *Solid Earth* in its original form. Please note that the publication contains its own reference list and refers to its own figure and page numbers. The manuscript is reproduced with permission of the European Geophysical Union.

Solid Earth, 12, 2467–2477, 2021
https://doi.org/10.5194/se-12-2467-2021

Solid Earth Open Access EGU

Marine forearc structure of eastern Java and its role in the 1994 Java tsunami earthquake

Yueyang Xia[1], **Jacob Geersen**[2], **Dirk Klaeschen**[1], **Bo Ma**[1], **Dietrich Lange**[1], **Michael Riedel**[1], **Michael Schnabel**[3], and **Heidrun Kopp**[1,2]

[1]Research Division 4: Dynamic of the Ocean Floor, GEOMAR Helmholtz Centre for Ocean Research, Kiel, Germany
[2]Christian-Albrechts-Universität zu Kiel, Kiel, Germany
[3]Bundesanstalt für Geowissenschaften und Rohstoffe (BGR), Hanover, Germany

Correspondence: Yueyang Xia (yxia@geomar.de)

Received: 2 May 2021 – Discussion started: 17 May 2021
Revised: 17 September 2021 – Accepted: 27 September 2021 – Published: 1 November 2021

Abstract. We resolve a previously unrecognized shallow subducting seamount from a re-processed multichannel seismic profile crossing the 1994 M_w 7.8 Java tsunami earthquake rupture area. Seamount subduction occurs where the overriding plate experiences uplift by lateral shortening and vertical thickening. Pronounced back-thrusting at the landward slope of the forearc high and the formation of splay faults branching off the landward flank of the subducting seamount are observed. The location of the seamount in relation to the 1994 earthquake hypocentre and its co-seismic slip model suggests that the seamount acted as a seismic barrier to the up-dip co-seismic rupture propagation of this moderate-size earthquake.

1 Introduction

Tsunami earthquakes represent a special class of seismic events that rupture the very shallow portion of a subduction plate boundary (Kanamori, 1972; Satake and Tanioka, 1999). They are characterized by a longer source duration compared to conventional earthquakes with a similar magnitude that nucleate at greater depth (e.g. Bilek and Lay, 2002). Despite being of only moderate surface wave magnitude, tsunami earthquakes commonly trigger an anomalously large tsunami. Due to the lack of severe ground shaking, coastal communities are often caught by surprise by the associated tsunami, resulting in potentially high numbers of fatalities (Satake et al., 2013). In spite of their often severe consequences, our current knowledge on tsunami earthquakes is insufficient to comprehensively understand their seismotectonic genesis and to identify regions that are particularly endangered.

The reduced rupture speed, large shallow slip, and moderate shaking of earthquakes that break the shallow plate boundary might be preconditioned by low rigidity in the outermost forearc (Bilek and Lay, 2002; Sallarès and Ranero, 2019; Şen et al., 2015). Structural features invoked to explain the unusual slow rupture of tsunami earthquakes include the presence of excess topography on the subducting plate, which may act as a localized asperity (Abercrombie et al., 2001; Tanioka et al., 1997). Further explanations include rupture within unconsolidated subducted sediments (Kanamori, 1972; Satake and Tanioka, 1999), re-activated splay-faulting in the upper plate (Fan et al., 2017; von Huene et al., 2016; Wendt et al., 2009), vertical pop-up expulsion (Hananto et al., 2020), or inelastic shoving of unconsolidated sediments under the action of shallow slip (Seno, 2002; Tanioka and Seno, 2001).

With only 13 known events since 1896, tsunami earthquakes occur sporadically but are observed globally (Geersen, 2019). The Java margin, which constitutes the eastern portion of the Sunda Arc (Kopp et al., 2006) was, however, affected twice by tsunami earthquakes in recent times (1994 and 2006). The 1994 M_w 7.8 earthquake (2 June 1994 18:17:34 UTC) ruptured the shallow part of the plate boundary off the coast of easternmost Java (Fig. 1; Abercrombie et al., 2001). The co-seismic slip model is characterized by a non-uniform pattern, with the maximum slip under the forearc high (Abercrombie et al., 2001; Bilek and Engdahl,

Published by Copernicus Publications on behalf of the European Geosciences Union.

2007). The induced ground motion and seafloor perturbation resulted in a severe tsunami with run-up heights of up to ∼ 14 m (Tsuji et al., 1995), causing significant damage to the local coastal area and approximately 250 casualties (Polet and Kanamori, 2000). The tsunami modelling for the 1994 Java earthquake reveals that the source of the larger-than-expected tsunami run-up could be linked to the horizontal displacement of the steep seafloor slope on the overriding plate (Tanioka and Satake, 1996).

The 1994 Java tsunami earthquake has been interpreted as having ruptured over a subducting seamount that induces a localized asperity within an overall low-coupled shallow plate boundary environment (Abercrombie et al., 2001; Bilek and Engdahl, 2007). This interpretation is based on the presence of multiple seamounts within the Java trench as recognized in early side-scan data (Masson et al., 1990), the presence of a well-developed shallow forearc high (Fig. 1b), a positive gravity anomaly under the forearc high (Fig. 1c), and the dominance of normal faulting aftershocks in the outer rise (Abercrombie et al., 2001). To date, the presence of the seamount in the peak slip region of the 1994 earthquake has not been confirmed by marine seismic data (Lüschen et al., 2011; Shulgin et al., 2011). The previous interpretation (Abercrombie et al., 2001; Bilek and Engdahl, 2007) is in contrast to the notion that subducting seamounts affect the plate interface as a geometrical irregularity, induce permanent brittle deformation of the overriding plate, and develop a heterogeneous stress field which does not support the generation of large earthquakes ($M > 8$) but rather favours moderate and small events ($4 < M < 8$) or aseismic creep (Kodaira et al., 2000; Ruh et al., 2016; Wang and Bilek, 2011; Martínez-Loriente et al., 2019).

In this study, we image the structure of the Java margin using multichannel reflection seismic data (MCS) in the region of the 1994 tsunami earthquake in order to resolve the relation of subducting lower plate topography and upper plate structure to the co-seismic slip distribution. Our study is based on enhanced processing of a multichannel seismic reflection line crossing the epicentral area. Re-processing of the profile aimed to improve the subsurface velocity model and to enhance the multiple suppression to augment the imaging quality. Pre-stack depth migration refines a combined P-wave velocity model from a MCS reflection tomography (Xia et al., 2021) and ocean bottom seismometer (OBS) refraction tomography (Shulgin et al., 2011).

2 Data and methods

The multichannel seismic reflection profile SO190 BGR06_305 was acquired in 2006 under the scope of the Sindbad Project during R/V *Sonne* cruise SO190 conducted by the Federal Institute for Geosciences and Natural Resources (BGR) (Müller and Neben, 2006). The profile is part of a 2D survey covering the marine forearc off the coast of eastern Java and the Lesser Sunda Islands (Lüschen et al., 2011; Planert et al., 2010; Shulgin et al., 2011). BGR's G-Gun airgun array was used as a seismic source with a maximum total volume of 3100 in^3 (50.8 L) and a towing depth of 6 m. Seismic signals were recorded by the 3000 m long digital cable of BGR's SEAL System, which consists of 20 seismic sections with 240 channels in total.

Seismic pre-processing is summarized in Table S1 and is based on a routine that includes geometry set-up, common midpoint (CMP) binning, zero offset traces padding, bandpass filtering, shot interpolation, and random noise attenuation. We employed a free surface-related multiple prediction method to predict the multiple waves from the primary events based on the Kirchhoff integral (Verschuur et al., 1992) (Fig. S1 in the Supplement). An adaptive subtraction was used to eliminate the multiple (Guitton and Verschuur, 2004) and was applied using cascaded frequency bands (Table S1, Figs. S1, S2). Three bands of frequency (0–12, 12–50, and 50–90 Hz) are defined in the adaptive subtraction to fit the spectrum discrepancies of the two inputs of the original data and modelled multiple (Fig. S2). This novel multiple suppression strategy greatly improved the resolution at depth by unveiling and preserving the deeper reflections previously blurred and covered by the seafloor multiple (Figs. S3, S4). Figure S4 illustrates the efficiency of this application. The multiple overprinted on the primaries in Fig. S4a are step-by-step eliminated by the adaptive subtraction, Radon dip filter, and the amplitude clipping. Remarkably, the adaptive subtraction of modelled multiple (Fig. S4c) removed most of the multiples with similar dipping angle as the primaries, which are difficult to discriminate using a conventional dip filter (e.g. Radon filter in Fig. S4d) at the near-offset. The initial velocity analysis is performed in the time domain with a CMP increment of 250 m and converted to the depth domain. This MCS p-wave velocity (vp) model is subsequently merged with the OBS refraction model of Shulgin et al. (2011) to correct the vp field at greater depth (2–4 km below seafloor), from where little effective MCS reflection signal and move-out sensitivity is recorded (marked as the white band in Fig. S5). The merging of the velocity models is conducted with a smooth taper zone with a width of ∼2 km to eliminate any abrupt vp changes. We used the final merged vp model as the initial model for the pre-stack depth migration. Subsequently, we conducted an iterative ray-based reflection depth tomography with a warping method to minimize the residual depth error to retrieve an optimized vp model (Xia et al., 2021). Most significant are the image improvements compared to Lüschen et al. (2011, Fig. 3) in the shallow subsurface structure of splay faults a, b, and c (Fig. 2) and in the deeper parts where the seafloor multiple overprinted the primary reflections.

Multibeam bathymetric data were collected during the SO190 cruise, using a SIMRAD EM120 multibeam echo sounder. The bathymetry survey was edited and merged with the GEBCO_2020 bathymetry (GEBCO, 2020) in the areas

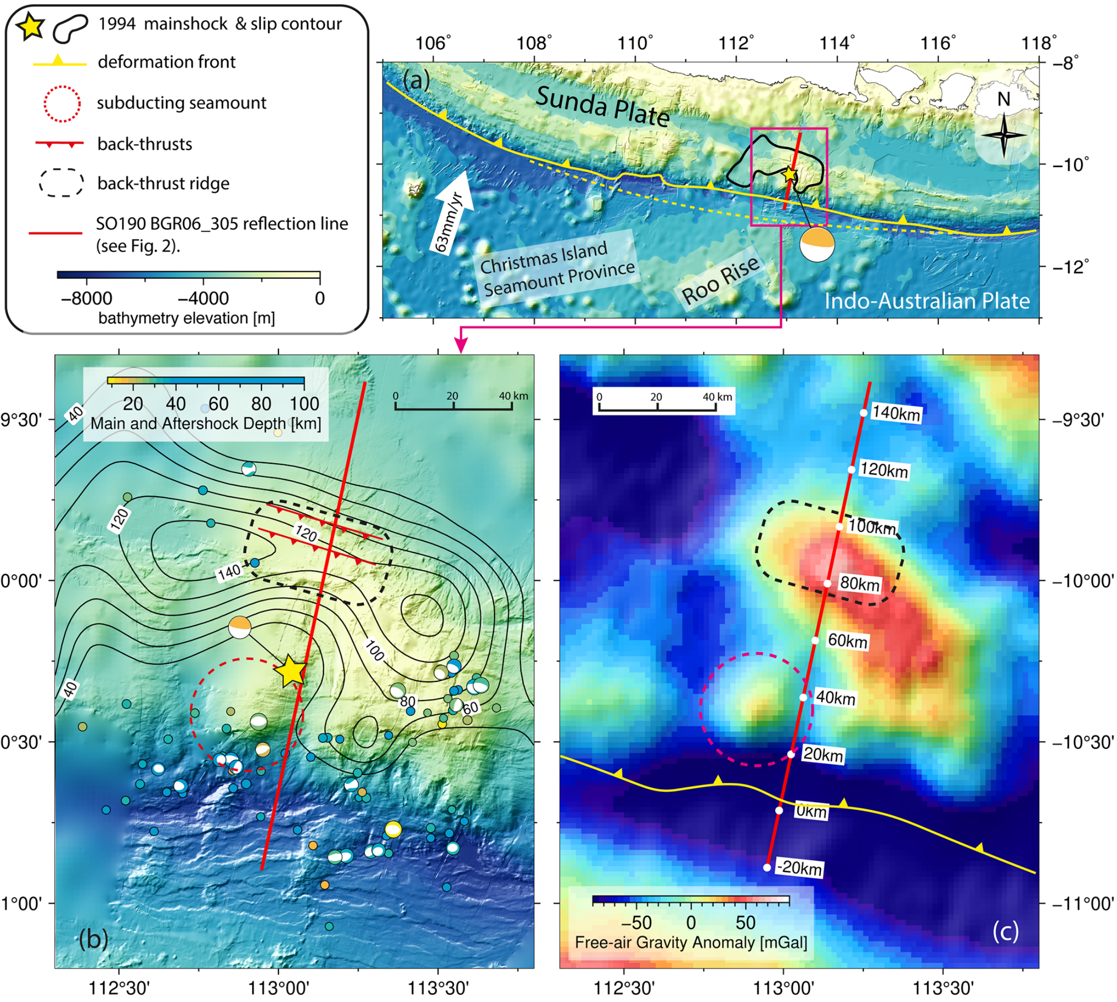

Figure 1. (a) Bathymetric overview, from the General Bathymetric Chart of the Oceans (GEBCO, 2020), of the eastern Java Margin. Yellow line: deformation front. Dashed yellow line: assumed trend of the deformation front prior to frontal erosion related to the Roo Rise (Kopp et al., 2006). Yellow star: 1994 Java Tsunami earthquake epicentre. The moment tensor of the 1994 mainshock (gCMT, Dziewonski et al., 1981; Ekström et al., 2012) is plotted at the position of the 1994 epicentre from the ISC-EHB Bulletin catalogue (Engdahl et al., 2020). Black line: rupture area of the 1994 Java Tsunami earthquake (Bilek and Engdahl, 2007). Red line: Seismic line SO190 BGR06_305 shown in Fig. 2. **(b)** Local bathymetry acquired during SO190 cruise overlain on the GEBCO_2020 grid. Black lines are slip contours (in cm) of the 1994 Java tsunami earthquake from Bilek and Engdahl (2007). The locations of the mainshock and largest aftershocks (3 June–14 October 1994) are from the ISC-EHB Bulletin catalogue (Engdahl et al., 2020) and focal mechanisms from the gCMT catalogue (Dziewonski et al., 1981; Ekström et al., 2012). The black dashed rectangle and the red triangle markers indicate the back-thrust ridge. The red dashed circle marks the bathymetric elevation associated with the shallow subducting seamount. Note the decrease in co-seismic slip and bending of contour lines around the subducting seamount. **(c)** Free-air gravity anomaly (Sandwell et al., 2014).

not covered by the multibeam soundings. Gravity data in this study are from Sandwell et al. (2014) based on satellite radar measurements.

3 Results

The oceanic Indo-Australian Plate off Java features a large number of seamounts and oceanic plateaus (e.g. the Roo Rise) that form the northern extension of the Christmas Island Seamount Province (Fig. 1a). In the region of the 1994 earthquake, oceanic basement relief breaching the sediment infill is observed in the trench and currently colliding with the marine forearc (Fig. 1b) (Masson et al., 1990; Kopp, 2011). The oceanic plate, which locally carries up to 1000 m of sediment, is shaped by bending related normal faults. The normal faults repeatedly offset the oceanic basement and shallow trench sediments, including the seamounts, leading to prominent seafloor escarpments (Fig. 1b). From around kilometre 5 landward of the trench, the décollement forms a ~40 km wide bulge or topographic elevation (Fig. 2c). The

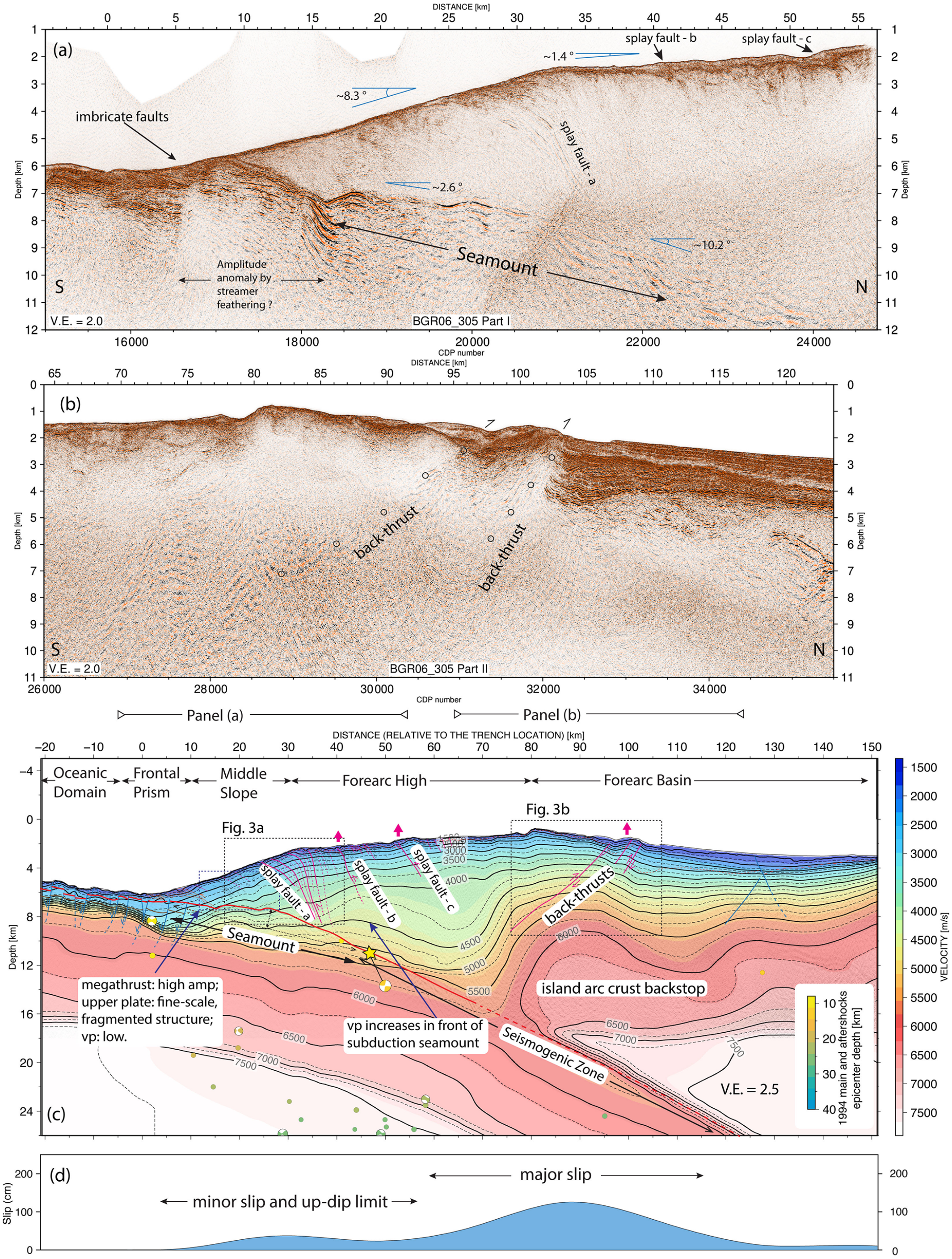

Figure 2. **(a)** Pre-stack depth-migrated section of seismic profile SO190 BGR06_305 from the trench to the forearc high domain. **(b)** Pre-stack depth-migrated section of seismic profile SO190 BGR06_305 covering the transition from the forearc high to the forearc basin.**(c)** Seismic section overlain by the vp model (based on MCS reflection tomography above 3 km depth, velocities below from Shulgin et al., 2011; see Fig. S5), our structural interpretation, and the aftershock seismicity (from catalogue ISC-EHB Bulletin; Engdahl et al., 2020) of the 1994 Java tsunami earthquake. The hypocentre is marked as a yellow star. Coloured circles and beach balls are aftershocks (time span: 3 June 1994–14 October 1994) from the ISC-EHB Bulletin catalogue (Engdahl et al., 2020) and focal mechanisms from the gCMT catalogue (Dziewonski et al., 1981; Ekström et al., 2012). The well-developed forearc high (75–100 km) results from back-thrusting above the island arc crust backstop. A subducting seamount between kilometres 5–45 is overlain by upper plate splay faults. **(d)** Co-seismic slip model of the 1994 earthquake along the profile (Bilek and Engdahl, 2007). Peak slip occurred underneath the backstop (55–105 km) and decreased towards the subducting seamount (5–45 km).

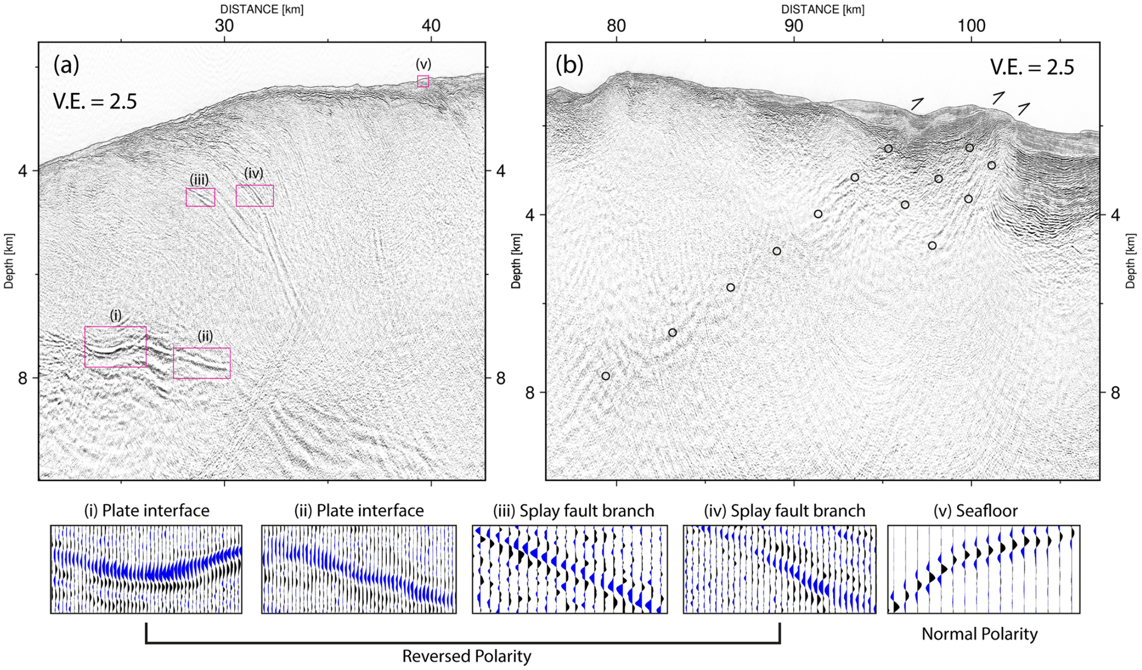

Figure 3. (a) Seismic section with a close-up view of the splay fault a (compare Fig. 2c for location) branching from the landward side of the subducting seamount. Red boxes indicate close-up views shown in the lower panels. Reversed polarity reflections (relative to the seafloor) are observed at the plate interface seaward of the seamount and along the splay fault. The black and blue colours present positive and negative wavelet polarity, respectively. **(b)** Seismic section with a close-up view of the back-thrust (compare Fig. 2c for location). Black circles mark the back-thrust fault planes.

dip angle of the subducting oceanic basement increases from 2.6° on the seaward side of the bulge to ∼10.2° on its landward side (Fig. 2a). With a height of ∼2 km (Fig. 2) and a possible width of 40 km (interpreted from the bathymetry and free-air gravity; Fig. 1b–c), this large subducting ridge or seamount (hereafter referred to as seamount) corresponds to some of the broad and wide topographic highs observed in the seafloor bathymetry that are associated with the Christmas Island Seamount Province (Fig. 1a). The seismic reflection pattern of the plate boundary differs substantially up-dip and down-dip of the seamount (Fig. 2a). High amplitude and negative polarity patches are imaged on the seaward side of the seamount crest (Figs. 2a, 3a, kilometres: 15–30), and associated a low vp (2500–3500 $\mathrm{m\,s^{-1}}$) in the outermost forearc (Fig. 2c, depth 6–8 km, kilometres: 15–30). On the landward side, an increased vp (4000–5000 $\mathrm{m\,s^{-1}}$) is inferred from the wide-angle seismic data (Shulgin et al., 2011) at the leading edge of the seamount (Fig. 2c, kilometres: 35–60, depth: 8–12 km) followed by a slight decrease farther landward (kilometres: 60–70, depth: 12–14 km).

Below the lowermost continental slope (Fig. 2a, kilometres: 0–12), a distinct set of landward-dipping imbricate faults with high amplitudes defines the actively deforming frontal prism. The internal structure of the middle slope regime (Fig. 2a, kilometres: 12–32) is characterized by lower amplitudes and an overall fine-scale fragmented reflection pattern (Fig. 2a). Comparable imbricate faults are much less distinct underneath the middle slope (Fig. 2a) than underneath the frontal prism. Both the frontal prism and middle slope domain host a steep seafloor with an inclination of about 8.3° (Fig. 2a, c). A distinct change in the slope of the seafloor at kilometre 32 defines the transition from the steeply inclined middle slope to the almost flat forearc high that extends between kilometres 32–102 (Fig. 2). The transition correlates with a prominent splay fault system that connects from the landward flank of the subducting seamount to the seafloor (Fig. 2a, c: "splay fault – a", and 3a). At shallow depths (<5 km), the main splay fault divides into several branches that crop out at the seafloor between kilometres 24–30 (Figs. 2a, c, 3a). Reversed polarity reflections relative to the seafloor are observed along the splay fault branches (Fig. 3a, insets iii and iv). At kilometres 40 and 52 in the forearc high, splay faults are also imaged from the seafloor to a depth of 3.5 km below the seafloor (Fig. 2a, c: "splay fault b" and "splay fault c". The transition from the forearc high into the forearc basin (Fig. 2, kilometres: 95–105) is defined by a pronounced back-thrust (Figs. 2b, c, and 3b). The back-thrust dips seaward and is traced to 9–12 km depth, where seismic resolution diminishes and blurs a possible connection to the plate boundary below (Figs. 2b, 3b). It offsets the shallow sediments (vertical throw of 600 m) and links to a compressional ridge at the seafloor (Figs. 1b, 2b, 3b, 4b).

A distinct positive gravity anomaly outlines the forearc high (dashed rectangle in Fig. 1c). This anomaly, however, does not correlate with a subducting topographic feature, as suggested in previous studies (Abercrombie et al., 2001; Bilek and Engdahl, 2007). Projected onto the seismic line (Fig. 2b), it correlates with a prominent block of high vp (6–7 $\mathrm{km\,s^{-1}}$) in the island arc crust that has been interpreted as a forearc backstop (Shulgin et al., 2011). The above-mentioned back-thrust evolves along the edge of this high-velocity feature (Figs. 2c and 5). A smaller, circular positive gravity anomaly is visible farther up-dip close to the deformation front (red dashed circle in Fig. 1c). This anomaly correlates to the shallow subducting seamount under the middle slope identified in the seismic line.

4 Discussion

The depth section of seismic line SO190 BGR06_305 (Fig. 2a–b), which is based on advanced seismic processing techniques, resolves the tectonic structure in the region of the 1994 Java tsunami earthquake at a level of detail that largely exceeds earlier studies (Lüschen et al., 2011; Shulgin et al., 2011). In contrast to Lüschen et al. (2011), who interpreted multiple small subducting seamounts in the shallow subduction zone, the improved imaging quality of the seismic profile reveals a single broad subducting seamount at the shallow plate boundary seaward of the forearc high. The distinct change in the dip of the décollement from $\sim 2.6^\circ$ under the outermost forearc to $>10^\circ$ seaward of kilometre 40 outlines the flanks of the seamount. The seamount modulates the seafloor bathymetry, causing a small circular bathymetric elevation (red circle in Fig. 1b) and is further manifested in the circular free-air gravity anomaly close to the trench (red circle in Fig. 1c). Consistent with other well-imaged subducting seamounts (e.g. Kodaira et al., 2000; Bell et al., 2010) and results from analogue and numerical modelling (Ruh et al., 2016; Sun et al., 2020), we observe intensified compressional features at the leading edge of the seamount (Fig. 2a, c, kilometres: 32–65). In contrast, gravitational relaxation (e.g. decreased vp, fine-scale fragmented internal reflection, and high plate-boundary amplitudes with reversed polarity) is observed at the trailing edge of and above the seamount (Fig. 2a, c, kilometres: 15–32). Based on the extent of the seamount (2 km high, possibly 40 km wide) and the moderate crest angle ($\sim 10^\circ$), we speculate that the true dimension of the seamount is even larger ($\sim$40–60 km) as the seismic line might only cross the seamount's eastern flank (compare the location of the bathymetry and gravity anomaly in Fig. 1c).

In the seismic profile, we observe splay faults, which feature seismic reflections with a strong amplitude, merging at the landward side of the seamount (Figs. 2a, c: splay fault a, b, and c, 3a, 4b). The reversed reflection polarity on the splay fault branches and shallow décollement (Fig. 3a) suggest that these faults act as fluid conduits and are weak, likely due to high porosity and high fluid content. Splay fault b (Fig. 2a) causes a minor seafloor offset in the seismic section, while splay fault c offsets the seafloor by $\sim$500 m as seen both in the seismic section (Fig. 2a) and bathymetry map (Fig. 4b), indicating recent activity. Generically, splay faults form when the primary fault, in this case the plate interface, becomes critically misaligned with the original principal stresses on the optimum plane (Scholz et al., 2010). Though a variety of scenarios could result in such a change of principal stress, we note that the structural modification of the plate boundary dipping angle induced by the subducting seamount at its leading edge will cause such a misalignment of the primary stress with the basal fault and further enhances the vertical thickening and lateral shortening of the upper plate (Lallemand and Le Pichon, 1987).

The forearc high in the region of the 1994 Java tsunami earthquake is more evolved (i.e. shallower seafloor) compared to the adjacent regions along the margin (Fig. 1). This, in combination with the collocated gravity anomaly (dashed rectangle in Fig. 1b–c; kilometres: 75–105 in Fig. 2b), has fostered speculations about the presence of a subducting seamount in the peak slip region of the 1994 earthquake (e.g. Abercrombie et al., 2001). The re-processed seismic reflection image, however, suggests that the shallow forearc high is associated with lateral shortening and vertical thickening of the upper plate ahead of a seamount currently underthrust at shallow depth. Regional uplift of the forearc slope might be enhanced by the presence of an island arc backstop (Byrne et al., 1993). The backstop underneath the forearc high is expressed as a high vp block interpreted as crystalline island arc crust due to its vp of 6–7 $\mathrm{km\,s^{-1}}$ (Shulgin et al., 2011). The strong lateral velocity gradient underneath the crest of the forearc high is associated with an abrupt change in material properties, manifested in back-thrusting along the well-imaged fault plane (Fig. 3b–c) and the development of thrust ridges in the bathymetry at the seafloor outcrop of the back-thrust fault (Figs. 1b and 4b). Along this line of argumentation, the mature forearc high reaching shallower water depths compared to its vicinity (Figs. 1b and 4b), in the peak slip region of the 1994 Java tsunami earthquake, likely results from the combined effect of increased horizontal stress (pushing) ahead of the seamount and the presence of island arc crust serving as a rigid backstop. The resulting shortening and thickening of the upper plate are elucidated through a series of seaward vergent upper plate splay faults above the seamount and at least two well-imaged landward vergent backthrusts along the edge of the island arc backstop.

The rugged topography of the marine forearc in the central-eastern Java segment of the Sunda margin between 110–115° E stands in contrast to adjacent regions off the coast of western Java or the Lesser Sunda islands (Kopp, 2011). Figure 4 shows high-resolution bathymetric data acquired during cruises SO176, SO179, and SO190 with R/V *Sonne*, merged with global satellite bathymetry (GEBCO, 2020). The subduction of the pronounced seafloor relief of

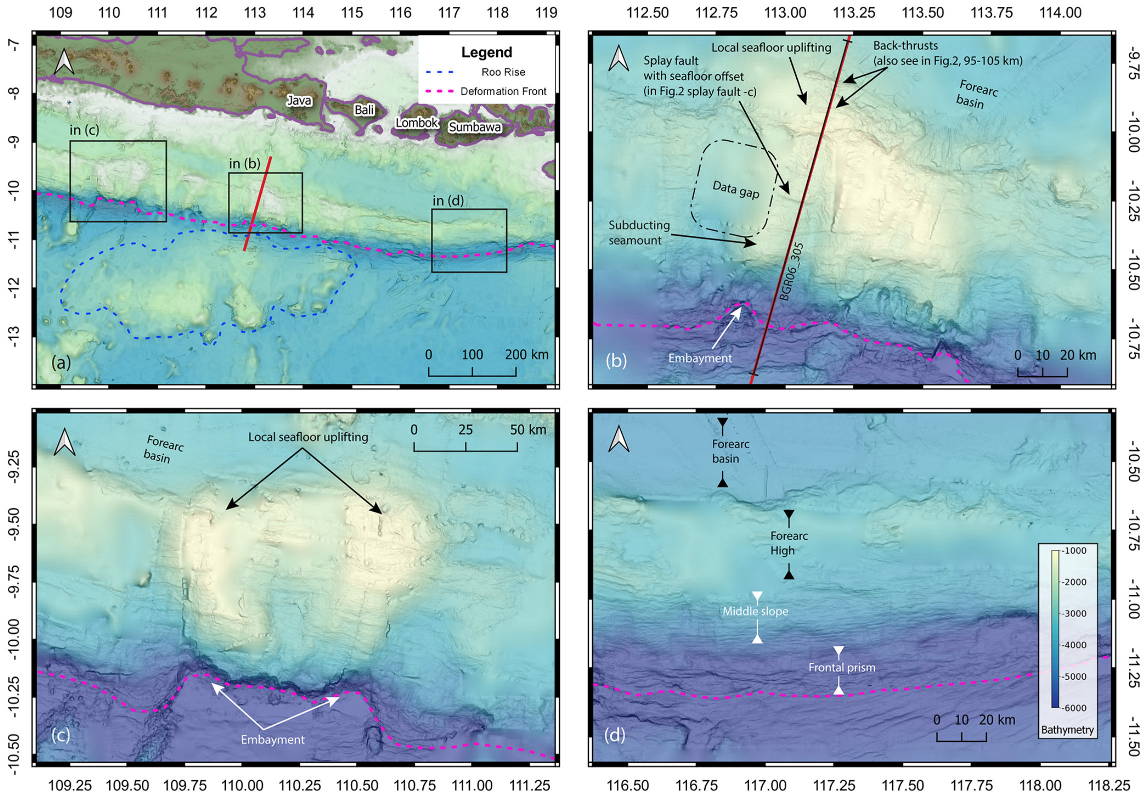

Figure 4. Global satellite bathymetry merged with ship-based multibeam data along the Java margin and Lesser Sunda islands (Bali, Lombok, and Sumbawa). Black squares indicate locations of close-up views in **(b–d)**; red line indicates location of MCS profile BGR06_305 discussed in this study. **(a)** Bathymetry from 108.5 to 119.5° E. The accretionary wedge from 109 to 115° E is deformed and disturbed by the subducting seamounts and ridges associated with the Roo Rise. In comparison, the accretionary wedge from 115 to 119° E forms a more homogeneous structure compared to the western area. **(b)** A close-up view of the bathymetry in the vicinity of MCS profile BGR06_305. An embayment of the deformation front is observed at the trailing edge of the subducting seamount. A thrust fault offsets the seafloor landward of the seamount. The forearc high and the southern margin of the forearc basin experience uplift to a water depth less than 1000 m. **(c)** A close view of the seafloor bathymetry off central Java. The accretionary wedge and forearc high are uplifted to shallow water depth of ∼750 m, and the deformation front is characterized by a large embayment at the trench. **(d)** The seafloor bathymetry map off the coast of Lombok–Sumbawa reveals a much more homogenous accretionary wedge compared to its western counterparts.

the Christmas Island Seamount province literally breaks up the formerly coherent slopes of the forearc (Fig. 4a), as observed to the west and east. This is evident from the crooked trend of the deformation front in this segment (Fig. 4b–c) compared to the uniformly developed lower and middle slope to the east (Fig. 4d). Between 110–114° E the pronounced forearc basin found off the coast of western Java and the Lesser Sunda islands is virtually squeezed together, as the forearc high and middle and lower slopes are offset to the north (Figs. 1a, 4a). These regional-scale processes are associated with local seafloor uplift, as observed in our study area (Fig. 4b) or around 110° E (Fig. 4c), where water depth above the forearc high is even shallower (750 m). It should be noted in this context, though, that the 2006 Java tsunami earthquake (Ammon et al., 2006; Bilek and Engdahl, 2007), for which the reactivation of splay faults has been discussed (Fan et al., 2017), occurred west of the subduction of the Christmas Island Seamount province at 107.4° E and that splay faults have also been imaged off the coast of the Sunda Strait and western Java (Kopp and Kukowski, 2003).

Abercrombie et al. (2001) and Bilek and Engdahl (2007) relocated the 1994 hypocentre and modelled the co-seismic slip. Both studies share a similar event location and a grossly similar characteristic of the co-seismic slip models. The relocated hypocentre of the 1994 earthquake and the main co-seismic slip patch are located at the leading edge of the shallow subducting seamount (Fig. 1). The co-seismic slip further seems to taper around the subducting seamount, whereas in the seamount region (red dashed circle in Fig. 1b), the slip value decreases significantly (Figs. 1b, 2c–d, kilometres: 5–45). These observations lead us to reconsider if the 1994 Java tsunami earthquake ruptured across a subducting seamount or if the seamount might have played a different role in the event. From numerical models, there is evidence that subducting seamounts induce overpressures and increase shear stress at their leading edge in a region that is equivalent to

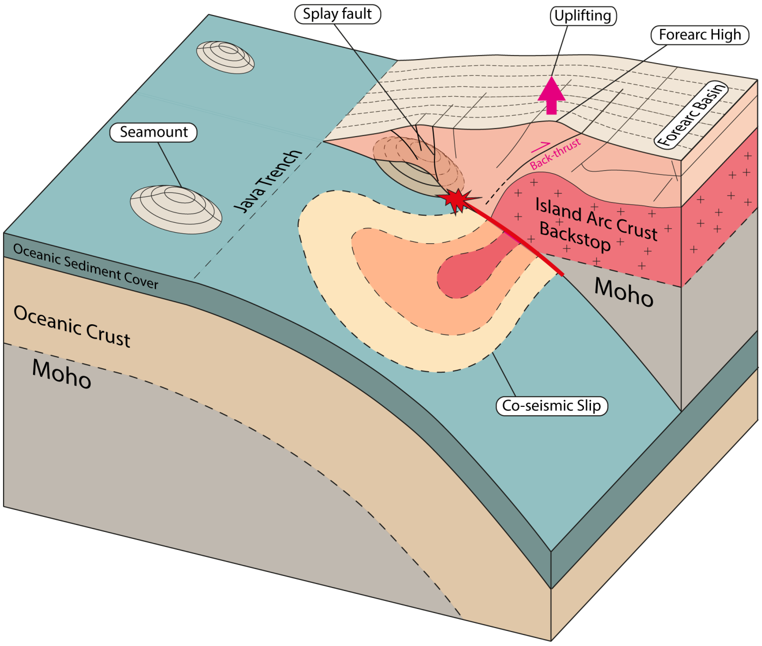

Figure 5. Conceptual seismo-tectonic model of the eastern Java margin in the region of the 1994 tsunami earthquake. Back-thrusting above the island arc crust backstop causes locally enhanced uplift of the forearc high. The 1994 hypocentre (red star) originated at the leading edge of a subducting seamount. The seamount stalled the co-seismic slip propagation locally along the plate boundary.

their own size (Ruh et al., 2016). This would be approximately 1250 km^2 for a seamount of over 40 km in diameter, as is the one observed, which could be enough to generate an earthquake of M 7–8 (Blaser et al., 2010). From this, we conclude that increased shear stress in front of the subducting seamount may have preconditioned the 1994 Java tsunami earthquake.

The warping of the slip model isolines around the subducting seamount (Fig. 1b) indicates that the seamount acted as a geometrical barrier at shallow depth during the co-seismic phase. Along the seismic section BGR06_305, the co-seismic slip value tracked from the model of Bilek and Engdahl (2007) illustrates a low slip value in the seamount region, compared to a much higher value further down-dip (Fig. 2d). Yang et al. (2012, 2013) modelled a dynamic rupture scenario with a seamount as a seismic barrier. The seamount imaged on our seismic profile may have halted seismic rupture at its leading edge, while rupture might have progressed closer to the trench to the west and east of the seamount (Figs. 1b and 5). Due to the lack of 3D seismic coverage of the rupture area, the exact structural control on the three-dimensional evolution of the rupture cannot be constrained. A similar mechanism of plate boundary rupture terminating against subducting lower plate relief is, however, discussed for the 2006 Java tsunami earthquake (Bilek and Engdahl, 2007) as well as numerous other plate boundary events (Wang and Bilek, 2011, and references therein).

5 Conclusions

A re-processed multichannel seismic reflection image with effective seafloor multiple suppression and a combined subsurface velocity from reflection and refraction tomography reveals a large subducting seamount at shallow depth (2–8 km below seafloor) trench-ward of the rupture area of the 1994 Java tsunami earthquake. Lateral shortening and vertical thickening of the upper plate control the uplift of the forearc high, manifested in active back-thrusting along distinct fault planes above the island arc crust backstop (Fig. 5). The 1994 earthquake main shock hypocentre and main co-seismic slip patch were located in front of the shallow subducting seamount. The wrapping of the co-seismic slip contours around this seamount suggests that it may have acted as a seismic barrier during the 1994 Java tsunami earthquake (Fig. 1). These observations suggest that the seamount diverted the co-seismic rupture propagation in the up-dip direction and document the control of the shallow marine forearc structure on co-seismic rupture distribution (Fig. 5).

Data availability. The pre-stack depth migration section of the profile BGR06_305 is available upon reasonable request. Bathymetric data from R/V *Sonne* cruise SO190 can be requested through the German Bundesamt für Seeschifffahrt und Hydrographie (2021, BSH; http://www.bsh.de). Aftershock data displayed in Figs. 1b and 2c are available through the ISC-EHB Bulletin catalogue (https://doi.org/10.31905/PY08W6S3; Engdahl et al., 2020). Focal mechanisms are available through the gCMT catalogue (https://

www.globalcmt.org/; Dziewonski et al., 1981; Ekström et al., 2021). The free-air gravity data shown in Fig. 1c are available through https://topex.ucsd.edu/marine_grav/mar_grav.html (Sandwell et al., 2014).

Supplement. The supplement related to this article is available online at: https://doi.org/10.5194/se-12-2467-2021-supplement.

Author contributions. YX and DK performed the computations and are responsible for the main processing. YX, JG, DK, BM, MR, MS, DL and HK helped to strengthen the overall scope and added to interpretational aspects and the discussion of the presented results. MS made the data available and was responsible for the navigation and geometry processing. YX, JG, and HK wrote the article, and all authors contributed equally to proofreading and final preparation of the paper.

Competing interests. The contact author has declared that neither they nor their co-authors have any competing interests.

Acknowledgements. The seismic data were processed with Schlumberger's Omega2 seismic processing suite OMEGA and Seismic Unix – an open-source software package for seismic research and processing, Centre for Wave Phenomena, Colorado School of Mines. Bathymetry and seismic images are plotted by the Generic Mapping Tools (GMT). We thank Susan L. Bilek, and Rachel E. Abercrombie for sharing the co-seismic slip models of the 1994 Java tsunami earthquake. We thank Nathan L. Bangs and Sara Martínez-Loriente for insightful comments and suggestions that helped us improve the paper. Figs. 1 and 4 were prepared using GMT (Wessel et al., 2019).

Financial support. This research has been supported by the Bundesministerium für Bildung und Forschung (grant nos. 03G0190A and 03G0190B) and the China Scholarship Council (grant no. 201506400067).

The article processing charges for this open-access publication were covered by the GEOMAR Helmholtz Centre for Ocean Research Kiel.

Review statement. This paper was edited by Mark Allen and reviewed by Sara Martínez-Loriente and Nathan Bangs.

References

Abercrombie, R. E., Antolik, M., Felzer, K., Ekstrom, G., and Ekström, G.: The 1994 Java tsunami earthquake: Slip over a subducting seamount, J. Geophys. Res. Solid Earth, 106, 6595–6607, https://doi.org/10.1029/2000jb900403, 2001.

Ammon, C. J., Kanamori, H., Lay, T., and Velasco, A. A.: The 17 July 2006 Java tsunami earthquake, Geophys. Res. Lett., 33, 1–5, https://doi.org/10.1029/2006GL028005, 2006.

Bell, R., Sutherland, R., Barker, D. H. N., Henrys, S., Bannister, S., Wallace, L., and Beavan, J.: Seismic reflection character of the Hikurangi subduction interface, New Zealand, in the region of repeated Gisborne slow slip events, Geophys. J. Int., 180, 34–48, https://doi.org/10.1111/j.1365-246X.2009.04401.x, 2010.

Bilek, S. L. and Engdahl, E. R.: Rupture characterization and aftershock relocations for the 1994 and 2006 tsunami earthquakes in the Java subduction zone, Geophys. Res. Lett., 34, L20311, https://doi.org/10.1029/2007GL031357, 2007.

Bilek, S. L. and Lay, T.: Tsunami earthquakes possibly widespread manifestations of frictional conditional stability, Geophys. Res. Lett., 29, 1–4, https://doi.org/10.1029/2002GL015215, 2002.

Blaser, L., Krüger, F., Ohrnberger, M., and Scherbaum, F.: Scaling relations of earthquake source parameter estimates with special focus on subduction environment, Bull. Seismol. Soc. Am., 100, 2914–2926, https://doi.org/10.1785/0120100111, 2010.

Bundesamt für Seeschifffahrt und Hydrographie (BSH): Homepage, available at: https://www.bsh.de/, last access: 25 October 2021.

Byrne, D. E., Wang, W., and Davis, D. M.: Mechanical role of backstops in the growth of forearcs, Tectonics, 12, 123–144, https://doi.org/10.1029/92TC00618, 1993.

Dziewonski, A. M. and Anderson, D. L.: Preliminary reference Earth model, Phys. Earth Planet. Inter., 25, 297–356, https://doi.org/10.1016/0031-9201(81)90046-7, 1981 (data available at: https://www.globalcmt.org/, last access: 4 December 2018).

Ekström, G., Nettles, M., and Dziewoński, A. M.: The global CMT project 2004–2010: Centroid-moment tensors for 13,017 earthquakes, Phys. Earth Planet. Inter., 200–201, 1–9, https://doi.org/10.1016/j.pepi.2012.04.002, 2012 (data available at: https://www.globalcmt.org/, last access: 4 December 2018).

Engdahl, E. R., Di Giacomo, D., Sakarya, B., Gkarlaouni, C. G., Harris, J., and Storchak, D. A.: ISC-EHB 1964–2016, an Improved Data Set for Studies of Earth Structure and Global Seismicity, Earth Sp. Sci., 7, 1–13, https://doi.org/10.1029/2019EA000897, 2020 (data available at: https://doi.org/10.31905/PY08W6S3).

Fan, W., Bassett, D., Jiang, J., Shearer, P. M., and Ji, C.: Rupture evolution of the 2006 Java tsunami earthquake and the possible role of splay faults, Tectonophysics, 721, 143–150, https://doi.org/10.1016/j.tecto.2017.10.003, 2017.

GEBCO Bathymetric Compilation Group 2020: The GEBCO_2020 Grid – a continuous terrain model of the global oceans and land. British Oceanographic Data Centre, National Oceanography Centre [data set], NERC, UK, https://doi.org/10/dtg3, 2020.

Geersen, J.: Sediment-starved trenches and rough subducting plates are conducive to tsunami earthquakes, Tectonophysics, 762, 28–44, https://doi.org/10.1016/j.tecto.2019.04.024, 2019.

Guitton, A. and Verschuur, D. J.: Adaptive subtraction of multiples using the L1-norm, Geophys. Prospect., 52, 27–38, 2004.

Hananto, N. D., Leclerc, F., Li, L., Etchebes, M., Carton, H., Tapponnier, P., Qin, Y., Avianto, P., Singh, S. C., and Wei, S.: Tsunami earthquakes: Vertical pop-up expulsion at the forefront of subduction megathrust, Earth Planet. Sci. Lett., 538, 1–14, https://doi.org/10.1016/j.epsl.2020.116197, 2020.

Kanamori, H.: Mechanism of tsunami earthquakes, Phys. Earth Planet. Inter., 6, 346–359, https://doi.org/10.1016/0031-9201(72)90058-1, 1972.

Kodaira, S., Takahashi, N., Nakanishi, A., Miura, S., and Kaneda, Y.: Subducted seamount imaged in the rupture zone of the 1946 Nankaido earthquake, Science 289, 104–106, https://doi.org/10.1126/science.289.5476.104, 2000.

Kopp, H., Flueh, E. R., Petersen, C. J., Weinrebe, W., Wittwer, A., and Meramex Scientists: The Java margin revisited: Evidence for subduction erosion off Java, Earth Planet. Sci. Lett., 242, 130–142, https://doi.org/10.1016/j.epsl.2005.11.036, 2006.

Kopp, H.: The Java convergent margin: Structure, seismogenesis and subduction processes, Geol. Soc. Spec. Publ., 355, 111–137, https://doi.org/10.1144/SP355.6, 2011.

Kopp, H. and Kukowski, N.: Backstop geometry and accretionary mechanics of the Sunda margin, Tectonics, 22, 1072, https://doi.org/10.1029/2002TC001420, 2003.

Lallemand, S. and Le Pichon, X.: Coulomb wedge model applied to the subduction of seamounts in the Japan Trench, Geology, 15, 1065–1069, https://doi.org/10.1130/0091-7613(1987)15<1065:CWMATT>2.0.CO;2, 1987.

Lüschen, E., Müller, C., Kopp, H., Engels, M., Lutz, R., Planert, L., Shulgin, A., Djajadihardja, Y. S.: Structure, evolution and tectonic activity of the eastern Sunda forearc, Indonesia, from marine seismic investigations, Tectonophysics, 508, 6–21, https://doi.org/10.1016/j.tecto.2010.06.008, 2011.

Martínez-Loriente, S., Sallarès, V., R. Ranero, C., B. Ruh, J., Barckhausen, U., Grevemeyer, I., and Bangs, N.: Influence of Incoming Plate Relief on Overriding Plate Deformation and Earthquake Nucleation: Cocos Ridge Subduction (Costa Rica), Tectonics, 38, 4360–4377, https://doi.org/10.1029/2019TC005586, 2019.

Masson, D. G., Parson, L. M., Milsom, J., Nichols, G., Sikumbang, N., Dwiyanto, B., and Kallagher, H.: Subduction of seamounts at the Java Trench: a view with long-range sidescan sonar, Tectonophysics, 185, 51–65, https://doi.org/10.1016/0040-1951(90)90404-V, 1990.

Müller, C. and Neben, S.: Research Cruise SO190 Leg 1, SINDBAD, Seismic and geoacoustic investigations along the Sunda-Banda Arc transition (Seismische und geoakustische Untersuchungen entlang des Übergangs vom Sunda- zum Banda-Bogen) with RV SONNE, Jakarta, Indonesia 9 October, Bundesanstalt für Geowissenschaften und Rohstoffe, Hannover, Germany, 142, https://doi.org/10.2312/cr_so190_1, 2006.

Planert, L., Kopp, H., Lueschen, E., Mueller, C., Flueh, E. R., Shulgin, A., Djajadihardja, Y., and Krabbenhoeft, A.: Lower plate structure and upper plate deformational segmentation at the Sunda-Banda arc transition, Indonesia, J. Geophys. Res.-Sol. Ea., 115, 1–25, https://doi.org/10.1029/2009jb006713, 2010.

Polet, J. and Kanamori, H.: Shallow subduction zone earthquakes and their tsunamigenic potential, Geophys. J. Int., 142, 684–702, https://doi.org/10.1046/j.1365-246X.2000.00205.x, 2000.

Ruh, J. B., Sallarès, V., Ranero, C. R., and Gerya, T.: Crustal deformation dynamics and stress evolution during seamount subduction: High-resolution 3-D numerical modeling, J. Geophys. Res.-Sol. Ea., 121, 6880–6902, https://doi.org/10.1002/2016JB013250, 2016.

Sallarès, V. and Ranero, C. R.: Upper-plate rigidity determines depth-varying rupture behaviour of megathrust earthquakes, Nature, 576, 96–101, https://doi.org/10.1038/s41586-019-1784-0, 2019.

Sandwell, D. T., Müller, R. D., Smith, W. H. F., Garcia, E., and Francis, R.: New global marine gravity model from CryoSat-2 and Jason-1 reveals buried tectonic structure, Science, 346, 65–67, https://doi.org/10.1126/science.1258213, 2014 (data available at: https://topex.ucsd.edu/marine_grav/mar_grav.html, last access: 8 July 2021).

Satake, K., Fujii, Y., Harada, T., and Namegaya, Y.: Time and space distribution of co-seismic slip of the 2011 Tohoku earthquake as inferred from Tsunami waveform data, Bull. Seismol. Soc. Am., 103, 1473–1492, https://doi.org/10.1785/0120120122, 2013.

Satake, K. and Tanioka, Y.: Sources of Tsunami and Tsunamigenic Earthquakes in Subduction Zones, Pure Appl. Geophys., 154, 467–483, https://doi.org/10.1007/s000240050240, 1999.

Scholz, C. H., Ando, R., and Shaw, B. E.: The mechanics of first order splay faulting: The strike-slip case, J. Struct. Geol., 32, 118–126, https://doi.org/10.1016/j.jsg.2009.10.007, 2010.

Şen, A. T., Cesca, S., Lange, D., Dahm, T., Tilmann, F., and Heimann, S.: Systematic changes of earthquake rupture with depth: A case study from the 2010 M_w 8.8 Maule, Chile, earthquake aftershock sequence, Bull. Seismol. Soc. Am., 105, 2468–2479, https://doi.org/10.1785/0120140123, 2015.

Seno, T.: Tsunami earthquakes as transient phenomena, Geophys. Res. Lett., 29, 1419, https://doi.org/10.1029/2002gl014868, 2002.

Shulgin, A., Kopp, H., Mueller, C., Planert, L., Lueschen, E., Flueh, E. R., and Djajadihardja, Y.: Structural architecture of oceanic plateau subduction offshore Eastern Java and the potential implications for geohazards, Geophys. J. Int., 184, 12–28, https://doi.org/10.1111/j.1365-246X.2010.04834.x, 2011.

Sun, T., Saffer, D., and Ellis, S.: Mechanical and hydrological effects of seamount subduction on megathrust stress and slip, Nat. Geosci., 13, 249–255, https://doi.org/10.1038/s41561-020-0542-0, 2020.

Tanioka, Y. and Satake, K.: Tsunami generation by horizontal displacement of ocean bottom, Geophys. Res. Lett., 23, 861–864, https://doi.org/10.1029/96GL00736, 1996.

Tanioka, Y., Ruff, L., and Satake, K.: What controls the lateral variation of large earthquake occurrence along the Japan Trench?, Isl. Arc, 6, 261–266, https://doi.org/10.1111/j.1440-1738.1997.tb00176.x, 1997.

Tanioka, Y. and Seno, T.: Sediment effect on tsunami generation of the 1896 Sanriku Tsunami Earthquake, Geophys. Res. Lett., 28, 3389–3392, https://doi.org/10.1029/2001GL013149, 2001.

Tsuji, Y., Imamura, F., Matsutomi, H., Synolakis, C. E., Nanang, P. T., Jumadi, Harada, S., Han, S. S., Arai, K., and Cook, B.: Field survey of the East Java earthquake and tsunami of June 3, 1994, Pure Appl. Geophys. PAGEOPH, 144, 839–854, https://doi.org/10.1007/BF00874397, 1995.

Verschuur, D. J., Berkhout, A. J., and Wapenaar, C. P. A.: Adaptive surface-related multiple elimination, Geophysics, 57, 1166–1177, 1992.

von Huene, R., Miller, J. J., Klaeschen, D., and Dartnell, P.: A Possible Source Mechanism of the 1946 Unimak Alaska Far-Field Tsunami: Uplift of the Mid-Slope Terrace Above a Splay Fault Zone, Pure Appl. Geophys., 173, 4189–4201, https://doi.org/10.1007/s00024-016-1393-x, 2016.

Wang, K. and Bilek, S. L.: Do subducting seamounts generate or stop large earthquakes?, Geology, 39, 819–822, https://doi.org/10.1130/G31856.1, 2011.

Wendt, J., Oglesby, D. D., and Geist, E. L.: Tsunamis and splay fault dynamics, Geophys. Res. Lett., 36, 1–5, https://doi.org/10.1029/2009GL038295, 2009.

Wessel, P., Luis, J. F., Uieda, L., Scharroo, R., Wobbe, F., Smith, W. H. F., and Tian, D.: The Generic Mapping Tools Version 6, Geochemistry, Geophys. Geosystems, 20, 5556–5564, https://doi.org/10.1029/2019GC008515, 2019.

Yang, H., Liu, Y., and Lin, J.: Effects of subducted seamounts on megathrust earthquake nucleation and rupture propagation, Geophys. Res. Lett., 39, 2–7, https://doi.org/10.1029/2012GL053892, 2012.

Yang, H., Liu, Y., and Lin, J.: Geometrical effects of a subducted seamount on stopping megathrust ruptures, Geophys. Res. Lett., 40, 2011–2016, https://doi.org/10.1002/grl.50509, 2013.

Xia, Y., Klaeschen, D., Kopp, H., and Schnabel, M.: Reflection tomography by depth warping: A case study across the Java trench, Solid Earth Discuss. [preprint], https://doi.org/10.5194/se-2021-40, in review, 2021.

Supplement of Solid Earth, 12, 2467–2477, 2021
https://doi.org/10.5194/se-12-2467-2021-supplement

Solid Earth
Open Access

Supplement of

Marine forearc structure of eastern Java and its role in the 1994 Java tsunami earthquake

Yueyang Xia et al.

Correspondence to: Yueyang Xia (yxia@geomar.de)

Table S 1. Seismic processing sequences.

Sequence Step Names
Normal and Nominal Geometry Establishment with Common Midpoint (CMP) spacing of 6.25 m
Anomalous and Random Noise Attenuation
Offset regularization and Interpolation to Zero Offset
Interactive Velocity Analysis in Time Domain
Initial Time-domain Velocity building
Shot Interpolation for Aliasing Elimination (from 50 m to 12.5 m shot distance)
Free Surface-Related Multiple Prediction
Multiple Attenuation 1: Frequency-Split 2D Cascaded Adaptive Filter
2: Radon Dip Filter
3: Inside Mute and Amplitude Clipping
Kirchhoff Pre-stack Time Migration
Initial Depth Domain Velocity Building (Merge with Wide-angle model)
Kirchhoff Pre-stack Depth Migration with Common Image Point (CIP) gather output (Initial)
Iteration Loop:
CIP Gather Pre-filtering for Non-Rigid-Matching (NRM) Calculation
NRM Displacement Field Calculation
CIP Gather Residual Move-Out (RMO) Calculation from NRM Field
Dip and Coherency Field Estimation from Depth Migrated Stack
Ray-based RMO Depth-Tomography with preconditioning of Dip and Coherency Field
Update the Tomography Model Properties to Reduce the CIP-gather RMO
Kirchhoff Pre-stack Depth Migration with CIP-gather Output
Iteration Stopped if RMO is Minimized
Stacking of the Pre-stack Depth Migrated Gathers

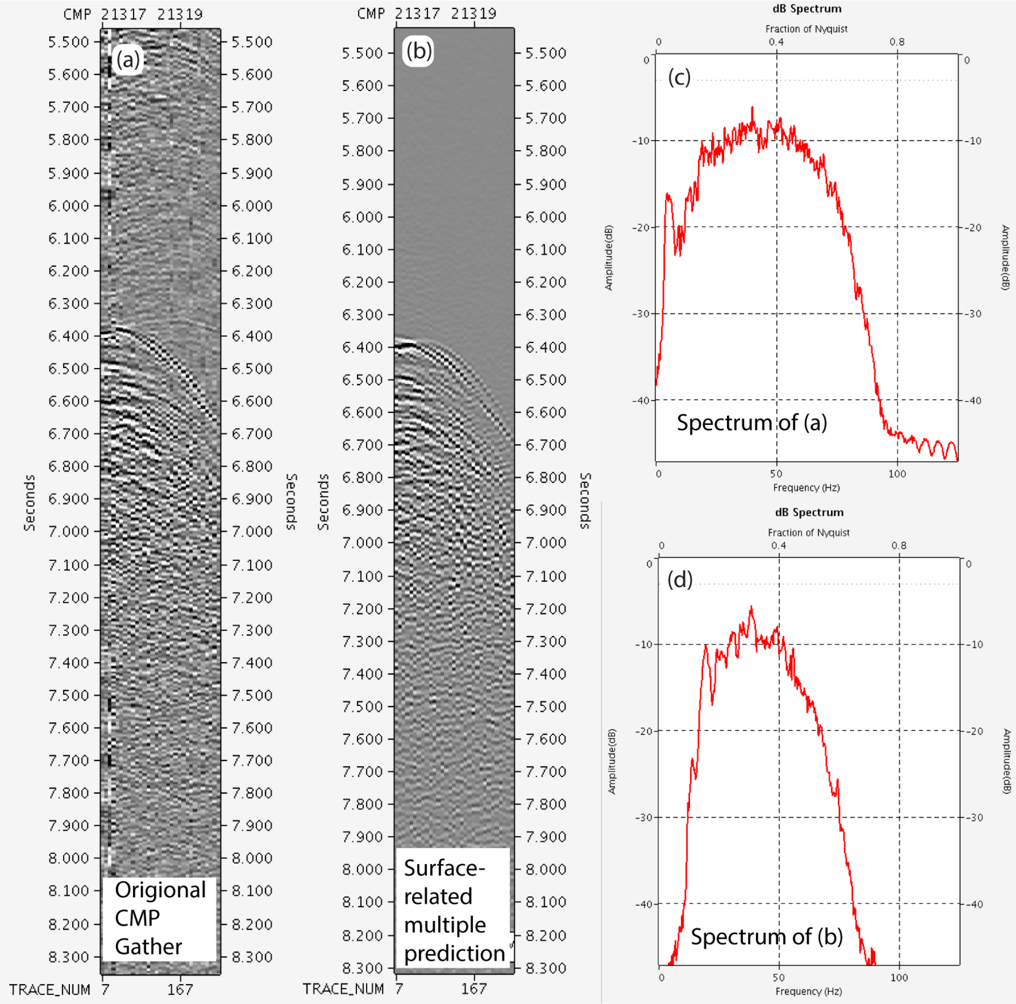

Figure S1. (a) Original CMP gather with multiple contamination. (b) Free Surface-related predicted multiple model. (c) The frequency spectrum of the original data. (d) The frequency spectrum of the modelled multiple.

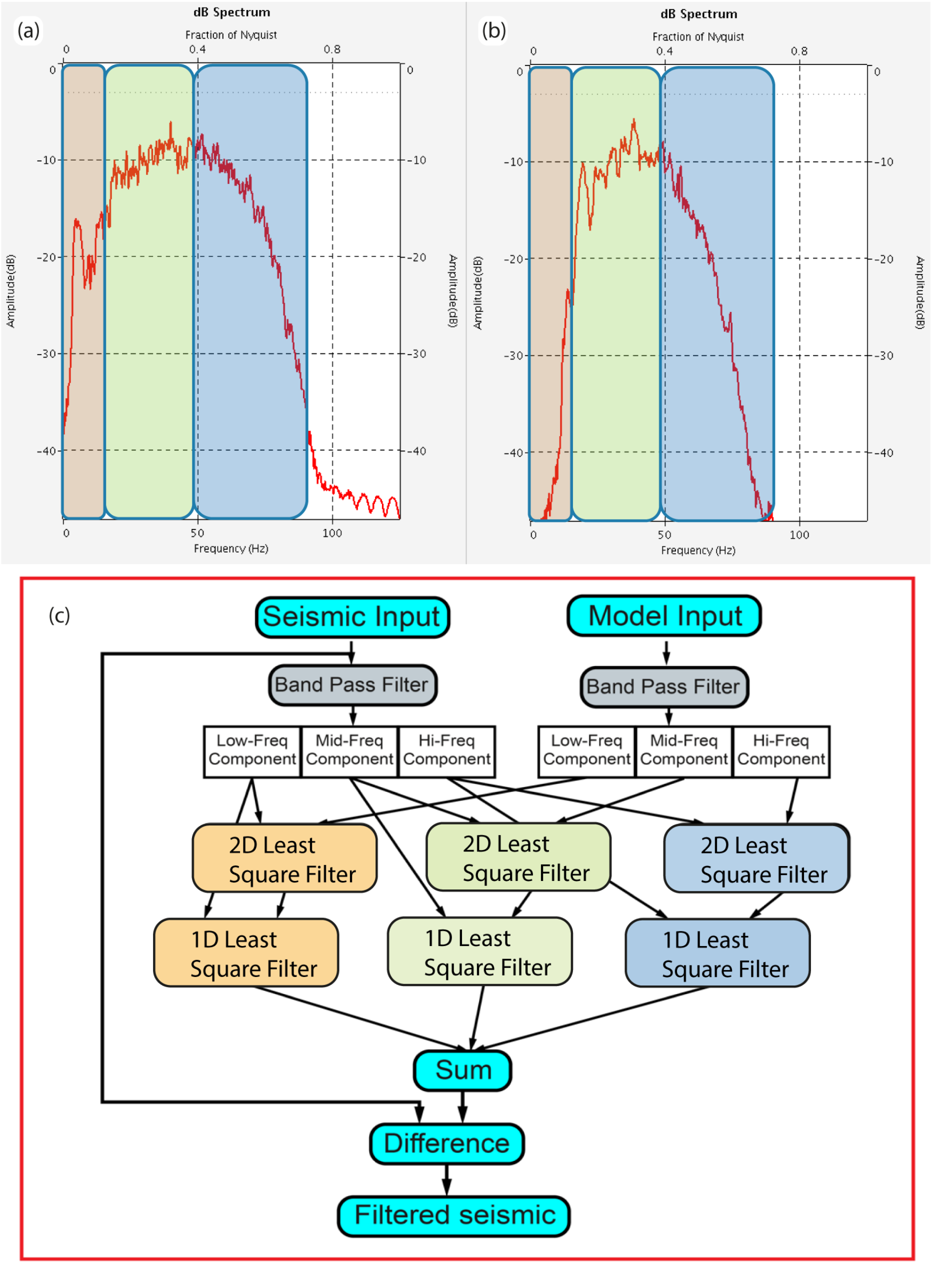

Figure S2. (a) Frequency bands segmentation of the original data used in the adaptive subtraction. (b) Frequency bands segmentation of the modelled multiple used in the adaptive subtraction. (c) Adaptive subtraction strategy.

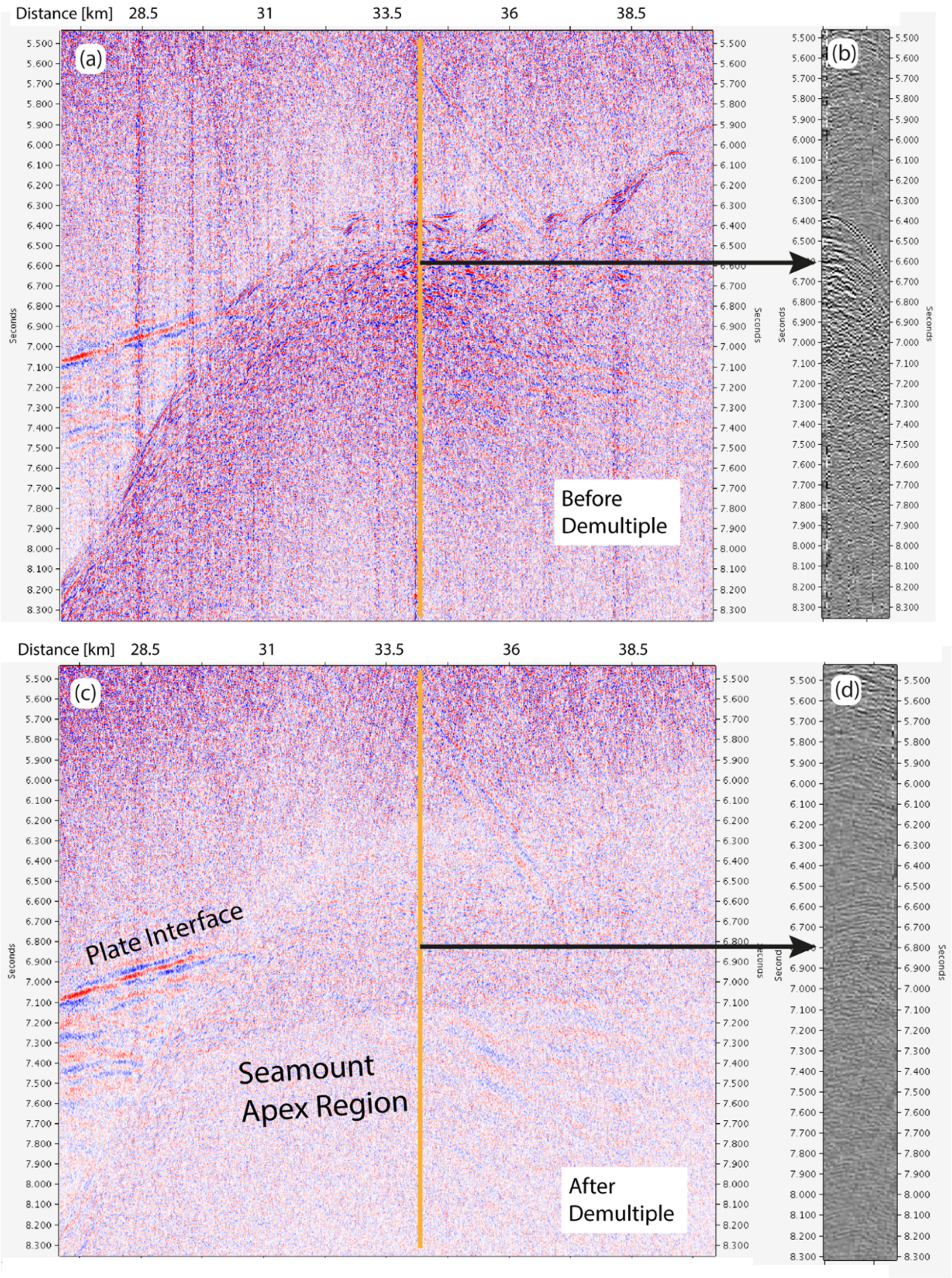

Figure S3. (a) Original MCS stacked image with multiple contamination. (b) Original CMP gather. (c) MCS stacked section after multiple attenuation. (d) CMP gather after multiple attenuation.

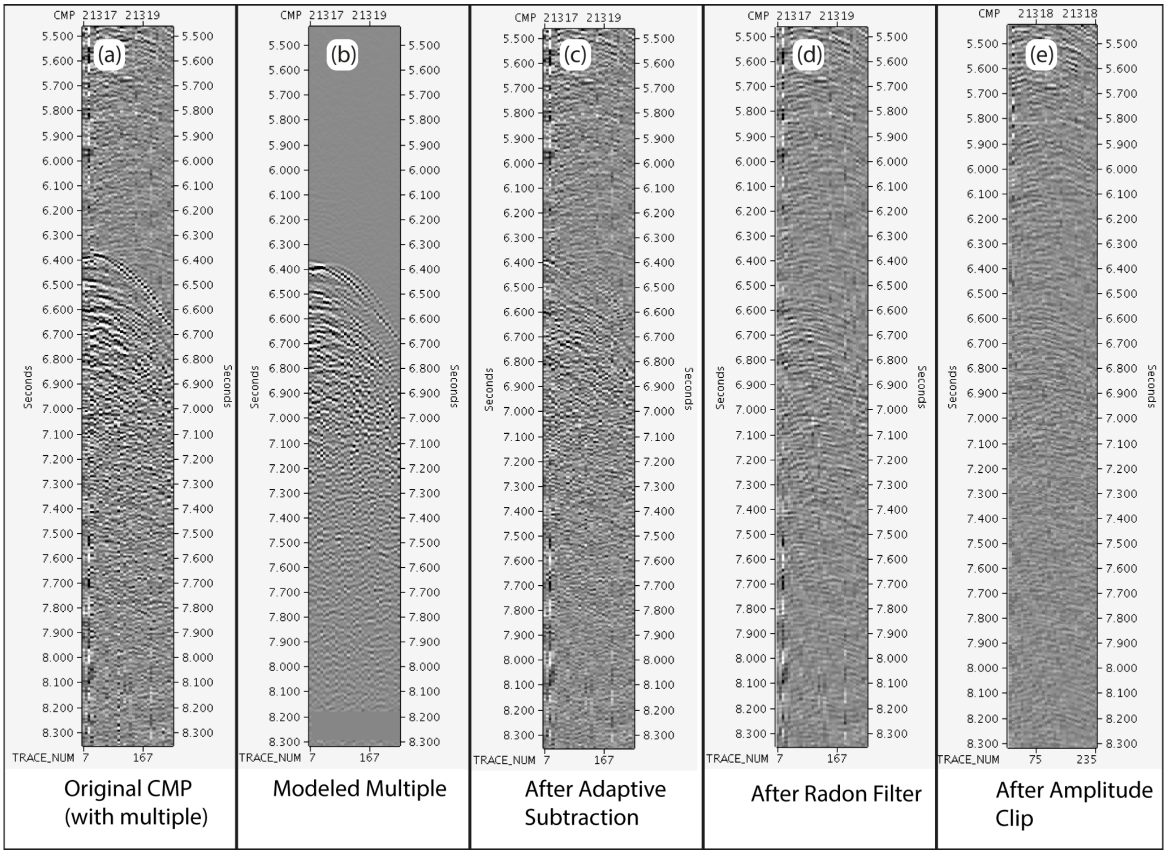

Original CMP (with multiple)

Modeled Multiple

After Adaptive Subtraction

After Radon Filter

After Amplitude Clip

Figure S4. Multiple attenuation working flow in CMP domain (panels a to e). (a) Original CMP gather with multiple contamination. (b) Surface related modelled multiple. (c) CMP gather after frequency split adaptive subtraction. (d) CMP gather after additional Radon filter. (e) CMP gather after additional amplitude clip.

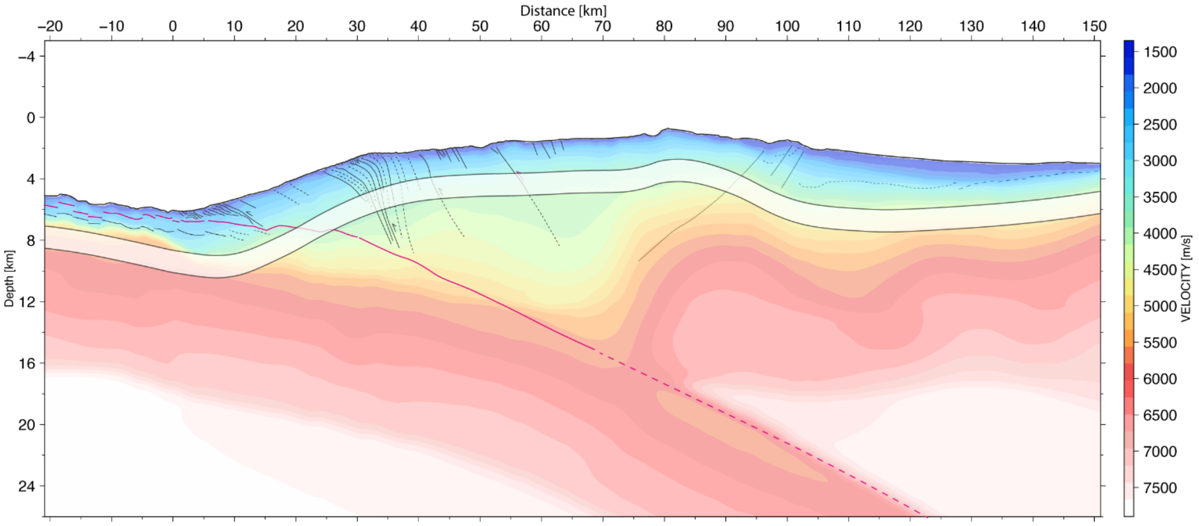

Figure S5. The final velocity model merged from the multi-channel seismic velocity analysis (above the white transparent band) and the wide-angle velocity model (Shulgin et al., 2011) (below the white transparent band). The line drawing is based on the final pre-stack depth migrated image.

CHAPTER 6

CONCLUSION AND OUTLOOK

6.1 Conclusion

The analyses of subducting seamounts and the processes of subduction accretion vs erosion are important to understand the tectonic evolution of the Java margin and the physical mechanism of the earthquake phenomena. Since thin (< 600 m) pelagic sediment covers the oceanic crust and the volume of the accretionary wedge is large, distinct basement relief breaches the sediment cover and is directly in contact with the upper plate accretionary wedge. This induces significant upper plate deformation as the seamount subducts. The eastern Java margin thus becomes one of the best candidates to study these tectonic and seismogenic effects related to seamount subduction.

The old subducting slab (oceanic plate age maximum 150 Ma) and the long convergence history (50 Ma) in the Java margin result in highly complex tectonic characteristics in the upper plate. Thus, it requires leading-edge processing approaches to correctly reveal the detailed structure from the seafloor surface to the plate interface. By using the innovative processing techniques (in Chapter 3) of reflection seismic tomography, Non-rigid matching, and the pre-stack depth migration, the multi-channel seismic profiles of eastern Java illustrated different sizes of the subducting oceanic relief (in Chapter 4), which are consistent with the bathymetry observation of the oceanic seafloor in the Roo Rise region.

Fortunately, different scales of subducting seamounts (diameters from 1 km to 40 km) with the corresponding upper plate deformation are observed in three of our four seismic profiles (Chapter 4). In principle, the numerous subducting features on the Roo Rise pushed the deformation front a maximum of 50 km from its idealized trend and uplifted the accretionary wedge to a much shallower water depth. The pushing and shortening processes result in enhanced compressional structures (e.g., fore-thrust, splay faults) at the leading edge of the subducting relief. In contrast, gravitational collapse (e.g., landslides, extensional escarpment, and slumps) occurs at the trailing edge of the subducting relief. As the material at the trailing edge of the seamount would anyway be firstly compressed before they experience gravitational collapse, the material behind the seamount always features a complex and chaotic signature due to the history of continuous reconstruction. This upper plate deformation related to large-scale relief (e.g., diameter 40 km in BGR06_305) would still be distinct and observable at 70 km away from the trench. The small-scale subducting features would only impact the upper plate in the outer regions (0-20 km from the trench) as is the case for the subducting ridges in lines BGR06_303 and 313 (width 4 – 7 km).

Being a rigid geometrical irregularity, the subducting seamounts abraded, deformed, and permanently removed material from the lower part of the accretionary wedge. As a result, a distinct plate interface reflection with a reversed polarity wavelet (compared to the seafloor reflection) is observed branching out from the reflection of the top of the oceanic crust on both leading and trailing edges of the subducting relief. These are direct geophysical observations of subduction erosion, which reduced the volume of the upper plate accretionary wedge in eastern Java.

Though lacking historical recorded catastrophic earthquakes (M>8.5), the subduction of the Indo-Australia plate still poses a significant risk to the coastal populations due to the high risks of tsunamis (e.g., tsunami earthquakes in 1994 and 2006) at the Java segment. In Chapter 5, we compared the hypocentre and the inverted co-seismic slip model (Bilek & Engdahl, 2007) of the 1994 Java earthquake (Mw = 7.8) with the seamount location observed in profile BGR06_305. The earthquake ruptured a large area in front of the subducting seamount, and the co-seismic slip model illustrates that the slip value at the seamount region is relatively low compared to its vicinity. This comparison indicates that even though the large subducting seamount could host large locking patches in front of it, the seamount itself stops the propagation of the co-seismic rupture as a geometrical irregularity. The abundant normal faulting aftershocks and the complete absence of thrust fault aftershocks of the 1994 earthquake imply a complete stress release of the main event and further a decoupled plate interface in the seamount region.

6.2 Outlook

The study presented here successfully identifies the existence and the exact locations of the subducting oceanic basement relief in the eastern Java margin from legacy seismic data. We observed seamounts in the along-dip seismic profiles, but we did not confirm their lateral extent in the along-strike direction due to the limited geophysical data coverage. The accretionary wedge here shows a pronounced along-strike structural heterogeneity, which could not be fully and effectively scanned and imaged by the sparse 2-dimensional seismic lines. Also, as the SO190 multibeam bathymetry data reveal possible strike-slip faults at the eastern flank of the subducting seamount at the location of profile BGR06_305, whether the western flank is presenting a symmetrical signature is unknown due to the lack the bathymetry data coverage. Thus, multibeam bathymetry scanning and denser seismic lines, especially lines covering the crests of the major forearc uplift, should be acquired to resolve the subducting reliefs' exact 3-D geometries and upper plate deformation.

Despite a weakly coupled and creeping plate interface inferred from this study, the exact physical properties of the plate interface's gouge and the coupling status at the seamount region could only be surveyed by long-term seafloor geodesy and heat flux observations. Deep-water pressure sensors would be helpful in detecting the creeping and slow slip events at the seamount region, as they are observed similarly from the Hikurangi subduction zone and Nankai trough (Araki et al., 2017; Wallace et al., 2016).

Geodynamic and geologic studies of the eastern Java subducting seamount should be continued to understand the seamount's physical connection to the megathrust earthquake. Serious attention should be paid to other regions with abnormal upper plate deformation, which indicates possible subducting seamounts underneath (e.g., at 110°E) in the Java segment. The lack of large earthquakes in recorded history in that region does not preclude the potential earthquake and tsunami from rupturing in a similar moderate size, but with high tsunami run-up events like the 1994 earthquake. The high population density of Java might still be threatened by another significant impact of the earthquake hazard in the future.

Reference:

Araki, E., Saffer, D. M., Kopf, A. J., Wallace, L. M., Kimura, T., Machida, Y., et al. (2017). Recurring and triggered slow-slip events near the trench at the Nankai Trough subduction megathrust. *Science*, *356*(6343), 1157–1160. https://doi.org/10.1126/science.aan3120

Bilek, S. L., & Engdahl, E. R. (2007). Rupture characterization and aftershock relocations for the 1994 and 2006 tsunami earthquakes in the Java subduction zone. *Geophysical Research Letters*, *34*(20), 1–5. https://doi.org/10.1029/2007GL031357

Wallace, L. M., Webb, S. C., Ito, Y., Mochizuki, K., Hino, R., Henrys, S., et al. (2016). Slow slip near the trench at the Hikurangi subduction zone, New Zealand. *Science*, *352*(6286), 701–704. https://doi.org/10.1126/science.aaf2349

Acknowledgement

First and foremost, I am very grateful for the supervision and support from Prof. Heidrun Kopp and Dr. Dirk Kläschen during the past seven years of study in GEOMAR for mentoring me and guiding me in the earth-science research. Thank you, Heidrun, for giving me this great opportunity to come to GEOMAR in Kiel to make this exciting adventure in Germany and in Europe. You always supported me in every aspect when I was down and encouraged me to keep on fighting. Dirk, thank you for teaching and mentoring me day after day and year after year, from geophysical theories to house renovation skills. The geophysical knowledge you taught me is the backbone of my life career. It is a pleasure to work and learn from both of you and to feel the enormous kindness inside you, which supported my life and study all the time! I look forward to ongoing and future collaborations with you.

I want to thank Dr. Jörg Geldmacher for lifting Xiaojun Long and me from the Hamburg Airport, offering us accommodation, and providing us with living information in Kiel on our first day in Germany. Many thanks to Jasmin Mögeltönder, Ann-Marie Völsch, and Julia Schätzel, who helped me greatly throughout the seven years at GEOMAR in dealing with all the paperwork, and other constructive help when I was struggling with my work. I want to thank Prof. Christian Berndt and your family for giving me my first Christmas gift in Kiel. Thanks to Stephanie Koch, Kuan-Ting Lin, Margit Wiprich, Felix Kästner, Tzu-Ting Chen, and Bo Ma who shared the office with me. Thanks for all the nice conversations, memorable vacations, and nice working climate, and your tolerance of my messy desk and arrogant mind.

Many thanks to Dr. Jacob Geersen, Dr. Dietrich Lange, Dr. Michael Schnabel, Dr. Michael Riedel, Dr. Gareth Crutchley, Dr. Tianhaozhe Sun, and Dr. Jonas Ruh for all the scientific discussion and writing contributions to our publications.

I would like to thank the China Scholarship Council and GEOMAR for financing my doctorate. Many thanks to all the scientists, friends, crews, and captains, on the research vessel Marian S. Maria for making a wonderful Chinese New Year party for me in the spring of 2018.

Thank you, Dr. Xiao Ma, and your wife, Mingshuang Sun, for inviting me to visit your home and offering me dinners time after time during the past years. Special thanks to my best friend Li Zhou for

helping me with my life, tolerancing my arrogant habit, organizing and having the greatest vacations, and cooking the best meal that I have ever tasted in my life. Thank you, my best buddies, Fengjie Li, Kai Deng, Huang Huang, Zhao Pan, Xiaojun Long, Bo Ma, and Hongpu Zhou, for having the best parties, and thank you for all your kind support. Special thanks to Ruixin Guo for supporting me during the past few years when I was down as the kindest friend and buddy. Thank you to all my friends in Kiel, Mario Veloso, Avrinder Singh, Habeeb Thanveer, Anne Krabbenhöft, Yu Ren, Yuhan Li, Anke Dannowski, Mbani Benson, Anouk Beniest, Helene Hilbert, Elisa Klein, Thore Sager, and so many of you.

I am very grateful for the support from Dr. Dachen Kang, Prof. Rongjie Bai, Mrs. Yanli Chai, Prof. Hao Liu, and Prof. Xin Su for inspiring me at the beginning to do my PhD and advising and mentoring me in my career development.

Of course, I would like to say thank you to my parents, Mr. Wei Xia and Mrs. Wanzhi Ji, and all my families for their infinite support, advice, and backing me up in the doctorate Odyssey.